

V. M. Biryukov
Y. A. Chesnokov
V. I. Kotov

Crystal Channeling and Its Application at High-Energy Accelerators



Springer



Accelerator Physics

Editors: F. Bonaudi
C.W. Fabjan

Springer-Verlag Berlin Heidelberg GmbH

Valery M. Biryukov Yuri A. Chesnokov
Vladilen I. Kotov

Crystal Channeling and Its Application at High-Energy Accelerators

Translated by V. M. Biryukov

With 122 Figures



Springer

Dr. Valery M. Biryukov
Dr. Yuri A. Chesnokov
Professor Vladilen I. Kotov
Institute for High Energy Physics
142284 Protvino, Moscow Region, Russia

Editors:

Professor F. Bonaldi
Professor C. W. Fabjan
CERN, Div. PPE
CH-1211 Genève 23, Switzerland

Library of Congress Cataloging-in-Publication Data

Biryukov, Valery M., 1961-
Crystal channeling and its application at high-energy accelerators / Valery M. Biryukov, Yuri A. Chesnokov, Vladilen I. Kotov.
p. cm.
Includes bibliographical references.

1. Channeling (Physics) 2. Crystals--Effect of radiation on.
3. Particle accelerators. I. Chesnokov, Yuri A., 1955- .
II. Kotov, V. I. (Vladilen Ivanovich) III. Title.
QC176.8.C45B57 1996

530.4'16--dc20

96-28616

CIP

ISBN 978-3-642-08238-2 ISBN 978-3-662-03407-1 (eBook)
DOI 10.1007/978-3-662-03407-1

This work is subject to copyright. All rights are reserved, whether the whole or part of the material is concerned, specifically the rights of translation, reprinting, reuse of illustrations, recitation, broadcasting, reproduction on microfilm or in any other way, and storage in data banks. Duplication of this publication or parts thereof is permitted only under the provisions of the German Copyright Law of September 9, 1965, in its current version, and permission for use must always be obtained from Springer-Verlag. Violations are liable for prosecution under the German Copyright Law.

© Springer-Verlag Berlin Heidelberg 1997

Originally published by Springer-Verlag Berlin Heidelberg New York in 1997.

Softcover reprint of the hardcover 1st edition 1997

The use of general descriptive names, registered names, trademarks, etc. in this publication does not imply, even in the absence of a specific statement, that such names are exempt from the relevant protective laws and regulations and therefore free for general use.

Typesetting: Data conversion by Springer-Verlag

Cover design: *design & production* GmbH, Heidelberg

SPIN 10467741 55/3144 - 5 4 3 2 1 0 - Printed on acid-free paper

Preface

“Nature performs nothing vainly,
and makes nothing unnecessary”

Aristotle

Interest in the passage of charged particles through crystals first appeared at the beginning of this century following experiments on x-ray diffraction in crystal lattices, which provided the proof of an ordered distribution of atoms in a crystal. Stark [1] put forward the hypothesis that certain directions in a crystal should be relatively transparent to charged particles.

These first ideas on the channeling of charged particles in crystals were forgotten but became topical again in the early 1960s when the channeling effect was rediscovered by computer simulation [2] and in experiments [3] that revealed anomalously long ion ranges in crystals. The orientational effects during the passage of charged particles through crystals have been found for a whole range of processes characterized by small impact parameters for collisions between particles and atoms: nuclear reactions, large-angle scattering, energy losses. Lindhard explained the channeling of charged particles in crystals [4]. The results of the numerous investigations into the channeling of low-energy (amounting to several MeV) charged particles in crystals have been summarized in several monographs and reviews [5–8].

A new stage in the investigation into the channeling of charged particles is its extension to high energies. This stage began at the European Laboratory for Nuclear Research (CERN) in Geneva in 1974. In 1976, Tsyganov proposed the possibility of bending the high-energy charged particles by means of bent crystals. This idea was confirmed in pioneering experiments carried out in 1979 in a collaboration between the Joint Institute of Nuclear Research (JINR) in Dubna and the Fermi National Accelerator Laboratory (FNAL) in Batavia, IL. In the first experiments on bent crystals the efficiency of the particle beam deflection (i.e., the ratio of the intensity of the deflected beam to that incident on a crystal) was very low (a fraction of 1%). But in the subsequent experiments it has been improved to 10%, and has recently reached a record value of $\sim 50\%$ in experiments on the deflection of a 450-GeV proton beam at CERN.

Experiments carried out in 1990 on the accelerator at the Institute of High Energy Physics (IHEP) in Protvino, in collaboration with the Sankt-

Peterburg Institute of Nuclear Physics (PINP) in Gatchina, demonstrated that it is possible not only to deflect charged particle beams in a bent crystal but also to focus them in the bending plane. This can be achieved if the exit face of the crystal is shaped to form a cylindrical surface, so that all the planes tangential to the atomic planes in the exit face of a crystal intersect at some distance from the crystal. Bent crystals, with their extremely high interplanar electric fields (10^9 Vcm^{-1} or higher), can thus be used to control beams of charged particles with high and superhigh energies. This possibility has been realized by many research centers working in high-energy physics. Studies are being carried out into the use of bent crystals for the extraction of accelerated proton beams, in beam lines, and in certain experiments. In all three cases some interesting and promising results have been obtained. In particular, bent crystals have been used to extract accelerated protons with energies up to 8 GeV at JINR (1984), up to 70 GeV at IHEP (1989), and 120 GeV at CERN (1993). In the JINR experiment the extraction efficiency was 10^{-4} , but it has been improved to $\sim 10^{-2}$ at IHEP and to 10^{-1} at CERN. The experiments proceeding at CERN and started at FNAL are designed to achieve a highly efficient extraction of a proton beam, so that the results can then be used to develop an extraction system for supercolliders such as the large hadron collider (LHC), because the use of crystals for this purpose seems to be the only method that can ensure simultaneously both the beam extraction and the experiments carried out in the collider mode.

Considerable interest is generated by the studies into channeling radiation, in crystals, of electrons and positrons with energies of hundreds of GeV, which are being carried out at CERN under the leadership of Uggerhøj. These studies show that at high energies, using the aligned crystals as radiators, one can obtain photon beams with an intensity two orders higher than the corresponding value in amorphous matter. Therewith, in a crystal as thin as $< 1 \text{ mm}$ the particles lose more than 50% of their energy by radiation. Under certain conditions narrow ($\sim 10\%$) peaks appear in the photon spectra at energies 0.7–0.8 times the primary energy of the electron. The results open up the possibility for experimental study of, e.g., the photoproduction of particles (also rare) in a new energy range of photon beams.

This book presents from a unified point of view the results of numerous studies in high-energy charged-particle channeling in crystals, which imply a possibility for their application at the modern accelerators in the extraction systems of accelerated particle beams, in beam lines, and in experiments.

The book is addressed to not only the specialists but also the broad audience of physicists and engineers working at accelerators and carrying out the experiments in high-energy physics.

The first two chapters consider the physical aspects of the charged-particle channeling in the straight and bent crystals. Different mechanisms of the particle capture into the channeling mode are analyzed, the diffusion theory of

the particle dechanneling is presented, and the effects due to various imperfections of the crystal lattice are considered.

The third chapter is devoted to the experimental studies directed at investigating the basic foundations of the channeling theory. The requirements for machining the crystals are formulated, the bending methods are discussed, and the experimental techniques are considered in detail. The experimental results are analyzed and compared to the theoretical predictions.

In the second half of the book (Chaps. 4–6) the crystal applications at high-energy accelerators are considered.

Chapter 4 is devoted to the problems of particle extraction by means of a bent crystal. The methods of calculation are presented. The systems for proton beam extraction from the 70-GeV accelerator at IHEP and 120-GeV SPS at CERN are considered. The possibilities of beam extraction from the accelerators at FNAL and LHC are discussed.

Chapter 5 considers the questions of crystal application to particle beam lines. The results of the studies into the resistance of crystals to radiation are discussed. The experience of the use of bent crystals for splitting the beams extracted from an accelerator, and for the creation of the test areas is generalized. The method of beam focusing by a bent crystal is presented, and its experimental results are analyzed. Based on the experimental data, the possibility of using a bent crystal for the diagnostics of particle beams is shown.

The final chapter is dedicated to the problems of crystal applications in an experiment. The ideas and proposals for how one can use bent crystals to measure the characteristics of short-lived particles (decay modes, lifetimes, magnetic moments) are discussed. The scheme of the experiment at FNAL for measuring the Σ^+ -hyperon spin precession in a bent crystal and determining its magnetic moment is considered. The process of the radiation of high-energy electron and positron beams in crystals is qualitatively considered. The results of the studies performed at CERN of the crystal channeling radiation for the hundreds-GeV electrons and positrons, which open up possibilities for the experimental research in a new energy range of photon beams, are reported. The scheme of formation of a polarized tagged photon beam is described and the characteristics of such a beam created at CERN for the experiments at the Ω spectrometer are given.

In conclusion we express our gratitude to Profs. H. Lengeler, C. Fabjan and F. Bonaudi for their active support of the idea to write this book. We are much indebted to Profs. E. Uggerhøj, N.F. Shulga and S.S. Gershtein, and to Drs. V. Maisheev and S. Bityukov for a number of useful comments, and in particular to Prof. Fabjan whose advice and suggestions have essentially helped us to improve the book. We are also grateful to L.M. Komarova, T.K. Lesnikova, and O.P. Laskovaya for a lot of technical help in the work on this book.

Table of Contents

1.	Channeling Phenomenon	1
1.1	Structure of Crystals	1
1.2	Electric Fields in Crystals	7
1.3	Particle Motion in the Potential of Atomic Planes	12
1.4	Dechanneling	17
1.4.1	Diffusion Theory	17
1.4.2	Single Electronic Scattering	21
1.4.3	Comments on the Diffusion Approach	23
1.5	Energy Loss	25
1.6	Axial Channeling	27
2.	Beam Deflection by Bent Crystals	31
2.1	Particle Motion in a Bent Channel	31
2.2	Deflection Efficiency	34
2.2.1	Acceptance of a Bent Crystal	34
2.2.2	Dechanneling in a Bent Crystal	38
2.2.3	Bending Efficiency	40
2.2.4	The Influence of Temperature on the Efficiency	42
2.2.5	Channeling in Crystal with Variable Curvature	46
2.3	Feed-in Mechanisms	50
2.3.1	Scattering	50
2.3.2	Bending	55
2.3.3	Conclusion	60
2.4	Computer Simulation	60
2.4.1	Introduction	60
2.4.2	Simulation Procedure	62
2.4.3	Scattering	62
2.4.4	Simulation of the Dechanneling Process	64
2.5	Channeling in an Imperfect Lattice	67
2.5.1	Classification of Lattice Defects	67
2.5.2	Dislocations	69
2.5.3	Computer Simulation of Dislocation Dechanneling	77
2.5.4	Radiation Damage	80
2.5.5	Conclusion	81

3. Experimental Studies of High-Energy Channeling and Bending Phenomena in Crystals	83
3.1 Introduction	83
3.2 Crystals and Bending Devices	83
3.3 General Experimental Methods	87
3.4 Deflection Efficiency Measurements	90
3.4.1 Simulation of Bending Experiments	92
3.4.2 Conclusion	94
3.5 Energy Loss in Bent Crystals	94
3.6 Dechanneling Investigation	98
3.6.1 Fermilab Experiment	98
3.6.2 Protvino Experiment	101
3.6.3 Dechanneling Simulations	104
3.7 Dynamic Equilibrium	105
3.8 Volume Capture	109
3.9 Influence of Crystal Lattice Imperfections on Beam Deflection	115
3.9.1 Spatial Lattice Imperfections	115
3.9.2 Surface Imperfections and Edge Effects	117
3.9.3 Conclusion	122
3.10 Topics Under Development	122
3.10.1 Bending Particles with Axial Channeling	122
3.10.2 Bending Negative Particles	124
3.10.3 Deflection of High-Energy Heavy Ions	124
4. Crystal Extraction	125
4.1 Introduction	125
4.2 Single-Pass and Multiple-Pass Modes of Extraction	126
4.2.1 Scattering in a Crystal	127
4.2.2 Motion in the Accelerator	129
4.2.3 Estimate of the Multi-pass Efficiency	131
4.2.4 Angular Acceptance of a Crystal in the Multi-pass Mode	133
4.2.5 Extraction with High-Z Crystals	134
4.2.6 Dependence of Efficiency on Machine Parameters	134
4.2.7 Some Ideas on Multi-pass Channeling	137
4.3 Extraction from the CERN SPS	140
4.3.1 Crystal Transmission of a Single Pass	140
4.3.2 The SPS Extraction Set-Up	142
4.3.3 A ‘Twisted’ Crystal	143
4.3.4 Computer Simulation of Extraction	144
4.3.5 A ‘U-shaped’ Crystal	148
4.3.6 A Crystal with an Amorphous Layer	149
4.3.7 A More Realistic Simulation	149

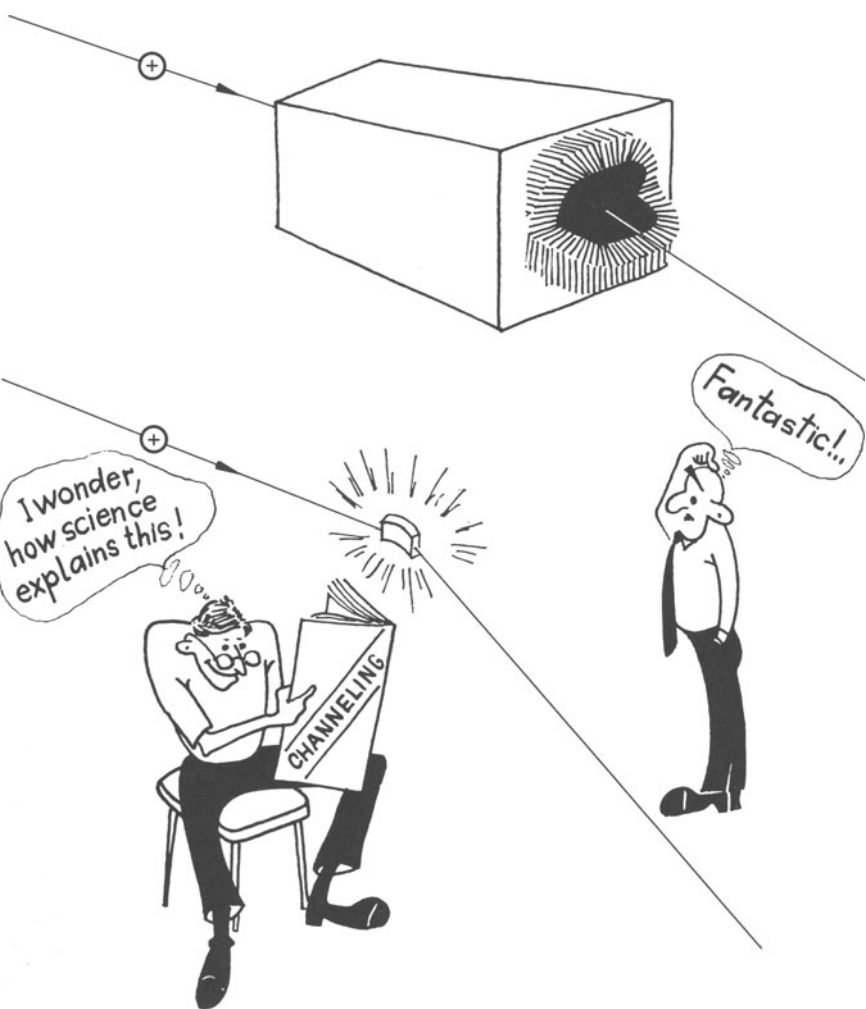
4.3.8	Crystal Optimization	150
4.3.9	Conclusions	152
4.4	Crystal Extraction from the Tevatron	152
4.4.1	Qualitative Discussion of the Extraction	152
4.4.2	Simulation	156
4.4.3	Conclusions	161
4.5	Proton Extraction from the Large Hadron Collider	162
4.5.1	Introduction	162
4.5.2	Simulation of a Single Pass	163
4.5.3	Simulation of the Extraction	165
4.5.4	Conclusions	168
5.	The Use of Crystal Deflectors in Beam Lines	169
5.1	Crystals in Intense Particle Beams	169
5.2	Beam Attenuator	170
5.3	Beam Splitting	172
5.4	Creation of New Experimental Areas	174
5.5	Beam Diagnostics	175
5.5.1	Method of Measurement	176
5.5.2	Determination of the Spatial and Angular Characteristics of a Beam	176
5.5.3	Determination of the Distribution of the Particle Momentum	178
5.6	Beam Focusing with Crystals	178
5.6.1	The Focusing Method	178
5.6.2	Focusing of a Parallel Beam to Form a Point in the Particle Deflection Plane	179
5.6.3	Focusing a Beam Diverging from a Point-Like Source into a Parallel Beam	181
6.	Application of Crystal Channeling to Particle Physics Experiments	185
6.1	Studying Short-Lived Particles: Ideas and Proposals	185
6.1.1	The Study of Decay Modes of Short-Lived Particles . .	185
6.1.2	Measurement of Magnetic Moments	186
6.1.3	Measurement of Short-Lived-Particle Lifetimes	187
6.2	Measurement of the Magnetic Moment of the Σ^+ Hyperon Using a Bent Crystal	188
6.3	Radiation of High-Energy Electrons and Positrons in Aligned Single Crystals and Its Application in Physical Research	191
6.3.1	Coherent Bremsstrahlung	191
6.3.2	Channeling Radiation	196
6.3.3	Application of the Results to High-Energy Physics . .	201

XII Table of Contents

Epilogue	209
References	211
Subject Index	217

The Most Frequently Used Symbols

a_{TF}	Thomas-Fermi screening radius; 0.194 Å in Si
c	Velocity of light
d_p	Interplanar distance
e, m_e	Electron charge and rest mass
p, v, E	Incident particle momentum, velocity and energy
x	Distance measured normal to planes
x_c	Critical distance for channeling
z	Depth in crystal measured parallel to beam direction
A_S	Beam fraction trapped in channeling in straight crystal
A_B	Fraction of channeled beam survived in bent crystal
E_T	Transverse energy
E_c	Critical transverse energy
L	Crystal length
L_D	Dechanneling length
L_N	Nuclear interaction length
L_R	Radiation length, see (6.14)
N, n_e	Volume density of atoms and electrons
R	Bending radius of crystal
R_c	Critical bending radius
$U(x)$	Interplanar potential
Z, A	Atomic number and weight of crystal atom
$Z_i e$	Charge of incident particle
α	$=e^2/\hbar c=1/137$, fine-structure constant
γ	Relativistic factor
\hbar	$=h/2\pi$, reduced Planck constant
λ	Oscillation period of channeled particle
θ_c	Critical angle for channeling, see (1.28)
θ_L	Lindhard angle, see (1.26)
Θ	Angle of particle deflection by a bent crystal
ω	Radiation frequency



1. Channeling Phenomenon

1.1 Structure of Crystals

The characteristic property of any crystal is the ordered and symmetrical arrangement of the atoms in it; that is, the presence of the spatial structure called the crystal lattice. The crystal lattice is usually represented by a spatial grid of the straight lines (Fig. 1.1). The intersection points are called the lattice nodes. Only in the simplest case does a single node correspond to a single atom. If there are several kinds of atoms in the crystal structure, then a group of atoms is related to every node; these groups form the basis and are identical in constitution, position, and orientation.

The crystal lattice has an infinite number of different translation periods, which may be dependent. In the lattice one can always choose three basic periods \mathbf{a} , \mathbf{b} , and \mathbf{c} with directions which do not lie in the same plane. Then any other period can be written as a sum of three vectors, each of them being a multiple of one of the basic periods:

$$\mathbf{r} = n_1 \mathbf{a} + n_2 \mathbf{b} + n_3 \mathbf{c} . \quad (1.1)$$

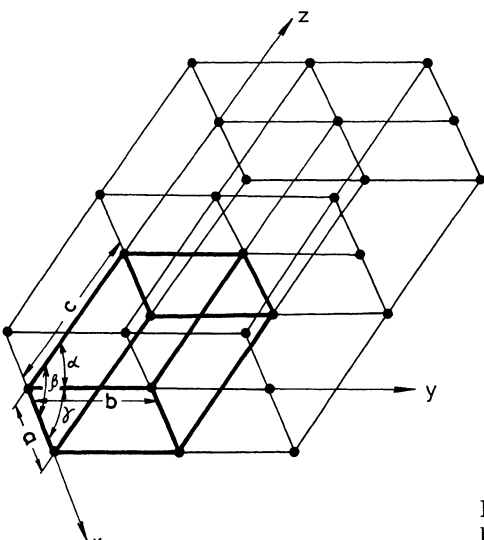


Fig. 1.1. The structure of the crystal lattice and its primitive cell.

Here n_1, n_2 , and n_3 are positive or negative integers, including zero.

Let us make any node in the lattice coincident with an atom, and plot from this node in the corresponding directions the basic periods a , b , and c . The parallelepiped patterned after these periods is a primitive (the minimal) cell of the lattice. It is uniquely determined by six parameters: the lengths of the three vectors (a, b, c) and the angles between them α, β, γ (see Fig. 1.1). The vertices of this parallelepiped, occupied by the same atoms, are the equivalent nodes. Each of them can be made coincident with any other by the operation of translation (1.1). Filling all the space with the properly placed primitive cells, by translating them in three directions, we get the so-called Bravais lattice.

As well as translation symmetry, crystals may also have other kinds of symmetry, for instance, related to rotations and reflections. These latter symmetries are due to the systems of crystal axes and planes, which cross an infinite number of the lattice nodes. Different combinations of these symmetries (which make up 32 point groups¹) lead to 14 types of Bravais lattices, the cells of which are schematically drawn in Fig. 1.2. The Bravais lattices are subdivided into seven crystal systems: cubic, tetragonal, orthorhombic, monoclinic, rhombohedral or trigonal, and triclinic. Each system has one primitive cell (it is single in the trigonal, hexagonal, and triclinic systems), satisfying certain constraints for its parameters a, b, c and α, β, γ .

The remaining seven cells of the Bravais lattices are not primitive. They are chosen because they reflect more fully the symmetry properties of the system. These cells, patterned after the non-basic periods, and having the property that with use of the translation operations the cells fill the whole space, are called *elementary*. The primitive cells patterned after the basic periods are the minimal elementary ones.

The cubic system is the most symmetrical of the seven systems of Bravais lattice. As follows from Fig. 1.2, the cubic system contains three types of Bravais lattice: the simple cubic lattice, the body-centered cubic (bcc) lattice, and the face-centered (fcc) lattice.

If one represents atoms schematically with spheres, the volume of the spheres will correspond to one atom ($1/8$ volume of every atom placed in the cube vertices) in the simple cubic cell, two atoms in the bcc cell, and four atoms in the fcc cell ($1/8$ volume of every atom placed in the cube vertices, and $1/2$ volume of every atom placed in the face centers).

The primitive cells for bcc and fcc lattices may be patterned with the basic periods chosen as vectors drawn from some vertex to the center of the bcc cell, and from a vertex to the center of a face of the fcc cell. The primitive cells patterned after these vectors are rhombohedrons (Fig. 1.3). It is easy to show that the volume of the first rhombohedron (for bcc) is one half that

¹ The point group is a certain set of operations, viz. rotations and reflections with respect to some point of the body. The body is brought into coincidence with itself as a result of any of the operations.

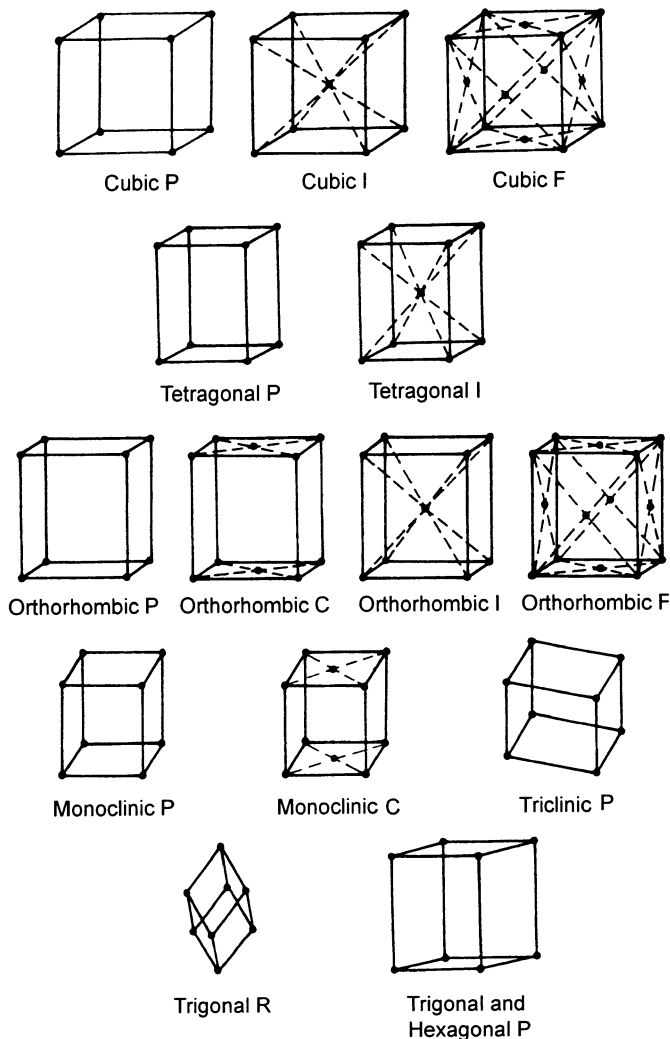


Fig. 1.2. The family of the Bravais crystal lattices. P: simple lattice (in trigonal system one uses R instead of P). C: base-centered lattice. I: body-centered lattice. F: face-centered lattice.

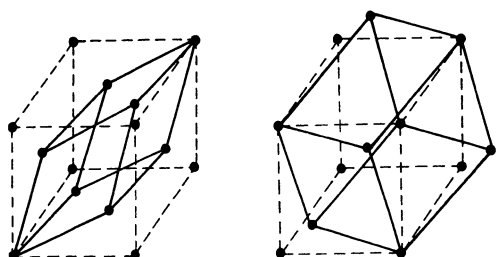


Fig. 1.3. The body-centered (right) and face-centered cubic lattices, and their primitive cells.

of the cube; the volume of the second one is one forth. So, the number of atoms in the bcc and fcc elementary cells is the same as that in two and four corresponding primitive cells. The structures of bcc and fcc elementary cells (multiples of their primitive ones) fully reflect the cubic symmetry, while the primitive cells (rhombohedrons) themselves do not have all the elements of cubic symmetry.

Any detailed description of the symmetries of all the Bravais lattices would take too much space, and take us away from the major subject of this book. A rather complete and readable consideration of the crystal symmetries may be found in [9–11].

Crystal Planes and Axes. Crystal planes, passing through an infinite number of lattice nodes, are specified by the Miller indices determined in the following way.

It is well known that the equation of a plane is given by

$$\frac{x}{x_0} + \frac{y}{y_0} + \frac{z}{z_0} = 1 , \quad (1.2)$$

where x, y, z are the coordinates of an arbitrary point on the plane, and x_0, y_0, z_0 are the coordinates of the intersections between the plane and the three axes. We assume that the coordinates are given in the units of the lattice constant. Since a crystal plane contains an infinite number of lattice nodes, with coordinates given by (1.1), one may replace x, y, z in (1.2) with the coordinates n_1, n_2, n_3 of any of the lattice nodes:

$$\frac{n_1}{x_0} + \frac{n_2}{y_0} + \frac{n_3}{z_0} = 1 . \quad (1.3)$$

As the n_1, n_2, n_3 are integer numbers, (1.3) is fulfilled if $1/x_0, 1/y_0$, and $1/z_0$ are rational numbers. This means that their ratios may be expressed as the ratios of some integer numbers h, k, l : that is $1/x_0 : 1/y_0 : 1/z_0 = h : k : l$. Let us bring $1/x_0, 1/y_0, 1/z_0$ to a common divider m . Then we have for h, k, l

$$h = \frac{m}{x_0} , \quad k = \frac{m}{y_0} , \quad l = \frac{m}{z_0} . \quad (1.4)$$

Introduced in this way, and enclosed in parentheses, the mutually simple numbers (hkl) represent the Miller indices. These indices define not a single plane, but a set of parallel planes. Indeed, substituting the values for $1/x_0, 1/y_0$, and $1/z_0$ from (1.4) into (1.3), we get an equation

$$hn_1 + kn_2 + ln_3 = m , \quad (1.5)$$

which, for fixed h, k, l and different m , defines a set of parallel planes.

If a plane intersects a coordinate axis at some negative value, $-y_0$, the corresponding Miller index is also negative. For such a plane the notation (h, \bar{k}, l) is used.

The planes parallel to the coordinate planes (y, z) , (x, z) , and (x, y) intersect the corresponding axes at infinity; hence, their Miller indices are $(h00)$, $(0k0)$, and $(00l)$. Since for Miller indices the minimal possible numbers are

used, the planes from the above families are represented by (100), (010), and (001). The exception is the case when some extra information on the plane is needed. The planes of these families are equivalent by a character of symmetry, and their set is denoted with the same indices enclosed in figure parentheses, $\{hkl\}$.

As an example, Fig. 1.4 shows the main planes of the simple cubic lattice. The cube faces that stand as the planes equivalent by the character of symmetry may be denoted as {100}. A plane passing through the diagonals of the opposite faces of a cube, has indices (110), and the diagonal plane has (111).

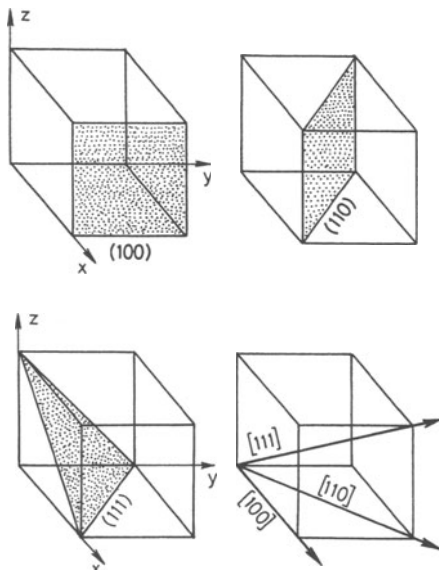


Fig. 1.4. The main planes and axes of the simple cubic lattice.

For a description of a direction in the crystal we take a straight line passing through the origin of the coordinates. The identical nodes of the lattice are placed equidistant along this line. The line position is given by the coordinates of the nearest node n_1, n_2, n_3 , which are three minimal numbers by definition. Let them be h, k, l . Enclosed in square brackets, $[hkl]$, they are the symbol of an axis. This symbol defines a family of parallel axes. The set of axes equivalent by a character of symmetry is denoted with $\langle hkl \rangle$. For example, in a cubic crystal the coordinate axes [100], [010], [001] are labelled with $\langle 100 \rangle$. The major axes of a cubic crystal are shown in Fig. 1.4. They are normal to the planes that have the same indices. In crystals of the other systems, the normality of axes to the planes with the same indices is, in general, not satisfied. The basic data of the structure of cubic crystals are given in Table 1.1.

Table 1.1. The basic data for the structure of cubic crystals (spacings are given in the units of the lattice constant a).

Structure	Atoms per unit cell	Interatomic spacing in axial direction			Interplanar spacing		
		$\langle 100 \rangle$	$\langle 110 \rangle$	$\langle 111 \rangle$	$\langle 100 \rangle$	$\langle 110 \rangle$	$\langle 111 \rangle$
simple	1	1	$\sqrt{2}$	$\sqrt{3}$	1	$1/\sqrt{2}$	$1/\sqrt{3}$
bcc	2	1	$\sqrt{2}$	$\sqrt{3}/2$	$1/2$	$1/\sqrt{2}$	$1/2\sqrt{3}$
fcc	4	1	$1/\sqrt{2}$	$\sqrt{3}$	$1/2$	$1/2\sqrt{2}$	$1/\sqrt{3}$

Crystals of the Diamond Group. Many elements of the periodic table and their compounds are organized in a cubic structure, in particular body-centered and face-centered. Below we consider only the crystals of the diamond group, which are used in the experimental studies of high-energy channeling at accelerators. Carbon (diamond itself), silicon, germanium, and grey tin are crystallized with the structure of diamond.

The diamond lattice is face-centered cubic but, unlike the fcc Bravais lattice, its cell contains eight atoms instead of four. It may be viewed as two identical fcc Bravais lattices, pushed one into another and shifted along the bulk diagonal by one quarter of its length. The structure of the diamond cubic lattice is shown in Fig. 1.5, where the solid spheres are the atoms of the shifted fcc Bravais lattice. It is seen from the figure that every atom has four neighbors placed in the vertices of a regular tetrahedron. Such a structure comes from the so-called covalent bond (due to electron exchange) of the atoms. The atoms of the diamond group have four electrons in the outer shell. To create a stable eight-electron shell, they lack four electrons, which they compensate for through electronic exchange with the four nearest neighbors. Because of the tetragonal covalent bond, the diamond lattice is not closely packed. The atoms, represented by spheres, occupy only 34% of the lattice volume; for the closely packed lattice this value is 74%. The spacing between the $\langle 100 \rangle$ planes of the diamond lattice is half that of the fcc Bravais lattice, and equals $a/4$; for the $\langle 110 \rangle$ planes the spacing is conserved and equals $a/2\sqrt{2}$; the $\langle 111 \rangle$ planes are placed with two different alternating spacings: $a/4\sqrt{3}$ and $a\sqrt{3}/4$. The atoms along the $\langle 111 \rangle$ axis are also placed with two different alternating spacings: $a\sqrt{3}/4$ and $a3\sqrt{3}/4$.

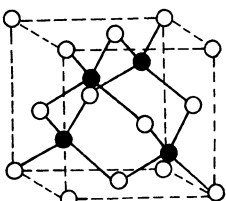


Fig. 1.5. The diamond cubic lattice: two identical fcc lattices, pushed one into another and shifted along the bulk diagonal by one quarter of its length. The solid spheres are the atoms of the shifted lattice.

Mostly single crystals of silicon and, more rarely, germanium are used in high-energy particle beams. This is due to the high degree of perfection of the crystal lattice in semiconductor materials and the well-developed technology of growing large semiconductor crystals [12].

The major characteristics of the crystalline structure of the elements of the diamond group are listed in Table 1.2.

Table 1.2. The major characteristics of the crystalline structure of the elements of the diamond group.

Element	Lattice constant [Å]	Interatomic spacing in axial direction [Å]			Interplanar spacing [Å]		
		$\langle 100 \rangle$	$\langle 110 \rangle$	$\langle 111 \rangle$	$\langle 100 \rangle$	$\langle 110 \rangle$	$\langle 111 \rangle$
C	3.56	3.56	2.52	1.54	0.89	1.26	0.51
				4.59			1.54
Si	5.43	5.43	3.85	2.35	1.36	1.92	0.78
				6.99			2.35
Ge	5.65	5.65	4.00	2.45	1.41	2.00	0.81
				7.29			2.45

1.2 Electric Fields in Crystals

To understand how the crystal symmetry may be used for steering a particle beam, let us briefly consider first the particle interaction with a single atom. Let the atomic number be Z , and the particle charge be $Z_i e$. In the Thomas–Fermi model of the atom the potential of an particle–atom interaction is of the form:

$$V(r) = \frac{Z_i Z e^2}{r} \Phi\left(\frac{r}{a_{TF}}\right), \quad (1.6)$$

where r is the distance between the particle and the atom. The first factor in (1.6) represents the potential of the point-like charge, while the screening function $\Phi(r/a_{TF})$ takes into account the charge distribution of the atom; the screening distance is $a_{TF} = 0.8853 a_B Z^{-1/3}$, $a_B = 0.529 \text{ \AA}$. The widely applied analytical approximation for Φ was given by Moliére [13]:

$$\Phi(r/a_{TF}) = \sum_{i=1}^3 \alpha_i \exp\left(-\frac{\beta_i r}{a_{TF}}\right), \quad (1.7)$$

here $\alpha = (0.1, 0.55, 0.35)$, $\beta = (6.0, 1.2, 0.3)$. Another often-used approximation was suggested by Lindhard [4]:

$$\Phi(r/a_{\text{TF}}) = 1 - \left(1 + \frac{3a_{\text{TF}}^2}{r^2}\right)^{-1/2}. \quad (1.8)$$

Any particle traversing an amorphous matter or a disaligned crystal experiences a number of uncorrelated collisions with single atoms. As these encounters may occur with any impact parameters, small or large ones, a variety of processes take place in the collision events; most common are, for instance, angular scattering in multiple collisions with the atomic nuclei, and energy loss in collisions with atomic electrons. In disordered matter one may consider just a single collision, then simply make a correction for the matter density.

The first realization that the atomic order in crystals may be important for these processes dates back to 1912, thanks to Stark [1]. These old ideas of the directional effects for a charged particle moving in a crystal were dormant until the early 1960s, when the channeling effect was discovered in computer simulations [2] and experiments [3], which observed abnormally large ranges of ions in crystals. The orientational effects for charged particles traversing crystals were found for a number of processes requiring a small impact parameter in a particle–atom collision: nuclear reactions, large-angle scattering, energy loss, and so on.

The theoretical explanation of the channeling effects has been given by Lindhard [4], who has shown that when a charged particle has a small incident angle with respect to the crystallographic axis (or plane) the successive collisions of the particle with the lattice atoms are correlated, and hence one has to consider the interaction of the charged particle with the atomic string (plane). In the low-angle approximation one may replace the potentials of the single atoms with an averaged *continuous potential*. If a particle is misaligned with respect to the atomic strings but moves at a small angle with respect to the crystallographic plane, one may take advantage of the continuous potential for the atomic plane, where averaging is made over the two planar coordinates:

$$U_{\text{pl}}(x) = N d_p \int_{-\infty}^{+\infty} \int_{-\infty}^{+\infty} V(x, y, z) dy dz, \quad (1.9)$$

where $V(x, y, z)$ is the potential (1.6) of a particle–atom interaction, N is the volume density of atoms, d_p is the interplanar spacing.

The atomic plane (string) gently steers a particle away from the atoms, thus suppressing the encounters with small impact parameters. The angle by which the particle is reflected by the plane is equal to the angle of incidence. The orientational effects mentioned above are the result of the influence of the crystal lattice on the motion of energetic charged particles.

We will consider further only planar channeling; therefore we take an example of the potential (1.9) in the approximation of Moliére,

$$U_{\text{pl}}(x) = 2\pi N d_p Z_i Z e^2 a_{\text{TF}} \sum_{i=1}^3 \frac{\alpha_i}{\beta_i} \exp\left(-\frac{\beta_i x}{a_{\text{TF}}}\right), \quad (1.10)$$

and in the approximation of Lindhard,

$$U_{\text{pl}}(x) = 2\pi N d_p Z_i Z e^2 \left(\sqrt{x^2 + 3a_{\text{TF}}^2} - x \right). \quad (1.11)$$

The thermal vibrations of atoms modify the static-lattice potential (1.9) near the plane at a distance of the order of the thermal vibration root-mean-square amplitude u_T . One may assume that the individual atoms vibrate independently and that in each of the translational degrees of freedom the probability $P(x)$ of a displacement x has the Gaussian distribution

$$P(x) = \frac{1}{\sqrt{2\pi u_T^2}} \exp\left(-\frac{x^2}{2u_T^2}\right). \quad (1.12)$$

The modified potential is obtained by averaging (1.9) over the Gaussian distribution of the atom displacement. In Moliére's form the potential of a 'warm' atomic plane is

$$\begin{aligned} U_{\text{pl}}(x, u_T) &= 2\pi N d_p Z_i Z e^2 a_{\text{TF}} \\ &\times \sum_{i=1}^3 \frac{\gamma_i}{2} \exp(\tau_i) \left\{ \exp(-\beta_i x / a_{\text{TF}}) \operatorname{erfc} \left[\frac{1}{\sqrt{2}} \left(\frac{\beta_i u_T}{a_{\text{TF}}} - \frac{x}{u_T} \right) \right] \right. \\ &\left. + \exp(\beta_i x / a_{\text{TF}}) \operatorname{erfc} \left[\frac{1}{\sqrt{2}} \left(\frac{\beta_i u_T}{a_{\text{TF}}} + \frac{x}{u_T} \right) \right] \right\}, \end{aligned} \quad (1.13)$$

where

$$\operatorname{erfc}(x) = \frac{2}{\sqrt{\pi}} \int_x^\infty \exp(-t^2) dt \quad (1.14)$$

is the complementary error function, $\gamma_i = \alpha_i / \beta_i$, and $\tau_i = \beta_i^2 u_T^2 / (2a_{\text{TF}}^2)$ with α_i and β_i as defined earlier. Figure 1.6 shows the potential (1.13) of the Si(110) planes at different temperatures, and the potential (1.10) of the static lattice. Although the full depth of the interplanar well is considerably affected by temperature variations, the potential beyond the atomic layers is much the same.

In a crystal the particle moves in a potential that is the sum of the potentials of the single planes:

$$U(x) \approx U_{\text{pl}}(d_p/2 - x) + U_{\text{pl}}(d_p/2 + x) - 2U_{\text{pl}}(d_p/2)$$

(contributions of two nearest atomic layers dominate). Here x is defined already with respect to the midplane between the atomic layers, and we have defined $U(0) = 0$. The silicon crystal with the (110) orientation represents

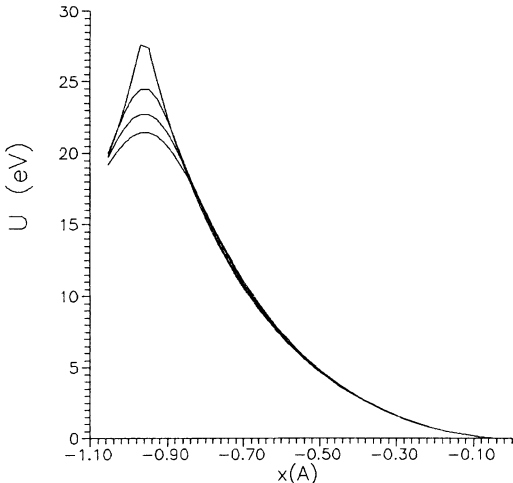


Fig. 1.6. The Molière potential of the Si(110) planes at different temperatures, and the potential of the static lattice. Top to bottom at the left edge: static, 77 K, 300 K, 500 K.

a regular structure with equal distances $d_p = 1.92 \text{ \AA}$ between planes. In the crystal with the (111) orientation the large distance $d_p^L = 2.35 \text{ \AA}$ between atomic planes changes periodically into a small one d_p^S ; note that $d_p^L = 3d_p^S$ (Table 1.3). Examples of the potential for the (110) and (111) planes of silicon are shown in Fig. 1.7. The harmonic approximation $U \sim x^2$, plotted with a dashed line in Fig. 1.7a, fits the interplanar potential rather well, and is often used for analytic estimates.

Table 1.3. Parameters of some planar channels of the crystals of silicon, germanium, and tungsten, at room temperature. The potentials are given at $x_c = d_p/2 - 2u_T$ in the Molière approximation.

Channel	d_p [\AA]	a_{TF} [\AA]	u_T [\AA]	$U(x_c)$ [eV]	$U'(x_c)$ [GeV/cm]
Si		0.194	0.075		
(110)	1.92			16	5.7
(111)L	2.35			19	5.6
(111)S	0.78			4.2	3.5
Ge		0.148	0.085		
(110)	2.00			27	10
(111)L	2.45			30	9.4
(111)S	0.81			7.2	6.4
W		0.112	0.050		
(100)	1.58			63	30
(110)	2.24			105	43

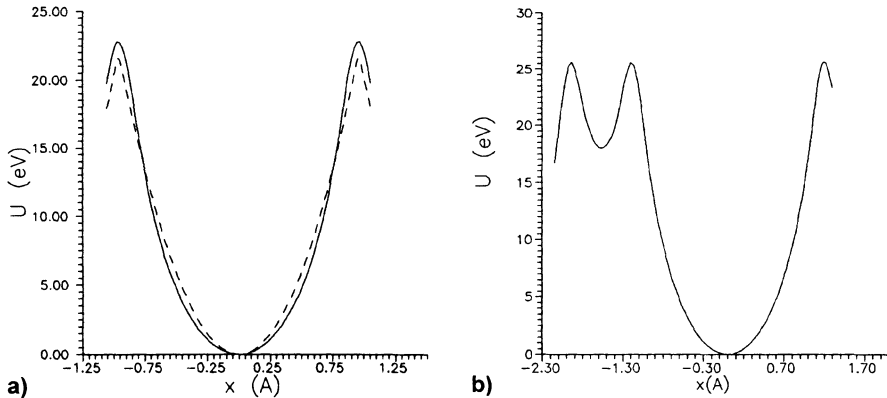


Fig. 1.7. The interplanar Moliére potential for (a) the Si channels (110) and (b) the Si channels (111). The dashed line is the harmonic approximation.

The potential-well depth U_0 in silicon is of the order of 20 eV. The interplanar electric field $U'(x)$ is shown in Fig. 1.8 for the planar channels (110) and (111) of silicon. The maximal field value is $\sim 6 \times 10^9$ V/cm. In the crystals of heavy materials, such as tungsten, the planar field may achieve values up to $\sim 10^{11}$ V/cm. Some parameters of the major planar channels of the crystals of silicon, germanium, and tungsten are listed in Table 1.3.

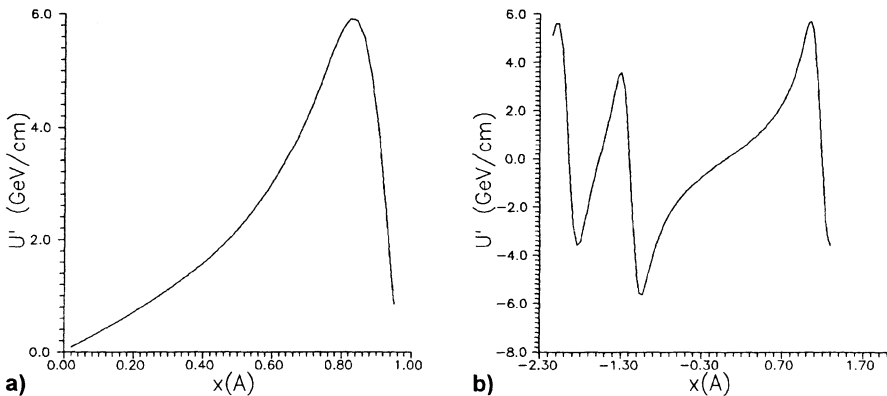


Fig. 1.8. The interplanar electric field (Moliére) for (a) the Si channels (110) and (b) the Si channels (111).

1.3 Particle Motion in the Potential of Atomic Planes

The transverse motion of a particle incident at some small angle (the typical scale of the angles will be defined below) with respect to one of the crystal axes or planes is governed by the continuous potential of the crystal lattice. From the above consideration one can see that the fields of the atomic axes and planes form the potential wells, where the particle may be trapped. In this case one speaks of *channeling* of the particle: an *axial channeling* if the particle is bound with atomic strings, and a *planar channeling* if it is bound with atomic planes.

The interaction of the channeled particle with a medium is very different from a particle interaction with an amorphous solid or a misaligned crystal. For instance, a channeled proton moves between two atomic planes (layers) and hence does not collide with nuclei; moreover, it moves in a medium of electrons with reduced density. Such a proton is very sensitive to the crystal lattice defects, which is the basis for an efficient method of crystal perfection analysis [7]. For light particles such as electrons the coherent effects increase the probability of a photon being radiated (the creation of a pair) [14–17]. In the channeling mode a particle may traverse some centimeters of crystal (in the GeV range of energy).

Qualitatively, different kinds of particle motion in an aligned crystal may be illustrated with the scheme of Fig. 1.9. If an electron is aligned with respect to an atomic plane only (zone 2), it may be captured by this plane and then oscillate about it; if the electron is aligned also with respect to a crystallographic axis (zone 1), it is recaptured by the atomic string (which has a stronger field). Between the zones 1–2 and the zone 7 of a completely disaligned motion in a crystal, there are zones 4–6 where the motion is influenced by the field of atomic strings and planes. A particle not bound by an atomic plane (or axis) but influenced by its field is called *quasi-channelized*. Zone 3 corresponds to channeling in the transition region (between axial and planar channeling), where a planar channeling occurs under the influence of the atomic string as well (axial quasi-channeling).

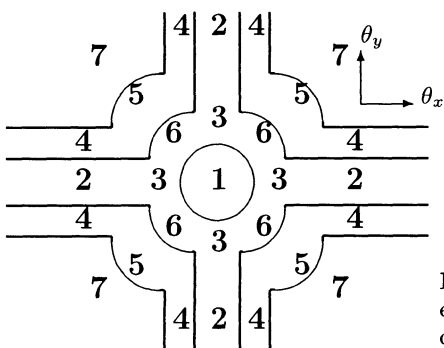


Fig. 1.9. Qualitative scheme of different kinds of particle motion in an aligned crystal (see the text for details).

We shall concentrate on the case of planar channeling, because it is this process that is normally used in particle beam steering with a crystal.

Lindhard has shown [4] that the motion of particles in the channeling case (a series of correlated collisions) may be considered in the framework of classical mechanics, even if the individual scattering events are of quantal character. The accuracy of the classical approach improves as the particle energy increases. The region where classical mechanics is applicable may be estimated as follows [8]. From the quantum mechanics of the harmonic oscillator with mass M it is known that the difference between the neighboring levels of energy in the potential well $U_0(2x/d_p)^2$ is equal to $\hbar(8U_0/d_p^2M)^{1/2}$. Below it will be shown that a relativistic particle oscillates in a channel as if it has a relativistic mass $M\gamma$. Therefore the number of energy levels in the well of a depth U_0 equals

$$N_l = \frac{d_p}{\hbar\sqrt{8}} \sqrt{U_0 M \gamma}. \quad (1.15)$$

Classical mechanics is applicable if $N_l \gg 1$. For heavy particles, such as protons and ions, this condition is always fulfilled. For the light particles (electrons, positrons) the classical approach starts to work in the 10–100 MeV range.

Let us consider the classical equations of motion of a particle with energy $\sqrt{p^2c^2 + m^2c^4}$ in the transverse potential $U(x)$. When the transverse component p_x of the particle momentum p is much smaller than the longitudinal component p_z (i.e., the angle $\theta = p_x/p_z$ is small), one may rewrite the law of conservation of the total energy

$$E = \sqrt{p_x^2 c^2 + p_z^2 c^2 + m^2 c^4} + U(x) = \text{const}$$

in the form

$$\frac{p_x^2 c^2}{2 E_z} + U(x) + E_z = \text{const}, \quad (1.16)$$

where $E_z = \sqrt{p_z^2 c^2 + m^2 c^4}$. The sum of the first two terms in (1.16) is called the *transverse energy* E_T . For motion in the potential $U(x)$ the longitudinal component of the momentum is conserved, implying the conservation of E_T :

$$E_T = \frac{p_x^2 c^2}{2 E_z} + U(x) = \frac{p_z^2 c^2}{2 E_z} \theta^2 + U(x) = \text{const}. \quad (1.17)$$

Assuming $E_z \approx E$, $p_z \approx p$ and using the known relation $pc^2 = vE$, where v is the particle velocity, we may rewrite (1.17) as:

$$E_T = \frac{pv}{2} \theta^2 + U(x) = \text{const}. \quad (1.18)$$

The particle trajectory for an arbitrary $U(x)$ may be obtained by integration of the expression

$$dz = \frac{dx}{\sqrt{\frac{2}{pv}[E_T - U(x)]}}. \quad (1.19)$$

that follows directly from (1.18). Differentiating (1.17) with respect to z , taking into account that $\theta = dx/dz$, and using the same substitutions, one obtains

$$pv \frac{d^2x}{dz^2} + U'(x) = 0 \quad (1.20)$$

for the one-dimensional transverse motion in the potential $U(x)$. It describes the particle oscillation in the potential well of the planar channel. In the harmonic potential

$$U_h(x) = U_0 \left(\frac{2x}{d_p} \right)^2, \quad (1.21)$$

the solution of (1.20) is a sinusoidal oscillation:

$$x = \frac{d_p}{2} \sqrt{\frac{E_T}{U_0}} \sin \left(\frac{2\pi z}{\lambda} + \phi \right), \quad (1.22)$$

$$\theta = \sqrt{\frac{2E_T}{pv}} \cos \left(\frac{2\pi z}{\lambda} + \phi \right), \quad (1.23)$$

with the oscillation period being

$$\lambda = \pi d_p \sqrt{\frac{pv}{2U_0}}. \quad (1.24)$$

The period λ takes a value from $\sim 30 \mu\text{m}$ for the 100 GeV proton up to $\sim 0.5 \text{ mm}$ for the 20 TeV proton in silicon. The spatial distribution over x of the oscillating particle is given by (1.19), which should be normalized to λ .

The condition for the capture of the particle into the channeling mode is

$$\frac{pv}{2} \theta^2 + U(x) \leq U_0. \quad (1.25)$$

Hence, assuming $x = 0$, one obtains the limiting angle of capture:

$$\theta_L = \sqrt{\frac{2U_0}{pv}}. \quad (1.26)$$

The angles θ_L for planar and axial channeling were introduced by Lindhard. For the planes (110) of silicon the angle θ_L amounts from $20 \mu\text{rad}$ at an energy of 100 GeV to $7 \mu\text{rad}$ at 1 TeV. The scattering from the nuclei rapidly removes the particle from the channeling mode; a particle approaching the atomic plane as close as $\sim a_{TF}$ may be considered as lost from the channeling mode. For the channeled particle the critical transverse coordinate

$$x_c \approx \frac{d_p}{2} - a_{TF} \quad (1.27)$$

and the critical angle of channeling

$$\theta_c = \sqrt{\frac{2E_c}{pv}} \quad (1.28)$$

are defined, with $E_c = U(x_c)$ as the critical transverse energy. In the definition of x_c one may introduce the dependence on the thermal vibrations of the atoms. Experiments [18] and computer simulations [19] show that a good estimate of the ‘half-thickness’ of an atomic layer is $2.5u_T$. The simulations of multi-TeV channeling [20, 21] have shown that this ‘half-thickness’ may be as low as $\sim u_T$ at very high energies, because of the reduced scattering.

It is convenient to illustrate the condition of particle capture into a channeling mode by the phase diagram in the plane (x, θ) . Figure 1.10 shows the two-dimensional (x, θ) distribution of 450 GeV protons in a silicon crystal with an alignment of (111), obtained by computer simulation [37]. Ellipses represent phase trajectories (1.18) of the particles for different values of E_T . The outer ellipse corresponds to the critical transverse energy E_c . The phase area inside this ellipse is occupied by the channeled particles. The particles outside this area are not channeled.

Upon incidence on a crystal the particles are uniformly distributed over x from $-d_p/2$ to $d_p/2$. If their distribution over angles in the range $-\theta_c$ to θ_c is uniform as well (this is typical for GeV beams), then the probability of the particle being captured into the channeling mode is the ratio of the area of the phase ellipse $E_T = E_c$ (i.e., the planar channel acceptance) to the total phase area occupied by the incident beam (its emittance). For the case of a harmonic interplanar potential and a straight crystal this probability amounts to

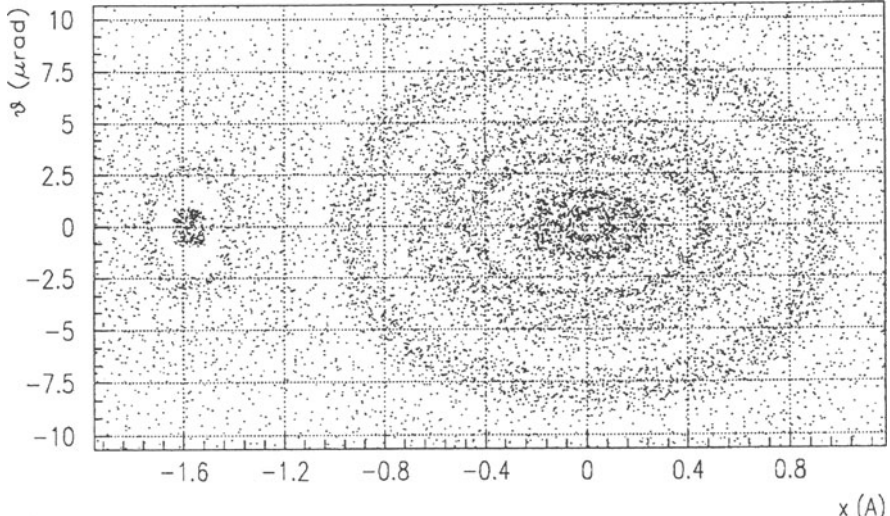


Fig. 1.10. The simulated phase trajectories of 450 GeV/c protons on the plane (x, θ) in Si(111) for a straight crystal.

$$A_S = \frac{2x_c}{d_p} \frac{\pi}{4} \frac{\theta_c}{\Phi} \quad (1.29)$$

for the beam divergence of 2Φ . If the particle is incident exactly parallel to the crystallographic planes, then the probability of its capture into the channeling mode is simply $2x_c/d_p$. For incidence at some fixed angle θ this probability, in the harmonic approximation, is reduced by the factor $\sqrt{1 - \theta^2/\theta_c^2}$.

The trapped particles have different transverse energies, depending on their incidence parameters x and θ . The particle distribution over E_T is found from the incident-beam distribution over the angle, $g(\theta)$, and the x coordinate, $1/d_p$, with use of (1.18):

$$\begin{aligned} f(E_T) &= \int_{-d_p/2}^{d_p/2} \frac{dx}{d_p} \int_{-\infty}^{\infty} g(\theta) \delta \left(p v \frac{\theta^2}{2} + U(x) - E_T \right) d\theta \\ &= \frac{1}{p v d_p} \int_{-x_{\max}}^{x_{\max}} \frac{g \left(\sqrt{2 [E_T - U(x)] / p v} \right)}{\sqrt{E_T - U(x)}} dx, \end{aligned} \quad (1.30)$$

where δ is Dirac function, and x_{\max} is defined from $U(x_{\max}) = E_T$.

The spatial distribution of the channelled beam may be obtained by averaging (1.19) over $f(E_T)$. The result may be viewed, for instance, by projecting the two-dimensional plot of Fig. 1.10 onto the x axis. The channelled beam is peaked at the channel center ('flux peaking' effect).

For a typical GeV beam the angular distribution within $\pm\theta_c$ is flat, $g(\theta) = 1/(2\Phi)$. Hence the phase space of Fig. 1.10 is uniformly filled with particles. As a result, for the harmonic potential $f(E_T)$ is constant for E_T from 0 up to the critical value E_c . In Molière's approximation the $f(E_T)$ function is approximately flat (see figures in Chap. 2).

Another simple case is that in which the incident beam is perfectly parallel (zero divergence) to the atomic planes. This is typical for MeV ion beams (the so-called 'pencil beam'); at this energy the Lindhard angle θ_L is much greater than the typical beam divergence. Then $f(E_T) = 1/\sqrt{E_T}$ in the harmonic approximation; that is, the distribution is peaked at small E_T .

Oscillation of the individual particles means rotation of the two-dimensional distribution $g(x, \theta)$ on the phase plane of Fig. 1.10, as the particles penetrate the crystal depth. In the case of parallel incidence, the trapped particles have initially the same oscillation phases. Interestingly, this leads to oscillation of the whole flux distribution in the channel. Such oscillations (for example, in a plot of the nuclear encounter probability against the depth) have already been observed [22, 23]. In the harmonic potential, and without scattering, the flux oscillation would continue infinitely far. In reality, the potential unharmonicity and scattering limit this effect to only a few oscillations. The initial phases of the particles are rapidly 'forgotten' in the crystal depth, and one may consider the particle ensemble *averaged* over the oscillation phase. Then one says that these particles are in the state of *statistical*

equilibrium. This assumption, that any oscillation phase is equally probable, is often applied in a theoretical analysis. Notice that the particles trapped from a divergent beam are already in the statistical equilibrium state, since they uniformly populate the phase space.

1.4 Dechanneling

Scattering of the channeled particle from the electrons and nuclei (as well as from the crystal lattice defects) causes non-conservation of the transverse energy E_T . The E_T evolution may be considered as a random-walk process with the E_T changes being positive or negative in any single event:

$$\Delta E_T = p v \theta \theta_s + \frac{p v}{2} \theta_s^2 , \quad (1.31)$$

here θ_s is the angle of scattering in the event. As a result of this evolution, E_T may be higher than the potential-well depth E_c , and thus the particle leaves the channeling mode (*dechanneling* process). Reverse transitions, from the random fraction to the channeled one, are also possible and will be discussed in Sect. 2.3.

Since the most frequent collisions of the particle are soft, one way to treat scattering in the channeling process is to apply the well-known formalism of a diffusion theory. A full description, which includes the rare hard encounters as well as the realistic details of an imperfect crystal, is based on a Monte Carlo computer simulation. We discuss these two approaches in this section.

1.4.1 Diffusion Theory

Evolution of the particle distribution in a crystal may be described within the framework of the kinetic approach. From the above sections we know that the length λ of one oscillation of a particle channeled in the crystal planes is quite small (only $\sim 30 \mu\text{m}$ for a 100 GeV proton in silicon). Later we shall see that the typical length along which a GeV particle stays in the channeling mode is a factor of 1000 times bigger than λ (namely, $\sim 10 \text{ cm}$ for the above example). This means that the particle state (represented by E_T) changes slowly, and therefore the idea of a transverse energy (no longer invariant) may be still useful in the presence of scattering. Although the description in the terms of x, θ is also possible [24], characterization of the particle with E_T simplifies the consideration.

As the E_T hardly changes over one oscillation, all the functions (such as the probability of interaction, etc.) of the particle position x may be averaged along the particle trajectory in order to replace the dependence on x with that on E_T . Denoting by $w(E_T, q)dz$ the probability that the transverse energy will change (as a result of scattering) from E_T to $E_T + q$ over the length dz ,

we write the change in the particle distribution function $f(E_T, z)$ with the transverse energy in the form:

$$\frac{\partial f}{\partial z} = \int [f(E_T - q)w(E_T - q, q) - f(E_T)w(E_T, q)] dq . \quad (1.32)$$

To solve this *master equation* one has to know the function of two variables, $w(E_T, q)$. Assuming the change in E_T in any single event is small, and expanding the above equation in powers of q , we may transform (1.32) to a simpler Fokker–Planck equation:

$$\frac{\partial f}{\partial z} = -\frac{\partial}{\partial E_T}(Af) + \frac{1}{2}\frac{\partial^2}{\partial E_T^2}(Df) , \quad (1.33)$$

$$A = \left\langle \frac{\Delta E_T}{\Delta z} \right\rangle = \int q w(E_T, q) dq , \quad (1.34)$$

$$D = \left\langle \frac{(\Delta E_T)^2}{\Delta z} \right\rangle = \int q^2 w(E_T, q) dq , \quad (1.35)$$

where A and D are, respectively, the mean and mean-squared change in the transverse energy over the unit length; the averaging in the above equations is also assumed to be over the particle trajectory. From the consideration of particle scattering a connection between the friction factor (1.34) and the diffusion one (1.35) follows [25]:

$$A(E_T) = \frac{1}{2}\frac{\partial}{\partial E_T} D(E_T) . \quad (1.36)$$

With use of this relation the Fokker–Planck equation (1.33) may be transformed further into the diffusion equation:

$$\frac{\partial f}{\partial z} = \frac{1}{2}\frac{\partial}{\partial E_T} \left[D(E_T) \frac{\partial f}{\partial E_T} \right] . \quad (1.37)$$

It is assumed that the particles with $E_T > E_c$ escape the channeling mode immediately owing to the strong nuclear scattering; as the particle reaches the $E_T = E_c$ boundary, it is excluded from further consideration. The equation (1.37) may be solved for the diffusion factor in the form of $D = D_0 E_T^m$ [25, 26]. In semiconductors, like silicon and germanium, the electron density in most of the channel (far from nuclei) is rather uniform, being due to outer, valence electrons. For this reason the friction factor (1.34) is roughly independent of the position x , while the diffusion factor (1.35) tends to be a linear function of E_T [see (1.36)]. Calculations of $D(E_T)$ have shown that a linear approximation is valid in semiconductors until the channeled particle approaches nuclei at a distance of $\sim a_{TF}$ [8]. In the case of $D = D_0 E_T$ the solution of (1.37) is [25, 26]:

$$f = \sum_{k=1}^{\infty} C_k J_0 \left(j_{0,k} \sqrt{E_T/E_c} \right) \exp \left(-\frac{D_0 j_{0,k}^2 z}{4E_c} \right) , \quad (1.38)$$

where C_k is determined by the particle initial distribution f_0 :

$$C_k = \frac{1}{E_c J_1^2(j_{0,k})} \int_0^{E_c} f_0(E_T) J_0 \left(j_{0,k} \sqrt{E_T/E_c} \right) dE_T. \quad (1.39)$$

In this relation $j_{0,k}$ is the k th zero of the Bessel function J_0 , E_c is the critical energy of the transverse motion. As (1.38) demonstrates, the attenuation rate of row terms with $k > 1$ is proportional to $j_{0,k}^2 \sim k^2$. The terms with $k > 1$ attenuate along some initial segment, and after that the particle distribution is described by the first term of (1.38):

$$f = C_1 J_0 \left(j_{0,1} \sqrt{E_T/E_c} \right) \exp \left(-\frac{D_0 j_{0,1}^2 z}{4E_c} \right), \quad (1.40)$$

Therefore, in the depth of a crystal the fraction of channeled particles decreases exponentially $\sim \exp(-z/L_D)$, with the *dechanneling length*

$$L_D = \frac{4E_c}{j_{0,1}^2 D_0}, \quad (1.41)$$

which no longer depends upon the initial particle distribution. The value D_0 (friction factor) is proportional to the average electron density in the channel and will be discussed in detail below.

The length of relaxation from (1.38) to (1.40) is, on the whole, determined by the attenuation of the second factor in (1.38) and has the order of [27]

$$L_{\text{rel.}} = \left(\frac{j_{0,1}}{j_{0,2}} \right)^2 L_D \simeq 0.2 L_D. \quad (1.42)$$

That is, strictly speaking, the dechanneling relation becomes exponential with the characteristic dechanneling length only at a considerable crystal depth. If the crystal length is less than that characteristic value, the dechanneling length measured in experiments depends upon the initial conditions of the beam hitting the crystal: for example, upon the kind of capture (the end face or the volume one) or upon the beam divergence (it can be small, close to the critical angle of channeling, or much larger).

D_0 is determined by the square of the average angle of scattering from electrons and nuclei [see (1.31, 1.34)]:

$$D_0 = \frac{pv}{2} \left\langle \frac{(\delta\theta_s)^2}{\delta z} \right\rangle. \quad (1.43)$$

The contribution of the potential fluctuation caused by the discreteness of the crystal lattice is much smaller than that of the multiple nuclear scattering, for the case of planar channeling [28]; note that λ is a factor of 10^5 larger than the interatomic spacing. Limiting $x_c \leq d_p/2 - a_{\text{TF}}$, one may consider only scattering from electrons. From the consideration of a particle scattering from an electron [4] one has

$$\left\langle \frac{(\delta\theta_s)^2}{\delta z} \right\rangle = \frac{m_e}{2p^2} \left(\frac{\delta E}{\delta z} \right)_{\text{am}} \frac{n_e(x)}{n_{\text{am}}} . \quad (1.44)$$

In this relation $n_e(x)$ is the electron density, n_{am} is the average (amorphous) electron density, m_e is the electron rest mass. The mean energy loss by ionization in an amorphous substance is given by the equation

$$\left(\frac{\delta E}{\delta z} \right)_{\text{am}} = 4\pi N_A r_e^2 m_e c^2 \frac{Z}{A} \rho \left(\frac{Z_i}{\beta} \right)^2 L_e , \quad (1.45)$$

where N_A is the Avogadro number, A is the atomic weight of the crystal, r_e is the classic electron radius, ρ is the substance density, and β is the particle's velocity divided by the velocity of light c . L_e is the Coulomb logarithm for the particle-electron collisions:

$$L_e = \ln \frac{2m_e c^2 \beta^2 \gamma^2}{I} - \beta^2 - \frac{\delta}{2} , \quad (1.46)$$

where $\delta \simeq 2 \ln \gamma$ is the correction caused by the density effect at high energies, I is the ionization potential ($I \simeq 16 Z^{0.9}$ eV; for silicon $I \simeq 172$ eV). This leads to

$$L_D = \frac{16}{j_{0,1}^2} \frac{pv A E_c}{4\pi N_A r_e^2 m_e^2 c^4 \rho Z Z_i^2 L_e} \frac{n_{\text{am}}}{\langle n_e(x) \rangle} . \quad (1.47)$$

In (1.47), $\langle n_e(x) \rangle$ means the average value for the ensemble of channelled particles. Further simplification of (1.47) to an analytic form would be useful. For this purpose we average as follows:

$$\langle n_e \rangle = \frac{1}{x_c} \int_0^{x_c} n_e(x) dx . \quad (1.48)$$

As $n_e(x) = (1/4\pi r_e m_e c^2)(\partial^2 U(x)/\partial x^2)$, one obtains

$$L_D = \frac{16}{j_{0,1}^2} \frac{pv}{Z_i L_e r_e m_e c^2} \frac{U(x_c)x_c}{U'(x_c)} , \quad (1.49)$$

where $U(x_c) = E_c$, the second factor contains the dependence upon energy, the third one contains that upon the substance properties. The dependence $L_D \sim U(x_c)x_c/U'(x_c)$ agrees well with experimental data [29]. Replacing $j_{0,1}$ by $\simeq 3\pi/4$, taking into consideration that the potential in the channel is the superposition of two planar potentials, and using the Lindhard potential for an atomic plane (1.11) we rewrite (1.49) in the final form (for $\gamma \gg 1$) [27]

$$L_D = \frac{256}{9\pi^2} \frac{pv}{\ln(2m_e c^2 \gamma/I) - 1} \frac{a_{\text{TF}} d_p}{Z_i r_e m_e c^2} . \quad (1.50)$$

As (1.50) demonstrates, the dechanneling length is proportional to the interplanar distance d_p . The Si(110) planes are equidistant with $d_p = 1.92$ Å. For the Si(111) planes the large spacing $d_p^L = 2.35$ Å alternates with the

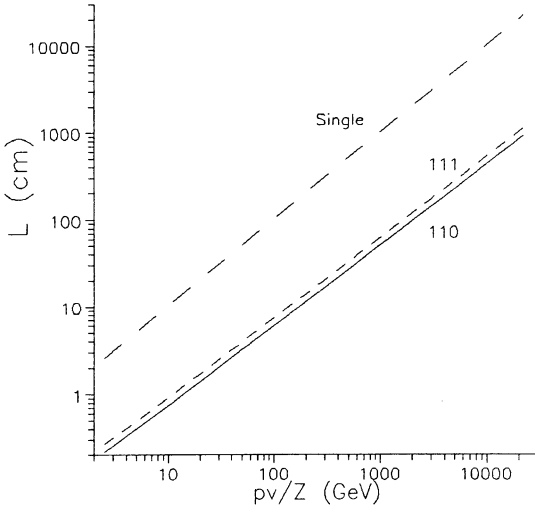


Fig. 1.11. Calculated functions $L_D(pv)$, (1.50) for the Si(110) (solid line) and Si(111) (short dashes) channels. The line with the long dashes is the length L_{single} , (1.59), for single-scattering dechanneling.

small one d_p^S (see Fig. 1.7); note that $3d_p^S = d_p^L$. Thus, particles moving inside the small interplanar interval d_p^S in a long crystal Si(111) can be ignored.

In the case of $E = 70$ GeV, (1.50) gives the value $L_D^{(111)} = 5.4$ cm in Si(111) and $L_D^{(110)} = 4.4$ cm in Si(110), providing a satisfactory agreement with experimental data (Chap. 3). Calculated functions (1.50) are given in Fig. 1.11. A comparison of (1.50) with the experimental data for Si(110) and Si(111) channels in the energy range from 8 to 200 GeV is given in Chap. 3.

Logarithmic correction to the linear extrapolation $L_D \sim pv$ makes up dozens of percent in the experimentally investigated field of energies. The dependence upon substance properties reduces to the factor $a_{TF}d_p$, and results in the dependence $L_D \sim Z^{-1/3}$ in isomorphous ($d_p = \text{const.}$) lattices (for example, Si and Ge). According to (1.50) the ratio $L_D^{(111)}/L_D^{(110)}$ should be of the order of $d_p^{(111)}/d_p^{(110)} = 1.23$ for silicon. The experimental ratio is 1.4 ± 0.2 .

Further analysis of dechanneling, in particular the analysis of the applicability of the diffusion approach, is discussed below. Later, in Chap. 2, we shall discuss the dechanneling process in a curved crystal, and the dechanneling on the crystal lattice imperfections.

1.4.2 Single Electronic Scattering

Beam steering by a crystal is due to the trapping of some particles in the potential well $U(x)$, where they then may follow the direction of the atomic planes. This simple picture is disturbed by scattering processes which could cause (as a result of one or many events) the trapped particle to come to a free state (*feed-out*, or *dechanneling* process), and an initially free particle to be

trapped in the channeled state (*feed-in*, or *volume capture*). Here the physics of particle scattering in an aligned crystal is considered in more detail.

The particles trapped in the stable channeled states move far from the nuclei. The transitions from or to the stable states are, therefore, possible mainly through electronic scattering [8]. It is convenient to relate this angular scattering to the energy lost by the particles in the electronic collisions [4]. The mean energy loss in the electronic scattering can be written as a function of the position x [39]:

$$-\frac{dE}{dz} = \frac{D}{2\beta^2} \left[\ln \frac{2m_e c^2 \beta^2 \gamma^2}{I} - \beta^2 - \delta + C(x) + \rho_e(x) \left(\ln \frac{T_{\max}}{I} - \frac{T_{\max}}{2m_e c^2 \gamma^2} \right) \right], \quad (1.51)$$

where $D = 4\pi N_A r_e^2 m_e c^2 Z_i^2 \frac{Z}{A} \rho$. Here T_{\max} is the maximal energy transfer to a single electron:

$$T_{\max} = \frac{2m_e c^2 \beta^2 \gamma^2}{1 + 2\gamma m_e/M + (m_e/M)^2} \approx 2m_e c^2 \beta^2 \gamma^2. \quad (1.52)$$

The term $C(x)$ is a correction found in [39]. It equals

$$C(x) = \sum_{G \neq 0} e^{iGx} n_e(G) \ln \left(\frac{2m_e I}{\hbar^2 G^2} \right), \quad (1.53)$$

where $n_e(G)$ is the Fourier transform of the electron density and \mathbf{G} is the reciprocal lattice vector; for further details see [39].

The last term in the brackets of (1.51) is due to single collisions and is responsible for the angular scattering; it depends on the local density $\rho_e(x)$ (normalized to the amorphous one, $\rho_e(x) = n_e(x)/n_{\text{am}}$) of the electrons. The value of $\rho_e(x)$ is computed from the potential $U(x)$ via Poisson's equation (subtracting the nuclear density, which is discussed below).

The energy T transferred in such a single collision is generated according to the distribution function [40]:

$$\frac{d^2N}{dT dz} = \frac{D \rho_e(x)}{2\beta^2} \frac{1}{T^2}. \quad (1.54)$$

The $1/T^2$ distribution is quite easy to generate by a computer. The overall probability of a collision with $I \leq T \leq T_{\max}$ per unit length can be obtained by integration of the above equation over T . It should be mentioned that deviations from the above formula at $T \approx I$ or $T \approx T_{\max}$ are of no concern at all because of the nature of dechanneling, as discussed below. The momentum q transferred in a collision is equal to $\sqrt{2m_e T + (T/c)^2}$. The transverse component of q produces a (round) angular kick of

$$\theta_s = \frac{\sqrt{2m_e T (1 - T/T_{\max})}}{p}. \quad (1.55)$$

Its projections are used to modify the angles θ_x and θ_y of the particle. The energy is returned modified according to the E loss in the crystal. In the simulation no difference is made between the scatterings with small or large T ; they are just treated as small or large kicks. The frequent small kicks produce, in fact, a diffusion-like angular scattering, with a mean-square value given by

$$\theta_{\text{rms}}^2 = \frac{2m_e}{p^2} \left\langle \sum_i T_i (1 - T_i/T_{\max}) \right\rangle. \quad (1.56)$$

The rare hard scattering may knock the particle out of the channeling mode at once. The distribution of (1.54) is continuous, and there is no sharp distinction between the ‘soft’ and ‘hard’ kicks, both in the nature and in the considered algorithm. It must be mentioned that the problem of a ‘catastrophic’ dechanneling, owing to a single collision of a heavy particle with an electron, arises only in the high-energy range, starting at ~ 1 GeV [36]. In the MeV range the maximal momentum transfer in such a collision is lower than the one required for this ‘knock-out’. This is discussed in some detail below.

1.4.3 Comments on the Diffusion Approach

Here a difficulty with the diffusion approach specific to the high-energy ($>\text{GeV}$) range is discussed [36]. The diffusion approximation for electronic scattering is employed by many authors, even in computer simulations [34, 43]. In this approach one assumes that scattering from electrons is diffusion-like. That is, the angular kick has $\theta_s \ll \theta_c$ in any single collision. Then the angle of the particle is changed by frequent infinitesimal steps, with the rms value of the scattering angle, θ_{rms} , given by (1.56). It is worth mentioning that θ_{rms} value depends on the total amount of the transferred energy, not on the detail of the distribution of (1.54).

In the MeV energy range (where most of the experimental and theoretical efforts for crystal channeling have been made) this approximation for heavy ions works perfectly well, because even the maximal possible angular kick per collision, $\theta_s^{\max} = \sqrt{m_e T_{\max}}/p \approx 1.4m_e/M$ (M for the particle mass), is always smaller than θ_c . For example, for protons $\theta_s^{\max} \approx 0.77$ mrad, whereas $\theta_c > 1$ mrad in silicon for proton energies up to 10 MeV.

In the energy range of ~ 100 GeV (the range of modern applications of bent crystals), $\theta_c \sim 10$ μ rad. Therefore rare catastrophic collisions with $\theta_s > \theta_c$ may happen. More generally, the weight of the hard collisions with θ_s comparable to θ_c is strongly increased. The problem for the diffusion approach is that the integration up to T_{\max} in the diffusion coefficient, (1.56), is no longer justified. The *energy* transferred with catastrophic collisions ($\theta_s > \theta_c$) is of no importance for dechanneling and therefore need not be included in the diffusion coefficient.

Although θ_{rms}^2 depends on T_{\max} via $\ln(T_{\max}/I)$, it will be shown below that removal of the energy transfers of catastrophic collisions from (1.56) reduces the diffusion coefficient by a factor of 2–3.

Nevertheless, some authors [28, 34, 35] use the maximal possible value for T_{\max} , given by (1.52). Others [43–44] try a ‘cutoff’, defining T_{\max} as the energy transfer T_c causing the angular kick of the order of θ_c (or even much smaller [45]), because at higher T the diffusion approach is certainly invalid.

The weak points of both choices may be clarified with a numerical example. For a 100-GeV proton the maximal transfer is $T_{\max} = 10$ GeV. However, the transfer T_c causing the angular kick (projection) to be equal to θ_c is quite moderate [36]:

$$T_c \approx \frac{p^2 \theta_c^2}{m_e} = \frac{2M\gamma}{m_e} E_c . \quad (1.57)$$

In silicon $T_c = 4$ MeV for a 100-GeV proton. One finds that from the energy transferred via single collisions, about one half of it is carried away by the scattering with $\theta_s > \theta_c$. Taking these events into account in (1.56) is inconsistent with the diffusion approximation. The problem is even deeper, because for collisions with $T > T_c$ the T value is no longer important. Scattering with $T = 10$ MeV or with $T = 1$ GeV is equally important, since they knock the particle out of the channeling mode immediately. It is the *probability* of ‘knockout’ that is important, not the energy transferred with it. Therefore, including in (1.56) the *energy* transferred in scattering with $T > T_c$ (i.e., $T_{\max} = 10$ GeV in our example) increases the inconsistency further.

In order to take into account the above argumentation, some authors [43–45] remove large transfers: $T_{\max}^{\text{cut}} \leq T_c$. One problem then is the arbitrariness of the cutoff parameter T_{\max}^{cut} . For example, the use of (1.57) instead of (1.52) for T_{\max} decreases the diffusion coefficient by a factor of two. In order to fit the experimental data the allowed angle of scattering is sometimes restricted further, e.g., down to $\theta_c/20$ [45], thus reducing that coefficient even further. Such freedom in the selection of T_{\max} reduces the usefulness of diffusion theory in the GeV energy range. Neglect of the rarer hard scattering events is another difficulty, since their contribution is lost. This may be particularly important, for example, for the rare process of feeding-in in the bent crystals. Another example may be the energy-loss spectrum in an aligned crystal. The rarer hard events form the spectrum tail; on the other hand, such events influence the channeled-particle state. In a diffusion-based description this link is lost. Finally, in crystal-assisted beam extraction the energy-loss fluctuations may be important for the particle multi-turn dynamics in the accelerator ring.

Nevertheless, the diffusion model often provides a good description of dechanneling in bent crystals. The reason may be understood if we look at the influence of hard collisions on dechanneling. From (1.54) and (1.57) the characteristic length, along which such a ‘single’ feed-out occurs, may be estimated [36] as

$$L_{\text{single}} = \frac{2\beta^2 T_c}{D\langle\rho_e(x)\rangle} = \frac{4pvE_c}{Dm_e c^2 \langle\rho_e(x)\rangle}. \quad (1.58)$$

It has much the same functional dependence (except for a logarithmic factor) on the properties of the crystal and the incident particles, as has the dechanneling length in the diffusion model [see (1.47)]. The similarity remains in a bent crystal: $L_D, L_{\text{single}} \sim E_c(pv/R)$. Therefore in a regular case the diffusion approach may fit the experimental data reasonably well, as does the diffusion estimate (1.50). The ratio of the estimates (1.58) and (1.47) is roughly equal to L_e [Coulomb logarithm (1.46)]. Thus, of the order of $1/L_e$ particles dechannel from a single electronic collision (with transfer $T_c < T < T_{\max}$). Transforming (1.58) further in the way used earlier for the diffusion estimate (1.50), one obtains

$$L_{\text{single}} = \frac{4a_{\text{TF}} d_p p v}{Z_i e^2}. \quad (1.59)$$

The value of L_{single} is plotted in Fig. 1.11 as a function of $p v$, together with L_D from (1.50).

1.5 Energy Loss

Energetic charged particles in solids lose energy mostly in electronic collisions. In an amorphous substance or a disaligned crystal, the energy lost by a relativistic particle shows the well-known Landau distribution [46]. At high energies, the contributions to energy loss come roughly equally from the distant soft and the close more violent collisions ('equipartition rule' [4]). The frequent soft scatterings provide a Gaussian-like peak in the loss spectrum, and the rare hard collisions contribute to the long high-energy tail [see (1.51)]. The spread of the energy-loss distribution is mostly determined by the close collisions.

When a beam is aligned with respect to the atomic planes, the particle distribution over the transverse coordinate x undergoes an important change, resulting in the beam being split into the channeled and random fractions. This change affects the energy-loss spectrum of the beam particles in the aligned crystals.

Figure 1.12 shows the electron density in a silicon crystal (averaged along the (110) and (111) planes) as a function of the transverse coordinate; the density is obtained from the second derivative, $\rho_e(x) \sim U''(x)$, of the interplanar Moliére potential. The well-channeled particles are confined in a region with an electronic density much lower than the averaged, amorphous value.

The reduction in the local electron density seen by the channeled particles suppresses the contribution from the close scatterings. As a result, both the mean value and the spread of the energy losses are reduced for these particles.

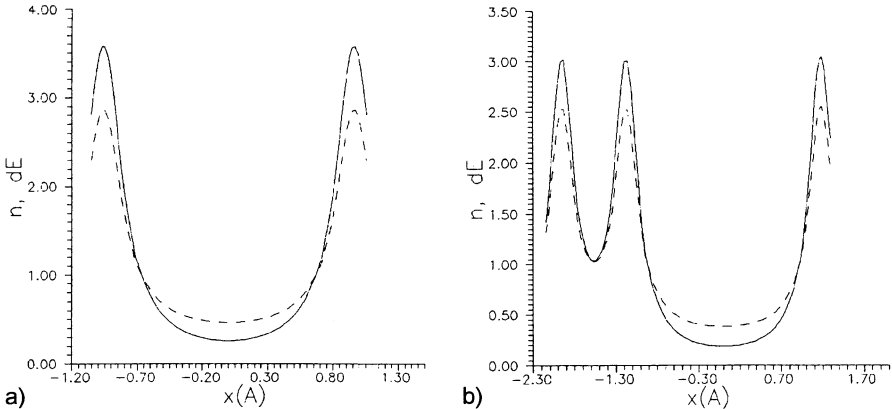


Fig. 1.12a,b. The electron density (solid line) and the mean energy-loss (dashed line) in an aligned crystal, normalized to the amorphous values, as functions of the transverse coordinate. (a) Si(110), (b) Si(111).

From the equipartition rule, one might expect that at high energies the energy loss of the best-channeled particles (those with lowest E_T) should be of the order of

$$\frac{\langle \Delta E \rangle_{\text{chan}}}{\langle \Delta E \rangle_{\text{ran}}} = 0.5 [1 + \rho_e(0)] = \frac{12(d_p/a_{TF})}{[(d_p/a_{TF})^2 + 12]^{3/2}} \approx 0.6 , \quad (1.60)$$

where the reduced electronic density $\rho_e(0)$ for the channel center was estimated from the Lindhard potential, with the numerical value given for the most open Si planes (111) and (110). The above relation also follows from (1.51) in the limit of high energies, $\gamma \rightarrow \infty$. The energy-loss spectrum, therefore, is remarkably split into the ‘channeled’ and ‘random’ (or quasi-channeled) fractions, thus providing an easy way to distinguish between these two sorts of particle motion (see figures in Chap. 3).

The quantitative description of the position-dependent energy-loss was given by Esbensen and Golovchenko [39]. Their result for the mean energy-loss is written in a relativistic form in (1.51). In the case of random incidence this expression gives the right mean energy-loss, whereas the shape of the distribution is determined by close collisions. Figure 1.12 shows the mean energy-loss (1.51) as a function of the coordinate x , for Si planes (110) and (111).

In aligned crystals, the observed spectrum depends essentially on the distribution function of the particles: that is, on the incident beam divergence, on the scattering and bending processes in the crystal depth, and so on. This sensitivity makes ΔE a very useful observable. Fortunately, there is an experimental technique, based on the implantation of the diodes in semiconductor crystals, that allows the measurement of the energy *deposited* in the depleted zone of the crystal. The deposition is somewhat different from the total loss,

because of the escape of the most-energetic, $T > T_0$, electrons from a crystal (T_0 is of the order of 1 MeV). To estimate the ΔE deposit, one should use T_0 instead of T_{\max} in (1.54). A crystal may be supplied with several depleted zones along its length, thus making it possible to trace the evolution of individual particles in the crystal depth. See [48–51] for many details of the method.

The technique provides an important link between the electronic properties of a crystal and the state of a particle in it. It has been extensively used for studies in both fields. In particular, tagging particles by ΔE has been applied since the earliest steps of relativistic channeling, as it greatly simplifies the channeling measurements with divergent beams, where the fraction of channeled particles is small. Energy-loss measurements and simulations are considered in some detail in Chap. 3.

1.6 Axial Channeling

When an incident particle is aligned with a crystallographic axis, the transverse electric field of the crystal shows a rather complicated structure (Fig. 1.13). The strong field of an atomic string may capture a negatively charged particle, which then moves along a screw trajectory in the axial direction. To a good approximation, one may consider the potential of an isolated atomic string $U(r)$. According to Lindhard

$$U(r) = \frac{Z_i Z e^2}{a_i} \ln \left(1 + \frac{3a_{TF}^2}{r^2} \right), \quad (1.61)$$

where a_i is the interatomic spacing in the string, and r is the distance from the particle to the axis. The particle motion in the field $U(r)$ with axial symmetry is known [52] to be characterized by two conserved quantities: the angular momentum J and the energy E_T in the transverse plane.

Suppose the particle is incident at a small angle ψ with respect to the axis and has a projection $\psi_r = dr/dz$ directed toward the axis and a projection $\psi_\phi = rd\phi/dz$ perpendicular to it; $\psi^2 = \psi_r^2 + \psi_\phi^2$. The conserved angular momentum is then $J = p\psi_\phi r = pr^2 d\phi/dz$. With the transformations from Sect. 1.3, E_T can be expressed as

$$E_T = \frac{pv}{2} \psi^2 + U(r) = \frac{pv}{2} \left(\frac{dr}{dz} \right)^2 + \frac{J^2}{2M\gamma r^2} + U(r). \quad (1.62)$$

The radial oscillation $r(z)$ of the particle can be found from (1.62) by integration:

$$z = \int \frac{dr}{\sqrt{\frac{2}{pv}[E_T - U(r)] - \frac{J^2}{p^2 r^2}}} + \text{const}. \quad (1.63)$$

With the use of $d\phi = (J/pr^2)dz$, one finds the particle trajectory $r(\phi)$ in the transverse plane as follows

$$\phi = \int \frac{\frac{J}{r^2} dr}{\sqrt{2M\gamma(E_T - U(r)) - \frac{J^2}{r^2}}} + \text{const} . \quad (1.64)$$

The above formulas define the particle motion. It is finite in the transverse plane (i.e., the particle is trapped) if E_T is below the critical value defined by the potential well depth U_0 (Table 1.4). The corresponding maximal angle of particle capture in the axial channeling mode $\psi_L = \sqrt{2U_0/pv}$, is approximately given by the Lindhard critical angle

$$\psi_L = \sqrt{\frac{4Z_iZe^2}{pva_i}} . \quad (1.65)$$

Table 1.4. The potential-well depth (in eV) of some axial channels of the crystals of silicon, germanium, and tungsten, calculated in the Molière approximation at room temperature.

Si			Ge			W		
$\langle 100 \rangle$	$\langle 110 \rangle$	$\langle 111 \rangle$	$\langle 100 \rangle$	$\langle 110 \rangle$	$\langle 111 \rangle$	$\langle 100 \rangle$	$\langle 110 \rangle$	$\langle 111 \rangle$
89	114	105	157	203	185	842	576	979

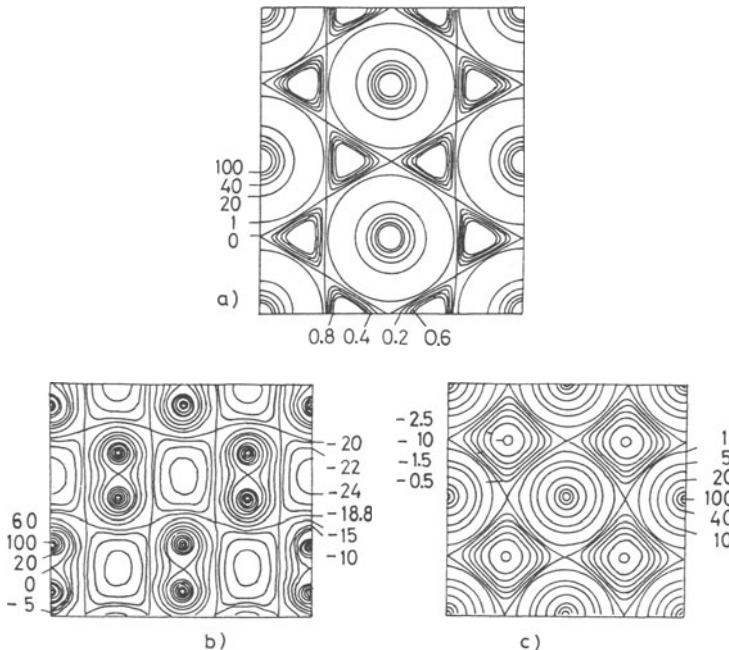


Fig. 1.13a–c. Axial potential calculated in [14] with use of the Molière approximation: (a) $\text{Si}\langle 111 \rangle$; (b) $\text{Si}\langle 110 \rangle$; (c) $\text{Si}\langle 100 \rangle$. The numbers give the potential in eV.

Comparing ψ_L to the Lindhard critical angle θ_L for the planar case, (1.11),

$$\theta_L = \sqrt{4Z_i Ze^2 N d_p \sqrt{3} a_{TF} / p v}, \quad (1.66)$$

one finds that the axial critical angle is a factor of ~ 3 greater than the planar angle.

The negative particles channeled with small E_T move in the vicinity of the atoms and therefore experience an enhanced scattering. The particles with small J and arbitrary E_T regularly pass close to the atoms and strongly scatter as well. These two groups of particles may be rapidly lost from the channeling mode. The particles with nonsmall J and nonsmall E_T move far from atoms and therefore experience a reduced scattering.

The positively charged particles move freely between the atomic strings and may be captured in the minor potential wells between the strings. These wells are small, asymmetric and rather dependent on the axial direction (Fig. 1.13).

2. Beam Deflection by Bent Crystals

2.1 Particle Motion in a Bent Channel

One may expect that in a slightly bent monocrystal the channeled particles would follow the direction of the bent atomic planes (or axes), thus bending from the initial direction by the angle of the crystal bend. The possibility of such an effect and the proposal to use it for steering high-energy particle beams were suggested by Tsyganov in 1976 [56], and then realized in a pioneering experiment [57] in Dubna in 1979 by a joint Soviet–American team.

Let us consider the motion of a charged particle in a curved channel. For a macroscopical radius of curvature (say one meter), the bending of a crystal has no effect on the potential of the atomic lattice in the range of angstroms. However, it causes a centrifugal force in the non-inertial frame related to the channel. Later we shall use this frame, where the z axis follows the direction of the bent atomic planes, and the coordinates x and θ are defined with respect to the local atomic planes at some point z . In this frame, (1.19) for particle motion in the channel is modified [63],

$$pv \frac{d^2x}{dz^2} + U'(x) + \frac{pv}{R(z)} = 0 , \quad (2.1)$$

to take into account the local curvature of the channel, $1/R(z)$, in the bent plane x, z . The centrifugal force $pv/R(z)$ tends to push the particle across the channel. Consideration of the particle motion becomes elementary if the curvature $1/R$ is independent of z . The particle moves as if it were in the *effective interplanar potential*

$$U_{\text{eff}}(x) = U(x) + \frac{pv}{R}x \quad (2.2)$$

with the transverse energy

$$E_T = \frac{pv}{2}\theta^2 + U_{\text{eff}}(x) . \quad (2.3)$$

Examples of the potential $U_{\text{eff}}(x)$ for various ratios of pv/R are shown in Fig. 2.1 in comparison with the undisturbed potential $U(x)$ for the planes (110) of silicon. The expressions describing the particle motion, which are given in Sect. 1.3 for an arbitrary $U(x)$, remain valid for the bent channel, if

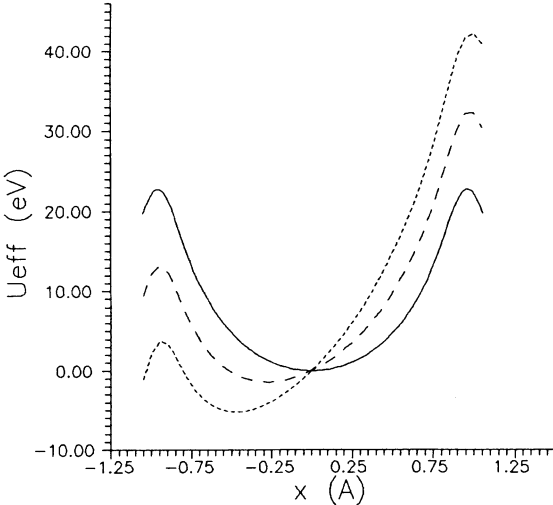


Fig. 2.1. The interplanar Molière potential for Si(110) (solid line) and the effective potential $U_{\text{eff}}(x)$ for pv/R of 1 GeV/cm (dashed line) and 2 GeV/cm (dotted line).

$U(x)$ is replaced with $U_{\text{eff}}(x)$. Notice that the radius R appears only through the ratio of pv/R . For the different energies but the same pv/R ratio the character of motion is the same.

Clearly, as the curvature pv/R increases, the depth of the effective potential well decreases, and the minimum of the well is shifted towards the atomic plane. At some critical value $(pv/R)_c$ the well disappears and channelling is no longer possible. The critical bending curvature is defined by the maximal interplanar field U'_{\max} [56]. Its values are 6, 12, and 48 GeV/cm for the planes (110) of silicon, germanium, and tungsten, respectively. Since this maximum is achieved near the atomic plane, where the nuclear scattering is appreciable, the practical *critical radius* R_c is determined better by the field $U'(x_c)$ at the channel border $x_c \approx d_p/2 - a_{\text{TF}}$:

$$R_c = \frac{pv}{U'(x_c)} \approx \frac{pv}{\pi N d_p Z_i Z e^2} . \quad (2.4)$$

In silicon $U'(x_c) \approx 5$ GeV/cm (see Table 1.3). The dependence of the effective well depth (that is, of the critical transverse energy E_c in a bent channel) on the curvature pv/R is drawn later in Fig. 2.5 for the Molière approximation.

For the harmonic $U(x)$, the $U_{\text{eff}}(x)$ is harmonic too. Then the well depth is

$$E_c(R_c/R) = E_{c,0} \left(1 - \frac{R_c}{R}\right)^2 , \quad (2.5)$$

where $E_{c,0}$ is the well depth in the straight crystal. The critical angle is reduced:

$$\theta_c(R_c/R) = \theta_{c,0} \left(1 - \frac{R_c}{R}\right) , \quad (2.6)$$

where $\theta_{c,0}$ is the critical angle for the straight crystal. The particles oscillate in the harmonic $U_{\text{eff}}(x)$ with the same, (1.24), period,

$$x = -x_c \frac{R_c}{R} + x_c \sqrt{\frac{E_T}{E_c}} \sin \left(\frac{2\pi z}{\lambda} + \phi \right), \quad (2.7)$$

around the new equilibrium point $x_e = -x_c R_c / R$; here ϕ is the initial phase. Figure 2.2 shows the phase trajectories on the plane (x, θ) of the protons channeled in the bent crystal of Si(111) computed for the Molière approximation.

For the variable $R(z)$, one should solve the dynamic equation (2.1). Strictly speaking, in this case there is no potential function like $U_{\text{eff}}(x)$ and E_T is not conserved (and hence it has no meaning). In practice, however, the crystal curvature may change appreciably (as compared to $1/R_c$) only over some millimeters. Along this length a ~ 100 -GeV particle makes about a hundred oscillations in the channel. Therefore the transverse energy remains practically unchanged in the presence of a curvature gradient. At any place one can consider the ‘local’ effective potential well (varying with z), where a trapped particle retains its E_T .

An increase in the channel curvature at a certain crystal depth may cause the initially channeled particle to become free. This process is called *bending dechanneling*. It applies to the particles with the higher amplitudes (higher E_T). A gradual increase in the curvature with depth causes a gradual dechanneling of the particles trapped at the surface. For a slow change in the cur-

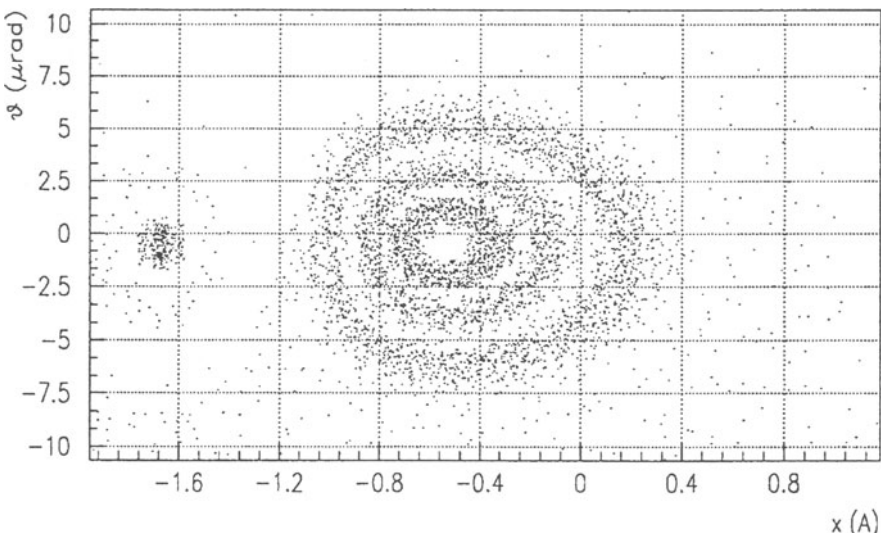


Fig. 2.2. The simulated phase trajectories of 450-GeV/c protons on the plane (x, θ) in Si(111) for the crystal bent with $p v / R = 1.5$ GeV/cm.

vature, the particles with $E_T > E_c(z)$ dechannel by the depth z , whereas the particles with smaller E_T survive in the channeled states.

The existence of particle trajectories, which start in the channeled mode and end up in the non-channeled mode, can be shown explicitly by following [58]. One of the widely used bending schemes is the so-called three-point bender (see Chap. 3). In this case the curvature is a linear function of z , say $1/R(z) = -k_0 z$. Then in the harmonic approximation (2.1) has the solution

$$x(z) = X \cos(\omega z + \phi) + (k_0/\omega^2)z, \quad (2.8)$$

where $\omega = 2\pi/\lambda$, $X^2 = x_0^2 + (\theta_0 - k_0/\omega^2)^2/\omega^2$, and x_0, θ_0 are the values of x, θ at $z = 0$; ϕ is the initial phase defined by x_0, θ_0 . It is obvious from (2.8) that with an increase in z any particle will have sooner or later $x(z) > x_c$ and thus will end up in a non-channeled state. Under the criterion of the slowly varying curvature, which is $k_0\lambda/\omega^2 x_c \ll 1$, the value of x oscillates about the equilibrium point $x_e = k_0 z / \omega^2$ several times before x_e changes considerably. The particles with x_0, θ_0 , which satisfy $X + k_0 z / \omega^2 \geq x_c$, have been dechanneled by the depth z .

Note that one can also consider, with the same equation (2.8), a reverse motion of a particle along such a trajectory. Starting in a non-channeled mode, a particle may be trapped into the channel if the crystal curvature decreases along the particle path. Therefore, the existence of the bending dechanneling means the existence of the corresponding mechanism of ‘feeding-in’. This mechanism, a ‘bending capture’, is considered in Sect. 2.3.2.

The unchanneled particles are influenced by the planar potential when they are moving in a trajectory nearly aligned to the crystal planes (‘quasi-channeled’ particles). This results in their angular spreading of order θ_c . Interestingly, in a bent crystal the mean exit angle of the unchanneled particles is not equal to the mean incident angle. These particles are deflected on average in a direction *opposite* to that of the crystal bending, that is, opposite to that of the channeled-beam deflection. This effect, the so-called ‘volume reflection’ [59], was found in computer simulations. The deflection angle for the ‘random’ beam in a bent crystal is of the order of the Lindhard angle.

2.2 Deflection Efficiency

In order to estimate the efficiency of beam deflection by a bent crystal one has to evaluate and combine various factors affecting the beam transmission – first of all, the bending dechanneling and the scattering in a bent crystal.

2.2.1 Acceptance of a Bent Crystal

Consideration of the question of how a particle enters or leaves the channeling mode in a bent crystal can be conveniently performed in the phase plane

(x, θ) . The phase area in which the particle channeling takes place in a bent crystal is shown in Fig. 2.2 for the case of a silicon crystal with alignment (111). It was shown above that the character of a particle motion in a bent crystal depends only on pv/R . As a comparison of Figs. 1.10 and 2.2 shows, as the crystal curvature pv/R increases, the phase space filled with the channeled particles decreases in size and moves toward the atomic plane. As a consequence, fewer particles can be trapped in this area in a bent crystal.

Let us suppose that particles with an angular distribution $f(\theta)$ are incident on a bent-crystal face. A particle will be channeled if its transverse energy in the crystal is below the critical value $E_c(pv/R)$. The fraction of particles trapped in the channeling mode (that is, the crystal acceptance) is then [60, 61]

$$A(pv/R) = \int_{-d_p/2}^{d_p/2} \frac{dx}{d_p} \int_{E_T < E_c} f(\theta) d\theta \delta \left(pv \frac{\theta^2}{2} + U(x) + \frac{pv}{R} x - E_T \right) . \quad (2.9)$$

In the most typical (for GeV beams) case of $f(\theta)$ being flat within $\pm\theta_c$ ($f = 1/2\Phi$), the acceptance value (2.9) is simply proportional to the area of the ellipse $E_T = E_c(pv/R)$:

$$A(pv/R) = \int_{-x_c}^{x_{\max}} \frac{dx}{\Phi d_p} \sqrt{\frac{2}{pv} [E_c - U(x) - pvx/R]} , \quad (2.10)$$

where the maximal allowable coordinate x_{\max} of a channeled particle is found from the equation $U(x_{\max}) + x_{\max}pv/R = U(x_c) - x_cpv/R$.

In the other case, which is a parallel incident beam with $f(\theta) = \delta(0)$, the acceptance is determined by the reduction of the allowable range of the x coordinate only:

$$A(pv/R) = \frac{x_{\max} + x_c}{d_p} . \quad (2.11)$$

With the harmonic $U(x)$, the elementary expressions for the above two cases, (2.10) and (2.11), may be derived [62, 63]. The area of the phase ellipse $E_T = E_c(pv/R)$ is reduced by the factor $(1 - R_c/R)^2$. Therefore the acceptance for a divergent beam (2.10) is

$$A(pv/R) = \frac{2x_c}{d_p} \frac{\pi}{4} \frac{\theta_{c,0}}{\Phi} \left(1 - \frac{R_c}{R} \right)^2 = A_S \left(1 - \frac{R_c}{R} \right)^2 , \quad (2.12)$$

where A_S is the straight-crystal acceptance (1.29). The phase ellipse axis is reduced by the factor $1 - R_c/R$. Therefore, for a parallel beam the acceptance (2.11) is

$$A(pv/R) = \frac{2x_c}{d_p} \left(1 - \frac{R_c}{R} \right) = A_S^* \left(1 - \frac{R_c}{R} \right) , \quad (2.13)$$

where $A_S^* = 2x_c/d_p$ is the straight-crystal acceptance for this case.

For an incident-beam divergence comparable to θ_c the acceptance reduction factor in a bent crystal lies between $(1 - R_c/R)$ and $(1 - R_c/R)^2$ [or between (2.10) and (2.11)], depending on the $f(\theta)$ structure within $\pm\theta_c$. We shall denote this factor as A_B .

If a curvature appears somewhere in the depth of the crystal, one must take into account the particle distribution function $f(E_T)$, which may be different there from that at the surface. Then the instant reduction of the critical boundary from E_c to E_c^* , caused by the corresponding instant reduction of curvature, leads to the bending dechanneling of some particles. The fraction of particles that survive in the channeled states is

$$A_B(pv/R) = \frac{\int_0^{E_c^*} f(E_T) dE_T}{\int_0^{E_c} f(E_T) dE_T}. \quad (2.14)$$

The function $A_B(pv/R)$ calculated with the Moliére approximation for a divergent beam for the silicon channels (110) and (111) is shown in Fig. 2.3. The planes (111) have two channels, wide and narrow; therefore the function $A_B(pv/R)$ is plotted separately for each of the two. Note that the narrow channel has weaker bending properties; this taken together with its low acceptance (Sect. 1.2) and low dechanneling length (Sect. 1.4) means its contribution can usually be ignored. As one can see from Fig. 2.3, the crystal acceptance declines well before the critical bend is achieved. For the silicon deflector this threshold value of pv/R amounts to about 1 GeV/cm; for germanium it is ≈ 2 GeV/cm.

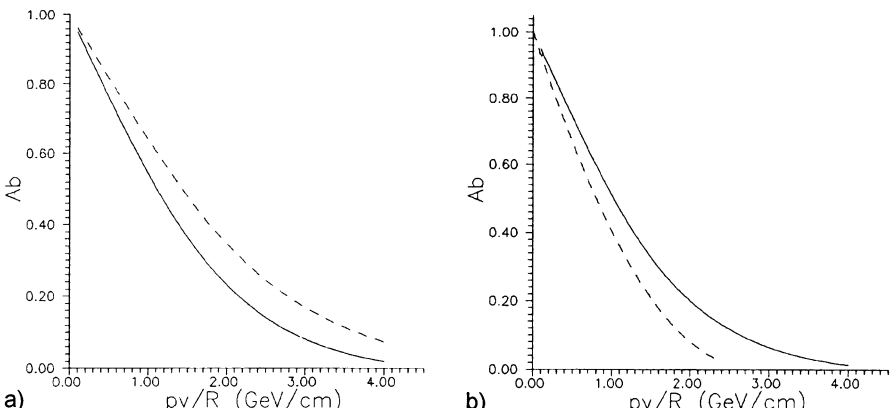


Fig. 2.3a,b. The reduction factor A_B calculated for a divergent incident beam as a function of pv/R for the Moliére approximation. (a) Si(110): $x_c = d_p/2 - a_{TF}$ (solid line) and $x_c = d_p/2 - u_T$ (dashed line). (b) Si(111): $x_c = d_p/2 - a_{TF}$. For wide planes (solid line) and narrow ones (dashed line).

The case of a parallel incident beam is illustrated in Fig. 2.4, where the reduction factor A_B of the bent-crystal acceptance is shown calculated as a function of pv/R with the Moliére approximation for Si(110) and (111). The solid lines represent A_B for the crystal curved along the whole length. The dashed lines are A_B for the crystal with an initial straight part but curved at some depth. In the latter case the state of statistical equilibrium must be assumed and (2.14) applied. As mentioned in Sect. 1.3, a divergent beam is already in a state of statistical equilibrium at the incidence.

It is worth mentioning that all the calculations in the well-known papers by Kudo [60] and Ellison [61] were made for a beam incident with zero divergence (the case of Fig. 2.4). This case is unusual when GeV beams are used. Figure 2.3 corresponds to a divergent ($> \theta_c$) incident beam, i.e., the case typical for high energies. For the (111) planes of the diamond-like lattice, there is some disagreement between [60] and [61]. Our results fully agree with those obtained by Kudo; that is, the narrow (111) planes have weaker bending properties than the wide ones. The opposite conclusion of [61] is probably due to the use of only two nearest planes in the calculation, unjustified in the (111) case.

The qualitative difference among all the above cases may be easily understood by considering phase-space pictures (like Fig. 2.2) filled with different starting populations of the particles. Experimental studies of bending dechanneling have been reported in many works, and will be discussed in Chap. 3. The measured data are in very good agreement with the predictions of the continuous-potential model.

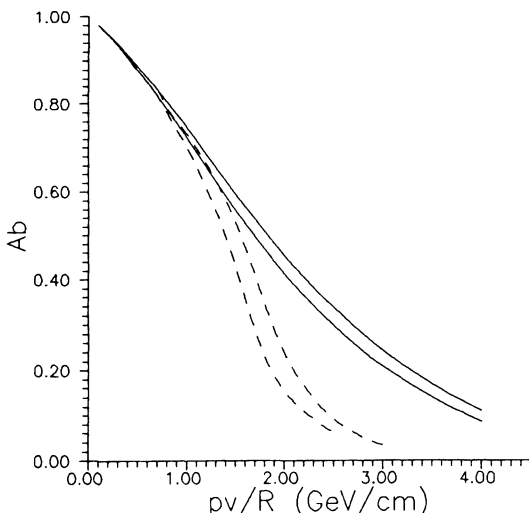


Fig. 2.4. The $A_B(pv/R)$ function calculated for a parallel incident beam for the Moliére approximation ($x_c = d_p/2 - a_{TF}$). The solid lines are for a crystal bent along the whole length. The dashed lines are for a crystal with an initial straight part. The top curves are for Si(110). The bottom curves are for the wide Si(111) planes.

2.2.2 Dechanneling in a Bent Crystal

The crystal curvature also modifies the influence scattering processes have on particle dechanneling. In general, channeling in a bent crystal should be considered with the kinetic methods of Sect. 1.4. The appearance of a centrifugal force pv/R changes the particle distribution in the channel to cause some change in the diffusion factor, and changes the critical transverse energy $E_c(pv/R)$.

As a result of a crystal bend, the channeled particles are shifted towards the atomic plane; therefore the diffusion factor for them is different from that in a straight crystal. Valence electrons in silicon and germanium have a roughly uniform distribution in the channel. Calculations [28, 44] show that the average electron density in a channel $\langle n_e \rangle$ and the diffusion factor are insensitive to the crystal curvature when R is roughly larger than $2R_c$. In a strongly bent crystal the diffusion of the transverse energy increases.

The transitions of the particles from the random to the channeled fraction of a beam are suppressed with the crystal bending. In a straight crystal the dechanneled particle retains some possibility of being scattered back to the channeled mode. In a bent crystal such a particle stays near the channel (in the phase space) for a short time because of a centrifugal force (see the discussion of feed-in processes in Sect. 2.3).

In a crystal with variable curvature, $1/R(z)$, the ‘drift’ of the boundary $E_c(z)$ may influence the dechanneling rate substantially under a certain condition [64]. This case will be discussed in Sect. 2.2.5. Further on in this section we consider dechanneling in a crystal with a constant curvature.

With crystal bending, the major influence on the dechanneling rate is caused by the reduction in the phase area where channeling takes place [44]. The formulas (1.41) (derived from the diffusion model) and (1.58) (derived from the consideration of a single scattering event) relate the dechanneling length L_D to the critical transverse energy E_c :

$$L_D(pv, R) \sim E_c(pv/R). \quad (2.15)$$

Denoting the dechanneling length for a straight crystal as $L_{D,0} \approx spv$, one can write the dechanneling length in a bent crystal as

$$L_D(pv, R) = L_{D,0} \frac{E_c(pv/R)}{E_c(0)}. \quad (2.16)$$

For the harmonic potential E_c changes as $(1 - R_c/R)^2$; therefore the dechanneling length may be written in the form

$$L_D(pv, R) = L_{D,0} \left(1 - \frac{R_c}{R}\right)^2. \quad (2.17)$$

Notice the similarity between the bending dechanneling factor A_B (2.10, 2.12) for divergent beams and the feed-out reduction factor (2.16, 2.17). In the harmonic case the factors (2.12) and (2.17) are identical. For the realistic

potential, the two factors are equal if the channeled particle distribution over E_T is flat (which is roughly valid at the incidence; see figures in Sect. 2.4). In a bent crystal the roughly linear dependence of L_D upon pv is valid only when pv/R is much smaller than $U'(x_c)$. As the pv/R ratio approaches the critical value, L_D declines and becomes zero at $R = R_c$. For a given radius R , the L_D dependence on pv in the harmonic approximation is

$$L_D(pv, R) = spv \left(1 - \frac{pv}{(pv)_{\text{crit}}} \right)^2. \quad (2.18)$$

L_D is maximal at $pv = (1/3)(pv)_{\text{crit}}$; this pv is optimal to minimize the dechanneling losses in a long crystal.

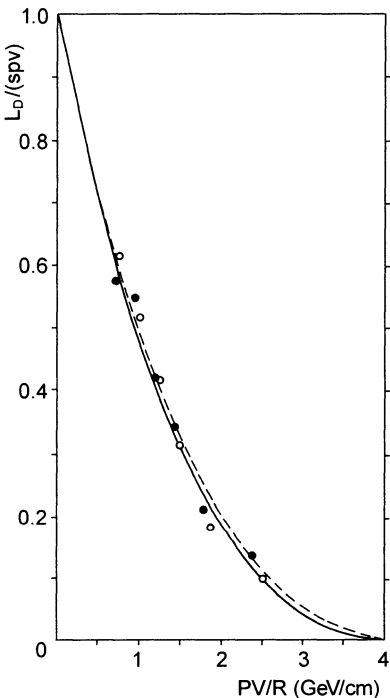


Fig. 2.5. Dependence of the Si(110) dechanneling length L_D / spv (spv is the dechanneling length in a straight crystal) on pv/R . The curves are obtained from (2.16), the points are from the FNAL experiment by Forster et al. The solid line and open dots are for the crystal at 20°C , $s = 0.54 \text{ mm/GeV}$; The dashed line and solid dots are for the crystal at -145°C , $s = 0.65 \text{ mm/GeV}$.

Forster et al. [18] have measured L_D for protons in the momentum range from 60 to 200 GeV/c in a crystal of Si(110) bent with a radius of about 80 cm, at room temperature and at -145°C . In Fig. 2.5 the experimental results are compared with the model (2.16). The dechanneling length in the straight

crystal, spv (used as a normalization constant), was a free parameter of the fit performed with (2.16) under the Molière approximation [29]. As one can see from this figure, the model adequately describes the L_D dependence on pv/R . The values obtained from the fit, $s = 0.54 \text{ mm/GeV}$ for room temperature, and $s = 0.65 \text{ mm/GeV}$ for -145°C , are also in fine agreement with the calculation by (1.50), 0.62 mm/GeV , and with the experimental data for the straight crystals (0.59 mm/GeV [27] and $\simeq 0.56 \text{ mm/GeV}$ [50] at room temperature) in this energy range. The observed temperature dependence of L_D in a bent crystal can be explained with the same model (see Sect. 2.2.4).

2.2.3 Bending Efficiency

The fraction of the particles trapped in the channeling mode at the crystal face is defined mainly by the incident beam divergence; see (1.29). From the general equations (2.1) and (1.38, 1.58) it follows that the fraction of these particles further deflected by the crystal at the angle Θ (i.e., the crystal efficiency F) depends on only two variables, pv/R and Θ , as well as on the crystal properties. This means that for any given bending angle Θ one can find an optimal curvature pv/R for which F is maximal. Therefore, the efficiency of the ideal crystal depends only on the bending angle and crystal properties, and does not depend on the particle energy.

We shall provide handy formulas for quick analytical estimates of the crystal efficiency. The trapping efficiency and bending dechanneling are described with (2.9–2.13). In a long crystal (the length L being of the order of L_D) the dechanneling losses caused by scattering may be taken into account by the exponential factor $\exp(-L/L_D)$. Then F may be roughly estimated by combination of these expressions:

$$F(\Theta, pv/R) = A_S A_B \left(\frac{pv}{R} \right) \exp \left(-\frac{R\Theta}{L_D} \right). \quad (2.19)$$

Note that L_D is roughly proportional to pv and is a function of $E_c(pv/R)$; therefore (2.19) depends on two variables, pv/R and Θ . Applying the asymptotic value (1.50) for L_D , we find that (2.19) may somewhat overestimate the efficiency (see discussion in Sect. 1.4.1). In the harmonic approximation, (2.19) takes the form

$$F(\Theta, \rho) = A_S (1 - \rho)^2 \exp \left(-\frac{\Theta}{\Theta_D \rho (1 - \rho)^2} \right). \quad (2.20)$$

For convenience the notation $\rho = R_c/R$ is used. The constant Θ_D was introduced which is the ratio of the dechanneling length in a straight crystal to the critical radius. With the theoretical approximations (1.50) for L_D and (2.4) for R_c one obtains:

$$\Theta_D = \frac{256}{9\pi} \frac{NZa_{\text{TF}}d_p^2}{\ln(2m_e c^2 \gamma/I) - 1}. \quad (2.21)$$

The Θ_D is weakly dependent on the energy, being mostly determined by the crystal properties. From (2.21), for Si(110) planes $\Theta_D \simeq 0.37$ rad, for wide Si(111) planes $\Theta_D \simeq 0.45$ rad, for Ge(110) planes $\Theta_D \simeq 0.67$ rad, and for W(110) planes $\Theta_D \simeq 2.2$ rad, given for a Lorentz factor $\gamma = 100$. The crystal properties are reflected in Θ_D and A_S only. Figure 2.6 shows the dependence of F/A_S on pv/R for some bending angles, calculated with the Moliére approximation [65]. For a comparison of the analytical estimates with measurements and simulations see Chap. 3.

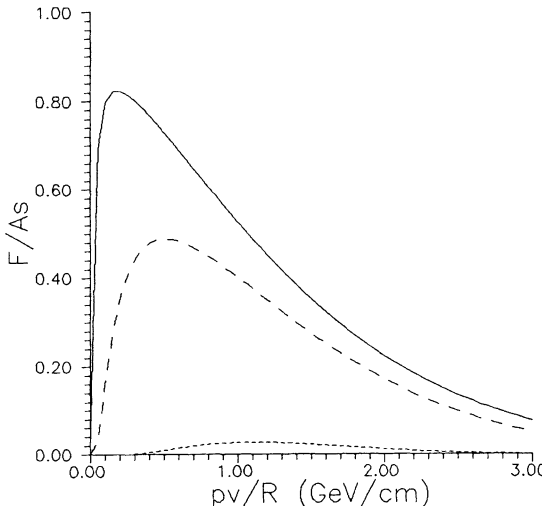


Fig. 2.6. Efficiency F/A_S of proton-beam deflection at angles 1 mrad (solid line), 10 mrad (dashed), and 100 mrad (dotted) by a Si(110) channel.

Optimal Curvature. The bending efficiency can be maximized by solving the equation $dF(\Theta, \rho)/d\rho = 0$. This allows for optimal curvature, $\rho_{\text{opt}}(\Theta)$, in the harmonic case [66]:

$$\frac{\Theta}{\Theta_D} = \frac{2\rho_{\text{opt}}^2(1 - \rho_{\text{opt}})^2}{1 - 3\rho_{\text{opt}}} . \quad (2.22)$$

Substituting $\rho_{\text{opt}}(\Theta)$ into (2.20) one obtains an upper limit $F_{\text{opt}}(\Theta)$ for the beam-deflection efficiency at an angle Θ :

$$F(\Theta, \rho) < F_{\text{opt}}(\Theta) = A_S [1 - \rho_{\text{opt}}(\Theta)]^2 \exp \left[-\frac{2\rho_{\text{opt}}(\Theta)}{1 - 3\rho_{\text{opt}}(\Theta)} \right] . \quad (2.23)$$

For any required deflection angle Θ , an optimal parameter pv/R could be chosen so that the upper limit of the efficiency does not depend on the beam momentum. The same optimization in the Moliére approximation was performed numerically and reported in [66] for different planar channels. Figure

2.7 shows (a) the optimal curvature, pv/R , and (b) the corresponding limit of efficiency, F/A_S , as functions of the deflection angle Θ for planes (110) of silicon, germanium, and tungsten.

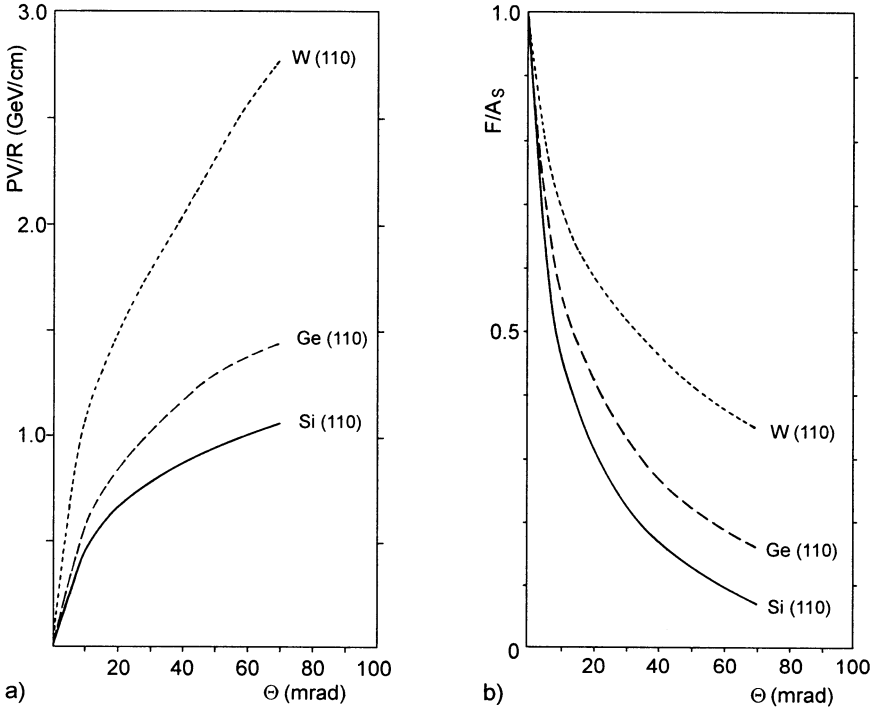


Fig. 2.7. Optimal curvature pv/R (a) and corresponding efficiency F/A_S (b) as functions of the deflection angle Θ .

For large Θ , the efficiency is maximal when

$$d(\rho E_c(\rho))/d\rho = 0 , \quad (2.24)$$

which means $\rho = 1/3$ for the harmonic case. As $\rho_{\text{opt}}(\Theta)$ saturates, the upper limit for efficiency becomes an exponential function of the bending angle Θ . In the harmonic case, (2.23) becomes, in the limit of high Θ ,

$$F_h(\Theta) = \frac{4}{9} A_S \exp \left(-\frac{27}{4} \frac{\Theta}{\Theta_D} \right) . \quad (2.25)$$

2.2.4 The Influence of Temperature on the Efficiency

The heating or cooling of a crystal has an effect on the deflection efficiency as it changes all the factors in (2.19): A_S , A_B , and L_D [66]. Each of these factors leads to a raise in the efficiency with falling temperature. The reason

is some increase in x_c with a decreasing amplitude of thermal vibrations u_T , and the corresponding increase in the potential-well depth $E_c = U(x_c)$. The magnitude and shape of the potential $U(x, u_T)$ are practically independent of u_T within the confines of the channel, and the change in the depth of the potential well is mainly determined by the change in the boundary of the channel x_c

$$\frac{\delta E_c}{E_c} = \frac{U'(x_c)}{E_c} \delta x_c . \quad (2.26)$$

Although the x_c change is a few percent even for the temperature change of $\sim 100^\circ\text{C}$, the effect on the efficiency may be stronger in the bent crystals, as E_c decreases with curvature.

We shall obtain the temperature dependence of the efficiency with the estimates of the preceding section. The form of the function $x_c(u_T)$, in particular its derivative dx_c/du_T , is important. In the following formulas the value of dx_c/du_T is not defined by theory; this factor should be obtained through a comparison between experiments and simulations. The measurements [18] of the bent-crystal acceptance at different temperatures (down to -145°C) show that its value is well described by theory with $x_c = d_p/2 - 2.5u_T$. Computer simulations [19] have also suggested the same function $x_c(u_T)$.

The relative change in the acceptance A_S is equal to

$$\frac{\delta A_S}{A_S} = \frac{\delta x_c}{x_c} + \frac{\delta \theta_c}{\theta_c} = \frac{\delta x_c}{x_c} + \frac{1}{2} \frac{U''(x_c)}{U'(x_c)} \delta x_c . \quad (2.27)$$

The temperature dependence of the acceptance A_B is determined by the curvature of the channel. In the harmonic approximation one has

$$A_B = (1 - \rho)^2 = \left(1 - \frac{pv}{RU'(x_c)}\right)^2 . \quad (2.28)$$

It is apparent from this expression that an increase in the curvature pv/R leads to a stronger temperature dependence for the acceptance A_B . Because of the smallness of δu_T the function $A_B(u_T)$ is practically linear even for large changes in the temperature and can be written in the form

$$\frac{\delta A_B}{A_B} = -\frac{2\rho}{1 - \rho} \frac{U''(x_c)}{U'(x_c)} \delta x_c , \quad (2.29)$$

where the curvature ρ is taken at room temperature, along with the derivatives $U''(x_c)$ and $U'(x_c)$. The overall change in the acceptance $A = A_S A_B$ is given by the sum of (2.27) and (2.29), and for a large curvature and a temperature change of $100\text{--}200^\circ\text{C}$ this can be some tens of 1%.

The effect of temperature on the dechanneling length shows up first of all in a change in the depth of the potential well, which determines the dechanneling length in accordance with (1.41, 1.58). As in the preceding case, the curvature of the crystal plays an important role. Because of the smallness of δu_T , the function $L_D(u_T)$ is also close to linear and can be approximated by

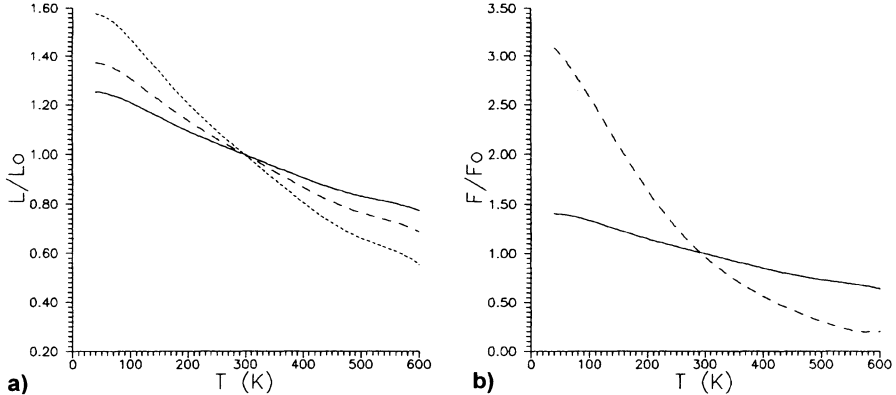


Fig. 2.8. (a) The dechanneling length in a bent crystal as a function of temperature for a straight crystal (*solid line*), $pV/R = 1$ GeV/cm (*dashed*), $pV/R = 2$ GeV/cm (*dotted*). (b) The efficiency with which a proton beam is steered at an angle Θ as a function of temperature. The deflection angle Θ (mrad) = 10 (*solid line*), 100 (*dashed*); for $x_c = d_p/2 - 2.5u_T$.

$$\frac{\delta L_D}{L_D} = \frac{\delta E_c}{E_c} = \frac{U'(x_c)}{E_c} \delta x_c . \quad (2.30)$$

For example, cooling the Si(110) planes from room temperature to -145°C ($\delta u_T = -0.018$ Å) increases L_D in a straight crystal by the order of 10%. In a strongly bent crystal the depth of the well E_c may be several times smaller and this leads to a change in L_D under the same conditions by some tens of 1% (Fig. 2.8). This last circumstance may be of considerable significance for the deflection of an intense beam by large angles. Figure 2.8 shows the temperature dependence of the efficiency of deflection at angles of 10 and 100 mrad for the Si(110) planes [66]. The curvatures of the crystal, $pV/R = 0.5$ GeV/cm (at 10 mrad) and $pV/R = 1.1$ GeV/cm (at 100 mrad), are optimal at room temperature.

The change in the average electron density $\langle n_e \rangle$ has less influence on the dechanneling length. Since the electron density within the confines of the channel, like the potential, depends only weakly on the temperature, one need only take the change in the channel boundary x_c into account. We characterize $\langle n_e \rangle$ with (1.48), i.e., $\langle n_e \rangle = \text{const } U(x_c)/x_c$. Then the relative variation in the electron density is given by

$$\frac{\delta \langle n_e \rangle}{\langle n_e \rangle} = \frac{U''(x_c)}{U'(x_c)} \delta x_c - \frac{\delta x_c}{x_c} . \quad (2.31)$$

This is zero for harmonic $U(x)$. For a simple model potential of the form $U_0(\cosh(bx) - 1)$ (2.31) gives

$$\frac{\delta \langle n_e \rangle}{\langle n_e \rangle} = (bx_c \coth(bx_c) - 1) \frac{\delta x_c}{x_c} . \quad (2.32)$$

For the above example with cooling of Si(110) to -145°C , this corresponds to about +2%, i.e., very much less than the variation in the depth of the potential well. One can write the overall change in L_D in the form

$$\frac{\delta L_D}{L_D} = \frac{\delta E_c}{E_c} - \frac{\delta \langle n_e \rangle}{\langle n_e \rangle}. \quad (2.33)$$

Experimental Behavior. Confirmation of these temperature dependences can be found in an experiment [18] on dechanneling in a bent crystal at room temperature and at -145°C . Figure 2.9 shows the experimental and theoretical dependences of the ratio of the dechanneling lengths in cooled and ‘warm’ crystals. The theoretical dependence is given by formula [66]:

$$\frac{L_D^c}{L_D^r} = \frac{E_c(pv/R^c, u_T^c)}{E_c(pv/R^r, u_T^r)}, \quad (2.34)$$

where $R^c = 84$ cm and $R^r = 80$ cm are experimental values of bending radii; the upper indices c and r denote the cooled crystal and that at the room temperature, respectively; $u_T^c = 0.057$ Å, $u_T^r = 0.075$ Å. The experimental points shown in Fig. 2.9 were fitted [67] by using formula (2.34) and the Moliére approximation. The value of $x_c^r \simeq d_p/2 - a_{TF}$ was taken at room temperature and dx_c/du_T was a free parameter of the fit. The best agreement

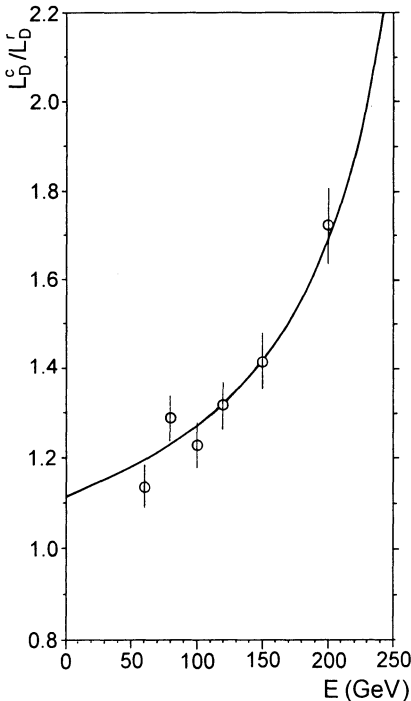


Fig. 2.9. The ratio of the dechanneling lengths in cooled and ‘warm’ crystals. The experimental data are from the FNAL experiment by Forster et al., and the fit is in accordance with (2.34).

was found for $dx_c/d\mu_T = -1.8 \pm 0.5$, which is in good accord with the results given in [18, 19] from experiment and simulation.

2.2.5 Channeling in Crystal with Variable Curvature

Channeling in a crystal with a constant curvature is well understood. The general case, when the curvature is an arbitrary function of z , is paid less attention. In practice the crystal curvature is variable rather than constant (see Chap. 3). This case will be briefly considered here, following [64].

Drift of E_T in the Curvature Gradient. A change of curvature, $k = pv/R$, determines, through the relation (2.3), a corresponding change in the transverse energy E_T of a particle channeled in an effective potential well. For rapid variations of k , when the effective well changes significantly over one period of oscillation λ , the term E_T loses its meaning, and one should solve the dynamical equation (2.1) for a given function $k(z)$. In an account of scattering we should apply either the Monte Carlo simulation or the kinetic equation for variables x, θ (not using E_T) [24].

In practice λ is quite small ($\sim 30 \mu\text{m}$ at 100 GeV) so the crystal curvature cannot considerably change along this length. Therefore, the case of a slowly varying curvature (when the ‘transverse energy’ concept remains useful) is general enough; it covers all the experiments done thus far. In this case, the particle continues to oscillate in the bent channel, with all the parameters changing slowly.

Instead of the consideration of a variable critical transverse energy $E_c(z)$, it is more convenient mathematically to keep E_c constant and to introduce an equivalent variation of E_T for any channeled particle. With a small instant variation δk , the transverse energy (2.3) of the particle (in a ‘new’ effective well at $z + \delta z$) varies, with respect to the critical value $E_c = U_{\text{eff}}(-x_c)$, by $(x + x_c)\delta k$. Since both δk and x are dependent on z , the total increase is $\delta E_T = f(x + x_c)\delta k$, where x may depend on the $k(z)$ function for a rapid variation of $k(z)$. For slow variations, one may rewrite it as

$$\delta E_T = k' \int (x + x_c) dz = k'(\langle x \rangle + x_c) \delta z, \quad (2.35)$$

where we have averaged x over the oscillation and kept $k' = dk/dz = \text{const}$ along it. This formula determines the E_T variation as a function of the curvature gradient $d(pv/R)/dz$ and of the mean coordinate $\langle x \rangle$ of a channeled particle. Notice that $\langle x \rangle$ is negative ($-x_c R_c / R$ in the harmonic case) as the centrifugal force is positive (see Fig. 2.1).

Neglecting scattering (which is valid for $L \ll L_D$), one can write the equation for a function of the particle distribution over E_T . Denoting the drift coefficient as

$$D_k(E_T, z) = \langle \delta E_T / \delta z \rangle = k'(\langle x \rangle + x_c), \quad (2.36)$$

one obtains, as the conservation law (Liouville theorem), the following equation

$$\frac{\partial f}{\partial z} + D_k(E_T, z) \frac{\partial f}{\partial E_T} = 0. \quad (2.37)$$

For a gradual increase in $k(z)$, E_T drifts towards the critical value E_c ; this drift causes a gradual bending dechanneling. For a gradual decrease in $k(z)$, E_T decreases with respect to E_c ; that is, this drift slows down the multiple scattering dechanneling. Below, we shall estimate the slow-down effect.

Dechanneling in a Crystal with Variable Curvature. A change in E_T caused by multiple scattering is characterized by the drift (1.34) and diffusion (1.35) factors. The distribution $f(E_T, z)$ of the channeled particles as a function of the depth is described by the Fokker–Planck equation (1.33). In a channel with a uniform electron density (the approximation used in Sect. 1.4 for semiconductor crystals), the drift factor is independent of E_T .

The criterion for when the curvature gradient may considerably influence the dechanneling is obtained by comparing the ‘gradient’ drift factor D_k with the electronic drift factor D_e . One may expect that for a big negative value of (2.36), $D_k < -D_e$, the dechanneling rate would depend considerably on the value of D_k .

Drift Approximation. An analytical estimate can be obtained in the simplified assumption that the transverse energy of a particle increases monotonously (the so-called steady increase approximation [5]):

$$\frac{dE_T}{dz} \simeq \left\langle \frac{dE_T}{dz} \right\rangle = D_k + D_e, \quad (2.38)$$

(D_e and D_k may be functions of E_T and z). This simplest (drift) approach was used in the earliest considerations of dechanneling in straight crystals (see [5] and the references therein); we just added the D_k term for a crystal with variable bending.

This approximation corresponds to neglecting the diffusion term in the Fokker–Planck equation (1.33). In this approach, all the particles are dechanneled by the depth $L_D = E_c/D_e$; this should be compared to the diffusion estimate (1.41), where the channeled fraction decreases by the factor $1/e$ over the length $L_D \simeq 0.7 E_c/D_e$. For depths smaller than L_D the agreement between the approaches is better [5].

Taking into account the additional (gradient) drift D_k , one can estimate the dechanneling length, in our case as

$$L_D \simeq \frac{E_c}{D_k + D_e} \simeq \frac{L_D^{R=\text{const}}}{1 + D_k/D_e}; \quad (2.39)$$

that is, L_D is affected if D_k is comparable to or larger than D_e . Formula (2.39) predicts a strong increase in the dechanneling length at $D_k/D_e = -1$, formally giving the infinity. It is clear that dechanneling for $D_k < -D_e$ should be considered kinetically only, with the use of (1.33).

Notice one interesting advantage of the approach considered. It provides a continuous transition from the continuum model of bending dechanneling (which considers the instant changes of curvature only, without scattering) to the Fokker–Planck equation for a general case when the dechanneling is determined both by the gradual curvature changes and the multiple scattering; the sign of D_k in the above formulas may be positive or negative.

In particular, if $D_k > 0$ and $D_k \gg D_e$ one obtains the continuum-model case: a rapid increase of curvature. Then formulas (2.38,2.39) determine the bending dechanneling losses with the crystal depth.

In an actual experiment D_k and D_e are comparable, so one can use the above formulas for a simple estimation. As was mentioned in Sect. 1.4.1, in semiconductor crystals D_e is to a good approximation a constant, independent of E_T and z , as given by (1.43). In the estimates one can take D_e just as $\approx 0.7E_c/L_D$ for a straight crystal.

The gradient drift (2.36) for an harmonic potential takes the form:

$$D_k = -\frac{pv}{R^2} \frac{dR}{dz} x_c \left(1 - \frac{R_c}{R} \right); \quad (2.40)$$

the drift decreases as the radius R approaches R_c .

For the widely used three-point bending scheme (Chap. 3), the curvature is a linear function of z , say $1/R = \text{const} \pm k_0 z$. Then (2.36) transforms to

$$D_k = \pm p v k_0 x_c \left(1 + \frac{\langle x \rangle}{x_c} \right) \approx \pm p v k_0 x_c, \quad (2.41)$$

which depends on the curvature (and hence on z) through the parameter $\langle x \rangle$ only. For a small bend, $\langle x \rangle \approx 0$. Then D_k is a constant along the crystal length (as is D_e).

If at $z = 0$ the particle distribution function is $f_0(E_T)$, then at a depth z it is

$$f(E_T, z) = f_0 \left(E_T - D_e z - \int_0^z D_k dt \right) \approx f_0 \left(E_T - (D_e + D_k) z \right). \quad (2.42)$$

A particle is dechanneled at the depth $z_D \approx (E_c - E_T)/(D_e + D_k)$.

Diffusion Approximation. Although the analytical approach in the above section provides more insight, its quantitative estimates are very simplified. In a general case, the Fokker–Planck equation (1.33) should be solved, taking into account the extra drift term (2.36). For a uniform electron density in the channel, and for $D_k = \text{const}$, such an equation has the form [64]:

$$\frac{E_c(z)}{D_e} \frac{\partial f}{\partial z} = -\frac{D_k}{D_e} \frac{\partial}{\partial \epsilon} (\epsilon f) + \frac{\partial}{\partial \epsilon} \left(\epsilon \frac{\partial f}{\partial \epsilon} \right), \quad (2.43)$$

where $\epsilon = E_T/E_c(z)$ is chosen as the independent variable instead of E_T , and $f(1, z) = 0$. In order to analyze the dependence of the dechanneling rate on the parameter D_k/D_e , especially at $D_k/D_e < -1$, (2.43) was solved numerically. It was found that for $D_k < -D_e$ the dechanneling rate is strongly

suppressed. For $-D_k/D_e = 3$ to 5, the local L_D exceeds $L_D(R = \text{const})$ by a factor of 2.0–2.5.

It should be noticed that a strong influence of the curvature gradient is possible even at low values of the curvature itself; i.e., the condition $D_k < -D_e$ could be valid at $R \gg R_c$ also. This condition is easily achieved at GeV energies and higher. Simply stated, when E_T diffuses slowly, the rapid (even small) variations of R are essential for the dechanneling rate. With increased energy, D_e reduces as $1/pv$ whereas D_k raises in magnitude; see (2.40).

Experiment. The only experimental estimates of the dechanneling length in a crystal with variable curvature are reported in [68]. In this experiment a Si(111) crystal, bent by either a 3- or a 4-point scheme, was used for bending a proton beam with energies of 12 to 180 GeV through an angle of 8 mrad. The dechanneling length was measured at the part of the crystal with decreasing curvature (5 mm long); the experimental data are published in [69].

The observed L_D values were much higher than those expected even for a straight crystal. For example, at 60 GeV, L_D was 140 mm, which is a factor of 2.5–3.0 larger than the values measured in the straight crystals, despite the fact that $(pv/R)_{\max} = 1 \text{ GeV/cm}$. Note that the parameter $-D_k/D_e$ was 3–5 in this case. In the energy range of 12 to 60 GeV the measured L_D grows faster than linearly (despite the use of a bent crystal); the theoretical interpretation of this fact is that the parameter $-D_k/D_e$ grows strongly. At 100 GeV, L_D is still somewhat higher than expected for a straight crystal, despite a very strong curvature: $(pv/R)_{\max} = 1.7 \text{ GeV/cm}$. This observation is in qualitative agreement with the theory.

Applications. The influence of the curvature gradient may be important in the interpretation of bent-crystal experiments. The suppression of the dechanneling rate under appropriate conditions allows us to remove the background caused by dechanneling. This may be important, for instance, for eliminating the radiation and heat loads on the beam-line equipment downstream from the crystal, for increasing the bent-beam quality, or for eliminating the long-lived particle background in the scheme of the short-lived particle separation [70] discussed in Chap. 6. In Sect. 2.3.2 the influence of the curvature gradient on feeding-in is discussed.

One interesting application may be the formation of a channeled beam that is *monochromatic* in its transverse energy, as proposed in Ref. [71]. In such a beam all the particles have the same transverse energy $E_T^0 \pm \delta E_T$, at some starting point, with the accuracy δE_T of about 1 eV. Here E_T^0 can be chosen from 0 to E_c . Such a distribution can be obtained with the particles *fed in* to the crystal with the curvature decreasing along the beam path; E_T^0 is E_c at the feed-in point. A simulation made for a real crystal at beam energies of 450 GeV and 1 TeV and divergences of 10 to 100 μrad has shown that the accuracy of $\delta E_T \simeq 1\text{--}2 \text{ eV}$ is possible. Such a beam would offer interesting possibilities for studying the processes related to channeling: energy loss, E_T diffusion, radiation, defect dechanneling.

2.3 Feed-in Mechanisms

Particle motion in a crystal is influenced by a series of collisions with the crystal constituents. For any trajectory of a particle in a crystal a time-reversed trajectory is possible. The starting point of a trajectory becomes the final one, and vice versa. This leads to the idea of *reversibility* of the dechanneling processes. In the depth of a crystal, as well as the particles leaving the channeling mode (dechanneling or *feeding out*), there may be particles entering the channeling mode (*feeding in*, also known as *volume capture*). The mechanisms responsible for these two opposite processes are essentially the same.

Lindhard has proposed the *reversibility rule* [4], according to which the probability of a channeled particle being scattered from a certain channeled state to a certain unchanneled state equals the probability for the opposite process. This rule is a good basis for considering the particle transitions from an unchanneled to a channeled state in the volume of a crystal.

In this section we consider two mechanisms changing the particle state in a crystal, namely the scattering and the centrifugal effects.

2.3.1 Scattering

Introduction. Scattering of a random ('over-barrier') particle can lead to its capture into a channeled state. These scattering-caused transitions were observed first in experiments with \sim MeV ion beams [72, 73]. This effect is potentially more interesting in the GeV energy range, because it might lead to increased efficiency of the crystal-optics for the charged beams. Experiments with GeV beams were used to study these transitions [32, 50, 51, 74]. These studies have proven Lindhard's reversibility rule, and will be discussed in some detail in Chap. 3.

Clearly, in the presence of two contributions, channeled and random, of a beam in a crystal, the effective dechanneling of the beam is also defined for the process of particle exchange between the channeled and random fractions of the beam. In particular, it is possible to have a *dynamic equilibrium* between the two fractions; in this case the transitions are balanced and effective dechanneling is absent. The reversibility rule allows us to consider the feed-in and feed-out processes from a unified point of view.

Dynamic Equilibrium. Let us consider this topic in a simple qualitative way. Since the estimates are rough, we shall not give strict definitions of the terms.

Let us denote by f_1 the density of the channeled particles ('under-barrier') population in the phase plane. In the absence of the flux from the over-barrier to the channeled states, the f_1 dynamics is known:

$$\frac{df_1}{dz} = -\frac{f_1}{L_D}. \quad (2.44)$$

So f_1 decreases with some length constant L_D , known as the dechanneling length. If the quasi-channeled particle ('over-barrier') density f_2 in the phase plane is not zero, a reverse flux (*rechanneling*) will exist:

$$\frac{df_1}{dz} = -\frac{f_1}{L_D} + \frac{f_2}{L'_D}. \quad (2.45)$$

Due to the reversibility rule we have $L'_D = L_D$, that is, the transition probabilities (per particle) are equal:

$$\frac{df_1}{dz} = -\frac{f_1}{L_D} + \frac{f_2}{L_D}. \quad (2.46)$$

Experimentally we observe f_1 dynamics as dechanneling with a new, *effective* dechanneling length L_{eff} :

$$\frac{df_1}{dz} = -\frac{f_1}{L_{\text{eff}}}. \quad (2.47)$$

Obviously, L_{eff} is bigger than L_D ; as f_2 approaches f_1 , L_{eff} increases. We can estimate L_{eff} by comparing (2.46) and (2.47):

$$L_{\text{eff}} \simeq \frac{L_D}{1 - f_2/f_1}. \quad (2.48)$$

If the densities in and near the channel are equal, i.e. $f_1 = f_2$, the dynamic equilibrium holds. The mean flux between the two fractions becomes zero; formally, L_{eff} becomes infinite. The experimental studies of the effective dechanneling and, in particular, of the state of dynamic equilibrium are considered in Chap. 3.

Rechanneling in a Bent Crystal. The crystal bending considerably influences f_2 near the channel, because the random particle rapidly loses its orientation with respect to the bent channel. The disorientation, at an angle of the order of the critical one θ_c , occurs along the length of the order of $R\theta_c$ (R is the bending radius). Since the incident beam has finite angular divergence Φ , the region where its particles are tangential to the atomic planes is limited in size by about $R\Phi$. Outside this region the incident, unchanneled beam is disaligned with respect to the crystal planes and f_2 is defined by the dechanneled particle number only:

$$f_2 \simeq f_1 \frac{\delta z}{L_D}. \quad (2.49)$$

The distance δz , along which the random particle keeps its orientation with respect to the channel, amounts to about $R\theta_c$, so the correction to the dechanneling length is approximately given by

$$\frac{f_2}{f_1} \simeq \frac{R\theta_c}{L_D}. \quad (2.50)$$

This number is normally small (for $R \simeq 10$ m, $\theta_c \simeq 20$ μ rad, $L_D \simeq 10$ cm the correction equals 0.002 only). So, in a crystal with a bending angle much

larger than the incident beam divergence, the contribution to f_1 coming from rechanneling of previously dechanneled particles is not sizable.

Volume Capture. The term ‘volume capture’ has been traditionally used for the feeding-in process in a bent crystal [75, 76]. In such a crystal, the trajectory of any incident particle from a broad angular range becomes tangential to the curved crystallographic planes somewhere in the crystal depth. Thus transitions to the channeled states become possible (in the region of tangency) for any particle of a divergent beam. One might even (naively) hope to trap the particles more efficiently than in the usual case of entry-face capture. The process of volume capture can be considered in analogy with that in the previous section.

The random particle stays near the channel (on the phase plane) along a length of the order of $R\theta_c$. The intensity of transitions to the channel is described by (2.47) where one assumes $f_1 = 0$. The number of particles scattered into the channel over the whole interaction length is about

$$\delta f_1 \simeq f_2 \frac{\delta z}{L_D} \simeq f_2 \frac{R\theta_c}{L_D}. \quad (2.51)$$

Therefore the transition probability per interacting particle, $\delta f_1/f_2$, amounts to

$$w_S \simeq \frac{R\theta_c}{L_D} = \text{const} \frac{R}{(pv)^{3/2}}. \quad (2.52)$$

Notice that w_S grows with R , and decreases as $1/(pv)^{3/2}$ with a momentum increase.

From a more detailed consideration of the reversibility of trajectories one can derive a rigorous formula for w_S [77]. Let us consider a beam with a uniform angular distribution, $1/2\Phi$, incident on a crystal with curvature $1/R$. The fraction of beam channeled is a function of the crystal depth z :

$$f(z) = \frac{2x_c}{d_p} \frac{\pi}{4} \frac{\theta_c}{\Phi} A_B(pv/R) F_D(z), \quad (2.53)$$

where $F_D(z)$ describes the feed-out of the channeled particles due to scattering; usually one writes $F_D(z)$ as $\exp(-z/L_D)$, and so $F'_D(z) = -F_D(z)/L_D$. The factor $\pi/4$ is exact in a harmonic case; for the realistic potential it is ≈ 0.8 . The number of particles dechanneled over the length δz equals

$$\begin{aligned} -\frac{df(z)}{dz} &= -\frac{2x_c}{d_p} \frac{\pi}{4} \frac{\theta_c}{\Phi} A_B(pv/R) F'_D(z) \\ &= \frac{2x_c}{d_p} \frac{\pi}{4} \frac{\theta_c}{\Phi} A_B(pv/R) \frac{F_D(z)}{L_D}. \end{aligned} \quad (2.54)$$

The particles dechanneled over dz exit in the angular range $d\Theta = dz/R$. Therefore the angular distribution downstream of the crystal is

$$\frac{df}{d\Theta} = R \frac{df(z)}{dz} = \frac{2x_c}{d_p} \frac{\pi}{4} \frac{\theta_c}{\Phi} A_B(pv/R) \frac{R}{L_D} F_D(z). \quad (2.55)$$

We do not take into account a small extra spreading, $\pm\theta_c$, in the dechanneled particles. Therefore, for big R (when L_D/R is comparable to θ_c), (2.55) overestimates the phase density.

Let us now consider the same beam incident on the same crystal in the *reverse* direction. Now the particles with upstream parameters (x_i, Θ_i) equal to the downstream parameters (x_f, Θ_f) of the dechanneled particles from the preceding case are captured along the same (reversed) trajectories. By consideration, the number of particles that have experienced transitions *from* the channeled states in the former case is equal to the number of transitions *to* the channeled states in the latter case (as the trajectories are the same).

Therefore the number of particles captured from the interval $d\Theta$ and then transmitted in the channeled states (over the length z) to the crystal face is given by (2.55). We write this number as $w_S F_D(z)$, the product of the capture probability and the transmission factor. The transmission factor $F_D(z)$, for particles channeled in the same states, is the same irrespective of the direction of motion. Normalizing (2.55) to the number of particles incident on the crystal in this angular range, $d\Theta/2\Phi$, one obtains the capture probability:

$$w_S = 2\Phi \frac{df(z)}{d\Theta} \frac{1}{F_D(z)} = \frac{\pi x_c}{d_p} \frac{R\theta_c}{L_D(pv/R)} A_B(pv/R). \quad (2.56)$$

For a harmonic $U(x)$, $A_B = (1 - R_c/R)^2$ and L_D is reduced in a bent crystal by the same factor $(1 - R_c/R)^2$ relative to L_D in the unbent crystal; for a realistic potential the ratio of the two factors is ≈ 1 . Hence we can omit A_B in (2.56) and imply L_D for a straight crystal; another simplification is $x_c/d_p \approx 1/2$. One obtains [77]:

$$w_S = \frac{\pi x_c}{d_p} \frac{R\theta_c}{L_D} \approx \frac{\pi}{2} \frac{R\theta_c}{L_D}. \quad (2.57)$$

This formula, which is, in fact, the result of the reversibility rule, has been confirmed within an accuracy of 10%–20% by experiments [75, 76] (see Chap. 3); the volume-capture probabilities were measured at 1 GeV and 70 GeV, respectively. Also, in [76] the linear dependence of the probability on the crystal bending radius was confirmed.

Numerical studies of volume capture were performed with computer simulations [27, 34, 43] (see also Chap. 3) and based on the kinetic equations [35]. Studies have shown that the ‘usual’ scattering processes are sufficient for the description of the experiments [75, 76]. The dependence of w_S on R was first qualitatively studied by computer simulation [34], where this dependence was found to be linear for small R and saturated as R grows. The quantitative predictions obtained from the ‘first principles’ by computer simulation are discussed in Chap. 3 in connection with the experimental measurements.

We may compare, from (2.57), the efficiencies of the entry-face and volume captures. The intensity of the beam captured at the entry face is $N_{ef} = (\pi x_c/d_p)\theta_c f_0$ (f_0 is the phase density, or ‘brightness’, of the incident beam).

For volume capture we should integrate $w_S f_0$ over the angular region of capture Φ :

$$N_{vc} = \int_0^\Phi \frac{\pi x_c}{d_p} \frac{R\theta_c}{L_D} f_0 \exp\left(-\frac{R\phi}{L_D}\right) d\phi = N_{ef} \left[1 - \exp\left(-\frac{R\Phi}{L_D}\right) \right]. \quad (2.58)$$

The presence of the exponential factor takes into account dechanneling along the crystal length. It is seen from the above that the volume capture could be comparable to the entry-face capture only in the case of a divergent beam and large bending radius $R\Phi \geq L_D$; the sum (volume capture + relics of entry-face capture) never exceeds the initial entry-face value. For narrow beams, $R\Phi \ll L_D$, the ratio $N_{vc}/N_{ef} = R\Phi/L_D$ increases linearly with the beam divergence, which is also obvious.

The relation between the various exchange processes of the channeled and random fractions, for different ratios of f_1 and f_2 , is illustrated by Fig. 2.10. This figure schematically shows: (a) dechanneling (in a bent crystal), (b) volume capture (in a bent crystal), and (c) the dynamic equilibrium state. The lines indicate the phase trajectories of particles without scattering; the points represent the particle population; the particle scattering events are shown by arrows.

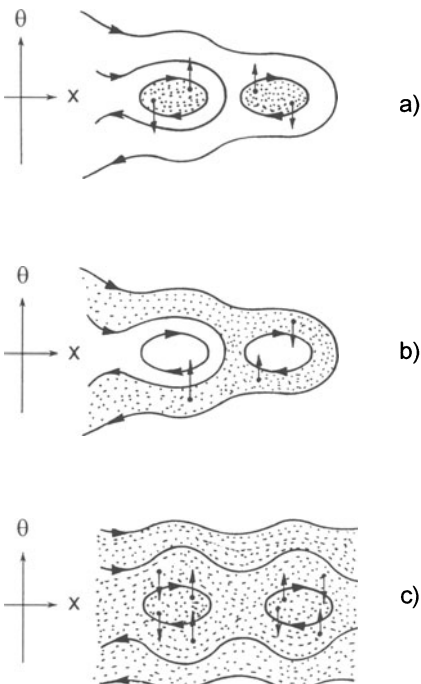


Fig. 2.10a–c. Phase drawing of the exchange process. (a) Dechanneling (in a bent crystal). (b) Volume capture (in a bent crystal). (c) Dynamic equilibrium state.

Note that the reversibility rule which gives a good basis for understanding the experiment, leaves no chance of using the rechanneling process to enlarge the efficiency of the crystal-optics (contrary to many opposite declarations in the earlier papers on this subject). The diffusion-like character of the scattering process can equalize only the population densities inside the channel and outside it; for this reason the efficiency of the volume capture, be it due to scattering or the curvature gradient, cannot exceed the efficiency of the entry-face capture.

2.3.2 Bending

In a bent crystal (or a straight crystal with lattice dislocations), the particle state may be changed by a change in the curvature. The existence of trajectories starting in the region of channeled states and ending outside of it (or vice versa) has been shown in Sect. 2.1. Along these trajectories the particles leave or enter the channeling mode. The bending dechanneling is a well-established phenomenon. Its theoretical description within the framework of the continuum model (Sects. 2.1–2) is in excellent agreement with experiment (Chap. 3). The same theory inevitably leads to the existence of the corresponding feed-in process [78, 79].

We shall consider the feed-in theory following [79, 80]. The central problem is to find the capture probability in a general case of charged-particle interaction with the potential of the crystallographic planes of variable curvature. We shall give below two derivations for the probability of capture: (1) from the consideration of particle dynamics [79], and (2) from the consideration of the reversibility of trajectories [80].

Derivation from Dynamics. Let us consider the capture efficiency for a planar channel with increasing bending radius R . We assume the crystal curvature changes slowly with z (the curvature change $\delta(1/R)$ over the oscillation period λ is much smaller than the critical curvature $1/R_c$), and hence the use of the concept of transverse energy is justified. Because of the smallness of λ , this approximation is valid over the GeV to TeV range. We shall follow the approach of Sect. 2.2.5 for the consideration of the channeling in a crystal with variable curvature. The local curvature $k(z) = pv/R$ varies as the particle moves in the crystal. We consider the corresponding variation (drift) of the particle's transverse energy with respect to the critical value $E_c = U_{\text{eff}}(-x_c)$. The drift is given by (2.35): $\delta E_T = (dk/dz)(\langle x \rangle + x_c)\delta z$.

Figure 2.11 helps us to understand the bending capture. The solid line gives the effective interplanar potential at some coordinate z ; the dashed line is the same parameter at $z + \lambda$. A random particle may be captured when it is passing over the potential well with a transverse energy in the range from U_0 to $U_0 + \Delta U$. The potential well gap $\Delta U = pvd_p/R$ is due to the centrifugal force. During oscillation over the well with $E_T \simeq U_0$, the E_T variation relative to E_c is

$$\delta E_T = k'(\langle x \rangle + x_c)\lambda. \quad (2.59)$$

Note that $\langle x \rangle < 0$ for positive pv/R . If R increases, $\delta E_T < 0$ and some particles (those with $E_T + \delta E_T < E_c$) are captured.

Figure 2.11 shows three kinds of particles. Particles with $E_T < U_0 + \delta E_T$ are captured; those with $E_T > U_0 + \Delta U - \delta' E_T$ (where $\delta' E_T$ is the variation over $\lambda/2$) are transmitted and interact with the next wall; the other particles are reflected by the channel wall. For slow variation the number of transmitted particles may be neglected; then we normalize the captured fraction to all the particles incident in the ΔU range. For the flat distribution of transverse energies in the interval U_0 to $U_0 + \Delta U$, the fraction of captured particles is

$$w_B(z) = -\frac{\delta E_T}{\Delta U} = \frac{R' \lambda}{R} \frac{x_c}{d_p} \left(1 + \frac{\langle x \rangle}{x_c} \right), \quad (2.60)$$

where $R' = dR/dz$ is the gradient of the radius of curvature. For slightly bent crystals the factor in the parentheses is close to unity.

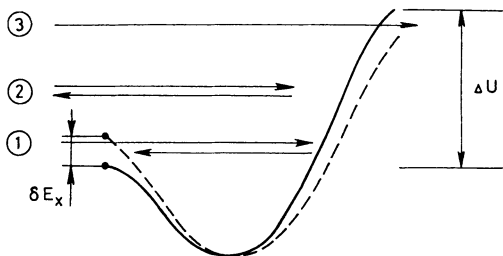


Fig. 2.11. Schematic picture of bending capture. The solid line is the effective interplanar potential $U_{\text{eff}}(x)$ at some coordinate z ; the dashed line is the same at $z + \lambda$. There are three kinds of particles: (1) captured, (2) reflected, (3) transmitted and interacting with the next wall.

In the harmonic approximation, (2.60) takes the form:

$$w_B(z) = \frac{R' \lambda}{R} \frac{x_c}{d_p} \left(1 - \frac{R_c}{R} \right). \quad (2.61)$$

In the widely applied 3-point bending scheme, the curvature is a linear function of z : $1/R(z) = \text{const} \pm k_0 z$. Interestingly, this leads to a linear dependence of w_B on R [like in the case of scattering, (2.57)] for not too strong bending:

$$w_B = k_0 \lambda R \frac{x_c}{d_p} \left(1 + \frac{\langle x \rangle}{x_c} \right) \approx \frac{k_0 \lambda}{2} R. \quad (2.62)$$

w_B is of the order of $2\lambda/L_B$, where L_B is the length of the bent part of a crystal. The probability grows with energy, and should be quite sizable, e.g., in conditions of the H8 experiment [102] at CERN, where (2.62) constitutes several per cent.

Derivation from Reversibility. The capture probability can be derived with no use of approximations, such as the existence of E_T or a slowly varying curvature (although these are well justified in all practical cases) [80].

Let us consider a beam with a uniform angular distribution, $1/2\Phi$, incident on a crystal with a curvature gradually *increasing* along the beam path from 0 to $1/R_c$. The fraction of the beam channeled will decrease from the starting value given by

$$f = \frac{2x_c}{d_p} \frac{\pi}{4} \frac{\theta_c}{\Phi}, \quad (2.63)$$

with the crystal depth, according to:

$$f(z) = \frac{2x_c}{d_p} \frac{\pi}{4} \frac{\theta_c}{\Phi} A_B \left(\frac{pv}{R(z)} \right), \quad (2.64)$$

where $A_B(pv/R(z))$ describes the reduction of the bent-crystal acceptance with depth z . The factor $\pi/4$ is exact in the harmonic case; for the realistic potential one should replace $\pi/4$ with a slightly different factor ≈ 0.8 .

The number of particles dechanneled over the length δz , from z to $z + dz$, is equal to

$$\frac{df(z)}{dz} = \frac{2x_c}{d_p} \frac{\pi}{4} \frac{\theta_c}{\Phi} \frac{\partial A_B(pv/R)}{\partial(pv/R)} \frac{pv}{R^2(z)} \frac{dR(z)}{dz}. \quad (2.65)$$

All the dechanneled particles are distributed in the angular range from 0 to the bending angle of the crystal. The particles dechanneled over dz are exiting in the angular range $d\Theta = dz/R(z)$. Therefore the angular distribution downstream of the crystal is

$$\frac{df}{d\Theta} = R(z) \frac{df(z)}{dz} = \frac{2x_c}{d_p} \frac{\pi}{4} \frac{\theta_c}{\Phi} \frac{\partial A_B(pv/R)}{\partial(pv/R)} \frac{pv}{R(z)} \frac{dR(z)}{dz}, \quad (2.66)$$

where z and Θ are related through the expression $d\Theta = dz/R(z)$. For an abrupt ($R' = \infty$) or very fast variation of the curvature, (2.66) overestimates the phase density, of course, as we do not take into account a small extra spreading, $\pm\theta_c$, in the dechanneled particles. The microscopic phase density of the particles is to be conserved; $df/d\Theta$ cannot exceed the initial value.

Let us now consider the same beam incident on the same crystal in the *reverse* direction. That is, the crystal curvature is gradually *decreasing* along the beam path. Now the particles with upstream parameters (x_i, Θ_i) equal to the downstream parameters (x_f, Θ_f) of the dechanneled particles from the preceding case are captured along the same (reversed) trajectories. By consideration, the number of particles that have experienced transitions *from* the channeled states in the former case is equal to the number of transitions *to* the channeled states in the latter case (as the trajectories are the same).

Therefore the number of particles captured from the interval $d\Theta$ is given by (2.66). Normalizing it to the number of particles incident on the crystal in this angular range, $d\Theta/2\Phi$, we obtain the capture probability:

$$w_B(z) = 2\Phi \frac{df(z)}{d\Theta} = \frac{\pi x_c}{d_p} \theta_c \frac{\partial A_B(pv/R)}{\partial(pv/R)} \frac{pv}{R} \frac{dR}{dz}. \quad (2.67)$$

The above quantity is a function of z through $R(z)$ and $R'(z)$. The derivation uses just the general arguments, relating the capture probability to the well-known function $A_B(pv/R)$ of bending dechanneling. We cannot show the equivalence of (2.67) and (2.60) for an arbitrary $U(x)$. For a harmonic $U(x)$, $A_B = (1 - R_c/R)^2$. Then (2.67) transforms into

$$w_B = \frac{2\pi x_c \theta_c}{d_p} \left(1 - \frac{R_c}{R}\right) \frac{R_c R'}{R} = \frac{x_c}{d_p} \lambda \left(1 - \frac{R_c}{R}\right) \frac{R'}{R}, \quad (2.68)$$

which exactly equals the result of the previous section, (2.61). The following relations were used here: $\lambda = 2\pi x_c / \theta_c$, $R_c = p v x_c / 2E_c = x_c / \theta_c^2$. The consistency found between the above two very different derivations of Sect. 2.3.2 makes us more confident about the theoretical predictions.

Integral Trapping Efficiency. A crystal may trap particles, with probability (2.60), in the angular range

$$\Delta\Theta = \int_{z_1}^{z_2} dz / R(z), \quad (2.69)$$

where z_1 and z_2 are defined by the interval with $R' > 0$ and $R > R_c$. The capture angle $\Delta\Theta$ may be arbitrarily large (with a corresponding loss in efficiency). For maximal efficiency, $\Delta\Theta$ should be within the divergence of the incident beam. From the preceding consideration it is already clear that the number of particles fed-in from a divergent beam through the considered mechanism equals, in the optimal case, the number trapped from the same beam at the entry face. It is interesting, however, to show explicitly for the harmonic potential, from (2.61), that the integral efficiency for a divergent beam coincides with the entry-face capture efficiency for the same beam, *independent* of the behavior of function $R(z)$.

The total number of particles, captured into the channeling mode from the beam with an angular distribution $P(\Theta)$ equals

$$N_B = \int w_B P(\Theta) d\Theta, \quad (2.70)$$

where one can integrate over z : $d\Theta = dz / R(z)$. For the uniform distribution $P(\Theta) = 1/2\Phi$, *covering* the angular region of capture $\Delta\Theta < 2\Phi$, we have

$$N_B = \int_{z_1}^{z_2} \frac{1}{2\Phi} \frac{dz}{R} \frac{R' \lambda x_c}{R d_p} \left(1 - \frac{R_c}{R}\right) = \frac{\lambda x_c}{2\Phi d_p} \int_{R_1}^{R_2} \frac{dR}{R^2} \left(1 - \frac{R_c}{R}\right), \quad (2.71)$$

which is independent of the $R(z)$ form. For the potential well deformation from $R_1 = R_c$ to $R_2 = R$, the number of captured particles equals

$$N_B = \frac{\lambda x_c}{4\Phi R_c d_p} \left(1 - \frac{R_c}{R}\right)^2 = \frac{\pi \theta_c}{4 \Phi} \frac{2x_c}{d_p} \left(1 - \frac{R_c}{R}\right)^2, \quad (2.72)$$

which is exactly equal to the efficiency (2.12) for the entry-face capture.

This conclusion, derived analytically in the harmonic approximation, is true also in the general case of an arbitrary potential, as a consequence of the Liouville's theorem. In the absense of dissipative processes the microscopic phase density of the captured beam equals the phase density of the incident beam.

The captured particle has the transverse energy $E_T = E_c(z^*)$, where z^* is the coordinate of capture. The transverse energy distribution of captured particles equals

$$P(\epsilon) = \int P(\Theta) d\Theta w_B(z) \delta[(1 - \rho(z))^2 - \epsilon] , \quad (2.73)$$

with $\epsilon = E_T/E_c$ and $\rho(z) = R_c/R(z)$. For $P(\Theta) = 1/2\Phi$ one finds

$$P(\epsilon) = \frac{\lambda}{4\Phi R_c} \int_0^{1-\rho} \xi d\xi \delta(\xi^2 - \epsilon) = \text{const.} \quad (2.74)$$

That is, the distribution is flat (like it is in the nominal case of entry-face capture), independently of the $\rho(z)$ function.

The angular acceptance of a crystal deflector could be made much wider than the divergence of the incident beam, $\Delta\Theta \gg 2\Phi$. In this case the intensity decreases according to (2.71), where R_1 and R_2 are the bending radii at the points, where the beam envelopes are tangential to the crystal planes.

Experimental Evidence. The first experimental indication of the role of the gradient effect in volume capture was made at 70 GeV [76]. The measurements found w_B to be factor of 2 higher than those predicted by (2.60). The dependence of w_B on R was measured to be that predicted by (2.60) (linear in case of [76]). This experiment is discussed in some detail in Chap. 3.

Additivity of the Two Mechanisms. In bent crystals both mechanisms, bending and scattering, may contribute to the feeding-in. In the following, we present a qualitative analysis, which indicates that the two mechanisms contribute in an additive way.

The ‘scattering feeding’ is efficient only at the tangential points. The particles pass over the potential well with the initial transverse energies being in the range from U_0 to $U_0 + \Delta U$. Having scattered during this oscillation, the particles get some distribution $f(E_T)$ with a (interesting to us) tail to smaller $E_T < U_0$. Those particles which have $E_T < E_c$ are trapped in the stable channeled states. Their number is

$$N_S = \int_0^{E_c} f(E_T) dE_T . \quad (2.75)$$

The curvature variability modifies E_c ; then the trapped fraction is

$$N = \int_0^{E_c + \delta E_c} f(E_T) dE_T = N_S + \int_{E_c}^{E_c + \delta E_c} f(E_T) dE_T . \quad (2.76)$$

Since normally $\delta E_c \ll E_c$ over one oscillation λ , we have

$$N = N_S + f(E_c)\delta E_c = N_S + N_B . \quad (2.77)$$

The term $N_B = f(E_c)\delta E_c \approx \delta E_c/\Delta U$ is the fraction of particles trapped through the bending mechanism, as it is defined in the beginning of Sect. 2.3.2.

For positive δE_c (the well grows), the two contributions are summed: $N = N_S + N_B$. For negative δE_c (the well shrinks), the contributions are subtracted: $N = N_S - N_B$.

2.3.3 Conclusion

Although the processes considered cannot increase the beam deflection efficiency, they contribute to a crystal deflector's wide angular acceptance ($\gg \theta_c$). The deflection efficiency (always smaller than in the regular case of entry-face capture) of such a deflector can be *designed* and varied over a broad range of values. Moreover, this efficiency is independent of the incident beam divergence (in contrast to the regular case). This may be valuable, for instance, for the proposed [81] measurements of CP violation with use of K_S and K_L meson beams at CERN, where beam attenuation, stability, and low background are important issues.

Obviously, the secondary particles produced in collisions with crystal nuclei can be captured into the channeling mode, from the crystal bulk, through the feed-in processes only. This may be applicable, e.g., in some ideas of crystal usage for experiments in particle physics (see Chap. 6).

As the energy increases, the rate of transitions from the random to the channeled states changes. For a given crystal, the rate w_S of the scattering-induced transitions, (2.57), decreases as $1/(pv)^{3/2}$ since the scattering vanishes. In contrast, the rate w_B of bending capture, (2.60), grows as $(pv)^{1/2}$ since the centrifugal effects strengthen. The ratio of the two feeding mechanisms changes in favor of bending with an energy increase.

At sufficiently high energies (above ~ 1 TeV), the processes of feeding-out and feeding-in in bent crystals are predominantly defined by the centrifugal effects. These processes are well described by the continuum model, which is a very well-established analytical theory (see Sects. 2.2.1 and 2.3.2). Furthermore, these centrifugal processes are easily controlled through the proper design of the $R(z)$ function.

2.4 Computer Simulation

2.4.1 Introduction

Here we present computational approaches to the description of the physics of particle scattering in an aligned crystal.

As crystal channeling may become a working tool for the next generation of accelerators, there is a need for a theoretical tool able to describe a whole set of experimental data on channeling in the high-energy range, and which also simulates the processes important for future applications.

The result should be the distribution of exiting primary and secondary particles, the energy loss in the crystal, and other interesting quantities related to channeling. Since these processes are sensitive to the orientation, the simulation should track every particle through the crystal lattice, computing the probability of any process as a function of the coordinates.

One of the independent discoveries of channeling, in the early 1960s, was done in a Monte Carlo simulation of low-energy (\leq MeV) ions propagating in crystals [2]. The very low ranges and the thin crystals used allowed the study of binary collisions of the incident ion with the atoms of the crystal (see [30, 31] and references therein). Such numerical studies were helpful in establishing the foundations of channeling. At GeV energies, crystals of a few centimetres in length are used, therefore tracking with binary collisions would be very time-consuming (this tracking, however, was applied for qualitative studies in [32]).

Instead, an approach with a continuous potential (Sect. 1.2) introduced by Lindhard [4] can be used. In this approach one considers collisions of the incoming particle with the atomic strings or planes instead of with separate atoms, if the particle is sufficiently aligned with respect to the crystallographic axis or plane. This approach has been used, in particular for the simulation of the crystal bending experiments [33], since the earliest works on bent-crystal applications.

As well as the motion in the potential one must take into account the scattering. This makes it necessary to use either kinetic equations or computer simulation to transport particles through a crystal. The diffusion approach, which omits single scattering events, is generally applied [8, 34, 35]. However, in Monte Carlo methods it is easy to include single collisions with nuclei and electrons [36]. It was shown in Sect. 1.4.2 that single electronic collisions have an important influence on the high-energy channeling. Such collisions with electrons shape interesting energy loss spectra in aligned crystals (discussed in Sect. 1.5), which are the essential part of the experimental technique in handling the channeled beams. Moreover, these close-encounter processes are the source of secondary particles emitted from the crystal, thus being responsible for the background.

Below we consider, as an example, the organization of the Monte Carlo code CATCH (Capture And Transport of CHarged particles in a crystal) [37, 36] for the simulation of planar channeling in the deformed crystal lattices, which does not use the diffusion approximation for the scattering.

2.4.2 Simulation Procedure

Continuous Potential. For the potential of the atomic plane the Molière approximation is used. The static-lattice potential is modified to take into account the thermal vibrations of the lattice atoms; this is done by integration over the Gaussian distribution of the atom displacement. The crystal channels may be curved because of either crystal deformation or distortions of the crystal lattice induced by defects. Bending of the crystal has no effect on the potential. However, it causes a centrifugal force in the non inertial frame related to the atomic planes. To solve the equation of motion in the potential $U(x)$ of the bent crystal as a first approximation to the transport of a particle,

$$pv \frac{d^2x}{dz^2} = -\frac{dU(x)}{dx} - \frac{pv}{R(z)} \quad (2.78)$$

($R(z)$ being the local radius of curvature), the fast form of the Verlet algorithm [38] is used:

$$x_{i+1} - x_i = (\theta_i + 0.5 f_i \delta z) \delta z, \quad (2.79)$$

$$\theta_{i+1} - \theta_i = 0.5(f_{i+1} + f_i)\delta z, \quad (2.80)$$

with θ standing for dx/dz , f for the ‘force’, and δz for the step. It was chosen over the other second order algorithms for non linear equations of motion, such as Euler–Cromer’s and Beeman’s, owing to the better conservation of the transverse energy shown in the potential motion. For the trapped particle (2.79–2.80) describe its oscillatory motion in the channel formed with atomic planes; then the angle θ is confined within the range of $\pm\theta_c$, where the critical angle θ_c is defined by the potential-well depth. Figure 2.2 shows the simulated phase trajectories of 450 GeV/c protons on the plane (x, θ) in Si(111): for the straight crystal (top figure) and for the crystal bent with $pv/R = 1.5$ GeV/cm (bottom). Scattering was also included; as a result, there are no channeled protons near the atomic planes.

2.4.3 Scattering

Beam steering by a crystal is due to the trapping of some particles in the potential well $U(x)$, where they then may follow the direction of the atomic planes. This simple picture is disturbed by scattering processes which could cause (as a result of one or many events) the trapped particle to come to a free state (*feed-out*, or *dechanneling* process), and an initially free particle to be trapped in the channeled state (*feed-in*, or *volume capture*).

The scattering from electrons has been discussed in detail in Sect. 1.4.2. The algorithm for the electronic scattering implemented in the simulation program precisely matches the consideration given in that section.

Scattering from Nuclei. Scattering from nuclei is divided into two parts. The soft frequent collisions are taken into account continuously at every step; the random deflection angle is computed as a Gaussian function with the root-mean-square value given by the Kitagawa–Ohtsuki approximation [41]:

$$\langle \theta_{\text{nucl.sc}}^2 \rangle = \langle \theta_{\text{sc}}^2 \rangle_{\text{am}} \rho_n(x), \quad (2.81)$$

that is, the mean angle of scattering squared is proportional to the local density of nuclei $\rho_n(x)$ (normalized to the amorphous value); $\langle \theta_{\text{sc}}^2 \rangle_{\text{am}}$ is the scattering angle squared in an amorphous substance. The density function $\rho_n(x)$ is Gaussian [see (1.7)].

The hard nuclear collisions are treated event by event. Their probability, proportional to $\rho_n(x)$, is checked at every step. If such a collision succeeds, the routine responsible for the event generation may be called. To simulate the single nuclear collisions one may use any specialized code, such as the LUND [42] routines; the CATCH program serves as a frame to provide the orientational dependence of these processes. This scheme may be used to describe any close-encounter process of interest; then one should define the collision length properly. The secondary particles (possibly produced in interactions of the particle in the crystal) may be, in principle, also tracked through the crystal lattice.

Crystal Imperfection. The crystal curvature, both longitudinal and transverse, and the crystal plane orientation can be arbitrary functions of the spatial coordinates. Any data measured (or assumed) for the real crystal shape can be implemented in the simulation. The imperfection of the crystal lattice, in the presence of dislocations, may be taken into account through the $R(z)$ term in (2.78) (see the theory of channeling in imperfect crystals in the section below).

In the case of the extraction of the beam from an accelerator, extremely small impact parameters are possible, making the surface effects essential. A particle entering the real crystal very close to its edge can suffer from various additional factors: a miscut angle (between the atomic planes and the surface); a roughness (that is, nonflatness) of the surface; a possible amorphous layer; a bent surface. Therefore one must pay particular attention to the near-surface tracking, where the particle is entering and leaving the crystal material (because of the roughness, holes, and bend), both coherent and noncoherent scattering in this peculiar region, bending in short channels, and so on. The surface effects mentioned above are simulated in CATCH. The roughness is expressed by a periodic function, $a \sin(2\pi z/l)$, where a is the amplitude of ‘bumps’ and l is their periodicity. The ‘rough’ crystalline material can be superimposed by a uniform amorphous layer. The positions of the surfaces are computed at every step in accordance with bending with a variable curvature. Every particle (both channeled and nonchanneled) is tracked in the crystal and can leak out through any surface. Near the rough surface it may even leak out and be caught again many times. That is, the

particle traverses sequentially the crystal bumps and the vacuum (or amorphous skin) between. A complete description of the program usage may be found in [37].

2.4.4 Simulation of the Dechanneling Process

Now we can consider again the evolution of the distribution function for the channeled particles with the crystal depth, in order to verify the analysis performed in Sect. 1.4.1.

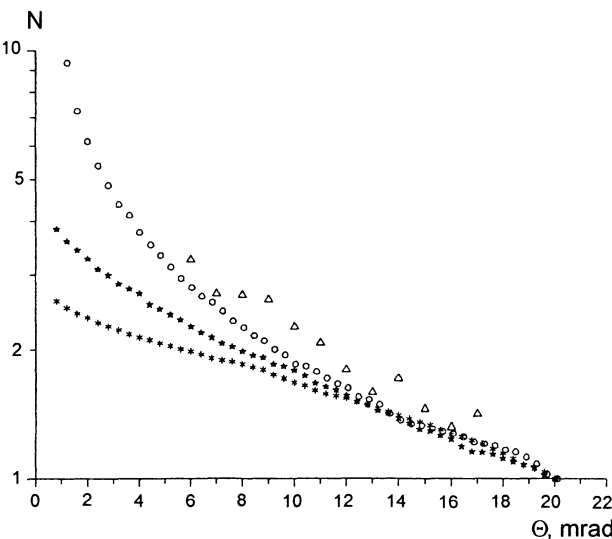


Fig. 2.12. Dependences of the number of deflected channeled particles upon the angle Θ on a logarithmic scale for a Si(110) crystal. The triangles are experimental points and the other marks are for simulations: open circles for volume capture, stars for entry-face capture of a $30 \mu\text{rad}$ rms divergent beam, asterisks for entry-face capture of a parallel beam.

Such an evolution has been studied in [27] via a detailed Monte Carlo simulation with CATCH. The program tracked several 100 000 70-Gev protons through the bent silicon crystal by small (of the order of $0.1 \mu\text{m}$) steps, taking into account the transverse electric field of the atomic planes and processes of scattering from electrons and nuclei. No diffusion approach was used and scattering in close encounters was considered in full detail. The crystal was bent with a constant radius $R = 3 \text{ m}$ of curvature, in order to match the condition of the experiment of [27]. The crystal bending allowed the exiting angle Θ of a proton to be related to the coordinate z at the crystal where the proton dechanneled: $z = R\Theta$. (More detail on this and other bending experiments may be found in Chap. 3.)

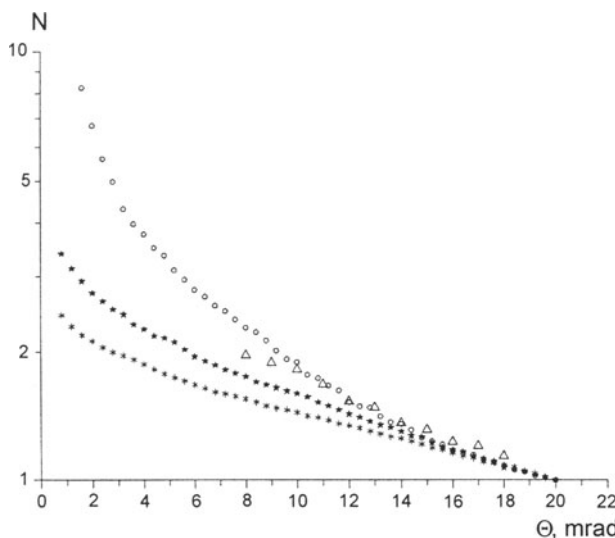


Fig. 2.13. The same as in Fig. 2.12 but for the Si(111) crystal.

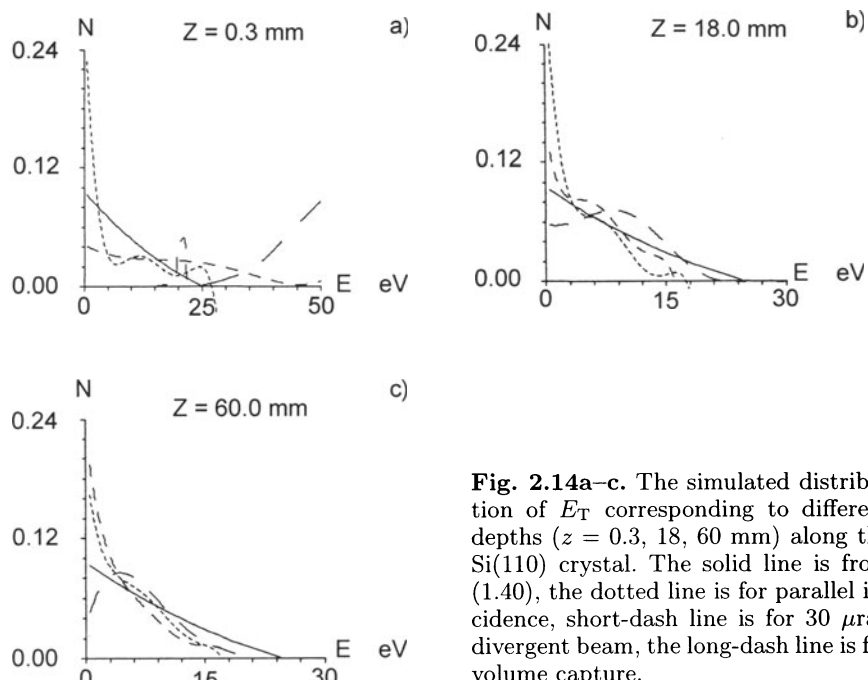


Fig. 2.14a–c. The simulated distribution of E_T corresponding to different depths ($z = 0.3, 18, 60$ mm) along the Si(110) crystal. The solid line is from (1.40), the dotted line is for parallel incidence, short-dash line is for $30 \mu\text{rad}$ divergent beam, the long-dash line is for volume capture.

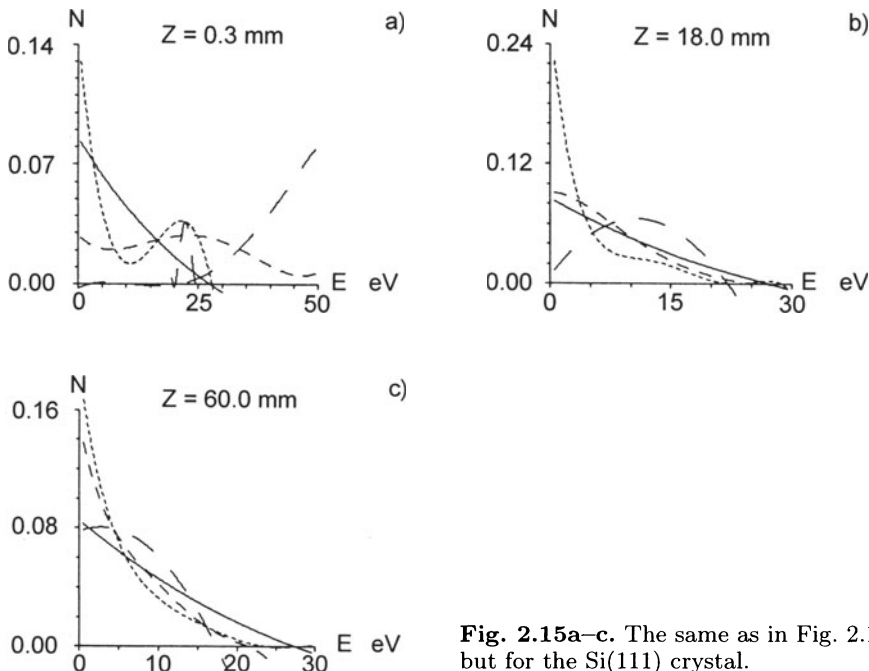


Fig. 2.15a–c. The same as in Fig. 2.14 but for the Si(111) crystal.

In order to provide different starting distributions over the transverse energy of the trapped protons, various options have been tried. For the parallel incident beam, the particles trapped at the crystal entry face were peaked at small E_T values. For the divergent ($30 \mu\text{rad rms}$) incident beam, the distribution at the entry face was roughly flat. Finally, the feeding-in was applied when the protons, nonchanneled initially, could be trapped in the crystal depth because of the scattering; in this case the trapped particles had high E_T values peaked at E_c .

Figures 2.12 (Si(110)) and 2.13 (Si(111)) show the dependences of the numbers of the deflected channeled particles upon the angle Θ (or coordinate, $z = R\Theta$) for various simulation options and for the experiment (volume-capture case). All the dechanneling curves are close to exponential in the crystal depth. In agreement with the earlier analysis the exponent slopes become the same in the depth of the crystal, independently of the option. Figures 2.14 and 2.15 provide the explanation. These figures show the starting distribution and their evolution in a 60-mm-long crystal. The particle distributions as a function of E_T , initially very different, relax in the depth of the crystal to some general shape roughly given by (1.40), in accord with the analysis given in Sect. 1.4.1.

2.5 Channeling in an Imperfect Lattice

2.5.1 Classification of Lattice Defects

We have considered dechanneling in a crystal with an ideal lattice. In a perfect straight crystal the scattering from electrons and nuclei leads to the proportion $L_D \sim pv$ (the logarithmic term is omitted here). At multi-TeV energies, L_D in a perfect crystal is some meters, therefore the corresponding loss is greatly reduced.

In a real crystal various defects disturb the lattice. It is convenient to classify all defects present in the crystal into a few groups – point-like defects (interstitial atoms and vacancies), linear (dislocations), two-dimensional (stacking faults) and three-dimensional (amorphous clusters) ones – because of their different influence on the particle channeling. This difference is particularly essential for the energy dependence of dechanneling from lattice defects. (The book by Feldman et al. [7] provides a good introduction to this field.)

Point-Like Defects. Scattering on a single isolated atom (of atomic number Z_a and mass M_a) in a channel, Fig. 2.16, may cause immediate dechanneling if the impact is close enough. For such a hard scattering event, with $\theta_s > \theta_c$, one may apply the unscreened Rutherford scattering cross-section,

$$\frac{d\sigma}{d\Omega} = \frac{4Z_i^2 Z_a^2 e^4}{p^2 v^2 \theta_s^4}, \quad (2.82)$$

written here for scattering with $\theta_s \ll 1$. Integration over $d\Omega = \theta_s d\theta_s d\phi$ for the projection angle $\theta_s \cos \phi$ greater than θ_c gives the cross-section of the planar dechanneling

$$\sigma_D = \frac{2\pi Z_i^2 Z_a^2 e^4}{p^2 v^2 \theta_c^2}, \quad (2.83)$$

which decreases with energy as $1/pv$ (notice that $\theta_c^2 \sim 1/pv$). The length L_D of dechanneling, if it is defined mainly by this kind of defects,

$$L_D = \frac{1}{n_D \sigma_D} \quad (2.84)$$

depends on the defect volume density n_D , and grows linearly with energy.

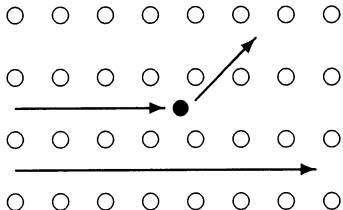


Fig. 2.16. Scattering of a channeled particle from an interstitial atom.

The contribution of the multiple Coulomb scattering from point-like defects to the diffusion of the transverse energy may be taken into account in the framework of kinetic theory (Sect. 1.4). Assuming a uniform distribution of interstitial atoms across the channel, we take the diffusion factor as $D = E_T E_s^2 Z_i^2 n_a / 2pvL_R$; here n_a is the volume density of interstitials normalized to its value in an amorphous medium; the constants $E_s = 14$ MeV and the radiation length L_R [9.4 cm in Si; see (6.14)] define the mean-squared angle of scattering along the length z in an amorphous medium: $\langle \theta_s^2 \rangle = (E_s/pv)^2 (z/L_R)$ [40]. This contribution becomes comparable to the electronic one only at $n_a \approx 0.01$. The diffusion-induced $L_D \approx pvE_c L_R / E_s^2 Z_i^2 n_a$ grows as pv/Z_i , as does (2.84).

Linear Defects. The extended defects of the crystal structure (such as dislocation lines, loops and walls; see Figs. 2.18–2.20 later) disturb the long-range order of the crystal lattice. For this reason the channeled particles could enter the region with a high density of nuclei and be scattered, and/or pass through the region with a strong local bend. This may lead to a considerable change in the transverse energy or to dechanneling.

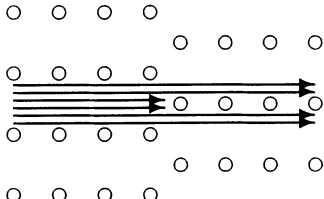
In the neighborhood of a linear dislocation the lattice planes are inclined by an angle of the order of b/r , where r is the distance to the dislocation and b is the Burgers vector value (the lattice period). This angle exceeds the critical value θ_c at distances of up to $r_D \simeq b/\theta_c$ from the dislocation. The disturbed space is a cylinder of thickness $\sigma_D \simeq r_D$ ('dechanneling cylinder') coaxial with the dislocation. Taking into account the dislocation density n_D (the total length of dislocations per unit volume, measured in cm^{-2}), we may estimate the probability of a particle entering the dechanneling cylinder as $n_D \sigma_D \simeq n_D b/\theta_c$ per unit length. The dechanneling length

$$L_D \approx \frac{1}{n_D \sigma_D} \approx \frac{\theta_c}{b n_D} \quad (2.85)$$

decreases by $\sim 1/\sqrt{pv}$, as the centrifugal effects become increasingly important with higher energy.

Two-Dimensional Defects. There may be a discontinuity in the positions of the atomic rows and planes (Fig. 2.17), called a stacking fault. The fault boundary separating the perfect blocks is a planar defect. Its area defines the probability of a particle meeting this discontinuity. The dechanneling probability per crossing of this defect is similar to that at the crystal surface: about $\pi x_c / 2d_p \approx 0.6$ ('surface transmission'; Sect. 1.3). Its value is practically independent of energy.

Three-Dimensional Defects. Volume defects, where the crystal structure is different from that outside (amorphous clusters, twins, etc.), contribute to the dechanneling in the same manner as the interstitial atoms do. This contribution vanishes with energy as $1/E$. If the size of the defect is comparable to λ , the behavior approaches that of a stacking fault.

**Fig. 2.17.** Stacking fault.

Of all the various defects present in crystals the dislocations are of most interest, because the contribution of other defects to dechanneling decreases with energy or remains constant. At today's energies (hundreds of GeV) and high perfection of the silicon crystals the defects do not affect the efficiency of beam deflection. There is good agreement between the theory for a perfect crystal, and experiments with real silicon crystals at energies up to ~ 1 TeV. Therefore one needs to consider only dislocations. The dechanneling theory for defects of dislocation nature is analyzed below, with emphasis given to the multi-TeV energy domain.

2.5.2 Dislocations

The Linear Dislocations. Linear edge dislocation may be viewed as the edge of an extra half-plane of atoms in the crystal lattice (Fig. 2.18). It is characterized by the Burgers vector \mathbf{b} , which is shown in Fig. 2.18 normal to the surplus (interstitial) half-plane, with a value equal to the interatomic distance (lattice period in the direction of \mathbf{b}). The atom displacement in the surrounding lattice, caused by this defect, is equal [82] to

$$u_x = \frac{b}{2\pi} \left(\arctan \frac{y}{x} + \frac{1}{2(1-\nu)} \frac{xy}{r^2} \right), \quad (2.86)$$

$$u_y = \frac{b}{4\pi(1-\nu)} \left((1-2\nu) \ln r + \frac{x^2}{r^2} \right) \quad (2.87)$$

in the reference frame shown in Fig. 2.18: the z axis is along the dislocation line ξ , the x axis is along the Burgers vector \mathbf{b} ; $r^2 = x^2 + y^2$. The Poisson ratio ν is 0.42 in Si. In the case of a screw dislocation, the dislocation line ξ and the vector \mathbf{b} are parallel (let it be the z axis). The only nonzero displacement takes place in the z direction:

$$u_z = \frac{b}{2\pi} \arctan \frac{y}{x}. \quad (2.88)$$

The particle motion in the disturbed lattice must be considered with the changed positions of the atoms taken into account. The equivalent approach is to go to the reference frame related to the lattice atoms. In this frame, instead of displacements, the centrifugal force appears. This is the same approach that was used throughout the Chap. 2 to describe the particle motion in a curved planar channel. Then (2.1) becomes:

$$pv \frac{d^2x}{dz^2} + U'(x) + pv \frac{\partial^2 u}{\partial z^2} = 0 . \quad (2.89)$$

The local curvature $\partial^2 u / \partial z^2$ in the plane of channeling depends on the mutual orientation of a dislocation ξ , the Burgers vector b , and the particle momentum p , as well as on the distance r from the defect.

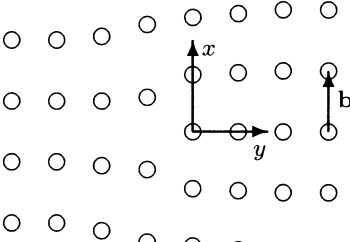


Fig. 2.18. Linear edge dislocation.

The centrifugal force has the order of pvb/r^2 ; it may remove the particle from the channeling mode if that approaches the dislocation at too small r . This consideration was first performed by Quéré [83]. Assuming that a particle dechannels if (and only if) the maximal local curvature along its path exceeds the critical value $1/R_c$, Quéré has derived the following cross-section for the planar dechanneling on a straight dislocation line:

$$\sigma_D = K \sqrt{\frac{bpv}{2Z_i Ze^2 N d_p}} = K \sqrt{\frac{\pi}{2} b R_c} . \quad (2.90)$$

For σ_D averaged over the possible orientations of ξ and p , the constant K is $\simeq 0.34$ for a screw dislocation and 0.56 for an edge one. The σ_D is the diameter of a cylinder (coaxial to ξ), that is opaque to the channeled particles in Quéré's consideration. For a 1-TeV proton in Si, σ_D is of the order of $10 \mu\text{m}$. The probability of dechanneling per unit length is $\sigma_D n_D$; the dechanneling length,

$$L_D = \frac{1}{n_D \sigma_D} , \quad (2.91)$$

decreases with energy as $1/\sqrt{pv}$.

The σ_D value is about one order of magnitude smaller than λ . This means that a particle does not make even one oscillation in a curved channel. Hence, Quéré's criterion of the critical curvature is a poor approximation. Instead of considering the static balance of two forces, $U'(x_c)$ and $p v / R$, one should solve (2.89), taking into account the flux distribution in the channel.

The approach used for (2.89) has been employed by many authors [84–88]. They followed the particle trajectory and applied the dechanneling criterion, $x > x_c$, along the path $x(z)$ or just at $z = +\infty$; this causes the nuclear

scattering in the dislocation core to drop from consideration, over- or underestimating it, respectively. Several [89, 90] computer simulations included the scattering. These investigations confirmed the $\sigma_D \sim \sqrt{E}$ scaling law predicted by Quéré. This \sqrt{E} law has also been found in the experiments [7, 91]. As compared to the observations, Quéré's formula underestimates σ_D for planar channels by a factor of ~ 2 [87] or less [7, 85], and overestimates it for axial channels by a factor of ~ 4 [88]. All the theorists [84–89] report good agreement between their calculations and the experiments.

Equation (2.89) can be solved with the harmonic potential [52]. In the final state ($z = +\infty$) the solution is a harmonic oscillation with the amplitude [85, 88]

$$x_f = (x_m^2 + x_d^2 + 2x_m x_d \cos \phi)^{1/2}, \quad (2.92)$$

where x_m is the amplitude at $z = -\infty$, ϕ depends on the initial phase and will be averaged later. The x_d is determined by the dislocation; for $\mathbf{p} \perp \xi$ it is equal to

$$x_d = \frac{b}{2} e^{-2\pi r/\lambda} \quad (2.93)$$

for the screw dislocation and

$$x_d = \frac{b}{2} e^{-2\pi r/\lambda} \left(\frac{1-2\nu}{2(1-\nu)} + \frac{\pi r}{(1-\nu)\lambda} \right), \quad (2.94)$$

$$x_d = \frac{b}{2} e^{-2\pi r/\lambda} \left(1 + \frac{\pi r}{(1-\nu)\lambda} \right) \quad (2.95)$$

for the edge dislocation, $\mathbf{p} \parallel \mathbf{b}$ and $\mathbf{p} \perp \mathbf{b}$ respectively. Equations (2.93–2.95) show that the influence of dislocation is limited to a distance of $\approx \lambda/2\pi$, which grows as \sqrt{pv} . The difference in E_T between the final and the initial states is

$$\delta E_T = \frac{E_c}{x_c^2} (x_d^2 + 2x_m x_d \cos \phi). \quad (2.96)$$

A particle dechannels if $\delta E_T \geq E_c - E_T$. Since ϕ is random, the dechanneling probability for a particle with E_T and impact parameter r is found as

$$q(E_T) = \frac{1}{\pi} \arccos \left(\frac{x_c^2 E_c - x_c^2 E_T - x_d^2 E_c}{x_d x_c \sqrt{E_c E_T}} \right) \quad (2.97)$$

for $E_T + \sqrt{E_c E_T} x_d / x_c > E_c (1 - x_d^2 / x_c^2)$, and zero for smaller E_T . The net probability is $\int_0^{E_c} q(E_T) f(E_T) dE_T$ for the particle distribution function $f(E_T)$ (which is approximately flat at the incidence for GeV beams, but different in the depth, Sect. 1.4). Finally, the dechanneling cross-section is the integral over the impact parameters:

$$\sigma_D = \int_0^\infty dr \int_0^{E_c} q(r, E_T) f(E_T) dE_T. \quad (2.98)$$

Above, only interactions with a single dislocation were considered. The particles that were not dechanneled in a single event, have experienced some change of E_T (due to the long range of the displacement field). As a result, the dechanneling may be caused by the multiple interactions with dislocations. A consistent theory should include all the contributions. Here we shall derive an analytical estimate following the diffusion approach. It is applicable only if $\delta E_T \ll E_c$. Then (2.96) may be written as $\delta E_T \approx 2E_c x_m x_d \cos\phi/x_c^2$. The diffusion factor is [92]

$$\left\langle \frac{(\delta E_T)^2}{\delta z} \right\rangle = \frac{2E_c E_T n_D}{x_c^2} \int_{r_{\min}}^{\infty} x_d^2 dr , \quad (2.99)$$

as the diffusion approach is valid starting with $r_{\min} \approx \lambda/2\pi$, according to (2.93–2.95). With the method used in Sect. 1.4.1 one can derive a ‘partial’ dechanneling length corresponding to (2.99) in order to estimate the contribution of the soft multiple interactions. For example, in the case of screw dislocation this length (for (2.99) averaged over the angle between \mathbf{p} and ξ) equals [92]

$$L_{\text{diff}} \approx \frac{6\pi e^{2\pi r_{\min}/\lambda}}{j_{0,1}^2} \frac{\theta_c d_p}{b^2 n_D} \approx 25 \frac{\theta_c d_p}{b^2 n_D} . \quad (2.100)$$

The contribution from the soft multiple collisions is, thus, a fraction of that from the single hard scatterings (2.90), and grows as b^2 . The estimate for the edge dislocation gives the same result. Although the quantitative predictions should take into account both single and multiple scatterings (in the Monte Carlo approach), both mechanisms provide a similar dependence. The results of this analysis may be expressed with a simple formula

$$L_D \approx \frac{\theta_c}{b n_D} , \quad (2.101)$$

which gives the right order of magnitude. The correct quantitative factor (of the order of unity), as well as the dependence on the distortion geometry, should be obtained with a more detailed theory. There are few measurements of L_D in imperfect crystals in high-GeV range (discussed in Chap. 3).

The theory was originally developed for MeV energies, and possible changes may be necessary to apply it in the TeV range. Both the distortion size σ_D and the particle oscillation period λ have the same dependence on energy. So there is no change in the character of the particle motion. On the other hand, scattering is strongly suppressed. For example, scattering angle along λ in amorphous silicon is one order higher than θ_c at 1 MeV, but it is two orders lower than θ_c at 1 TeV. Hence, the contribution from nuclear scattering in the dislocation core, substantial at 1 MeV, is negligible at 1 TeV. The estimates from the continuum model become even more justified in the \sim TeV domain. For the applications foreseen at the highest energies, ~ 7 TeV, the crystal purity required is $n_D \ll \theta_c/bL$, in order to

use crystals with length L . This means that a ‘perfect’ crystal should have not more than one linear dislocation per square centimeter. The quality of crystals is steadily improving; dislocation-free examples ($n_D \leq 1/\text{cm}^2$ [93]) can in principle be produced.

The Crystal Mosaicity. Linear dislocations may not be isolated. Because of interactions between them in a crystal, they can produce some more complicated structures. One example of such a structure is the crystal mosaicity (Fig. 2.19), which may be the most visual defect of a lattice. The crystal consists of a number of perfect blocks slightly disoriented with respect to each other.

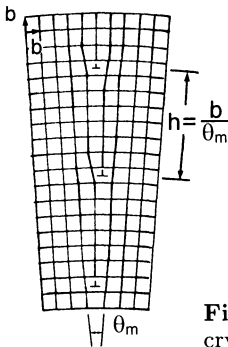


Fig. 2.19. Dislocation wall separating two perfect blocks of a crystal.

The crystal splitting is due to the edge dislocations being arranged in a pattern (dislocation wall), separating the crystal into blocks. To produce such a pattern, the dislocations should be mobile; for this reason this defect is more typical for metal crystals than for semiconductors. The angle of disalignment of the crystal blocks for each side of the wall is equal [82] to:

$$\theta_m = \frac{b}{h}, \quad (2.102)$$

where $h = b/\theta_m$ is the spacing between dislocations in the wall and b is the value of the Burgers vector. The channel orientation on θ_m differs along a distance of the order of h [82]. Along this distance the channel is bent with a radius roughly equal to

$$R_m = \frac{h}{\theta_m} = \frac{b}{\theta_m^2}. \quad (2.103)$$

The influence such a distortion has on particle channeling depends on the size of h relative to the oscillation period λ of the channeled particle. If $\lambda \ll h$, the particle makes a number of oscillations along h , and hence the dechanneling is determined by the maximal curvature along this distance. In the other case, if λ and h are comparable, the result of the particle interaction with the wall depends on the phase of its oscillation; its random character

leads, in addition, to some diffusion in phase space. Finally, for $\lambda \gg h$, the particle experiences only an angular kick. Since $\lambda \approx \pi d_p/\theta_c$, the latter case of $\lambda \gg h$ means that the mosaicity angle $\theta_m \gg \theta_c$, i.e. all the particles certainly dechannel at the wall.

For the available high-quality Si crystals very low values of θ_m (down to $0.05 \mu\text{rad}$ [94]) have been measured; this leads to b/θ_m being an order higher than λ , even at $\sim 10 \text{ TeV}$. For this reason one may estimate here the bending-like dechanneling only. As discussed above, the ‘intrinsic’ bend of the crystal channels leads to some ‘intrinsic’ acceptance of the imperfect crystal. The bent-crystal acceptance A_B is determined by the ratio of pv to the local radius of curvature, $pv/R_m = pv\theta_m^2/b$. This ratio should be added to the crystal global curvature pv/R , if present. The extra reduction in the crystal acceptance, owing to mosaicity, is equal [95] to

$$A_B \left(\frac{pv}{R} \right) - A_B \left(\frac{pv}{R} + \frac{pv\theta_m^2}{b} \right) \simeq - \frac{d A_B(pv/R)}{d \left(\frac{pv}{R} \right)} \frac{pv\theta_m^2}{b}. \quad (2.104)$$

The beam loss is proportional to $pv\theta_m^2$ (until it gets too high). For instance, in the case of a harmonic potential this produces a relative reduction in the crystal acceptance

$$\frac{\Delta A_B}{A_B} = \frac{2pv\theta_m^2}{b \left(1 - \frac{R_c}{R} \right)}. \quad (2.105)$$

A mosaic spread as low as $\theta_m = 0.05 \mu\text{rad}$ has a negligible effect, $\Delta A_B/A_B \approx 10^{-3}$, on the channeling, even at $\sim 10 \text{ TeV}$. Some dechanneling may occur at the dislocation cores in the wall.

The Dislocation Loops. The dislocation-loop defect can be imagined as an interstitial (vacant) piece of atomic layer (Fig. 2.20). In other words this is a closed edge dislocation. It is characterized by its size (radius R_{loop} , if it is circular), which is rather small. For example, for the silicon crystal used for 1-GeV proton-beam deflection, and tested in Gatchina for dislocation contamination [51], it was found that there are two types of clusters (associated with dislocation loops): the A-type with the size of 1–3 microns, and the B-type with the size of 0.06–0.08 microns. Their densities depend on their position: in the center of the crystal they equal $100/\text{cm}^2$ (A-type) and $10^4/\text{cm}^2$ (B-type).

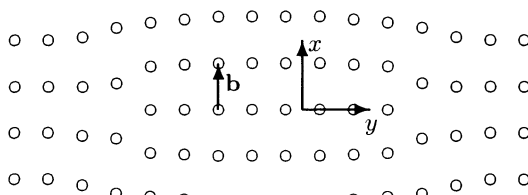


Fig. 2.20. Dislocation loop.

The lattice in the vicinity ($r \ll R_{\text{loop}}$) of the edge dislocation is displaced in rough accordance with (2.86–2.88). At distances r large as compared to R_{loop} the influence of the edge dislocation is suppressed, because outside the loop the Burgers vector sums to zero. The atom displacement at $r \gg R_{\text{loop}}$ is equal [82] (with the isotropic-matter approximation) to

$$u_i = \frac{\gamma_c^2}{4\pi r^3} \left((d_{ik} + d_{ki})x_k - d_{kk}x_i + \frac{3(1 - \gamma_c^2)}{\gamma_c^2 r^2} d_{kl}x_i x_k x_l \right), \quad (2.106)$$

where $\gamma_c^2 = \mu_1/(2\mu_1 + \mu_2)$, μ_1 and μ_2 are the Lame coefficients, $d_{ik} = S_i b_k$, and S_i and b_k are the projections of the loop area \mathbf{S} and the Burgers vector \mathbf{b} onto the coordinate planes. The displacement falls very fast, as $1/r^2$, so the channel curvature decreases as $1/r^4$ (to be compared to $1/r^2$ for linear dislocations). The curvature becomes critical at about the distance $(bR_{\text{loop}}^2 R_c)^{1/4}$.

The experimental and theoretical studies [7, 96, 88] performed for MeV ions have shown the following results for the dechanneling from loops. At low energy, when $\sigma_D \ll R_{\text{loop}}$, there is no difference with dechanneling on a linear dislocation, and σ_D scales as \sqrt{E} . As the energy grows, σ_D saturates at about R_{loop} .

At energies in the TeV range, the situation becomes rather different. First, scattering is very suppressed. Second, and more important point is that, for the multi-TeV channeled particle interaction with such a defect, it is essential that the oscillation period λ is much larger than the disturbed lattice region size. For example, for the 1-TeV proton in silicon $\lambda \simeq 100\mu\text{m}$ and $(bR_{\text{loop}}^2 R_c)^{1/4} \leq 5\mu\text{m}$. The usual criterion of dechanneling, i.e., when the channel curvature is larger than the critical one, is not valid here, because the channeled ion does not make an oscillation in the distorted channel. However, one must take into account a ‘kick’ due to the pass through the channel with the disturbed potential (long-range influence of the loop), as well as the multiple scattering of the ion passing through the loop core. The latter contribution is small too: at 1-TeV the scattering angle over $5\mu\text{m}$ of amorphous silicon is only $0.02\theta_c$.

The probability of dechanneling due to a single collision is small; the change in E_T per interaction with such a defect is also not large, because of the small size of the distorted region. For this reason the consideration could be in terms of the kinetic theory.

The distorted region is divided into two parts: a ‘core’ (with size D_{core}), where the atom displacement is larger than a_{TF} , and an ‘outer part’. The value of $D_{\text{core}} \approx \sqrt{3(1 - \gamma_c^2)} Sb / \pi a_{\text{TF}}$ is a few R_{loop} . We consider collisions in the core to be uncorrelated (amorphous approximation); for the outer part no multiple scattering is assumed, only the potential perturbation.

Let us first consider a high-energy particle interacting with the core. The change in the transverse energy is defined by the coordinate changes δx and $\delta\theta$: $\delta E_T = p\delta\theta + U'(x)\delta x$. Let us consider the second term first: $\delta E_T \simeq U'(x)\delta D_{\text{core}}$. It is due to a ‘missed’ potential in the core, since the particle is

not guided by the regular potential when passing the core. Possible correlated collisions in the core would lead to δE_T being of the same order [95].

The cross section of a particle interaction with distortion is $\sigma_D \simeq D_{\text{core}}^2$; the interaction length $\delta z = 1/n_v \sigma_D$, where $n_v = n_D/2\pi R_{\text{loop}}$ is the volume density of the dislocation loops. The diffusion coefficient (averaging is made both over the oscillation period and over the defect size distribution) is of the form:

$$\left\langle \frac{(\delta E_T)^2}{\delta z} \right\rangle = 2\langle (U'(x))^2(E_T - U(x)) \rangle \frac{\langle n_v D_{\text{core}}^4 \rangle}{pv}. \quad (2.107)$$

The noncoherent scattering from nuclei leads to the following diffusion coefficient

$$\left\langle \frac{(\delta E_T)^2}{\delta z} \right\rangle = 2\langle E_T - U(x) \rangle \frac{\epsilon^2}{L_R p v} \langle n_v D_{\text{core}}^3 \rangle. \quad (2.108)$$

Its value is two orders smaller than (2.107) for $R_{\text{loop}} \geq 0.06 \mu\text{m}$.

The core size, as defined above, is independent of the beam momentum; for this reason the above diffusion coefficients are inversely proportional to $p v$.

The long-range contribution can be estimated here as follows. Since the range of distortion is much less than λ , the particle interaction with it may be considered as a ‘kick’ at some point. The interplanar force can be expanded in the following way: $U'(x + u) \simeq U'(x) + U''(x)u$. The angle perturbation over the interval dz is $\delta\theta = U''(x)udz/pv$. The change in the E_T , integrated by z over the trajectory, is

$$\delta E_T = p v \theta \int \delta\theta = \theta(x) U''(x) \int u(r, z) dz. \quad (2.109)$$

As mentioned above, we keep x and θ constant during the interaction; thus a generalization is possible. Averaging over the impact parameters and defects distribution, one has

$$\left\langle \frac{(\delta E_T)^2}{\delta z} \right\rangle = \frac{2\langle (U''(x))^2(E_T - U(x)) \rangle}{pv} \left\langle n_v \int d\sigma \left(\int u dz \right)^2 \right\rangle. \quad (2.110)$$

For example, for a loop parallel to the plane of channeling and a \mathbf{b} vector orthogonal to it, the integration of (2.110) gives:

$$\left\langle \frac{(\delta E_T)^2}{\delta z} \right\rangle = \frac{\langle (U''(x))^2(E_T - U(x)) \rangle}{pv} \frac{\Gamma \gamma_c^2}{2\pi} \left\langle n_v S^2 b^2 \ln \frac{\lambda}{D_{\text{core}}} \right\rangle, \quad (2.111)$$

where $\Gamma = 1 + 3(1 - \gamma_c^2)/4\gamma_c^2 + 5(1 - \gamma_c^2)^2/8\gamma_c^4$. In silicon $\Gamma \gamma_c^2 = 4.15$. The result depends logarithmically on the limits of the integration over the impact parameters. The upper limit is set to be λ , since above this value the loop influence is suppressed by oscillations of the particle. The values of (2.107) and (2.111) are comparable.

The most important result of the above analysis is that there is no more saturation in the dechanneling from loops. The L_D becomes a linear function of pv . The net diffusion coefficient is proportional to $b^2 n_v R_{\text{loop}}^4 \sim b^2 n_D R_{\text{loop}}^3$; hence the dechanneling from smaller loops is slower by a big factor. The beam loss is roughly proportional to $n_v R_{\text{loop}}^4$, for sizeable dechanneling. In the harmonic approximation the net diffusion factor (2.107, 2.111) is

$$D(E_T) = E_T \frac{\theta_c^2}{x_c^2} n_v S^2 b^2 \left(\frac{E_c}{x_c^2} \frac{\Gamma \gamma_c^2}{2\pi} \ln \frac{\lambda}{D_{\text{core}}} + E_T \frac{9(1 - \gamma_c^2)^2}{2\pi^2 a_{\text{TF}}^2} \right). \quad (2.112)$$

For $\sim 7\text{-TeV}$ protons in Si this leads to the dechanneling length of the order of

$$L_D \approx \frac{10^9 [\text{cm}]}{n_v [\text{cm}^{-3}] R_{\text{loop}}^4 [\mu\text{m}]} , \quad (2.113)$$

if this defect dominates. The quantitative factor in this estimate may change if a more accurate numerical analysis is used.

2.5.3 Computer Simulation of Dislocation Dechanneling

In what follows the planar dechanneling from linear dislocations is studied by means of a Monte Carlo simulation. For this purpose the CATCH computer code has been upgraded [92], in order to include (2.86–2.89) in the equations of the particle motion in a crystal. We concentrate on the high energy (GeV and TeV) case, which means divergent beams (with respect to θ_c) and the long bent crystals (multiple interactions are involved); in contrast, the MeV case studied in [83–89] implied a parallel beam and a single interaction.

First dechanneling from a single interaction with a linear dislocation is considered. In the simulation [92] a proton beam with a divergence greater than θ_c was incident onto the Si (110) crystal. Soon after the incidence the particles meet a single dislocation. In order to more easily distinguish between the channeled and random particles in the crystal, and to provide the starting particle distribution typical for high-energy applications, a slight bending of the crystal with $pv/R = 0.1 \text{ GeV/cm}$ was applied. The channeled particles with $E_T < 18 \text{ eV}$ were selected upstream of the dislocation, and those with $E_T > U_0$ downstream were considered as dechanneled (the gap $U_0 - 18 \text{ eV}$ was to suppress the contribution from ‘ordinary dechanneling’). The dechanneling probability obtained in this simulation is plotted in Fig. 2.21 as a function of the impact parameter (the minimal distance between the particle and dislocation), for edge and screw dislocations with $b = 3.84 \text{ \AA}$ at 450 GeV and 7 TeV. The probability in Fig. 2.21 is averaged over the incident angles of the proton with respect to \mathbf{b} and the dislocation line.

The integration of the dependences shown in Fig. 2.21 gives the following dechanneling cross sections σ_D : 20 μm and 7 μm for the edge and screw dislocations, respectively, at 450 GeV, and 77 μm (edge) and 27 μm (screw) at 7 TeV [92]. The ratio $\sigma_D[7 \text{ TeV}]/\sigma_D[450 \text{ GeV}]$ is equal to 3.85, in accord

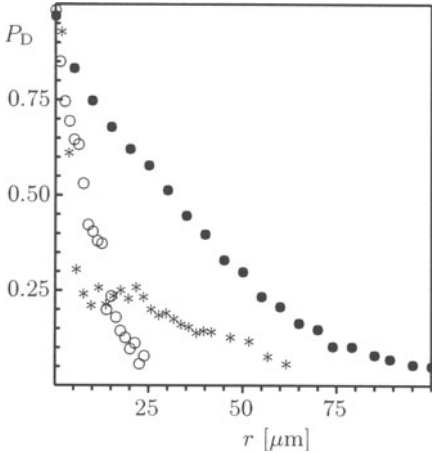


Fig. 2.21. The probability of dechanneling by a single dislocation as a function of the impact parameter for edge (●) and screw (*) dislocations at 7 TeV, and for edge dislocations at 450 GeV (o).

with that expected from the $(pv)^{1/2}$ law, i.e. $(7 \text{ TeV}/450 \text{ GeV})^{1/2} = 3.94$. The cross sections are rather close to those predicted by (2.90): 47 μm (edge) and 29 μm (screw) for the 7-TeV case. With a similar procedure repeated for stronger bending (1 GeV/cm) of the crystal, σ_D increased by the order of 10%.

The multiple interactions of the channeled particles with linear dislocations in the long bent silicon crystals have also been studied [92]. The same proton beam was incident onto a 3-cm long Si (110) crystal. The crystal bending was uniform with pv/R varied from 0.2 to 3.0 GeV/cm.

The dislocations were distributed randomly in the crystal bulk with some density n_D , with a uniform distribution of the position and orientation angles. There was an equal number of the dislocations of the edge and screw type. For simplicity, the same Burgers vector value $b = 3.84 \text{ \AA}$ was kept whatever the dislocation orientation.

Two energies, 450 GeV and 7 TeV, have been studied with the dislocation density varied from 0.1 to 500 cm^{-2} . The dechanneling lengths obtained in this simulation are plotted in Fig. 2.22. For a nearly perfect crystal ($n_D = 0.1\text{--}1 \text{ cm}^{-2}$) the dechanneling distribution along the crystal length was not truly exponential (because $L < L_D$), and L_D should be considered as ‘local’. For the higher values of n_D the dechanneling over the 3-cm-long crystal was exponential, and the corresponding length L_D was well defined. The influence of the dislocations starts to be seen for $n_D \geq 30 \text{ cm}^{-2}$ at 450 GeV, and for $n_D \geq 3 \text{ cm}^{-2}$ at 7 TeV. For much higher densities the defect dechanneling dominates, and L_D is well described by the formula

$$L_D = 1/n_D \sigma_{\text{eff}} . \quad (2.114)$$

The effective dechanneling cross section σ_{eff} , obtained from the fit of the simulation results, is equal to 19 μm at 450 GeV and 72 μm at 7 TeV. As it

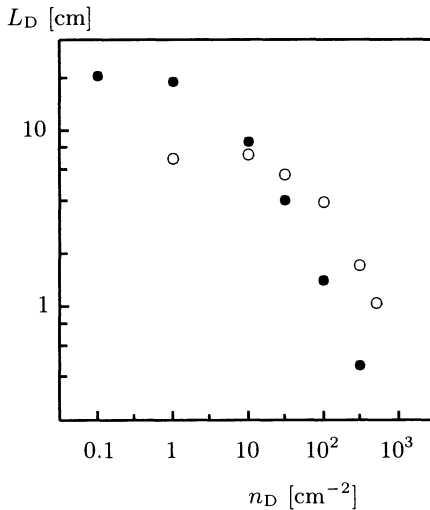


Fig. 2.22. The dechanneling length in the 3-cm long Si(110) crystal bent with $pv/R = 1$ GeV/cm, as a function of the dislocation density. For 450 GeV (o) and 7 TeV (●).

includes all the possible contributions from the single and multiple collisions with dislocations in the crystal bulk, σ_{eff} may be somewhat higher than the average (edge and screw) σ_D (52 μm for 7 TeV) computed from Fig. 2.21 for single interactions.

The results in Fig. 2.22 are given for $pv/R = 1$ GeV/cm. However, when the simulation for $n_D = 100 \text{ cm}^{-2}$ at 7 TeV is repeated with $pv/R = 0.2, 0.5, 1, 2, 3 \text{ GeV/cm}$, only a minor effect of the global curvature on L_D (which was 1.69, 1.70, 1.50, 1.24, 1.14 cm, respectively) was observed; of course, the number of the initially-trapped particles was very different in each case.

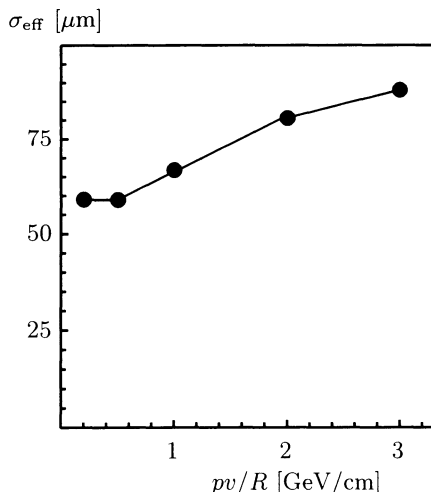


Fig. 2.23. The effective dechanneling cross section as a function of pv/R , for 7-TeV protons channeled in a long Si(110) crystal.

The dependence of the effective dechanneling cross section on pv/R is shown in Fig. 2.23, for 7-TeV protons channeled in the long Si(110) crystal. The qualitative explanation for the fact that the dependence is weak (found also for a single collision) may be as follows. The net local curvature is the sum of $1/R$ and of the dislocation contribution $\partial^2 u / \partial z^2$. The sign of the latter varies in the vicinity of dislocation. Therefore, the $1/R$ term may either enhance or cancel the contribution of $\partial^2 u / \partial z^2$, making a rather small effect on average [92].

2.5.4 Radiation Damage

An important consideration in accelerator applications is the resistance of crystals to radiation damage [92, 97]. Although the damage itself is practically independent of energy in the $>$ GeV range [see (2.115) below], the effect of it on the crystal channeling may be a strong function of the energy. The behavior of this function is determined by the kind and size of the accumulated defects. For this reason the study of the defects produced in irradiated crystals would be interesting. From the theory one sees that the defects produced are more dangerous if they are ordered in an extended pattern. The resistance to radiation damage must be scaled as E in the case of point-like defects or small dislocation loops, as $1/\sqrt{E}$ in the case of linear dislocations, and as $1/E$ in the case of mosaicity.

However, it seems unlikely that interstitials or vacancies (produced initially) may organize themselves in any extended patterns. For point-like defects, an elementary estimate of the resistance to radiation damage may be given. Let ϵ_d be the minimal energy transfer required for a displacement of the lattice atom. The corresponding momentum transfer is $q = \sqrt{2Am_p\epsilon_d}$, with Am_p being the mass of the atom. The cross section for knocking the atom from the lattice site is given by a formula similar to (2.83):

$$\sigma_{\text{def}} = \frac{2\pi Z_i^2 Z^2 e^4}{m_p A \epsilon_D v^2} . \quad (2.115)$$

As v^2 approaches c^2 for a relativistic particle, the value of (2.115) saturates. We do not take into account cascade effects. On the other hand, we do not take into account the probability of recombination of the produced interstitial-vacancy pair. Both effects may be important. For a relativistic proton in Si, σ_{def} is of the order of 10^{-23} cm^2 . The maximal allowable fluence F_{max} of protons per cm^2 is then $F_{\text{max}} = n_a / \sigma_{\text{def}}$, where n_a is the allowable relative density of interstitials. As mentioned earlier, the dechanneling on interstitials is comparable to the electronic one at $n_a \approx 0.01$. This corresponds to F_{max} of the order of 10^{21} protons per cm^2 in Si. Above 1 TeV, even the electronic dechanneling is negligible; therefore the practical threshold for F_{max} should become higher with energy.

Notice the factor Z_i^2 in (2.115). The number of atoms knocked from the lattice sites is very much increased for heavy ions. For example, in the case

of fully ionized ions of Pb, this is a factor of 6700. Independently of what the final structure of the produced defects is (amorphous clusters, dislocation loops or lines, etc.), Z_i^2 is the overall factor in the production rate of defects. Therefore, the crystal resistance to radiation damage is decreased by $1/Z_i^2$ for heavy-ion beams [92]. However, the typical beam intensity at accelerators is lower for heavy ions than for protons. For instance, at the 7-TeV Large Hadron Collider under construction at CERN (Geneva) the heavy ion (lead) option implies an intensity nearly a factor of $\simeq 6000$ lower than the intensity for the proton option.

At this time, the highest irradiation achieved in bent crystals with high-GeV beams is of the order of 10^{19} protons per cm^2 , with no substantial degradation of channeling properties observed. In the experiment described in [98] this value was achieved with 70-GeV rapidly-extracted beam and a 13-mrad bent Si crystal, where the crystal also experienced large dynamic and heating shocks (see Chap. 3). Studies of the crystals irradiated to 4×10^{20} [99] at 28 GeV, and to 2.4×10^{20} [101] at 450 GeV protons per cm^2 are in progress.

2.5.5 Conclusion

The theory of channeling in imperfect crystals has the same well-known foundations as those for the theory of particle motion in a perfect bent crystal. The theoretical predictions have been confirmed experimentally wherever it was possible. However, a principal problem is the precise measurement of the crystal imperfections. Ideally, one needs to know separately the densities and characteristics of all kinds of defects present in crystals. But normally a detailed measurement procedure destroys the crystal, in order to study its bulk. An accurate measurement of the imperfection-induced dechanneling at the highest energy in a crystal with a well-known structure would be very useful, especially in comparison with simulations.

The lattice of modern silicon crystals seems to be so near to perfect that they probably do not need this theory at all. Long Si crystals with a purity of < 1 dislocation per cm^2 are available for high-energy bending experiments [93]; this purity would be sufficient for channeling even over 20 TeV. One of the best experimental reference points is provided by the experiments [105] with the H8 beam at CERN. The measured bending efficiency of nearly 50% is in excellent agreement with the theory and implies that the contribution of any defects to dechanneling was considerably less than 10%. For the only dangerous lattice defect, linear dislocation, this contribution may grow not faster than \sqrt{E} ; that is, at the ~ 7 -TeV Large Hadron Collider of CERN their contribution would be (much) less than 40% in the same crystal (possibly sizable but not crucial) [92]. Note that from the above theory the purity of this crystal should have been $n_D < 30 / \text{cm}^2$. Nevertheless the theory is indispensable for the application of crystals of heavier materials, such as

tungsten; high- Z crystals are attractive because of their stronger fields, but have a poor-quality lattice at present [12].

The influence on channeling of the microscopic defects in the crystal lattice was discussed. For practical applications, the macroscopic distortions of a crystal body are also important, induced by the processes of cutting and bending the crystal. The experimental studies of these spatial and angular distortions are discussed in Chap. 3.

3. Experimental Studies of High-Energy Channeling and Bending Phenomena in Crystals

3.1 Introduction

In the preceding chapters we have outlined the classic theory of high-energy particle channeling in straight and bent crystals, making use of the continuum potentials introduced by Lindhard, which facilitate the consideration substantially.

The process of particle dechanneling was described within the framework of diffusion theory, and on the basis of computer simulation using the CATCH code. Much attention was given to the influence of the crystal defects on the dechanneling length.

This chapter is devoted to the experimental investigations at high-energy accelerators, which aim to check the foundations of channeling theory. The experimental techniques are discussed in detail, and the results obtained are thoroughly analyzed. The experimental data are compared with theory, and satisfactory agreement is found.

3.2 Crystals and Bending Devices

For bending beams of high-energy particles, the crystals are usually cut in the shape of right-angled slab, with the big faces parallel to the major crystallographic planes (110) or (111). The crystals are about 1 to 10 cm long, up to ~ 3 cm high and ~ 0.1 cm wide.

For efficient bending of high-energy particle beams one must ensure a high quality of alignment and machining of the monocrystal slab faces. In experiments performed with extracted beams the crystals should have an efficiently working layer with a width close to the total width of the crystal. This is achieved when the slab orientation is accurate to ~ 1 arc minute, and the nonparallelity and nonflatness of side faces is accurate to $\sim 10 \mu\text{m}$ over the total length of crystal. The depth of the disrupted crystal layer after polishing of the faces should be at the same level. These constraints are met, in principle, with the present technology.

In the planned applications of crystals at TeV accelerators, in particular for beam extraction for superconducting colliders, the demands for quality

of alignment and the machining of the faces of a crystal are more stringent. The impact parameter of beam particles at a crystal in the LHC accelerator would be a fraction of $1 \mu\text{m}$ [121], which may require new methods of control and machining the crystal surfaces. With an increase in the bent-particle energy to the TeV range, the demands on the quality of crystal material become more demanding. The crystal mosaicity should not exceed $\sim 1 \mu\text{rad}$, as defined by the critical angle of channeling.

According to a ‘rule of thumb’, a silicon slab of thickness H may be elastically bent over a cylinder of radius R provided that $R > 1000 \times H$. At the same time, for efficient bending of the beams an optimal bending radius R_{opt} exists, equivalent to several critical radii $\sim (3 \text{ to } 5) \times R_c$ for considerable angles of bending. For silicon $R_c/m = 0.0018 \times E/\text{GeV}$. Therefore, this strength criterion leads to limitation of the slab thickness used $H/\text{mm} \leq 0.007 \times E/\text{GeV}$. So, in the case of bending of 70 GeV particles, the optimal bending is performed by a slab of thickness $H \leq 0.5 \text{ mm}$. But for the TeV accelerators under construction the slab thickness may be some 10 mm, which is much bigger than the typical beam size, as a rule.

Crystal bending over a given surface is in general not a simple task. In the past bent crystals were widely used for focusing x-rays and gamma rays in the crystal-diffraction devices for the needs of nuclear spectroscopy. To solve this problem two general approaches have been used [122]: (1) bending with the use of cylindrical mirrors, (2) the method of bending moments.

In the first method the slab is placed between a convex and a concave mirror, and is bent by pressing the mirrors together. Here the bending shape is defined by the convex mirror; the concave one is used for the uniform pressing, and can be replaced with local supports. To vary the bending radius one must change the mirror surface. A simpler method is to apply bending moments at the slab edges with use of metal pins.

The elastic bending of a monocrystal slab in the ideal cases of the method of moments and cylinder mirrors was considered in [123] in the framework of the theory of elasticity of anisotropic solids. It was found that the slab not only is bent longitudinally, but it is also twisted transversally, taking the shape of a saddle, barrel, or, as a special case, a pure cylinder, depending on the concrete anisotropic properties of the material. The surface equation for the slab is

$$y = \frac{1}{2R}z^2 - kx^2 ,$$

where y is the sagitta, x and z are the longitudinal and transversal coordinates (see Fig. 3.1), and k is a coefficient dependent on the concrete anisotropic properties of the material. For $k > 0$ this is the equation of a hyperbolical paraboloid (‘saddle’), $k < 0$ gives the equation of an elliptical paraboloid (‘barrel’), and $k = 0$ is for a parabolic cylinder. In reality the crystal holder may cause extra moments and lead to a more complicated shape of bending, in particular near the slab edges.

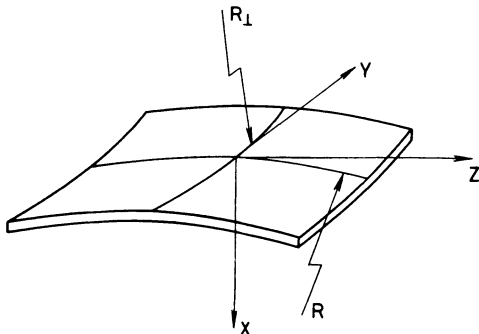


Fig. 3.1. The shape of a bent monocrystal slab.

In experiments performed with the bending of high-energy particle beams, various versions of the above methods are applied. Figure 3.2 shows a widely used device [98, 110, 120] based on a metal mirror, which is called the ‘bridge’ in the literature (see [124]). In this design the central part of a crystal is free of matter in order to minimize the particle loss. A crystal is clamped to the bent metal surface with the elastic spring fastenings which diminish mechanical stresses arising during interaction of an intense beam with a crystal. With this device a quasi-constant radius of bending is ensured.

Figure 3.3 shows several variants of the method of moments. Three-point bending (a) is featured with a variable curvature $R(l) = L^2/2\Theta l$, L being the distance between the end and center pins, l the coordinate along the crystal, Θ the total angle of bending along L . (For simplicity, we do not take into account a transverse bending of the slab. A detailed analysis of the slab curvature for a three-point bending can be found in [125]). Four-point bending (b) ensures a constant radius between the middle pins. The loaded console method (c) is similar to the three-point bending scheme between the end and center pins. The method of moments is simple, but it causes

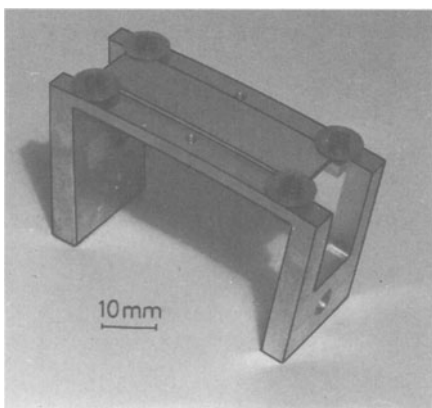


Fig. 3.2. A crystal-bending device based on a metal mirror.

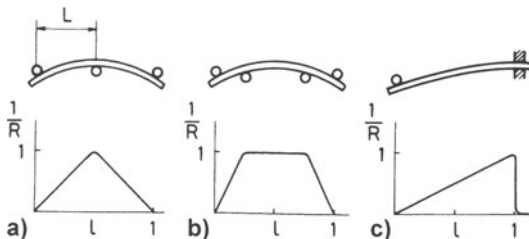


Fig. 3.3a–c. Schemes for bending devices based on different variants of the method of moments. The corresponding curvature graphics are presented. (a) Three-point bending; (b) four-point bending; (c) a loaded console.

local deformations of the crystal under the pins and an additional loss of the particles being deflected.

The requirements on bent crystals used for particle deflection are different from those used for the focusing gamma rays. This difference is connected to the directions of particle trajectories: the gamma rays traverse the slab normally to the big faces whereas charged particles move parallel to them. Therefore the requirements for the stability of the bending radius along the longitudinal coordinate, as a rule, are not too severe (an accuracy of $\Delta R/R \sim 1\%$ is sufficient). However, there arise some specific requirements at the edges of bent slabs. One must keep the total bending angle Θ within the angular acceptance of the existing magnet-optics lines for particle transportation, where the beams should be bent to. Usually this value is $\Delta\Theta \simeq 0.1$ mrad. Such an accuracy may be controlled by a laser beam reflected from the crystal as it is translated on the micrometer table (it is the simplest method as shown in Fig. 3.4). More precise methods for controlling the bending quality are based on the application of special optical devices: autocollimators and laser interferometers. As experience has shown, a big problem is to avoid nonuniformities in the bending over the transversal coordinate $\Delta\Theta_{\perp}$, which is called ‘anticlastic bending’ in the literature. Various defects in slab bending are shown in Fig. 3.5a–c where nuclear photoemulsions are used to show bent beams downstream from the crystal.

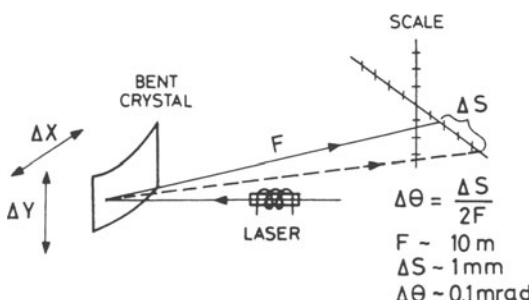


Fig. 3.4. The simplest method for quality control of the bending.

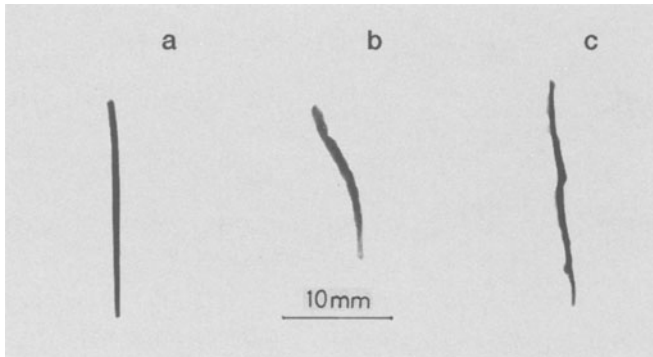


Fig. 3.5a–c. Demonstration of bending defects via nuclear emulsion layers placed a few meters downstream from the crystal. (a) Slow twist, nonuniform bending of $\sim 100 \mu\text{rad}$; (b) large twist, nonuniform bending of $\sim 1 \text{ mrad}$; (c) complicated nonuniform bending due to a local pressure of metal mirrors.

In nondemanding applications, such as in splitting an extracted beam with a crystal, one may have the same accuracy $\Delta\Theta_{\perp} \simeq 0.1 \text{ mrad}$, which as a rule is smaller than divergence of incident beam ($\sim 1 \text{ mrad}$). To extract a beam from big accelerator-colliders or to study the efficiency of particle capture into a channeling mode this accuracy is insufficient, and should be defined by the critical angle of channeling. In this case the crystal edges have to be left unbent. Alternatively, one could test the bending quality by laser interferometry, and correct the surface of the bending mirrors. A successful way to eliminate the twist effects is reported in [100], where planar faces of the crystal were ensured by making use of a U-shaped crystal slab (see details in Chap. 4).

3.3 General Experimental Methods

Channeling experiments have been started at low, MeV, energies. Various methods have been developed in these experiments [5]. The peculiarities of GeV-energy experiments on channeling are due to applications of large-size crystals, high resolution detectors, and counting technique for particle registration.

Charged particles with GeV and multi-GeV energies may pass over large distances in crystals, both in channeling and in nonchanneling modes. This circumstance requires special methods for identification of each channeling particle.

In a straight crystal, where nonchanneled particles make up the background, a channeled particle may be identified using the phenomenon of anomalously low ionization losses ($\sim 60\%$ in comparison with disoriented particle losses). As mentioned earlier this property of channeled particles is

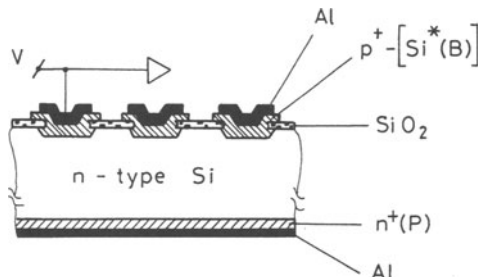


Fig. 3.6. Cross section of E-761 implanted detectors.

due to the lower electron density inside the interplanar channel. Ionization losses may be measured by semiconductor detectors. As the perfect crystals are also semiconductors, one may incorporate into the crystal target a surface barrier detector, by means of impurity implantation. For dynamic investigation of the channeling process several built-in detectors along the crystal may be used. This way one can follow the 'history' of each particle captured into the channeling mode.

As an example, the cross section of solid-state detectors used in [125] is shown in Fig. 3.6. The p-n junction was produced by boron diffusion from a boron-doped, poly-silicon layer $\text{Si}^*(\text{B})$. The n^+ layer was made by phosphorus implantation on the reverse side with an implantation energy of 110 keV and a fluence of 3.0×10^{15} particles per cm^2 . An aluminium layer with a thickness of about $1 \mu\text{m}$ was evaporated in vacuum on both sides for the contacts.

In working with bent crystals, however, the situation is quite different. The particles captured into the channeling mode are deflected at considerable angles and peak sharply at the bending angle of crystal, whereas the nonchanneled particles do not change the direction of motion. Downstream of the crystal both fractions of the beam are spatially separate. In this case the channeled particles may be identified as the component of the signal sensitive to the crystal alignment. When the crystalline planes have an optimal orientation with respect to the incident beam, the count at the detector sharply increases.

The peculiarity of channeling experiments is that the angles of incidence must be determined with an accuracy comparable to that of the critical angle. This requirement is met by using spatially separated coordinate detectors. An alternative approach is to use a beam with a small angular divergence. A very low divergence, $\sim 3 \mu\text{rad}$, has been achieved in experiments at CERN [102] on a special beam line H8 (so called 'microbeam'). In the Protvino experiments [76] a beam with a small divergence (a few critical angles) was formed by a bent crystal placed some distance upstream of the crystal target for the channeling experiment.

Using the two techniques mentioned above (energy-loss measurement, or feedback from the angular dependence of the signal at the detector), the alignment of the crystal target with respect to the beam is achieved. The

characteristics of exiting particles are measured with high-resolution detectors. For these purposes drift chambers with $\sim 100 \mu\text{m}$ resolution and large aperture are frequently used. However, microstrip detectors can increase the resolution by about one order of magnitude. With such detectors, detailed investigations of different kinds of imperfections due to the manufacturing and bending of the crystal become feasible. For investigations of the crystal surface imperfections, nuclear emulsions are sometimes used, which provide the best spatial resolution, $\sim 1 \mu\text{m}$, but demand much time for emulsion developing and analysis.

A necessary part of an experimental setup is a goniometer to rotate the crystal with respect to the beam. To align the crystal one needs an angular translation comparable to the critical angle of channeling (a few microradians in the GeV energy range). However, as a rule, only a limited range of angular displacement, $\sim 10 \text{ mrad}$, is needed in channeling experiments and therefore the goniometer design may be very simple. One well-known design is one of a compact device containing a lever moved by a micrometer screw coaxial with a stepping motor. Depending on the lever size and micrometer screw step, an angular step of $8\text{--}30 \mu\text{rad}$ was achieved in the first bent-crystal applications at JINR and IHEP. A similar design (see Fig. 3.7) was used at CERN [108], with an angular step of $4 \mu\text{rad}$. For applications at TeV energies a step size below one microradian is needed. It is not expected that this will be a difficult requirement to fulfill.

To avoid a long search of the channeling phenomena an accurate initial crystal alignment is important. This procedure is performed usually by reflecting a laser beam from the crystal surface, or more precisely by applying the autocollimation method. A typical accuracy of $\sim 1 \text{ arc minute}$ is sufficient.

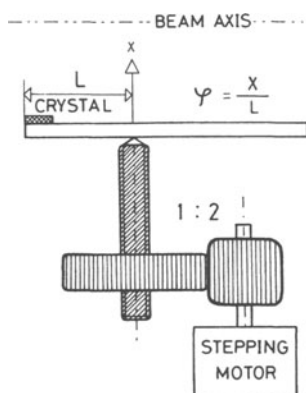


Fig. 3.7. Scheme of the goniometer device for SPS crystal extraction.

3.4 Deflection Efficiency Measurements

The first experiment on the deflection of a beam of charged particles with a bent single crystal was performed in 1979 in Dubna by the group lead by E.N. Tsyganov in collaboration with US colleagues [57]. A proton beam with an energy of 8.4 GeV was deflected at various angles ranging up to 25.7 mrad. Several Si crystals were used, oriented at (111), and with length of 20 mm and different thicknesses. The crystals were bent by the three-point scheme with the use of steel pins. In the entry part of the crystal a semiconductor detector was built in to measure the ionization losses. The fraction of bent protons amounted to $\sim 1\%$ of all particles that passed through the crystal. This result confirmed the basic theoretical ideas [56]. Subsequent experiments on high-energy particle bending were carried out at large accelerator centers CERN, FNAL, IHEP [32, 68, 120].

In the applications discussed so far the crystal efficiency was limited by a low ratio of the critical angle θ_c to the beam typical divergence. This limitation was overcome in a series of experiments at CERN with a highly parallel ‘microbeam’ of 450-GeV protons [55, 102, 103, 105]. These studies have made a breakthrough, bringing the beam bending efficiency to record values: 10 % in the first experiment [102], and then up to $\sim 50\%$ in the recent work [105]. The results directly confirm the theoretical predictions.

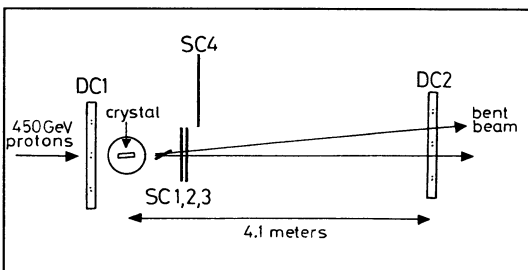


Fig. 3.8. The experimental set-up on the H8 beam.

Figure 3.8 shows the experiment performed with the extracted beam of the 450-GeV protons on the H8 beam line. The bent crystal was mounted on a goniometer turntable for horizontal rotation with steps of $1.7 \mu\text{rad}$, and was located near the drift chamber DC1 used to define the incident beam hitting the crystal. A second drift chamber, DC2, measured the position of the particles at a distance of 4.1 m downstream of the crystal. The $15 \times 15 \text{ cm}^2$ drift chambers had two (X and Y) planes each equipped with three pairs of double sense wires to resolve ambiguities, interspaced by 50 mm.

The trigger was formed with three scintillation counters (SC1, 2, and 3) in coincidence. Anticoincidence with a counter (veto) SC4 was used to reduce the background of nuclear interactions in the crystal and bending device.

The silicon crystal, 50 mm long, 10 mm high and 0.9 mm thick, was cut parallel to the (111) planes. It was bent with a classic three-point scheme and deflected the beam in the horizontal plane. The crystal had 10-mm-long straight parts at both ends. The bend was varied with a thumbscrew. The surface barrier detector was built-in in the straight part at the crystal entry, making it possible to measure the dE/dz of the incident protons. The protons channeled in the wide (111) planes have energy losses of ~ 0.6 times that of the random particles. Therefore, dE/dz spectra from the detector allowed to align the crystal with respect to the beam, and, moreover, to tune the beam divergence. See further discussion in Sect. 3.5.

It was noticed in [105] that tuning the beam with the use of feedback from the peak of low energy loss is easier than with any other method. Figure 3.9 shows the intensity of particles with low energy loss as a function of the angle of the (111) planes. A measured FWHM of $17 \mu\text{rad}$ for this scan agrees well with $2\theta_c = 18 \mu\text{rad}$. The very steep sides of the scan indicate that the beam divergence in the horizontal plane was less than $3 \mu\text{rad}$.

The measurements were carried out with several bending angles. A typical horizontal profile of the bent beam at DC2 is shown in Fig. 3.10 for a bending angle of 2.4 mrad . The bent fraction was $\simeq 50\%$ of all incident particles. Approximately 35% of the particles were unbent, and 15% were lost due to dechanneling. Detailed studies of dechanneling have shown that the losses occur mostly near the middle pin, which is typical for this kind of bending

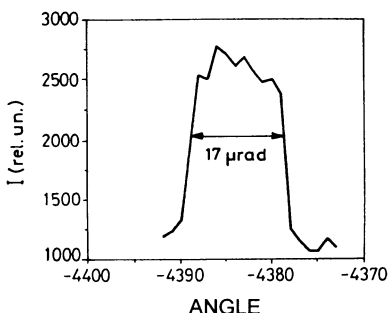


Fig. 3.9. Intensity of low-energy-loss particles as a function of angle to the (111) plane.

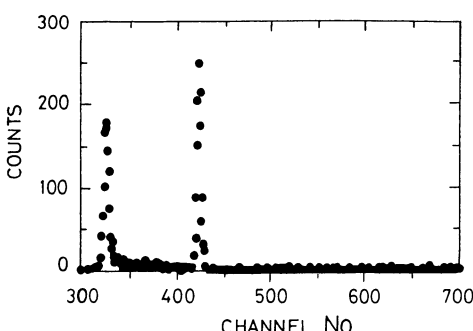


Fig. 3.10. Horizontal beam profile as seen in the downstream driftchamber DC2 for a deflection angle of 2.4 mrad . Undeflected (in ch. 320) and deflected beams are clearly visible, the latter containing about 50% of all protons hitting the crystal.

device. From the analysis of the ionization loss spectra the contribution of the narrow (111) planes was estimated to be $\sim 5\%$ for small bending angles. The measured bending efficiency is shown in Fig. 3.11 as a function of the bending angle in the range from 1 to 11 mrad; the squares are for Si(111) [105], the open dots are for Si(110) [103]. Only statistical errors are shown. The systematic errors caused by mechanical and other instabilities may be estimated from the scattering of the points in the figure. Notice that the experiment is sensitive to variations in the angle of incidence of the beam of $\sim 1 \mu\text{rad}$.

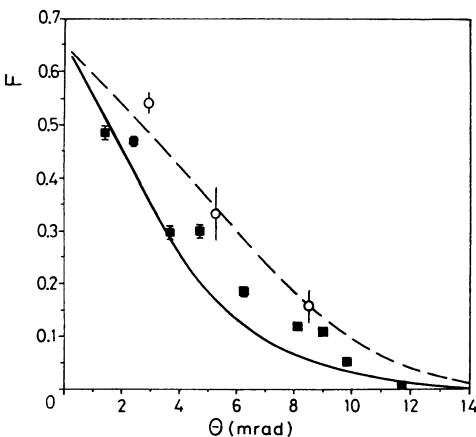


Fig. 3.11. The measured bending efficiency as a function of the bending angle (the squares are for Si(111), the open dots are for Si(110)) and the theoretical estimates for uniform curvature (dashed line) and an ideal 3-point bender (solid line).

The experimental results have been compared in [105] with the theoretical [61, 65] predictions. Figure 3.11 shows two theoretical curves for the efficiency: for uniform bending of the crystal (the dashed line), and for the ‘ideal’ three-point bending scheme (solid). The experimental points for Si(111) are found between these extreme models. The Monte Carlo simulation of this experiment is discussed below.

3.4.1 Simulation of Bending Experiments

One of the most detailed comparisons of the measured bending efficiencies with the theoretical predictions was performed in the course of the RD22 experiment at CERN’s H8 beam line. Both the crystal and the bending device were copies of those used later in the SPS extraction experiment [108] (see Chap. 4). The experimental set up was that shown in Fig. 3.8, with a few modifications. The complete report of the measurements and simulations may be found in [103], with some details given in [104, 107].

The beam of 450 GeV protons was bent by a silicon (110) deflector which was 30 mm long, 10 mm wide and 1 mm thick. The device allowed the bending angle to be changed with a screw. The study of the beam transmission by

the crystal was made with three different bending angles (8.5, 5.7, and 3.0 mrad). Detailed spatial and angular scans were done over the crystal face to investigate the channeling characteristics.

The incident beam was not tuned to the perfection reported in [102, 105]. From a study of an angular scan of the crystal transmission for a small spot (50 to 300 μm) selected at the entry face, the beam rms divergence was measured to be $16.0 \pm 2.1 \mu\text{rad}$, which may be compared to $\theta_c \approx 7 \mu\text{rad}$ in this case.

The peak efficiency values found in the angular scans were 7.7 ± 0.3 , 10 ± 1 , and 20 ± 2 % for bending angles of 8.5, 5.7, and 3.0 mrad respectively. As bending is possible only for particles in the $\pm \theta_c$ angular range, it is useful to determine the bending efficiency for these incident particles only. From the angular scans of efficiency, and by assuming $\theta_c = 7 \mu\text{rad}$, the following bending efficiencies for the incident angular range of $\pm \theta_c$ were measured (Fig. 3.11): 16 ± 3 , 33 ± 5 , and 54 ± 2 % for the bending of 8.5, 5.7, and 3.0 mrad respectively; the errors shown represent only the run-to-run spread of efficiency.

The simulation made by CATCH [36] took into account the variable longitudinal curvature of the crystal as measured with a laser for a bending of 8.5 mrad. For the other two bending angles the curvature was taken to be constant. In other respects the crystal was assumed to be perfect. The efficiencies found in the experiment and simulation are listed in the Table 3.1. The lower part of the table shows the efficiencies found for the particles incident in the $\pm 7 \mu\text{rad}$ angular range. The Table also shows the analytical estimates from (2.20), made for the uniform curvature in harmonic approximation.

Table 3.1. The efficiencies of the deflection of a 450 GeV proton beam with a Si(110) crystal. The bottom numbers show the efficiency for protons incident in the $\pm \theta_c$ range. The errors given are statistical only.

		Bending angle [mrad]		
		3.0	5.7	8.5
Efficiency (%)	Experiment	20 ± 2	10 ± 1	7.7 ± 0.3
	Simulation (rms = $15 \mu\text{rad}$)	20.9 ± 0.8	15.2 ± 0.5	8.8 ± 0.5
Efficiency (%) in $\pm \theta_c$ range	Experiment	54 ± 2	33 ± 5	16 ± 3
	Simulation	56 ± 4	39 ± 2	26 ± 2
	(2.20)	43	34	25

3.4.2 Conclusion

The good agreement between high-energy crystal channeling experiments and the theory indicates a good understanding of the feed-in and feed-out mechanisms for a high-energy beam channeled in a bent perfect crystal. The confidence achieved allows reliable predictions for use in a broad range of the current and future applications. Bent crystals could become a routine instrument for the optics of particle beams. Further work is needed along two directions: for a full understanding of crystal performance in the extraction mode at an accelerator (see Chap. 4), and for a better understanding of the influence of crystal lattice imperfections on the high-energy channeling (see Chap. 2).

3.5 Energy Loss in Bent Crystals

We have qualitatively discussed in Sect. 1.5 the energy-loss spectra of relativistic particles in aligned crystals. Because of the abnormally low energy losses shown by channeled protons, the technique of dE/dz detectors built-in in crystals has found wide application in the high-energy channeling experiments. Besides the obvious use for selection purposes, the dE/dz studies are of immediate interest as they give information about the distribution of the incident particles in aligned crystals, the distribution of atomic electrons in crystals, and the particle-electron interactions.

Energy-loss investigations become particularly informative if a substantial fraction of the incident particles are trapped in the channeling mode. Very interesting possibilities are opened with the use of bent crystals, as this allows to select the bent particles and to vary the selection criterion by varying the crystal bending. Such experimental investigations have been performed recently by the Aarhus-CERN group [105] who made use of a highly parallel beam of 450 GeV protons on the H8 beam line of CERN-SPS. In this section we follow this work in order to discuss the ΔE spectra of the channeled particles.

As the divergence of the H8 beam, less than $\pm 3 \mu\text{rad}$, is substantially lower than θ_c ($\simeq 9 \mu\text{rad}$ for the wide-spaced Si(111) planes), the trapping efficiency was quite high, of order 65%, with the bending efficiency reaching values of up to $\sim 50\%$ (see Sect. 3.4). By selecting the bent protons, one selects in fact the particles with transverse energies lower than some critical value $E_c(pv/R_{\min})$ defined by the minimal radius R_{\min} of the crystal curvature. The crystal bending (in the 3-point scheme) and other details of the experiment are discussed in Sect. 3.4 in relation to the high efficiency achieved in this work. The broad range of the crystal bending angles used, from 1 to 11 mrad, allowed the particles with E_T ranging from $< 12 \text{ eV}$ to $< 1-2 \text{ eV}$ to be sampled and studied.

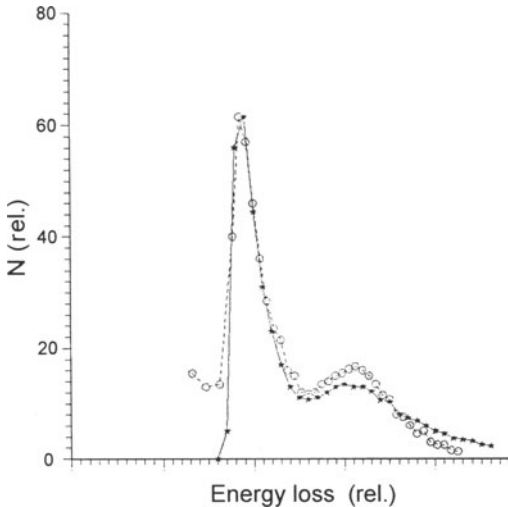


Fig. 3.12. Energy-loss spectrum in the front part of the aligned crystal for all incident particles (open circles are experimental points, stars are simulation).

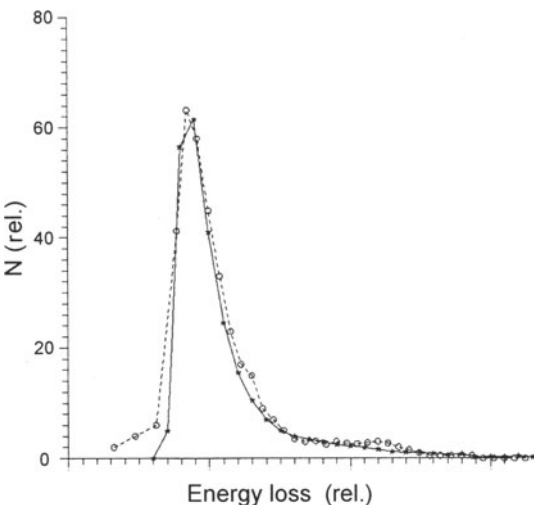


Fig. 3.13. Energy-loss spectrum in the front part for particles deflected by 2.4 mrad (open circles are experimental points, stars are simulation).

The most probable energy loss ΔE_p for the best channelled particles was measured to be $0.55 \times \Delta E_p$ at random incidence. As ΔE_p is somewhat dependent on E_T , the parameter to use to characterize the energy loss for the best channelled particles was found to be the energy loss at half maximum $\Delta E_{1/2}$ at the low energy-loss-side of the spectrum. The experiment found good quantitative agreement between the experimental ΔE and the theory by Esbensen and Golovchenko [39] for the path-dependent energy losses [see (1.54)].

Further comparison of the experimental spectra with theory requires a simulation of the particle distribution in a bent crystal and its evolution with

the depth. Such a simulation was performed with CATCH and is reported in [106], using the theory of [39] as an input. The electron density used in the simulation was calculated from the Moli  re potential. An ideal 3-point bending of the crystal was assumed. Here the experimental findings of [105] are compared with the theoretical expectations.

Figure 3.12 shows the energy-loss spectrum in the front straight part of the aligned crystal for all incident particles. Upon selection of the particles that were bent by 2.4 mrad, the spectrum takes the form shown in Fig. 3.13.

In the simulation one can also select particles with a given E_T value. One objective of the simulation was to explore how far these two ways of selection correlate. Figure 3.14 shows the spectrum for the bent particles superimposed on the spectra obtained for the particles with transverse energies less than (a) 12 eV, (b) 10 eV, and (c) 2 eV selected directly at the ΔE detector. There is very good agreement in part (a) between the two spectra. In part (b) some difference appears already, due to a slight difference in sampling the E_T values. Notice the difference of spectra in part (c), where the particles with lowest transverse energies, < 2 eV, were selected. Note also the trend the spectra show from (a) to (c), which corresponds to the selection of particles with lower E_T . In simulations the spectra were studied for the selection of particles with E_T below some threshold, which was varied from 12 eV to 2 eV. It was found that $\Delta E_{1/2}$ (low-side loss) was stable. At the same time the spread of the loss strongly decreased, down to the factor of ~ 0.5 [part (c)] for the lowest E_T values. These conclusions agree well with the experimental observations.

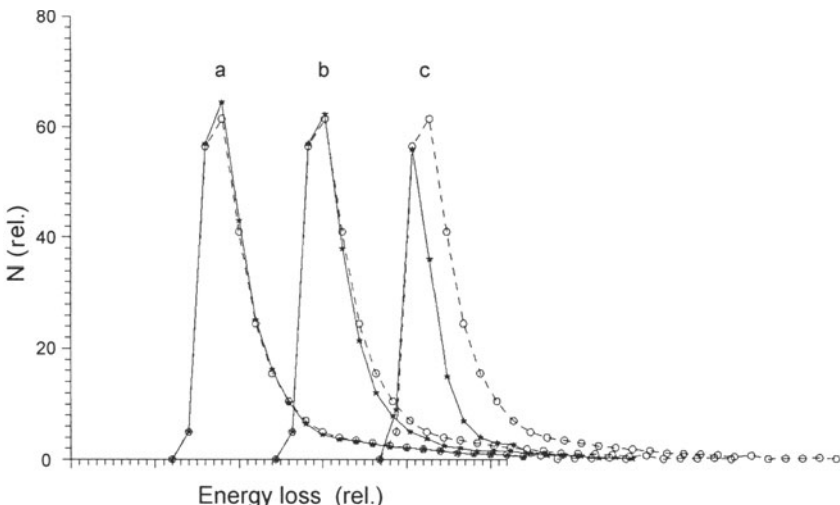


Fig. 3.14. The dashed line is the energy-loss spectrum for particles deflected by 2.4 mrad. The solid line is the spectrum for particles with E_T less than (a) 12 eV, (b) 10 eV, and (c) 2 eV selected directly in detector.

The experimental spectra, ΔE , for bent particles at small bending angles (< 4 mrad) show a sizable shoulder at higher ΔE . The shoulder was interpreted in [105] as the contribution from the narrow (111) planes, which cause an energy loss slightly above that for the amorphous substance [39]. It was possible, for the first time, to decompose the spectrum into the two distributions – for wide (111) planes and for narrow ones [105]. The ratio $\Delta E_{1/2}(\text{wide})/\Delta E_{1/2}(\text{narrow})$ was measured to be 0.52. This is in good agreement with the theoretical value of 0.54 [39].

Figure 3.15 shows the energy loss simulated for the particles channeled in narrow planes. The two spectra were obtained in two ways: (a) by direct selection of the particles channeled in narrow planes at ΔE detector, (b) by selection of those bent particles that exit the crystal from the narrow planes. The two spectra are in good agreement, thus justifying the experimental procedure for selection of the bent particles. The small left peak appearing in the second case is interpreted as due to feeding from the wide planes, since the position of this peak is perfectly that expected for wide planes. The loss spread for the narrow planes is much bigger because of a higher electron density leading to a large contribution from close collisions.

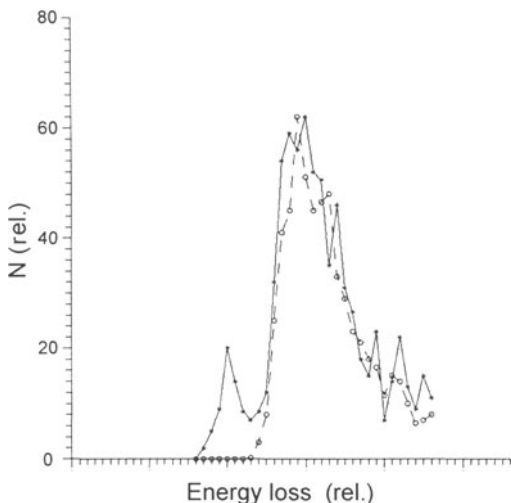


Fig. 3.15. Energy-loss spectrum simulated for particles channeled in narrow planes. The solid line is for particles bent by 2.4 mrad. The dashed line is for particles selected in the ΔE detector directly.

The bending efficiencies from simulation [106] agree well with the measured values. In case of 2.4 mrad bending the peak efficiency was found to be 51.9%. About 32 % particles leave the crystal undeflected ($\Theta < 0.1$ mrad); the remaining 16% particles have exit angles between the bent and unbent peaks. The experimental values are 50%, 35%, and 15% respectively.

In the simulation, 3.2% of the bent particles were found to be channeled in the narrow planes. In the experiment this fraction was measured as 5%. Also, in the simulation no distinct shoulder was observed in the energy-loss

spectrum for bent particles, as opposed to the case in the experiment. Notice nevertheless that the ΔE peak for the narrow planes is found in the correct position. Some underestimate of the narrow-planes efficiency in the simulation might be caused by (1) the fact that simulation used 3-point bending whereas the real curvature was more uniform [105] (narrow planes are more sensitive to bending), (2) the feed-out rate for narrow planes is much stronger (Sect. 1.4), so even a small inaccuracy in the calculation is much amplified over a long crystal.

3.6 Dechanneling Investigation

At high energies the dechanneling processes have been studied mainly in bent crystals. The method of measurement was proposed in the first works at JINR, CERN and FNAL [32, 57, 68]. The channeled particles were tagged at the crystal entrance with energy-loss detectors. From the angular distributions of the deflected particles reconstructed by the drift chambers, the path of the channeled particles in a crystal was determined. To do this, one should know the precise shape of the crystal bending. In the first works a three-point scheme of bending (see Fig. 3.3) was applied. Local spill of the particles near the middle pin allowed the bending dechanneling to be estimated. To measure ordinary dechanneling, the part of the crystal between the central and backward pins, which had a decreasing curvature, was used and the bending dechanneling was excluded. However, as shown in Sect. 2.2.5, the gradient effects may strongly affect the measured L_D value.

3.6.1 Fermilab Experiment

Dechanneling has been studied comprehensively in the Fermilab experiment [18], where the particle feed-out rate in the Si(110) crystal (bent with a radius of ≈ 80 cm) was measured as a function of the beam momentum in the range 60 to 200 GeV/c at two different crystal temperatures, 293 K and 128 K. Figure 3.16 shows the scheme of the experimental set up.

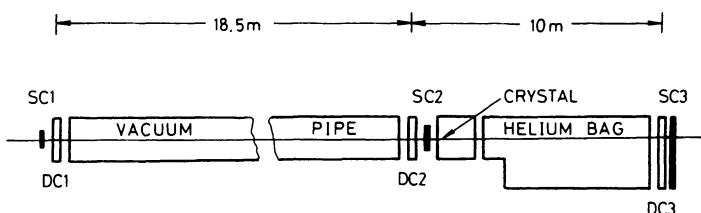


Fig. 3.16. Plan view of the experimental apparatus.

To monitor the beam, counters SC1, SC2, and two-coordinate drift chambers DC1 and DC2 were used 18.5 m apart. At the exit a similar chamber

DC3 and the counter SC3 were placed 10 m downstream of the crystal. The middle scintillator SC2 had a rectangular hole 1 mm wide and 5 mm high, and was used in anticoincidence. Scintillators and a semiconductor detector in the front part of crystal formed the trigger for the drift chambers. The goniometer rotated the crystal with the steps of 8.7 μ rads.

The silicon crystal, 43 mm long with the orientation (110), was coated with a thin $\sim 10 \mu\text{m}$ layer of ZnO along 26 mm of its length. The residual stresses caused a convex uniform circular bend on the side of the crystal to which the ZnO was applied. This original method gave a crystal bending angle of 32.5 mrad at room temperature and 30.9 mrad at 128 K. A number of particles were found to be dechanneled while entering the bend ('bending dechanneling'), and along the uniformly bent part of crystal ('ordinary dechanneling').

The crystal was 11 mm high and 0.72 mm thick. It was made of high-quality 50-kOhm-cm n-type silicon. The faces were parallel to the (110) planes with an accuracy of ≤ 1.7 mrad. An energy-loss detector was fabricated at each end of the crystal by implanting $\sim 10^{15}/\text{cm}^2$ B on one side and $\sim 10^{15}/\text{cm}^2$ P directly opposite (over an area of $3 \times 8 \text{ mm}^2$).

The (110) planes were aligned by small increments of the angle and corresponding observation of the ionization-loss spectrum in the front detector.

The measurements with the deflected beam were made at six values of the particle momenta, 60, 80, 100, 120, 150, and 200 GeV/c, both at room temperature and for the crystal cooled down to -145°C . In each case up to 100 000 events have been detected. With information from the drift chambers the angular distributions of the particles that traversed the crystal were reconstructed. Figure 3.17 shows the distributions in the angle Θ .

In this figure the intensity as a function of (similar spectra were obtained at -145°C). The spectra show two peaks corresponding to unbent particles and those bent at the full angle. The flattened curve corresponds to dechanneled particles. The unbent peak is defined mostly by the process of bending dechanneling. The distribution within $\simeq 2$ mrad to $\simeq 30$ mrad is due to the ordinary dechanneling caused by multiple scattering.

Figure 3.18 shows $I(\Theta)$ for the particles bent at an angle greater or equal to Θ for 150 GeV/c. [$I(\Theta)$ is obtained by summing the particles in each 0.5 mrad interval.]

The results demonstrate the exponential behavior of dechanneling at room temperature and for the cooled crystal. An exponential fit to the data determines the dechanneling length L_D . The fit results for all the measurements are listed in Table 3.2 (and plotted in later in Fig. 3.22).

The observed decrease in L_D with increased momentum is due to the increase in the centrifugal force pv/R , and is in good agreement with the theoretical model discussed in Sect. 2.2.2 (see Fig. 2.4). The temperature dependence of L_D is also satisfactory (Sect. 2.2.4 and Fig. 2.8).

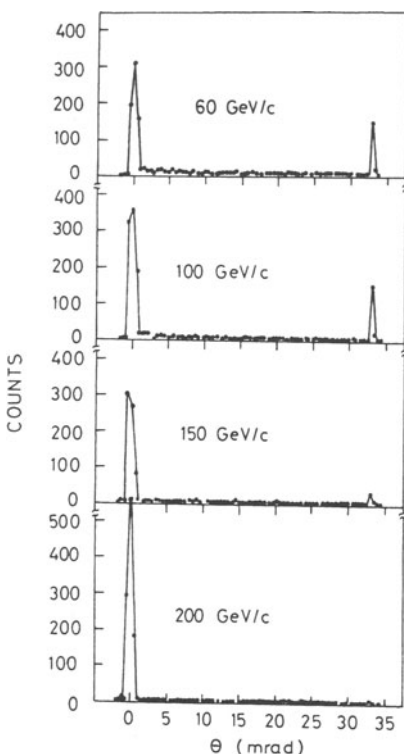


Fig. 3.17. Emergent particle distributions in the bent direction of the crystal at room temperature.

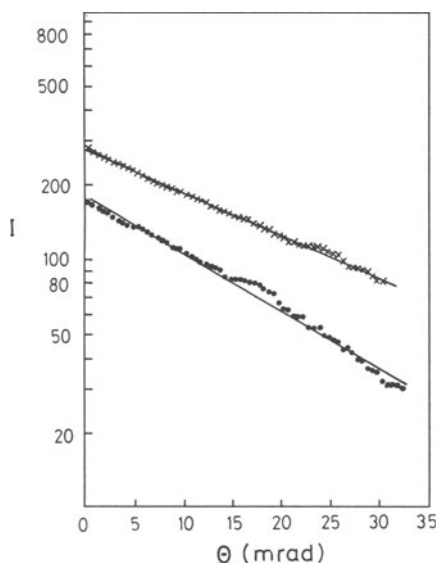


Fig. 3.18. The number of particles channeled as a function of bend angle. The top two curves are for simulation, and the bottom ones are for measurement. The dependences are for the crystal at room temperature (●) and cooled (x).

Table 3.2. The dechanneling lengths in bent silicon monocrystal.

p [GeV/c]	L_D [mm] (room temp.)	L_D [mm] (cooled)
60	19.9 ± 0.4	22.6 ± 0.6
80	22.3 ± 0.6	28.8 ± 0.4
100	22.6 ± 0.6	27.8 ± 0.7
120	20.4 ± 0.6	26.9 ± 0.8
150	14.7 ± 0.4	20.8 ± 0.6
200	10.5 ± 0.4	18.1 ± 0.8

As mentioned above, the unbent peak in Fig. 3.17 is mainly due to bending dechanneling. If one denotes the number of particles in the peak as N_1 , the total number of the particles as N , the particles lost due to ordinary dechanneling between the energy-loss detector and the bend as N_2 , then the fraction of particles that experience the bending dechanneling is equal to $F = (N_1 - N_2)/(N - N_2)$. This fraction is plotted in Fig. 3.19, along with the theoretical curves [61]. The best agreement is found if the critical coordinate is chosen as $x_c = d_p/2 - 2.5u_T$ (see also Sect. 2.2.4).

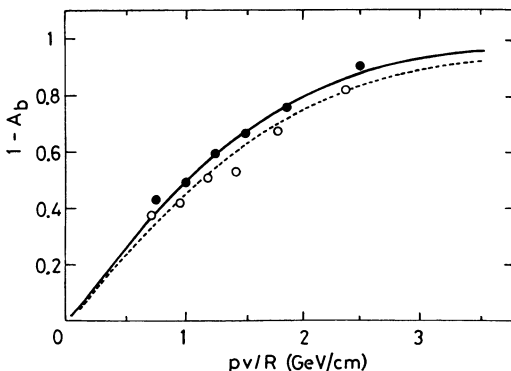


Fig. 3.19. The dechanneled fraction, F , as a function of the momentum parameter, $p v / R$, for the crystal at room temperature (solid line) and cooled (dashed line).

3.6.2 Protvino Experiment

Recently, another method based on the phenomenon of particle volume capture into the channeling mode ('feed-in') was used in IHEP work [27] to measure 70-GeV proton dechanneling lengths in silicon crystals with (111) and (110) orientations. The dechanneling of the particles volume-captured into the stable state was investigated in detail. The authors used the experimental scheme described in Sect. 3.8.

The silicon crystals were cut out of the same material (ingots of dislocation-free n-type silicon, 45 mm in diameter, produced by the Zaporozhsky titanium-magnesium plant to have a specific resistance of ~ 20 kOhm cm), and were

bent to follow a constant radius $R = 3.0$ m over the length of $L_0 = 60$ mm. The deviation of the radius from the mean value did not exceed 1%. The accuracy in the orientation of the side faces of the plates (0.5 mm thick) was not worse than $1'$ (0.3 mrad).

A 70-GeV proton beam with an angular divergence of $\Phi = 0.1$ mrad was directed in turn at the crystals. The efficiency of the particle deflection as a function of the angle of rotation of the crystal was measured experimentally. (Only particles coming from the back face of the crystal were observed, those dechanneled in the bent part of the crystal were not detected.) When the crystal is optimally oriented, end-face capturing is observed. Rotating the crystal towards its bend by an angle φ larger than the incident beam divergence, the authors created the conditions for particles to be tangential to the crystallographic planes in the crystal depth, i.e., the conditions for volume capturing.

As the crystal curvature is constant, the same number of particles, $Iw(R) = \text{const}$, are volume captured into the channeling mode; in this equation I is the intensity of the beam hitting the crystal, and $w(R)$ is the probability of volume capture. However, the path l of channeled particles from the capture point (as the volume-capturing region is localized within a small length of $R\Phi = 0.3$ mm, it may be considered as a point) to the crystal back face decreases linearly if the angle of rotation φ increases (see Fig. 3.20):

$$l(\varphi) = L_0 - R\varphi. \quad (3.1)$$

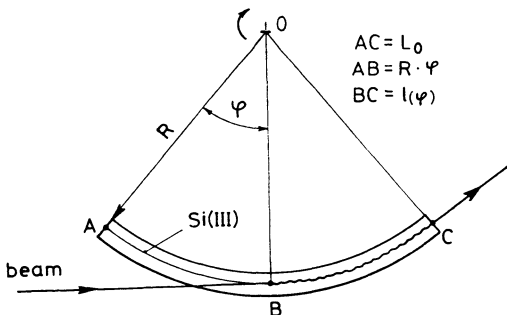


Fig. 3.20. Scheme showing how the proton beam was directed onto the crystals. Point B shows the region of volume capturing. The distance between points B and C is the path of the channeled particles, which decreases linearly as the angle φ increases.

By detecting the number of particles $N(\varphi) = IwX_D(l(\varphi))$, deflected by the crystal, one can determine the $X_D(l)$ law, according to which the particles leave the channeling mode. In analysing the measurements it is useful to introduce the angle Θ and to consider the dependence $N(\Theta) = N(\Theta_0 - \varphi)$, where $\Theta_0 = L_0/R$ is the crystal bending angle.

Figures 2.12 and 2.13 show the experimental dependences $N(\Theta)$ for each crystal. During the measurements the angle Θ was varied within the limits: $6 \text{ mrad} < \Theta < 18 \text{ mrad}$. For angles $\Theta \approx 20 \text{ mrad}$ distortions, caused by the end-face capturing of a beam fraction could occur. For small deflecting

angles, $\Theta < 6$ mrad, the background of protons, not channelled but deflected due to elastic scattering, grew rapidly. The critical angle θ_c of channeling in silicon is of the order of $20 \mu\text{rad}$ at 70 GeV energy.

Figures 2.12 and 2.13 show that the functions $N(\Theta)$ are governed by an exponential law. Substituting the value of the angle Θ for the path length l , one can establish that

$$X_D(l) = \exp(-l/L) \quad (3.2)$$

where

$$L^{(111)} = (52 \pm 2) \text{ mm}, \quad L^{(110)} = (37 \pm 5) \text{ mm},$$

are the measured dechanneling lengths.

The dechanneling length in bent crystals decreases as the curvature increases. To compare this data with other data it is convenient to use the ‘reduced’ dechanneling length L_D corresponding to an unbent crystal. According to the theory described in Sect. 2.2, the centrifugal force $pv/R = 70 \text{ GeV}/3 \text{ m}$ results in a ratio $L/L_D = 0.86$, and the ‘reduced’ dechanneling lengths are:

$$L_D^{(111)} = (61 \pm 2) \text{ mm}, \quad L_D^{(110)} = (42 \pm 5) \text{ mm}.$$

In the case of $E = 70 \text{ GeV}$, the diffusion model (1.50) gives the value $L_D^{(111)} = 53.5 \text{ mm}$ in Si(111) and $L_D^{(110)} = 43.7 \text{ mm}$ in Si(110), providing a satisfactory agreement with the experimental data. Calculated functions (1.50) together with the experimental data from JINR [57], CERN [32], IHEP [27] and FNAL [50] for Si(110) and Si(111) channels are given in Fig. 3.21.

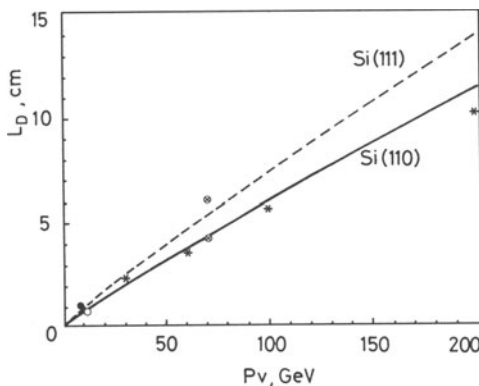


Fig. 3.21. Calculated functions L_D in Si(110) and Si(111) channels together with the experimental data: • JINR; ○ CERN; ★ FNAL; ⓧ IHEP (the data for the (111) plane are presented only by JINR and IHEP).

Note that in the Protvino experiment the particles were deflected by a crystal of length $L_0 \geq L_D$. From the analysis of Sect. 1.4 and the exponential behaviour observed, we may conclude that the ‘relaxation condition’ was fulfilled. Therefore, the measured dechanneling length must be equal to L_D , measured under the conditions of ordinary end-face capture.

According to (1.50) the ratio $L_D^{(111)}/L_D^{(110)}$ should be of the order of $d_p^{(111)}/d_p^{(110)} = 1.23$ for silicon. The experimental ratio is 1.4 ± 0.2 .

3.6.3 Dechanneling Simulations

Simulation of the Fermilab Experiment. The Monte Carlo simulation of the FNAL experiment on bent-crystal dechanneling [18, 36] followed the experimental procedure exactly. The incoming beam had a divergence larger than θ_c . The procedure included the selection of the particles with lower energy loss shown in the initial straight part of the crystal. The angular distribution of the selected particles at the exit was integrated from a variable Θ to the full bend angle and then fitted with an exponent. Because of the uniform curvature, this angular distribution is easily converted into the exponent-like dependence of the fraction of the channeled beam as a function of z , $\sim \exp(-z/L_D)$. The characteristic constant L_D is the dechanneling length.

Examples of the integrated angular distribution, together with the exponential fits, are shown in Fig. 3.18 in comparison with the experimental data. The dependences both in this simulation and in the experimental measurements [18] are very close to exponents, thus making L_D a well-defined quantity. The corresponding dechanneling lengths are plotted in Fig. 3.22, together with the experimental values. The simulation gives a reasonable approximation to the measured data, overestimating L_D by $\sim 10\%$. The simulated temperature dependence of L_D for a bent crystal is stronger than for an unbent one, in accord with the measurements. The interpretation of these dependences in the analytical model $L_D \sim E_c$ is discussed in Sect. 2.2. A simulation of this experiment in a diffusion approach and without selection of the particles by energy loss is given in [34].

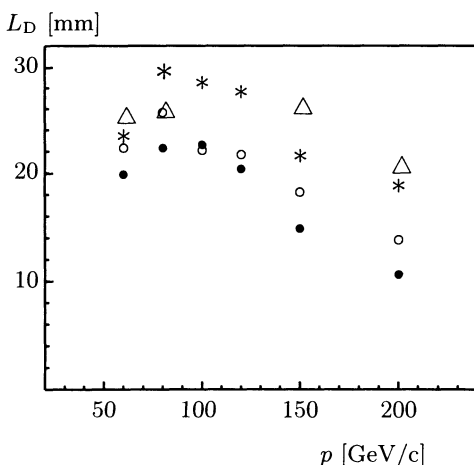


Fig. 3.22. The L_D values from the experiment by Forster et al. (\bullet , $*$) and simulation (\circ , \triangle). The \bullet and \circ are for 293 K, the $*$ and \triangle are for 128 K.

The bending dechanneling factors were determined in the same experiment by measuring the ratio N_1/N , where N is the number of particles selected by a low energy loss, and N_1 is the fraction that exits the crystal undeflected. The same procedure repeated in the simulation gave the N_1/N values close, within 10%, to the measured ones.

Simulation of the Protvino Experiment. In [27] results from investigation into the feed-in and feed-out processes in bent crystals are reported for the experiments with a 70-GeV proton beam, and a detailed Monte Carlo simulation. Through the studies of crystal transmission of the trapped (fed-in) protons, the dechanneling length for such particles was determined for silicon crystals with (110) and (111) orientations. The procedure was different from that of [18], with no selection of energy loss.

For this energy range the feed-in probability is quite low (fraction of 1%). The distribution of the trapped particles is unusual, being peaked at the top of the potential well. This case is a challenge for simulations, making the comparison with experiments very interesting.

The qualitative discussion of the results of this simulation was given in Chap. 2. The dechanneling in both the experiment and simulation was exponent-like in the angular range studied (see Figs. 2.12 and 2.13). For the bending radius of 3 m and the energy of 70 GeV, the following dechanneling lengths were obtained:

$$L_{\text{sim}}^{(110)} = 39 \pm 3 \text{ mm}, \quad L_{\text{sim}}^{(111)} = 40 \pm 4 \text{ mm}.$$

The simulation results are close to the experimental ones, although the difference between those for the (111) and (110) planes is not statistically significant. The feed-in probabilities are discussed in Sect. 3.8.

3.7 Dynamic Equilibrium

As discussed in Sect. 2.3, the reversibility rule (2.46) leads to the interesting physical phenomenon called dynamic equilibrium. In the state of dynamic equilibrium the phase density of the channeled particles is saturated at a constant level with the crystal depth, because of the balance of the dechanneling and rechanneling processes. At MeV energies this was hard to observe because of the strong dissipation of energy. At GeV energies an experiment demonstrating the dynamic equilibrium is feasible.

The first results for the equivalence of feeding-in and feeding-out were reported for a CERN experiment at 12 GeV [32].

FNAL Experiment. More detailed studies of the processes of rechanneling and dechanneling in a straight crystal were carried out in the experiment [50]. The studies were done with the set up similar to the one described in Sect. 3.6. A secondary beam with the momentum from 30 to 200 GeV/c incident on a Si(110) crystal was used. Three energy-loss detectors were incorporated

into the crystal. The essence of the experiment was the tagging of selected particles with low energy loss as measured by one of the detectors. Using this criterion the fraction of the particles channeled in the other two detectors was determined. The number of the channeled particles in the gated spectrum was calculated from the spectrum shape by fitting the two Landau shapes (for channeled and for random particles). A typical fitted gated spectrum is shown in Fig. 3.23.

If the energy-loss window is set in the first detector, at the crystal entrance, such spectra select the process of feed-out. If the window is set in the third detector, then the feed-in process is investigated. The fraction of the channeled particles versus crystal depth was obtained by using the gated spectrum. From the plots the feed-in and feed-out lengths were determined. The results are shown in Fig. 3.24.

Except for 200 GeV, the feed-in lengths are longer than the feed-out lengths. The authors [50] notice that the incident beam had an insignificant angular divergence, as compared to the critical angle, for the dynamic equilibrium to occur. The 35 GeV beam had FWHM divergence of $10\theta_c$, and the 200 GeV one had $16\theta_c$.

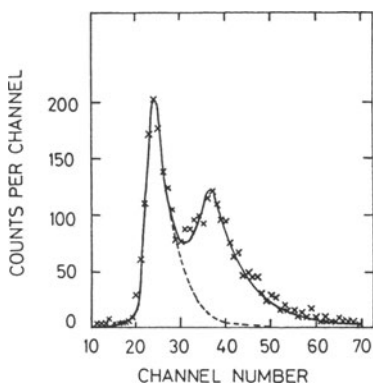


Fig. 3.23. Energy-loss spectrum in detector 3 for an energy-loss window on channelled particles in detector 1. The crosses represent the data and the solid line is the least-square fit to the data. The dashed line represents the high-energy tail of the channelled particle distribution.

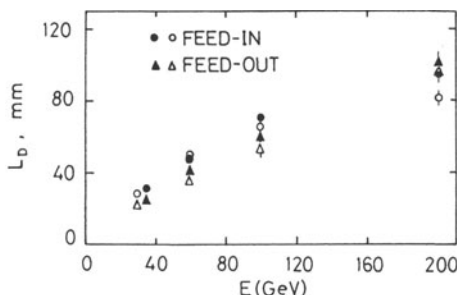


Fig. 3.24. Feed-in and feed-out lengths as a function of energy. The circles are for feed-in data and the triangles for feed-out. The open points are from the first experimental set and the closed points from the second.

We should emphasize that, in order to reach the equilibrium, the beam divergence should also be substantially greater than the angle of multiple scattering of the nonchanneled fraction. This was demonstrated in the IHEP experiment [74], where the consequence of dynamic equilibrium – no decreasing of the number of the channeled particles with the crystal depth – was directly observed.

Protvino Experiment. This experiment for investigating the rechanneling processes in a straight crystal was performed at the IHEP accelerator. An aligned bent single Si crystal was placed in the beam line as a beam deflector, instead of one of the bending magnets.

The crystal was cut along the (111) crystallographic planes. It was bent in a special way, similar to an ice-hockey stick (Fig. 3.25). The total length was 100 mm, with a straight part of $L_1 = 65$ mm; the other part of $L_2 = 35$ mm was bent uniformly with a radius $R = 1.75$ m to an angle of 20 mrad. A 70 GeV proton beam (note, that $\theta_c = 25 \mu\text{rad}$ in this case) was brought to the crystal. The undeflected beam was dumped into an absorber. Only the particles deflected with the crystal by the whole angle (bend angle) could be detected, since the angular acceptance of beam-line was sufficiently small. The particles dechanneled in the bent part of the crystal went to the absorber and could not be detected.

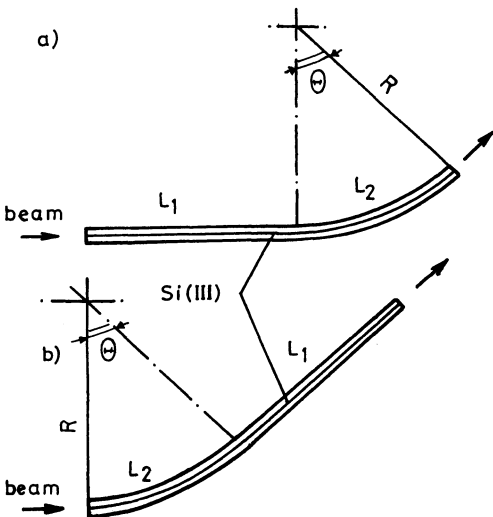


Fig. 3.25a,b. The crystal positions for 2 measurements of the deflected-beam intensity.

The measurement of the number of deflected particles was performed twice. First [case (a)], the beam hit the crystal at the straight part, as shown in Fig. 3.25a. Then [case (b)] the crystal was turned over in vertical plane, so that the particles hit the crystal at its bent part (Fig. 3.25b). In case (b) the presence of the straight part in the crystal was insignificant, because the

particles were already deflected by the crystal and detected independently of their path length in the channeling mode. One should only include a correction for the inefficiency of detection due to the low probability of the nuclear interactions of dechanneled particles (this correction is $\simeq 4\%$). In case (a) the particles, which were above the barrier at the end of the straight part, were not deflected and hence were not detected at all. Measuring the ratio of the deflected particles in these two cases N_a/N_b , one obtaines information on the proton dechanneling and rechanneling processes along the straight path L_1 . The angular divergence of the incident beam could be varied by the magneto-optical system. For the beam with small angular divergence $\Phi = 0.1$ mrad (standard deviation) the ratio $N_a/N_b = 0.72 \pm 0.03$ was measured. For the beam with the angular divergence $\Phi = 0.2$ mrad this ratio was equal to $N_a/N_b = 0.91 \pm 0.05$. For the beam with broad angular divergence $\Phi = 1$ mrad it turns out to be $N_a/N_b = 1.00 \pm 0.05$.

Analysis of Experiment. Two effects may produce the difference $N_a \neq N_b$. As mentioned, the particles that were dechanneled along the straight path in case (b), nevertheless hit the detector, but in case (a) they were lost. For this reason we should have:

$$\frac{N_a}{N_b} = \exp\left(-\frac{L_1}{L_{\text{eff}}}\right). \quad (3.3)$$

Another reason is a possible difference between the bent channel acceptances, $A_a \neq A_b$ due to different distributions of particles over the transverse energy E_T at the initial part of the crystal and at its depth L_1 . Since particles with a high E_T are predominantly dechanneled, at the crystal depth L_1 most of particles occupy relatively lower levels of E_T . In our case that means that after travelling along L_1 a relatively smaller fraction of the particles will be lost at the bend ($A_a \geq A_b$). Taking into account both effects, we obtain:

$$\frac{N_a}{N_b} = \exp\left(-\frac{L_1}{L_{\text{eff}}}\right) \frac{A_a}{A_b}. \quad (3.4)$$

In case (b) for a uniform angular distribution of particles incident on the crystal, the calculation gives $A_b = 0.76$. In case (a) A_a depends on the particles' distribution at the crystal depth L_1 , and could be found only by the solution of the corresponding kinetic equation or by simulation. General considerations bound A_a by $0.76 \leq A_a < 1$.

Let us consider the experimental data for the incident beam with divergence of $\Phi = 0.1$ mrad. The ratio $N_a/N_b = 0.72$ corresponds to the dechanneling length $11 \text{ cm} < L_{\text{eff}} \leq 20 \text{ cm}$, (11 cm for $A_a = 1$; 20 cm for $A_a = A_B = 0.76$). This is considerably larger than the value known from experiments with bent crystals $L_D \simeq 6 \text{ cm}$ (this result was described in Sect. 3.6).

This result can be qualitative understood by following the discussion of Sect. 2.3.1. As mentioned, in the experiment we observe the dechanneling with a new *effective* dechanneling length L_{eff} . To evaluate the L_{eff} along a

finite length one should solve (2.46). If the divergence of the incident beam is much greater than θ_c , then the fraction of the channeled particles is small, and hence the function $f_2(z)$ may be considered as known.

After the beam incidence on the crystal entry-face the phase densities of the particles in the channel and outside of it are equal to the phase density of the incident beam, $f_2^0 = f_1^0 = f_0$. Along the straight path $L_1 = 65$ mm the nonchanneled beam divergence increases due to multiple scattering:

$$\Phi_1 = \sqrt{\Phi^2 + \left(\frac{14 \text{ MeV}}{pv}\right)^2 \frac{z}{L_R}}, \quad (3.5)$$

where Φ is the initial divergence of the beam, p is the beam momentum, L_R is the radiation length. Accordingly, the density of particles near the channel f_2 will decrease:

$$\frac{f_2}{f_0} = \left(1 + \left(\frac{14 [\text{MeV}/c]}{p\Phi_0}\right)^2 \frac{z}{L_R}\right)^{-1/2}. \quad (3.6)$$

If we take this into account, the integration of (2.46) gives (see details in [74]) $L_{\text{eff}} = 23$ cm at $\Phi = 0.1$ mrad.

For an initial divergence of $\Phi = 0.2$ mrad the same consideration gives $18 \text{ cm} < L_{\text{eff}} \leq 69 \text{ cm}$ for the experimental dechanneling length, and 66 cm for its theoretical value.

In the case of the beam with broad angular divergence, $\Phi = 1$ mrad (which is substantially larger than the multiple scattering angle), its divergence does not change sizably along the length L_1 , and in the neighborhood channel the equality $f_2 = f_1 = f_0$ holds. That means that no effective dechanneling should occur (dynamic equilibrium state). Theoretical consideration gives $L_{\text{eff}} = \infty$ in this case.

The important consequence of this is the conservation of the initial E_T distribution in or in the neighborhood of the channel. The diffusion flux is proportional to the diffusion coefficient multiplied by the gradient of the distribution function: $D(E_T)(\partial f / \partial E_T)$. If it is negative (dechanneling), then $\partial f / \partial E_T < 0$ (which was mentioned above, in the discussion of $A_a \neq A_b$). If it is zero, as in this case, then $f = \text{const}$. The important result is the equality $A_a = A_b$. The general result is $N_a = N_b$, in excellent agreement with the experiment.

The experimental ratios (N_a/N_b) are shown in Fig. 3.26 in comparison with the theoretical curve, derived with the assumption $A_a = A_b$.

3.8 Volume Capture

In 1982 the authors of [75] discovered the phenomenon of capturing a 1-GeV proton into a channeling mode in the depth of a bent single crystal

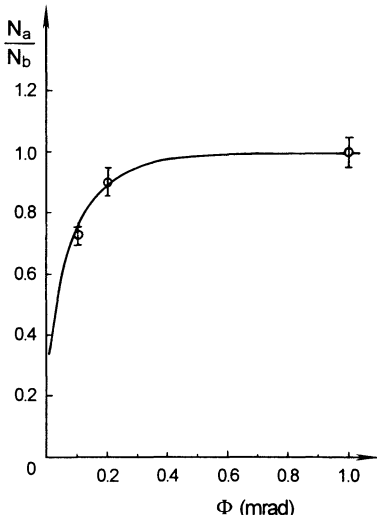


Fig. 3.26. The dependence of N_a/N_b on the angular divergence of the beam incident on the crystal (the curve is theoretical, the points are experimental).

in the region where the particle trajectories are tangential to the crystallographic planes. This new effect was called ‘volume capturing’. A mechanism involving ordinary multiple scattering was proposed to explain volume capturing and is described in Sect. 2.3.1. It was shown that volume capture in a bent single crystal was of the same nature as the known ‘feed-in’ process in a straight crystal. The development of crystal-optic transport systems for particle beams with higher energies stimulated further work on volume capturing, because of the advantages in practical applications as compared to end-face capturing. A detailed account of volume capture is given in [76]. The experiment was carried out in a 70-GeV proton beam line N21 at the IHEP machine. The layout of the equipment is presented in Fig. 3.27.

The goal was to find the dependence of the number of deflected channelled particles on the crystal orientation with respect to the incident beam. When the crystal is rotated towards its concave face by an angle φ , larger than the angular divergence of the incident beam, the conditions are created for the beam to be tangential to the curved crystallographic planes, which means that volume capture is present (Fig. 3.28).

Then the angle of deflection for the channelled particles is equal to $\Theta = \Theta_0 - \varphi$, where $\Theta_0 = 21$ mrad is the angle of bending in the crystal. So that the deflected particles strictly follow the axis of beam line N21 for any angles of crystal rotation φ , the magnet M1 translated the incident beam within the range shown in Fig. 3.27, and the magnet M2 was operated as a corrector, making up for the crystal rotation.

The remote counters S1, S2 were at a distance of about 100 m from the crystal and hence the angular acceptance of the particle detection system was ± 0.5 mrad both vertically and horizontally. Such an angular interval allowed

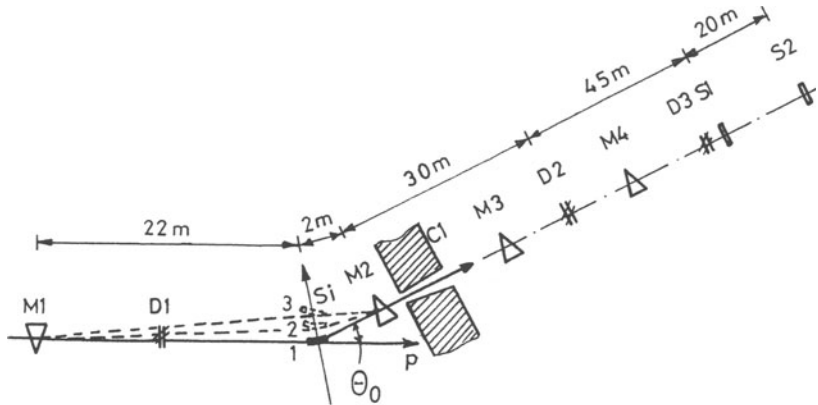


Fig. 3.27. The apparatus layout. M1–M4: bending magnets. Si: bent single crystal, placed in the goniometer. C1: steel collimator. D1, D2, D3: analog proportional chambers. S1, S2: scintillation counters.

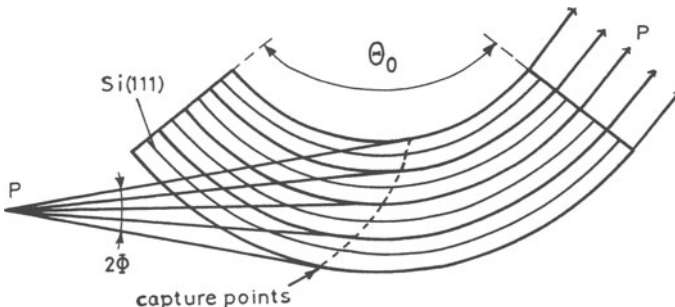


Fig. 3.28. Volume-capture conditions. A particle beam with a divergence of $\Phi < \theta_0/2$ may be captured into the channeling mode. The deflected beam may transform into a parallel one at the crystal output.

losses in the detection of all fully deflected channeled particles. At the same time none of the particles dechanneled in the bent part of the crystal, hit the counters. There was no secondary background owing to the presence of the three magnets. The insignificant background from the protons elastically scattered from the crystal and holder was subtracted as a signal that was crystal-orientation independent.

A plate cut from a dislocation-free silicon of (111) orientation was used as a test crystal. The dimensions of the crystal were $0.5 \times 15 \times 100 \text{ mm}^3$ (thickness, height, length along the beam).

An accuracy of $\Delta\theta = 1'$ (0.3 mrad) was provided in the production of the plate. This accuracy was checked by inverting the crystal with respect to the beam direction by 180° in the vertical plane. The maxima of the deflected particles for end-face capture in both cases coincided on the goniometer scale with an accuracy of about 0.2 mrad. With the angle $\Delta\theta < 1'$ taken into

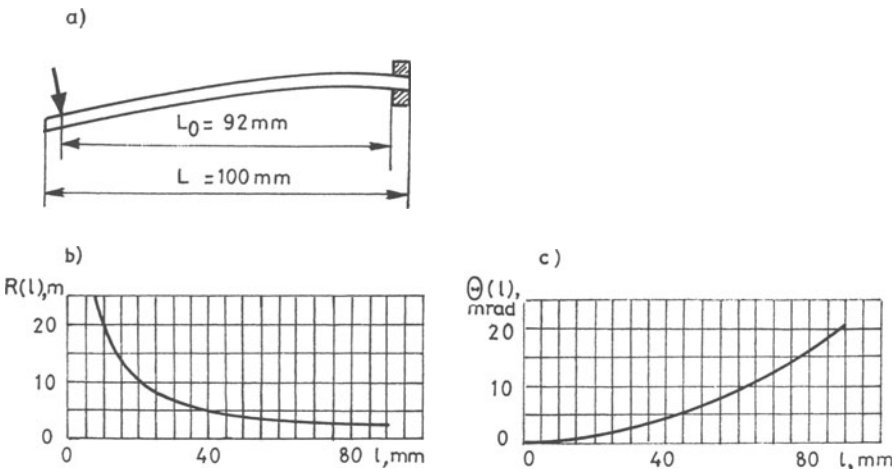


Fig. 3.29. (a) The scheme clarifying the way the crystal is bent. The right end is fixed, the left one is loaded. The dark arrow marks the point where loading is applied. The dependences of the radius of curvature (b) and the angle (c) on the distance from the point of loading.

account, under experimental conditions the particle standard capture through the side faces was 50 times less than for the observed volume capture.

To study the dependence of the probability for volume capture on the radius of curvature of the crystal, the crystal was bent nonuniformly, as shown in Fig. 3.29. One of the crystal ends was fixed between two flat mirrors, and the other one was loaded. In this case the radius of curvature and the angle tangential to the plane varied according to (Figs. 3.29b,c):

$$R(l) = L_0^2 / (2\Theta_0 l), \quad \Theta(l) = \Theta_0(l/L_0)^2, \quad (3.7)$$

where \$l\$ is the distance from the loading, \$L_0 = 92\$ mm is the length of the bent section, and \$\Theta_0 = 21\$ mrad is the total bending angle.

The dependence of the number of deflected particles on the rotation angle was measured twice. First, the beam entered the crystal at the loaded end so that under rotation of the crystal the curvature increased to the point at which the particle trajectory becomes tangential to the planes (we shall call this the case ‘a’). Subsequently the crystal was inverted so that the particles entered the fixed end of the crystal (case ‘b’). In this case, at the point of volume capturing the curvature decreased with the crystal rotation. A plot of the number of deflected particles (in units relative to the maximum) versus the angle of rotation in the cases a and b is presented in Fig. 3.30.

Sharp peaks on the left correspond to the end face capturing the particles into the channeling mode. The peak width was determined by the angular divergence of the incident proton beam. At negative angles \$\varphi\$ (the rotation of the crystal from the bend), a sharp decrease in the number of deflected

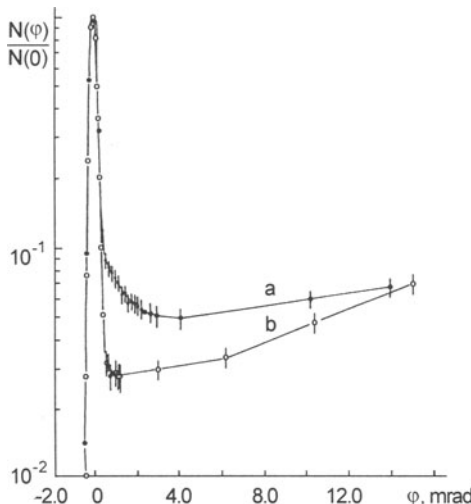


Fig. 3.30. The dependence of the number of deflected particles on the angle of rotation with respect to the direction of the incident beam. Curve a (*solid points*) corresponds to the position of the crystal when the particles arrived at the loaded end of the crystal (left in Fig. 3.29a), the curve b (*open points*) illustrates the situation when the crystal has been overturned (the beam incidence is from the right in Fig. 3.29a).

particles down to zero was observed, which is evidence for the absence of a halo in the incident beam. When the crystal was rotated towards the bend (φ positive) protons were volume-captured into the channeling mode. On the lower curve one can clearly see that at $\varphi \approx 0.5$ mrad there is a boundary between the end-face-captured protons and the volume-captured ones, since in this case the radius of curvature near the end face is quasi-constant (Fig. 3.29b). With increasing φ , the number of detected particles increases, because the probability for volume capture increases due to a larger crystal radius of curvature. Furthermore, the channeled particles travel a smaller distance in the crystal from the point of capture to the exit. The upper curve shows that with the growth of φ the decrease of the deflected proton number is observed near the end face peak, which is due to a sharp reduction of the single crystal radius of curvature. Then because of a shorter distance, covered by the particles when being channeled in the crystal, some increase of the deflected proton number is observed. From the curves A and B one may calculate the capture probability in the channeling mode.

The observed signal is determined by two factors: the capture probability $w(R)$ and the dechanneling losses. Because the shape of the bent crystal is known, (3.7), one can eliminate the dechanneling factor.

The calculated dependence for $w(R)$ is presented in Fig. 3.31. Two different groups of points (open and solid) show the results for the two experimental curves a and b in Fig. 3.30. The solid points correspond to the case when

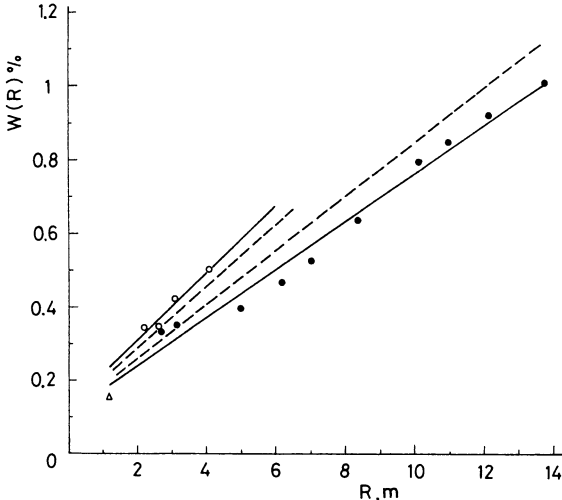


Fig. 3.31. Probability for 70-GeV protons being volume-captured into the channeling mode with a bent Si(111) crystal versus the bending radius. The sets of white and black points stand for the calculated results obtained for two positions of the crystal, with increasing and decreasing curvature. The broken line shows the values for $w(R)$, corrected to take account of the ‘gradient increment’.

channeled particles move in the crystal with an increasing curvature, whereas the open points are for a decreasing curvature.

Each $w(R)$ dependence, defined by different groups of points, is nicely approximated by a straight line when the radius of curvature is much larger than the critical one (for 70 GeV it is ≈ 15 cm). The observed dependence is in perfect agreement with theory, (2.57). Small deviations in the value for $w(R)$ of $\approx 20\%$ observed with an increase in the radius can be explained by gradient capture, as described in Sect. 2.3.2. For these experimental conditions one finds

$$w_B(R) = (\Theta_0 \lambda / L_0^2) R.$$

The dependences $w(R)$, corrected for this effect, are shown in Fig. 3.31 by broken lines.

Feed-in Simulations. The quantitative predictions for the experiments reported in [27, 76] were made by simulations [27], where up to half a million particles were traced in bent crystals of Si(110) and Si(111) by CATCH.

The feed-in probabilities obtained in this simulation, which are defined for the particles captured in ‘stable states’ and which dechannel in accordance with an exponential law, are summarized in Table 3.3. The values predicted by (2.57) are also given. The prediction for the feed-in rates is in good agreement with the experimental data obtained so far.

Volume capture allows one to work without any precise orientation of the crystal and without goniometric devices. The deflection effect is less sensitive

Table 3.3. The probability (in %) of the feed-in into ‘stable states’, for a 70-GeV proton in a Si crystal bent with $R = 3$ m: from experiment, simulation, and (2.57).

Crystal	(2.57)	Simulation	Experiment
Si(111)	0.20	0.17 ± 0.02	0.23
Si(110)	0.22	0.23 ± 0.02	—

to the beam instabilities, variations in the crystal bend, caused by beam heating, do not influence it.

3.9 Influence of Crystal Lattice Imperfections on Beam Deflection

3.9.1 Spatial Lattice Imperfections

As mentioned in Chap. 2, heavy-atom materials are preferable for use in a beam deflection. Experience shows, however, that at high energies the main factor governing the use of crystals is still the quality of the crystal structure. In this respect silicon is the best material. The high quality of this material is supported by the measured dechanneling lengths (Sect. 3.6) and by some of the experimental results on the deflection of beams in long crystals [126].

For example, tests have been carried out on a Si(110) crystal, 150 mm long and bent to an angle of 20 mrad. The fraction of the particles deflected by this crystal agrees with calculations, confirming its high quality.

In these tests a comparison has been made between the deflecting properties of long (up to 100 mm) silicon crystals obtained from different sources. It has been found that the results are reproducible to within 5% from crystal to crystal and this value is equal to the measurement error.

Even silicon slabs produced on a large scale and cut from a large-diameter ingot for the fabrication of microcircuits have good bending properties. One of the experiments was with a (111) slab that was 100 mm in diameter, had n-type conduction, and had a dislocation density not exceeding 100 cm^{-2} . Made into a 30-mm-long deflector, this crystal deflected $90 \pm 5\%$ of the particles that were deflected by a dislocation-free ‘standard’.

As pointed out in Sect. 2.4, dislocations are the greatest hazard at high energies because the dechanneling cross section of the other types of defects either falls or remains constant when the particle energy is increased. Figure 3.32 gives the theoretical curve, from (2.81–2.82), showing the reduction in the dechanneling length of 70 GeV particles with an increase in the dislocation density in a crystal. There is also an experimental point in this figure, which represents the dechanneling length in an imperfect silicon crystal under the assumption that the number of defects in this crystal agrees with the value given by the supplier.

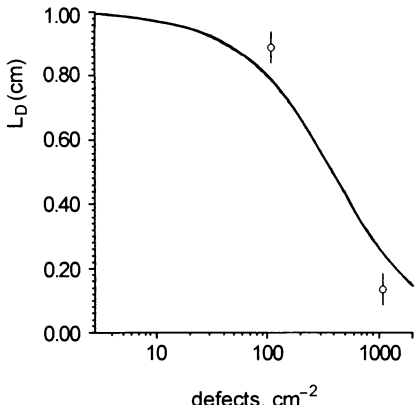


Fig. 3.32. Dechanneling length at 70 GeV as a function of the dislocation density in crystal. The curve is a theoretical model, the points are experimental.

Other materials are much inferior to silicon. Several germanium crystals (produced in Russia for the micro-chip industry) up to 45 mm long have been tested. The nominal dislocation density in the best samples is below 1000 cm^{-2} . A comparison of the fraction of deflected particles with a theoretical prediction, (2.19), has yielded estimates of $L_D \simeq 5 \text{ mm}$ (this point is plotted in Fig. 3.32).

It is worth noticing that there is another method to estimate the dechanneling length in imperfect crystals. As shown in Sect. 2.3.1, for the beams of moderate divergence Φ the efficiency ratio of the volume capture to that for the entry face capture is approximately $N_{vc}/N_{ef} = R\Phi/L_D$. If the beam divergence and the crystal bending radius are known, L_D can be determined from the experimental ratio immediately.

Figure 3.33 shows the orientation dependence of 70 GeV protons deflected by a Ge crystal with bending radius of $R = 3 \text{ m}$. The peak corresponds to entry face capture, the flattened curve corresponds to the volume capture. As one sees from the figure, $L_D \simeq 3 \text{ m} \times 1 \text{ mrad}/0.5 = 6 \text{ mm}$.

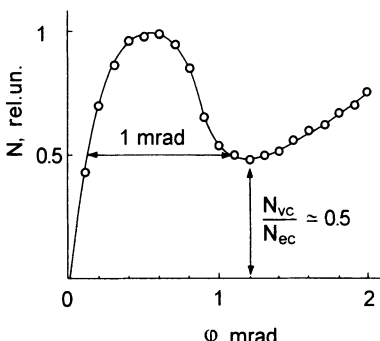


Fig. 3.33. Angular scan of the deflected proton intensity for a Ge crystal.

Two cases were studied in the CATCH simulations of this experiment. First, both edge- and screw-type dislocations were present in Ge crystal with an isotropic angular distribution. With $b = 4 \text{ \AA}$ and $n_D = 1000 \text{ cm}^{-2}$, the dechanneling length over a 3 cm crystal was found to be $(11 \pm 2) \text{ mm}$. In the second case, only edge dislocations were present, all of them aligned normally to the beam. The dechanneling length decreased to 4 mm. In both cases the dependence of the dechanneling cross section σ_D on b was found to be linear. Since no detailed data on the crystal quality were available, one may conclude that an agreement better than a factor of two was observed.

When looking for new materials capable of channeling high-energy particles, one should first investigate the crystal imperfections by alternative methods, prior to experiments on a beam. Most probably, this will not be a search but a synthesis of new crystals with very small imperfections.

The high-energy bending experiments recently started at CERN with high-purity European Ge crystals show promising results [101]. Also very interesting is the Dubna proposal on the possibility of using tungsten crystals [127].

We note that at GeV energies silicon crystals are ideal. This does not however guarantee that the situation at a few TeV will also be favorable. In this regard, it would be useful to study dechanneling at the highest energies available today, about 1 TeV. There, one has to use the long (some tens of centimeters) gently bent crystals, because strong bending of the crystal complicates the data interpretation: it is not easy to distinguish which of the factors, $p v / R$ or dislocations, is predominant.

3.9.2 Surface Imperfections and Edge Effects

Surface imperfections will be added to the volume defects in the machining of the monocrystal slabs from ingots.

Some problems arising in the use of crystals such as particle extraction from large hadron colliders, demand that the crystal has a high-quality near-surface layer.

From measurements with x-ray diffraction it is known that the width of the near-surface amorphous layer in a good polished crystal does not exceed $\sim 1 \mu\text{m}$. However, it is unknown so far, how efficient the channeling of high-energy particles in the layer adjacent to the crystal surface may be.

Preliminary results from the investigations into the influence of the surface imperfections on the deflection of a 70-GeV proton beam deflection are reported in [129]. In this work a direct measurement of the width of the nonchanneling layer has been performed for several crystals of silicon and germanium. A specific kind of mosaicity near the crystal faces was observed, which lead to the angular perturbations of the bent beam in excess of the critical angle of channeling.

The measurements were carried out with a setup similar to the one shown in Fig. 3.27. The crystal alignment was performed by monitoring the depen-

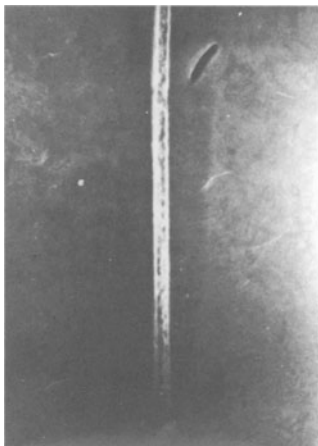


Fig. 3.34. An image of a bent beam split into two parts (the distance from the crystal was ~ 0.5 m).

dence of the signal at the remote scintillation counters on the angular position of the crystal.

A precise measurement of the bent-beam profile was performed by use of a few layers of nuclear photoemulsion placed at different distances downstream of the crystal. The images of the beam on the emulsions were analyzed with a microphotometer, or by direct counting of the particle tracks with a microscope. The grain size (the track width) of the photoemulsion in use amounts to about $\sim 0.5 \mu\text{m}$, which is more than one order better than the resolution of typical coordinate detectors (microstrips and drift chambers).

Several crystals as long as ~ 5 cm and of various thicknesses, from $300 \mu\text{m}$ to 2 mm, were bent to angles of ~ 10 to 20 mrad. The miscut angle of the crystal slabs was less than 1 arc minute. The crystals were bent with a by bending stresses. The incident protons had a divergence of ~ 1 mrad, much greater than the Lindhard angle to assure a uniform illumination of the crystal entrance.

The first crystal, $700 \mu\text{m}$ thick, gave a strange result: the bent beam was split into two parallel parts (Fig. 3.34). By manipulating the variables (changing the bending angle, varying the lengths of the straight ends of the crystal, modifying the shape of the crystal faces) it was discovered that the cause of the angular perturbations was the nonflat shape of the crystal exit face, where the optics specialist had bevelled the edges on each side for his convenience.

The different shapes of a crystal end face (cross section in the plane of beam bending), and a qualitative scheme of the particle's emerging, reconstructed with the use of several emulsions are shown in Fig. 3.35. One sees that the particles experience a focusing effect near the sharp edges at the crystal face. In the case of a semicircular end face (Fig. 3.35d), the whole beam gradually converges to a nondistinct crossover at ~ 2 m downstream

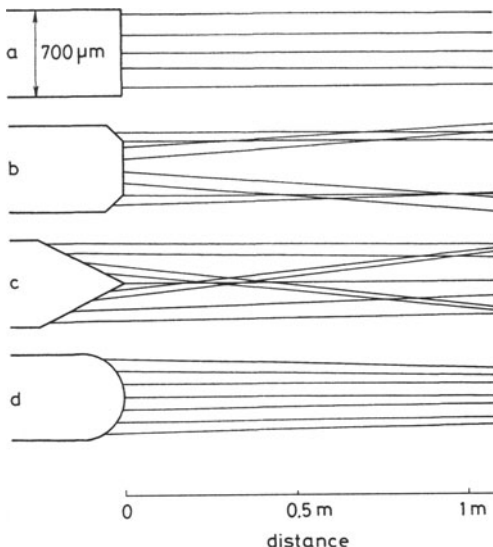


Fig. 3.35a–d. Different shapes of the end faces of crystals (cross section in the plane of beam bending), and a qualitative scheme of the emerging particles. (a) Classic rectangular face; (b) trapeze face; (c) triangular face; (d) semicircular face.

of the crystal. It is possible that shaping the crystal face with some circular form can become another method of beam focusing from parallel to point, in addition to the methods discussed in Chap. 5.

Analysis of beam profiles on emulsions has shown that the sharp bumps on the face cause the 70 GeV beam to be deflected by $\Delta\Theta \sim 1$ mrad. This indicates the presence of lattice distortions at a depth $h \sim (3R_c) \times \Delta\Theta = 50 \text{ cm} \times 1 \text{ mrad} = 0.5 \text{ mm}$. Here we adopt $3R_c$, the bending radius equal to three times the critical one, as the radius at which an efficient channeling is possible (at smaller radii of plane deformation, the particles will be dechanneled and will not give such a correlated picture, as one sees from the figures).

The crystals with ‘classic’ flat faces (Fig. 3.35a) did not show such strong effects. Figure 3.36 shows the evolution of the bent beam profile downstream of the crystals. The data are from emulsions positioned $\sim 15 \text{ cm}$ (bottom profiles) and $\sim 1 \text{ m}$ (top profiles) behind the flat exit faces of the crystals, analysed with a microphotometer. Further analysis of the beam image on the emulsions, by counting the particle tracks under a microscope, has shown that the beam borders are very sharp, $< 10 \mu\text{m}$, and are equal in size to the FWHM of the profiles processed by the microphotometer. From a comparison of the beam images on the nearest emulsion with the crystal thicknesses, it was found that all the crystals tested have a measurable layer in which channeling was not possible (see Table 3.4), which has a width in the range of 40 to 60 μm . (Notice that the lost cross section due to the miscut angle was smaller than $\sim 10 \mu\text{m}$ on each side of crystal.)

The channeled beam in the plane of bending had no appreciable angular distortion as in the case with a nonflat faces, but it was not ideally uniform,

either. At the distance of ~ 1 m from the crystal the beam fragmented into separate zones as wide as $\sim 100 \mu\text{m}$ (see Figs. 3.36 and 3.37a,c,f).

The observed angular distortions $\Delta\Theta \sim 100 \mu\text{rad}$ in this case are due to the lattice deformation at a depth of $h \sim (3R_c) \times (\sim 100 \mu\text{rad}) = 50 \mu\text{m}$ on the crystal end face. The image of the fragmented beam in Figs. 3.37a,c,f strongly reflects the character of the surface defects at the crystal faces. Photographs of these faces under a microscope are shown in Figs. 3.37b,d,g.

The side faces of the crystals were better polished (a surface roughness of $< 0.05 \mu\text{m}$), but also had several cracks as wide as $1 \mu\text{m}$, like those at the end faces. One may suppose that these cracks cause the presence of the $\sim 50\text{-}\mu\text{m}$ inefficient layer observed in the experiment.

We briefly conclude as follows. In the course of the studies three effects were observed:

- A The ‘shape effect’, in which a nonflat end face leads to a strong angular perturbation (much greater than the Lindhard angle) of the beam downstream of the crystal. A convex surface leads to particle focusing, whereas a concave surface leads to defocusing. We emphasize that this effect, observed in bent crystals with long straight ends, is due to just the shape of the end face of a crystal, and does not depend on the crystal bending angle.
- B The effect of beam fragmentation, that is, of local angular perturbations of the beam of order of the critical angle of channeling, which occurs

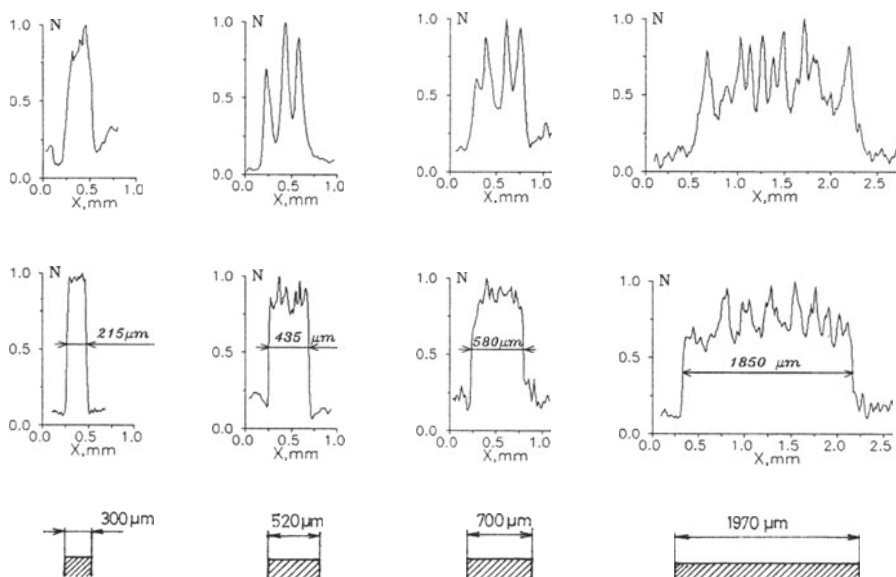


Fig. 3.36. The bent-beam profiles for several crystals with flat end faces at the distances of ~ 15 cm (bottom) and ~ 1 m (top). The bottom part of the figure also shows the corresponding thicknesses of the crystals.

Table 3.4. Characteristics of crystals and the sizes of the bent beams.

Type of crystal	Length [mm]	Thickness [μm]	Beam size [μm]	Inefficient layer [μm]
Si(110)	25	300	215	42
Si(111)	30	520	435	42
Ge(110)	17	600	510	45
Si(111)	47	650	550	50
Si(111)	80	700	580	60
Si(111)	28	1970	1850	60

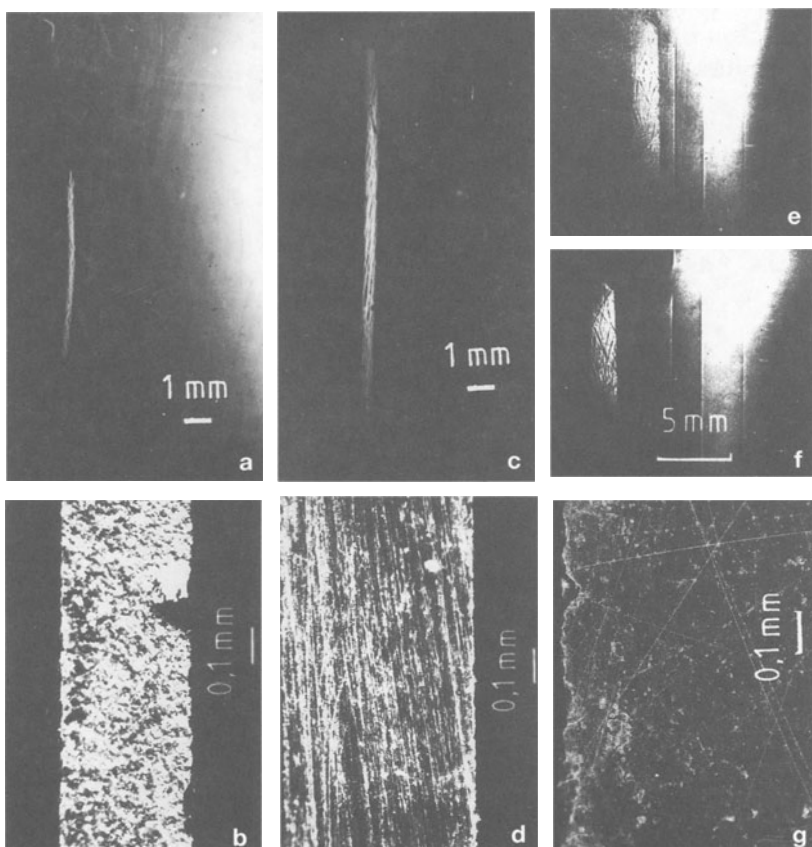


Fig. 3.37. (a,c,f) Images of bent beams at a distance of ~ 1 m. (b,d,g) The photographs of crystals with flat end faces and thickness of 300, 520 and 1970 μm . (e) The beam at ~ 0.5 m.

even at a flat end face if the surface is not adequately polished. Above the background of local angular distortions, no global effects were seen, as opposed to the case with a nonflat face. A violation of the plane parallelity may also be present with a flat end face, as a result of an edge effect. This point requires further study, since it is quite important for bending highly parallel beams (for instance, for beam extraction from supercolliders).

- C The presence of a nonchanneling layer, $50 \mu\text{m}$ thick, near the side faces, defined by the quality of the surface polishing.

Further investigation should show how far the parameters of the bent beams can be improved with better quality surface polishing. In this regard, it would be interesting to compare crystals of different origins. It would also be useful to obtain a detailed quantitative information on the angular distributions of the bent particles by using microstrip detectors.

Beam fragmentation is expected to be barely present at energies of $\sim 1 \text{ TeV}$, because the oscillation period of the channeled particle $\lambda \sim 100 \mu\text{m}$ starts to exceed the depth of the lattice deformation at a face of the crystal. But the thickness of the inefficient layer may increase with energy.

3.9.3 Conclusion

The theoretical and experimental results show that channeling of high-energy beams is quite sensitive to crystal defects, both bulk and surface ones. Perhaps, in the future relativistic channeling will be useful not only for high-energy physics, but also for crystallography as a unique method of testing the perfection of large crystals.

3.10 Topics Under Development

3.10.1 Bending Particles with Axial Channeling

The potentials along the crystal axes are several times higher than those on the planes. Axial channeling is very important for the study of electrodynamics in matter, in particular radiation. Some aspects of axial channeling in this regard will be considered in Chap. 6.

As concerns beam bending, the possibilities of axial channeling are rather limited. The reason is that there is no continuous potential wall in the axial symmetry (Fig. 1.17). The trajectories of positively charged channeled particles are mostly not rosette-type, that is, not bound to any axis. In a straight crystal the positive particles are freely wandering between the high potential ‘hills’, and do not approach the atomic strings. For crystal bending at a sufficient angle $\Theta \gg \psi_c$, particles are rapidly lost from the axial-channeling mode, ‘falling’ into the gaps between the potential hills. Some of them can be recaptured in planar channeling.

This complicated behavior was observed experimentally in one of the first studies on channeling in bent crystals, made at CERN [32]. Figure 3.38 shows the stereogram of the Si(111) crystal. Figure 3.39 shows the angular distribution of 12-GeV particles, passing through the crystal which was bent to 20 mrad. This picture is reminiscent of a shining star. The vertical ray corresponds to the particles trapped into the channeling mode by the horizontal plane (110) and bent at the maximal angle of 20 mrad. The side rays at the angle of 60° are due to bending with ‘skew’ planes (110) (see correspondence to the stereogram). One can also see rays at 30°, due to particle channeling in weaker skew planes (112). Recently a similar complicated picture of the angular distribution was confirmed [100], where the channeled particles had an energy of 450 GeV.

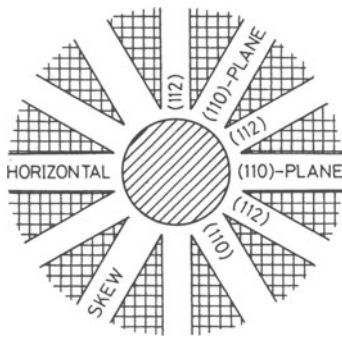


Fig. 3.38. Stereogram of a crystal aligned to Si(111). The circular region is the axial channeling region, of radius ψ_c , where planar effects disappear. The planes are shown with a width corresponding to $2\theta_c$.

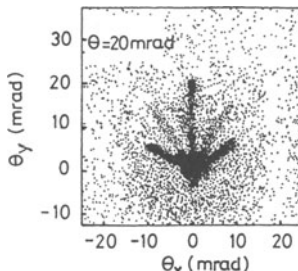


Fig. 3.39. Distribution of deflection angles for 12 GeV/c positive particles transmitted through a crystal bent by 20 mrad. The beam divergence is about ten times the critical angle ψ_c .

From the experimental results obtained, which are very interesting and beautiful in themselves, it is not clear yet where such complicated bending could be of use, as compared to the simple planar effect.

High bending efficiencies with axial channeling arise in a moderately bent crystal with $\Theta \sim \psi_c$, as shown theoretically in detail in [131]. At multi-TeV energies, where the multiple scattering angle $\theta_S \leq \psi_c$, even such insignif-

icant deflection may be useful, for instance, for particle extraction from a superconducting accelerator.

3.10.2 Bending Negative Particles

Negative particles, while channeling, make oscillations around atomic planes and strings, repeatedly crossing the dense layers of atomic nuclei. Therefore they scatter and dechannel much faster than the positive particles do. According to the experimental and theoretical data from the excellent review by R. Carrigan [130] the dechanneling lengths for negative particles are tenfold smaller than the corresponding values for positive particles. Steer negative GeV-beams with the use of channeling looks problematic for practical purposes [133, 32]. At higher energies the bending should be more efficient due to the dominance of the critical angle over the angle of multiple scattering.

Axial channeling for negative particles seems preferable, as it is characterized by a higher critical angle and dechanneling length. Notice that for negative particles the axial potential (Fig. 1.17) is also shaped as a well, not a bump. So the trajectories can be localized and be less sensitive to a centrifugal potential from crystal bending. As detailed simulations in [131] show, a moderate bending of TeV-energy negative particles with axial channeling may be effective enough. Also in this reference, the substantial role of the doughnut scattering for the process of particle bending was shown.

3.10.3 Deflection of High-Energy Heavy Ions

In recent years, heavy ions have been accelerated in many laboratories (CERN, BNL, Dubna); the question of the channeling of these particles may also become topical.

If one assumes that interaction of a relativistic nucleus with a continuum potential is linear, that is, at $Z_i \gg 1$ there is no noticeable influence on the value of the screening radius, then one may conclude that with the same value of pv/Z_i , often called the magnetic rigidity, the critical angle and the dechanneling length are the same for protons and nuclei.

For this simple and reasonable assumption there is an experimental proof obtained by Dubna [132]. In the course of the experiment in which a gently bent crystal was used, the dechanneling lengths were measured for protons with a momentum of 9 GeV/c to be $L_{D-p} = (9.6 \pm 1)$ mm and for relativistic nuclei of oxygen, O_8^{16} , with momentum 72 GeV/c, $L_{D-O_8^{16}} = (9.6 \pm 1)$ mm, in a Si(111) crystal. That is, within the statistical error the dechanneling lengths have been the same, as well as the parameter pv/Z_i .

4. Crystal Extraction

4.1 Introduction

A bent crystal may be considered as a compact septum with a strong electric field of the order of $10^9\text{--}10^{11}$ V/cm localized inside the crystal bulk and vanishing outside at already ~ 1 Å from the crystal surface. This suggests that a bent crystal can be used for extracting the circulating particles from an accelerator ring [134]. The crystal should intercept a fraction of the circulating beam and provide the trapped particles with a small deflection, in order to separate them. These particles can be further trapped with ordinary magnet optics to extract them from the accelerator vacuum chamber. The particles that miss the crystal are not disturbed and continue circulating in the accelerator.

To bring the particles onto a crystal situated in the accelerator vacuum chamber at the beam periphery, one can use the same methods applied in the work with internal targets: for instance, the method of a local distortion ('bump') in the closed orbit. The circulating particles can come from the beam core to the periphery (halo particles) also because of the natural processes of scattering. The halo particles can drift further towards the periphery because of the nonlinearities in the accelerator fields, or due to excitations by means of the noise applied to the circulating beam (see, e.g., [135, 136]). Trapping these particles with a crystal can also clean the halo and protect the accelerator elements from halo particles.

Compared to the application of crystals outside the accelerator ring (discussed in the preceding chapters), the steering of circulating particles has two important new features. One feature is the problem of the controllable supply of particles from the beam core to the crystal. Another feature is that particles have the possibility of passing several times through the crystal, which increases the extraction probability.

Up to now beam extraction has been realized at the Joint Institute of Nuclear Research (JINR) in Dubna (in 1984) [137] at 4.2 to 7.5 GeV, at the Institute for High Energy Physics (IHEP) in Protvino (1989) [138, 139] at 50 to 70 GeV, at CERN in Geneva (1993) [108] at 120 GeV, and at Fermilab (1995) [140] at the highest so far energy of 900 GeV.

Dubna Experiment, 1984. The pioneering experiment was performed in Dubna by the group working with E.N. Tsyganov [137]. The extraction of protons from the Dubna synchrophasotron was carried out by a silicon crystal, oriented along the (111) plane. The crystal was bent by 35 mrad, and had dimensions of 11 mm (length) by 10 mm by 0.4 mm. The crystal deflector was mounted on a goniometer turntable, which provided angular steps of 40 μ rads, and positioned at several fixed distances from the center of the accelerator vacuum chamber. The accelerated protons were brought onto the crystal by decreasing the radius of an equilibrium orbit. Extraction was carried out at a proton energy of up to 8.4 GeV. The measured efficiency was $\approx 10^{-4}$. It was defined mostly by the low geometrical efficiency, $\approx 0.4 \times 10 \text{ mm}^2 / (\pi 20 \times 25 \text{ mm}^2) = 2.6 \times 10^{-3}$, and by the large divergence of the incident beam, ≈ 2 mrad, as compared to $\theta_c \approx 70 \mu\text{rad}$.

Protvino Experiment, 1989. In 1989 crystal extraction of 70 GeV protons was realized at the IHEP accelerator [138]. Si(111) was used here also. The crystal deflector [141] had a wide angular acceptance, $\Phi_T = \pm 5$ mrad, due to the skewed entry face; this simplified the crystal alignment but reduced the geometrical efficiency by a factor of $\sim \Phi/\Phi_T$, $\Phi \approx 0.3$ mrad being the beam divergence. The 65-mm-long crystal was bent by 85 mrad, with a nonuniform curvature: 1.8 mrad/mm over a length of 30 mm and 0.8 mrad/mm over 35 mm. The crystal was placed ≈ 50 mm from the equilibrium orbit. Local distortion of the closed orbit was used to get the beam onto the crystal. The efficiency observed in the experiment was 0.4×10^{-4} to 1.5×10^{-4} . The extracted beam intensity was up to 4.6×10^6 protons per cycle, for an incidence of $\sim 10^{11}$ protons per cycle.

In further experiments [139], another scheme to direct the beam to the crystal was applied. This scheme used preliminary scattering of the protons in a thin, $\sim 50 \text{ mg/cm}^2$, internal carbon target. About 3×10^{11} protons per cycle hit the target. A fraction of them were scattered to the crystal. The extracted beam intensity was increased with this scheme to 9×10^6 protons per cycle. The researchers in this experiment calculated that only a fraction of about $\sim 1/100$ of the particles at the target should reach the crystal; therefore they estimated the crystal efficiency as $\sim 0.3\%$ at 70 GeV, and 0.2% at 50 GeV.

Beam extraction with such a crystal has been used over recent years for particle physics experiments.

4.2 Single-Pass and Multiple-Pass Modes of Extraction

A particle may be trapped in the channeling mode and extracted from an accelerator as the result of just a single interaction with the crystal. The consideration of this process, a single-pass extraction, is exactly the same as that performed in the previous chapters.

What makes this extraction process more interesting and complicated, is the possibility of multiple passages of the circulating particles through the crystal. Consideration of multi-pass extraction should take into account the motion of the nonchanneled particles in the fields of the bent crystal and of the accelerator.

As well as the particles deflected by the crystal at the required angle and particles lost because of their interaction with the crystal nuclei or because they are scattered at too-large an angle, there are a number of particles that remain in orbit in the ring and have the chance to pass through the crystal again. The angular distribution of such particles changes significantly after each passage through the crystal. In order to take these particles into consideration, the following effects should be taken into account:

- multiple scattering in the crystal;
- scattering on crystalline potential;
- capture into channeling regime and dechanneling of the particles;
- catastrophic collisions with nuclei;
- energy loss by ionization in the crystal;
- motion in the accelerator field.

The role of each factor will be estimated for a typical case.

4.2.1 Scattering in a Crystal

Multiple Coulomb Scattering. This increases the divergence of the nonchanneled particles with each passage through the crystal. As discussed in Chap. 1, this scattering in an aligned crystal may be somewhat different from that in an amorphous substance. The effective nuclear density (i.e., the density of the scatter centers), $\langle \rho_n \rangle_{cr}$, ‘seen’ by a quasi-channeled particle moving in a potential $U(x)$ can be obtained by averaging over the oscillation length λ using (1.19):

$$\langle \rho_n \rangle_{cr} = \frac{1}{\lambda} \int \rho_n(x) dz = \frac{1}{\lambda} \int \sqrt{\frac{0.5 pv}{E_T - U(x)}} \rho_n(x) dx . \quad (4.1)$$

As a rule, the crystal bending angle θ_B is much greater than the Lindhard angle θ_L , so nonchanneled particles move at large angles to the channel planes over most of their path. Multiple scattering in the crystal in this case is close to that in amorphous matter. For particles with $E_T \gg U_0$, (4.1) can be simplified as follows [143]:

$$\begin{aligned} \langle \rho_n \rangle_{cr} &\simeq \frac{1}{\lambda} \sqrt{\frac{pv}{2E_T}} \int \left(1 + \frac{U(x)}{2E_T}\right) \rho_n(x) dx \\ &\simeq \langle \rho_n \rangle_{am} \left(1 + \frac{U_0}{2E_T}\right) \simeq \langle \rho_n \rangle_{am} \left(1 + \frac{\theta_L^2}{2\theta^2}\right) , \end{aligned} \quad (4.2)$$

where $\langle \rho_n \rangle_{\text{am}}$ is the nuclear density in amorphous substance, and θ is the particle angle to the channel plane. Averaging the correction factor $(1 + \theta_L^2/2\theta^2)$ along the crystal, uniformly bent up to the total angle θ_B , gives:

$$\langle \rho_n \rangle_{\text{cr}} \simeq \langle \rho_n \rangle_{\text{am}} \left(1 + \frac{\theta_L}{2\theta_B} \right). \quad (4.3)$$

Typically the correction is less than 1%, so one may use an amorphous approximation. As a rule, the rms angle of multiple scattering along the crystal length exceeds the channeling critical angle θ_c and so multiple scattering may strongly affect the particle extraction efficiency.

Scattering from a Potential of the Bent Atomic Planes. This was considered in Sect. 2.1. The unchanneled particles nearly aligned to the crystal planes are scattered with the planar fields at angles of the order of θ_c . It is interesting to say that in a bent crystal the mean exit angle of the unchanneled particles is different from the angle of incidence. These particles are deflected on average in a direction *opposite* to the crystal bending, at angles of about $-\theta_c$. This effect, a *volume reflection* [59], was found in computer simulations. Calculation of the effect for the large hadron collider is discussed in Sect. 4.5.

The ‘reflection’ effect taken together with the betatron motion in the accelerator (see below) means that the simplified multipass simulations with an amorphous target do *not* model the crystal-extraction process precisely.

Dechanneling of the Initially Trapped Particles. This affects the angular distribution downstream of the crystal. These dechanneled particles leave the crystal at a large angle, a fraction of θ_B , and therefore are mostly lost, as they do not fit the acceptance of the accelerator nor the acceptance of the extraction beam line. Therefore this process very slightly affects the probability of further extraction of a particle. The process, however, may strongly contribute to the background, as it scatters some particles in a broad angular range from 0 to θ_B .

Collisions with Crystal Nuclei. The nonchanneled particles may interact with crystal nuclei. Some of the nonchanneled particles, equal to $q = 1 - \exp(-L/L_N)$, where L_N is an absorption length, are lost in these interactions. For particles moving at large angles to the planes, the nuclear cross sections could be taken as for an amorphous target. The correction for potential, (4.3), is the same as for multiple scattering. The length of a nuclear inelastic interaction (meson production) is 45 cm in silicon. Typically, $q \simeq L/L_N \simeq 0.1$ per single passage through the crystal.

After a nuclear elastic collision, the proton continues moving with the primary energy. However, the r.m.s scattering angle is quite large as compared to the channeling angle θ_c . The distribution for the scattering angle is Gaussian [142]:

$$P(\theta_{\text{elastic}}) = \text{const} \times \exp(-B_0 A^{2/3} p^2 \theta_{\text{elastic}}^2), \quad (4.4)$$

where $B_0 = 10.8 \text{ GeV}^{-2}$, A is the crystal atomic weight. The rms angle, projected into the plane, is

$$\theta_{\text{elastic}}^{\text{rms}} = \frac{1}{2pA^{1/3}\sqrt{B_0}} . \quad (4.5)$$

For 100-GeV protons in silicon this is 0.50 mrad – a factor of ≈ 25 greater than θ_c . The scattered protons are practically lost to channeling in the later passes. Therefore in the channeling calculations one can simply include the total nuclear cross section in a new definition of the ‘absorption’ length; then $L_N = 30 \text{ cm}$ in silicon.

Energy Losses. In the crystal energy losses can change a particle’s longitudinal momentum p distribution; e.g., a 0.9-TeV proton loses $\sim 2 \times 10^{-5}$ of its momentum in 4 cm of silicon. The energy loss along the nuclear interaction length is equal to $(dE/dz)L_N \simeq 200 \text{ MeV}$, independently of the matter; a corresponding momentum change of the 0.9-TeV proton is $\Delta p/p \simeq 2 \times 10^{-4}$, which is comparable to the undisturbed momentum spread in the Tevatron accelerator of Fermilab, $\Delta p/p = 1.5 \times 10^{-4}$.

4.2.2 Motion in the Accelerator

The process of crystal extraction may involve the circulating particles undergoing many turns in the accelerator and several scatterings in the crystal. In the meantime, between the successive passages through the crystal the particle makes some turns in the accelerator ring. For further understanding, one needs to learn some physics of accelerators.

The particle in a circular accelerator undergoes, to a first approximation, so-called *betatron oscillation* with respect to the equilibrium orbit in both transverse planes. The position x and the angle $\theta_x = x'$ of the particle with respect to the beam axis are functions of the path length s along the orbit:

$$\begin{aligned} x(s) &= \sqrt{\epsilon\beta(s)} \sin(\phi(s) - \phi_0), \\ x'(s) &= \sqrt{\epsilon/\beta(s)} [\cos(\phi(s) - \phi_0) - \alpha(s) \sin(\phi(s) - \phi_0)], \end{aligned} \quad (4.6)$$

where $\alpha(s)$ and $\beta(s)$ are functions of the machine optics. The values of ϵ (the particle ‘emittance’) and ϕ_0 (the starting phase) are defined by initial parameters of the particle. The oscillations are commonly described in the phase plane (x, x') where the particle trajectory is a phase ellipse with the area ϵ , Fig. 4.1. After one turn in the accelerator ring, the particle returns to the same location with the phase advance $\Delta\phi_{x,y} = 2\pi Q_{x,y}$, where $Q_{x,y}$ is the number (noninteger) of the betatron oscillations made over a single turn in the machine (in the x and y planes respectively), called the *betatron tune*. Figure 4.1 shows the particle coordinates (x, x') at the same location in the ring after successive turns: the particle moves along the same phase ellipse with phase steps of $2\pi Q$ per turn.

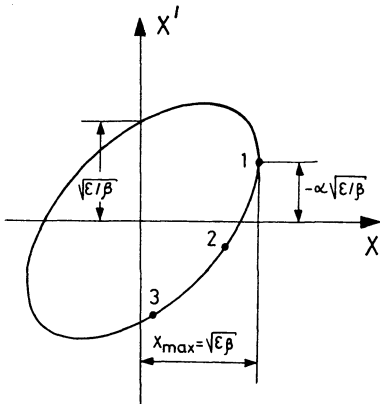


Fig. 4.1. Particle trajectories in the transverse phase plane (x, x') of a circular accelerator. The points show the particle's coordinates after successive turns.

The beam emittance ϵ may change considerably. The scattering processes and a field noise can modify ϵ to cause a particle diffusion in the transverse plane of the accelerator. Furthermore, in the nonlinear fields of the accelerator the particle motion may be unstable and cause a steady growth in the particle oscillation amplitude. These processes will eventually bring the circulating particles either to the vacuum chamber wall or to any element of the accelerator, for example, a crystal.

When a particle reaches the crystal, it usually has quite a small impact parameter b (depth of the penetration into the crystal) with respect to the edge, in the range from $< 1 \text{ \AA}$ to a few μm . This particle can be either trapped in channeling trajectories, or scattered through a sizable angle θ_s . In the latter case the particle continues an orbit but with a betatron oscillation amplitude increased from the initial x_{\max} to $\sqrt{x_{\max}^2 + \beta^2 \theta_s^2}$. After several turns, the particle hits the crystal again, with an impact parameter b increased by about

$$\Delta b \approx \sqrt{x_{\max}^2 + \beta^2 \theta_s^2} - x_{\max} \approx \beta^2 \theta_s^2 / 2x_{\max} \approx \beta^2 \theta_s^2 / 2X , \quad (4.7)$$

where $X \approx x_{\max}$ is the position of the crystal edge; $\Delta b \ll X$, and usually has the order $\Delta b \simeq 0.1 \text{ mm}$. The precise value of b depends on the phase of the betatron oscillation.

As discussed above, the unchanneled particles scattered in the bent atomic planes are deflected through an angle of about θ_c . For the betatron motion this is equivalent to a phase advance of $\arctan(\beta \theta_c / X)$. This phase advance per passage through the crystal has to interfere with the usual phase advance per turn in the accelerator.

Generally, not all the processes mentioned above are independent and should be considered together in a computer simulation [143, 144]. However, the simplified consideration is useful for a qualitative understanding of the dependence of the efficiency for proton-beam extraction on the experimental conditions and for making simple estimations.

4.2.3 Estimate of the Multi-pass Efficiency

The simplest estimate of the total efficiency (including the multiple passes) of the particle extraction F may be derived [143] using the following two simplifications:

- (a) the probability A_k of the particle capture into the channeling mode in the k th passage through the crystal is the same as that probability in the first passage, $A_k = A_1 = A$ (actually A_k decreases with k as the beam divergence grows with the scattering in a crystal);
- (b) the probability q_k of particle death, either in the crystal or at the vacuum chamber wall, with the k th passage through the crystal is the same as that probability in the first passage, $q_k = q_1 = q$ (actually q_k may increase with k if the particles reach the vacuum chamber wall with scattering).

The circulating particles are gradually removed from the ring with these two processes, crystal channeling and nuclear interaction, with the probabilities A and q per single passage through the crystal, respectively. The number of the particles remaining in the ring after k passages through the crystal is

$$N_k = N_0(1 - A)^k(1 - q)^k, \quad (4.8)$$

if the initial number was N_0 . The number of particles extracted by the $(k + 1)$ th passage equals

$$F_k N_0 = A N_0(1 - A)^k(1 - q)^k, \quad (4.9)$$

and the total efficiency amounts to

$$F = \sum F_k = \frac{A}{A(1 - q) + q} \exp(-L/L_D). \quad (4.10)$$

The exponential factor takes into account the dechanneling of the trapped particles. Since both our assumptions (a) and (b) above tend to overestimate the efficiency, the obtained formula (4.10) is the upper limit for the real multi-pass efficiency.

Equation (4.10) agrees fairly well, for example, with the results of a computer simulation [20] of the proton extraction from the 20-TeV Superconducting Supercollider. Figure 4.2 shows the overall extraction efficiency for this machine as a function of the Si(110) crystal length. The analytic curve was calculated with (4.10) [143] for 90 μrad bending; the points are from a more recent computer simulation for 100 μrad bending [20].

The same figure shows the efficiency function for a single passage through the crystal. We shall compare the single and multi-pass extractions in some detail in the sections below, when discussing the crystal-extraction experiments at CERN and Fermilab. Here we just note the qualitative behavior of the efficiency curve. Although the single-pass efficiency monotonically increases with L in this range, the overall efficiency (with multiple passes) has a peak at small L .

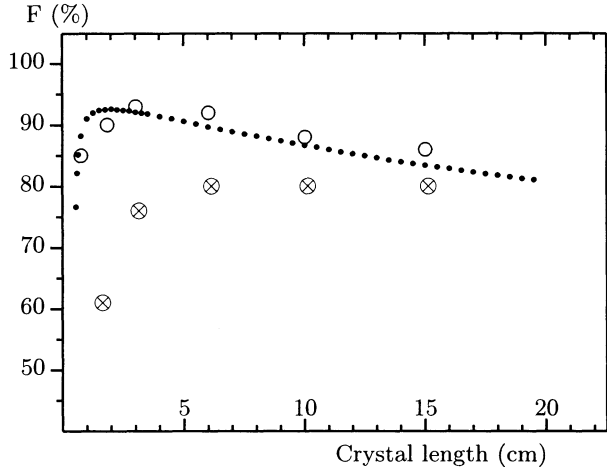


Fig. 4.2. Extraction efficiency for a 20-TeV collider as a function of the crystal length. The curve (\bullet) is from (4.10). The other data are based on a computer simulation: the first-pass (\otimes) and the overall (\circ) efficiency.

A shorter crystal disturbs the beam particles less. Since the nuclear interaction probability is $\approx L/L_N$ per single pass, the average number of passes made through the crystal before interaction is about L_N/L . That means more attempts (passes) per proton on average, multiplying the efficiency at smaller L . Furthermore, the scattering over the crystal length is reduced, and hence the scattered protons have a smaller divergence in the secondary passes.

On the other hand, a short crystal needs to be more strongly bent to keep the same deflection angle. With the bending $p v/R$ greater than ~ 1 GeV/cm in silicon, the crystal acceptance rapidly decreases. This decrease in acceptance cuts the extraction efficiency at too small L .

To understand (4.10) better, it is useful to consider several limiting cases.

- (1) If the probability q of the nonchanneled particle interaction with nuclei over the crystal length is very high, $q \simeq 1$, the secondary passages are not possible. Equation (4.10) is reduced, then, to the efficiency of a single pass: $F \simeq A \exp(-L/L_D)$.
- (2) Typically, $q \simeq L/L_N \simeq 0.1$ over a single passage through the crystal. If the probability of capture into the channeling mode is very small, $A \ll q$, (4.10) is reduced to $F \simeq (1/q)A \exp(-L/L_D)$. This is simply the efficiency of a single pass times the mean number of passes ($1/q$) before a nuclear interaction.
- (3) The opposite case, $q \ll A$, would mean that the circulating particles are removed from the ring mostly via crystal channeling rather than nuclear interactions. The trapping efficiency is then close to unity, with (4.10) being reduced to $F \simeq (1 - q/A) \exp(-L/L_D)$.

At TeV energies the exponential factor $\exp(-L/L_D)$ is close to unity. We shall optimize (4.10), taking q as L/L_N . This gives the following equation for the optimal length L :

$$A^2(L) - A(L) + L(dA(L)/dL) = 0 \quad (4.11)$$

One can probe this equation in the harmonic approximation (2.13) for a parallel beam, $A = A_S(1 - \rho)$, where $\rho = R_c\theta_B/L$. An optimal bend is then

$$\rho_{\text{opt}} = (A_S - 1 + (1 - A_S + A_S^2 - A_S^3)^{1/2})/A_S.$$

At TeV energies $A_S \simeq 0.9$, then $\rho_{\text{opt}} \simeq 0.3$; i.e., the optimal length is of the order of three critical lengths, independently of the required deflection angle: $L_{\text{opt}} \simeq 3L_c = 3R_c\theta_B$. With the Molière potential, as in Fig. 4.2, L_{opt} is about five critical lengths; i.e., $(pv/R)_{\text{opt}}$ is of the order of 1 GeV/cm in silicon. The optimal length of multi-pass extraction is essentially smaller than the length optimized for a single-pass deflection (see Sect. 2.2.3). The optimization will be studied later with a realistic simulation for the experiments of CERN and Fermilab.

4.2.4 Angular Acceptance of a Crystal in the Multi-pass Mode

In a single pass, the particles can be trapped if they come parallel to a crystal within the Lindhard angle. Because of the multiple passage, the angular range in which the particles may undergo extraction (the angular acceptance of a crystal in the multi-pass mode) is broader than the Lindhard angle. A particle misaligned to the crystal at the first incidence, modifies its angle through scattering and may become during a later pass parallel to the crystal within $\pm\theta_c$. It is clear that the full width of the acceptance is determined by the maximum angle of the particle scattering over many passes in the crystal before its eventual loss either in interaction with the crystal nuclei or at the vacuum chamber wall. One may estimate it as the rms angle of the multiple Coulomb scattering over the nuclear interaction length [143] :

$$\theta_N = \frac{14 \text{ MeV}}{pv} \sqrt{\frac{L_N}{L_R}}. \quad (4.12)$$

It depends only on the crystal properties. The angle θ_N may be much larger than the Lindhard angle. For instance, at 1 TeV in silicon $\theta_N \simeq 30 \mu\text{rad}$ while $\theta_c \simeq 6 \mu\text{rad}$.

If the extraction efficiency is small, the particles are removed from the ring mostly through nuclear interactions. Then (4.12) gives the rms width of the angular scan of the efficiency. The FWHM of this scan is more difficult to estimate. The angular distribution of the scattered particles averaged over many passages through the crystal is a sum of many Gaussians:

$$P(\theta) = \sum_{k=0}^{k_{\text{max}}} \exp\left(-\frac{kL}{L_N}\right) \frac{1}{\sqrt{2\pi(k\theta_s^2 + \theta_0^2)}} \exp\left(-\frac{0.5\theta^2}{k\theta_s^2 + \theta_0^2}\right). \quad (4.13)$$

Each term in this sum corresponds to one, the k th, passage through the crystal; θ_s is the rms angle of scattering per one pass, θ_0 is the starting rms divergence. The maximum number of terms in the sum, k_{\max} , may be set by the aperture of accelerator D : $k_{\max} \approx (D/\beta\theta_s)^2$. Otherwise, the terms vanish at $k \gg L_N/L$. Equation 4.13 estimates the angular dependence of the extraction efficiency.

4.2.5 Extraction with High- Z Crystals

Crystals with Z higher than in silicon (germanium and possibly tungsten) have evident benefits, such as a higher critical angle $\sim Z^{1/3}$, and a smaller critical radius $\sim 1/Z$. Therefore the application of high- Z perfect crystals for a ‘single-pass’ channeling is clearly advantageous (see Fig. 2.6). Interestingly, in crystal extraction (which is essentially multi-pass channeling) this may be not true [145].

The primary incident particles can be practically parallel due to a very small b at the crystal; then critical angle does not matter. In multi-pass mode, one has to trap the protons *scattered* in the crystal. Then the scattering angle and the nuclear interaction length do matter as do the channeling properties.

In general, one could consider a constant crystal lattice and vary the Z of the atoms (we keep $Z/A \approx \text{const}$ below). Then the critical angle is scaled as $Z^{1/3}$. The scattering angle per unit length is scaled as Z . Increasing Z , one scales the trapping efficiency as $Z^{-2/3}$ (i.e., the ratio of the critical angle to the particle divergence). Since the critical radius reduces as $1/Z$, one can shorten the crystal length which scales as $1/Z$. The scattering angle per single pass through the crystal is $\sim Z^{1/2}$, and the efficiency is $Z^{-1/6}$ (still decreasing with Z). The final answer is more complicated, as one takes into account the dechanneling loss (reduced in a shorter crystal: $L/L_D \sim Z^{-2/3}$), and the absorption length $L_N \sim Z^{-2/3}$ (the absorption loss is also reduced in a shorter crystal: $L/L_N \sim Z^{-1/3}$). Therefore, high- Z crystals are hardly advantageous in crystal extraction. This qualitative consideration has been confirmed by computer simulations [145] for the LHC beam crystal extraction with Ge crystals in the setup described in Sect. 4.5. As compared to the situation with the Si crystals, no gain in the extraction efficiency was observed.

4.2.6 Dependence of Efficiency on Machine Parameters

Beta Function. This affects the impact parameters b of the incident protons (to increase with β). This may influence the efficiency only if b are comparable to the ‘septum width’ t defined by the surface irregularities. The impact parameters are approximately $b \simeq \beta^2 \theta_s^2 / 2X$ on the secondary passes. The initial divergence of the incident protons decreases as $\beta^{-1/2}$. Therefore, a higher beta is preferable in all respects.

The Alpha Function. This defines the dependence of the mean angle of incidence of the particles upon the transverse coordinate:

$$x'_{\text{mean}} = -\alpha_x x / \beta_x \quad (4.14)$$

The angle of incidence changes by $\Delta x' = \alpha_x H / \beta_x$ over the crystal thickness of H . For example, with a thick crystal, $H = 3.5$ mm, at the SPS extraction experiment (Sect. 4.3) the x' variation over the crystal face becomes 2.07×3.5 mm / 90 m $\approx 80 \mu\text{rad}$, to be compared with $\theta_c = 14 \mu\text{rad}$ at 120 GeV in Si. Too thick a crystal with a big α could lose efficiency [146]. The upper limit for the optimal crystal thickness is approximately $\beta_x \theta_c / \alpha_x$ (≈ 0.6 mm at the SPS).

Since a particle penetrates into the crystal depth as a result of scattering, $b \simeq \beta^2 \theta_s^2 / 2X$, it is interesting to compare the alpha-induced angular spread $\alpha b / \beta$ at the crystal face with the angular spread θ_s from scattering:

$$(\Delta x')_\alpha = \frac{\alpha b}{\beta} = \frac{\alpha \beta \theta_s^2}{2X}. \quad (4.15)$$

Then

$$\frac{(\Delta x')_\alpha}{\theta_s} = \frac{\alpha \beta \theta_s}{2X}. \quad (4.16)$$

In the above example for the SPS, this ratio is of the order of 1; i.e., the alpha-induced angular spread and scattering contribute roughly equally.

Betatron Tune. An interesting effect may appear in the betatron tune dependence of crystal extraction. Because of very small impact parameters in the first pass, $b_0 \ll X$, the distribution in the accelerator phase plane (x, x') of the scattered particles downstream of the crystal is a narrow strip, with all particles having a big angular spread but the same (within $< 1 \mu\text{m}$) position (Fig. 4.3). After travelling around the accelerator, the particle returns to the crystal with a phase advance of $2\pi Q$. The new coordinate is $x = x_{\max} \cos(\phi_0 + 2\pi Q)$, where $\phi_0 = \arctan(\beta \theta_s / X)$ is the phase after the first pass. With some arbitrary Q , the particle hits the crystal (sooner or later) at some depth, of the order of $b \simeq \beta^2 \theta_s^2 / 2X$.

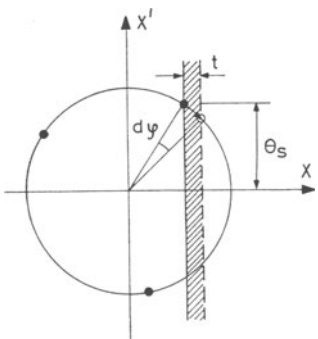


Fig. 4.3. The phase space with Q near the resonance.

Suppose that Q is a rational number, i.e., a ratio of two integers, m/n . Suppose also that the accelerator field is ideal, and there is no perturbation (no ‘resonance’) of the particle trajectory. At the rational values of tune the trajectory of a circulating particle becomes periodical. Then any particle may be at n points of the phase ellipse only. If n is small ($n < \pi/\phi_0 \approx 5-15$; Fig. 4.3), all but one of these points are outside the crystal. The only point at the crystal is that from which the particle has left the crystal after the preceding pass. After n turns a particle returns to the same phase point. Upon another scattering the particle moves up or down in the (x, x') plane, but stays in the same extreme proximity to the crystal edge, i.e., on the same strip in the (x, x') plane.

For an ideal crystal this peculiarity is of minor importance. But for a realistic crystal with septum width $t > b_0$ this may be a disaster. The particles will pass through the crystal edge many times, scatter and interact, but never come to the depth $b > t$ where the crystal is perfect. Therefore, with a tune fractional part like m/n the extraction is suppressed if $t > b_0$. That is, if the fractional part of Q is $\approx m/n$, and if the first pass in the crystal was through an inefficient layer, some later passes suffer in the same way resulting in a *dip* of efficiency at the rational tunes [107]. Since the case $t > b_0$ is possible, and may even be the only feasible one, one has to study it. Rational tunes m/n are well known in the physics of circular accelerators as *tune resonances*. When $Q = m/n$, the particle orbit is closed (periodic), and any perturbation has a regular (resonant) character, which strongly increases its effect on the particle motion. The real tune is always chosen far from the strongest resonances.

In our case of multi-pass extraction the efficiency dip is due to the *edge imperfection* of a crystal. To understand it, we keep the impact parameters of protons constant irrespective of Q . Fig. 4.3 shows what happens when Q is close to rational: $Q = m/n + dQ$. The small phase advance after n turns is $d\varphi = 2\pi n dQ$. The increment of the impact parameter is $\Delta b \simeq d\varphi X \sin \phi_0$ with each pass. Comparing Δb to t , one can estimate the width of the efficiency dip as

$$\Delta Q \approx \frac{t}{2\pi n X \sin \phi_0} \simeq \frac{t}{2\pi n \beta \theta_s} \sim \frac{tE}{n\beta}. \quad (4.17)$$

We make the replacement $\sin \phi_0 \simeq \phi_0 \simeq \beta \theta_s / X$ (Fig. 4.3). An accurate evaluation of the dip FWHM is difficult to perform analytically, because of the statistical character of the process. However, one sees qualitatively that the smaller the *order* of tune resonance, n , is the stronger effect it makes. The width (4.17) is proportional to the septum width t and $1/\beta$, and grows linearly with energy (due to a decrease in scattering). For instance, with conservative $t = 50 \mu\text{m}$ (Sect. 3.9), $\beta = 250 \text{ m}$ and $\theta_s = 2 \mu\text{rad}$ as expected at the $\sim 7 \text{ TeV}$ Large Hadron Collider (Sect. 4.5), one has $\Delta Q \simeq 0.017/n$; at the SPS (Sect. 4.3) $\Delta Q \simeq 0.001/n$ only.

Figure 4.4 shows the simulated dependence of the overall extraction efficiency for extracting 120-GeV protons with a 3-cm Si crystal in a geometry

somewhat different from that of the SPS experiment [107]. Results for both perfect and imperfect ($t = 1 \mu\text{m}$) crystals are shown. There are strong dips in the extraction efficiency with an imperfect crystal. The effect increases with smaller n . Precisely at a rational tune the efficiency is not zero; with growing scattering, our simplified assumption $n < \pi X / \beta \theta_s$ is no longer fulfilled (more than one hit point appear at the crystal). The efficiency depends sizably on Q already within ~ 0.01 from the dip position.

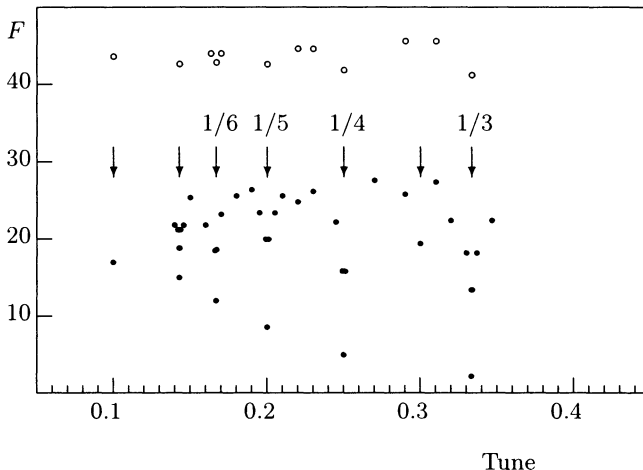


Fig. 4.4. The efficiency dependence on the tune. Open circles (o) are for a perfect surface. Solid circles (●) are for a crystal with nonperfect surface. Positions of the rational tunes are marked by arrows.

Let us note that if some resonance is excited, the situation changes. For instance, in the case of the 3rd order resonance excited, which is most frequently used in the classic systems of extraction, the protons, due to an increase in the amplitude of betatron oscillations, can directly hit the perfect part of the crystal, and, captured in the channeling mode, be efficiently extracted from the accelerator. Such a possibility of particle extraction with the use of a crystal was not investigated in detail.

4.2.7 Some Ideas on Multi-pass Channeling

In this section, several interesting ideas relevant to crystal extraction studies are briefly discussed.

Pre-scattering. The primary impact parameter of protons at a crystal can be quite low. Therefore, some ideas were proposed [147, 148] and even employed [139] to pre-scatter protons in a thin target before they hit a crystal. The angle of scattering in an amorphous target of length s is

$\theta_s = (E_s/E)\sqrt{s/L_R}$, $E_s = 14$ MeV. The impact parameters in the first pass through the crystal are of the order of (4.7), which gives a relation for s :

$$s \simeq \frac{2bXL_R E^2}{\beta^2 E_s^2}. \quad (4.18)$$

Note that $s \sim E^2$. For instance, requiring $b > 50 \mu\text{m}$ at the crystal, one needs a Si target as long as $s \geq 1 \text{ mm}$ at the 120-GeV SPS, but $s \geq 40 \text{ mm}$ at the 900-GeV Tevatron (Sects. 4.3–4.4). For comparison, an effective length of the first pass in a crystal at SPS is $\simeq 5 \text{ mm}$; in the 900-GeV case, 40 mm is as long as the crystal. Therefore, an amorphous pre-scatter might work at $\sim 100 \text{ GeV}$ and below. At $\sim 1 \text{ TeV}$ and higher, this idea can no longer be applied [145]. Notice that a pre-scatterer must be positioned (closer to the beam than crystal) with an accuracy of $\simeq b$ (i.e., $\simeq 50 \mu\text{m}$). Otherwise, protons traverse it many times, and the benefits are lost.

The pre-scatter becomes more interesting with a crystalline scatterer [147, 148], producing angular kicks of $\simeq \theta_c$. The minimal length required is $\lambda/4$, with λ from (1.24); $\lambda/4 \simeq 20 \mu\text{m}$ Si at 1 TeV. Notice that protons are kicked in one plane only, and are almost undisturbed in the normal plane. The drawback of the idea is the need to tune two extra parameters: the position (with accuracy of $\sim 10 \mu\text{m}$) and the angle (with accuracy of $< \theta_c$) of the pre-scatterer.

The alternative to the above ideas is the intrinsic scattering at the edge of a bent crystal. We show in Sects. 4.3–4.5 with simulations for 120 GeV, 900 GeV, and 7.7 TeV that a difference in efficiency between an ideal crystal and a crystal with imperfect surface vanishes with increasing energy E [158]. Therefore, the problem disappears in the TeV range.

dE/dz Spectrum of Extracted Protons. In [149] the idea was proposed that the energy loss dE/dz deposited in the crystal by a channeled proton may indicate, whether this proton was extracted in the first pass, or in the subsequent passes. In a diffusion mode of the crystal extraction, the first passage of protons through the crystal is very close to the surface, at a depth of the order of 1 μm . Then the escape of δ electrons (knocked out by a channeled proton) from the crystal modifies the dE/dz deposited in the crystal, thus making it depend on a depth (impact parameter) b . Hence one may hope to resolve the first pass or multi-passes, observing dE/dz deposition of the extracted protons in a crystal.

The difference between the energy loss and its deposition in the detector is a well-known effect due to the mentioned leakage of the most energetic electrons from the detector. Here this effect is brought to its extreme, going from typical thickness of $\sim 1 \text{ mm}$ to $< 1 \mu\text{m}$ for the first passage in crystal extraction. We give a very rough estimate of the magnitude of this effect.

The mean energy loss for a channeled particle is written in (1.54). To calculate the dE/dz deposition (so called *restricted* dE/dz) in $\sim 1 \text{ mm}$ thick silicon, one should use $T_{\max} \approx 1 \text{ MeV}$ [49] because the electrons with energy

$> T_{\max}$ have ranges > 1 mm in Si, and leak out. The practical range l in Si of the electron of T (keV) energy is [40]

$$l[\mu\text{m}] \approx 2.4T \left(1 - \frac{0.9841}{1 + 0.0030T} \right). \quad (4.19)$$

For instance, $l = 1 \mu\text{m}$ corresponds to $T = 10$ keV. With the average $\rho_e \approx Z_v/Z \approx 0.3$ ($Z_v \approx 4$ is the number of valence electrons), one finds the result from (1.54) to be reduced by $\sim 15\%$ if one restricts $T < 10$ keV instead of $T < 1$ MeV. In fact, some energy carried by electrons with $10 \text{ keV} < T < 1$ MeV may be deposited, while the rest of it escapes. The escape is a random-walk process. From intuition only, one may expect that somewhat more than 1/2 of these electrons escape from a ‘half-space’.

Therefore the reduction of the mean dE/dz signal for the protons extracted with a single pass may be of the order of 10%, with respect to the protons extracted with multi-passes. The halfwidth of dE/dz peak for the bent protons is $\sim 10\%$ (Sect. 3.5). Note that this width is due to energetic electrons, hence it should be greatly reduced for the ‘low- b ’ signal. Therefore, if the contribution of the first pass to the extraction efficiency is significant, it should be seen in the dE/dz spectrum. Ideally, this contribution may be sharply peaked, thus even splitting the dE/dz spectrum of extracted protons into the ‘first-pass peak’ and the ‘secondary-pass peak’.

Both energy loss and escape are statistical processes, and should be simulated. Such a simulation would check whether the idea is applicable, and provide a kind of calibration for the experiment. If the first-pass signal were easily recognized, this would give a great deal of possibilities for research. By reducing the primary b below $1 \mu\text{m}$, one may make the dE/dz signal even more pronounced, thus exploring the crystal at very small depths. Note that dE/dz in the secondary passes depends on the depth also, thus also providing information. One should study dE/dz spectra as a function of the crystal angle.

Crystal Microscope. One could distinguish the first and secondary passes based on their difference in time (first comes first) and space (secondary pass comes deeper in the crystal). The time-synchronizing (‘kick mode’) has a difficulty due to the unavoidable mixing of the first-pass protons from the later turns. So any method aiming to distinguish the single and multiple passes, is based on their different spatial distribution at the crystal. It is less informative to observe x downstream of the crystal since the resolution, θ_c times the distance to the detectors (0.3–0.5 mm at the SPS and Fermilab), is too poor and is worsened further by the detector resolution.

Applying a skew cut on the exit face of a crystal [149], one can make the bending angle depend on the coordinate b (the principle of any microscope). The profile of the bent beam downstream of the crystal is then a broadened profile of this beam at the crystal face, and can be studied in detail.

The resolution dx of this method is defined by the maximum allowed variance Θ of the bending angle ($\Theta \leq$ the acceptance of the extraction beam

line): $dx = \theta_c \times h/\Theta$, where h is the depth of the skew-cut corresponding to Θ (h/Θ is the slope of the skew cut). For example, at the SPS with $\Theta \simeq 16 \text{ mm}/20 \text{ m} \simeq 0.8 \text{ mrad}$ the resolution is $dx \simeq h/50$; if the x range of interest is $h < 0.5 \text{ mm}$ from the edge, the resolution can be $dx < 10 \mu\text{m}$. This is a unique way to observe the bent particle profile at the crystal directly.

The ‘microscope’ magnification can even be adjustable if the skew cut varies with the *vertical* position at the crystal. Then one just moves the crystal (or beam) in order to chose the needed factor of ‘magnification’.

4.3 Extraction from the CERN SPS

A series of crystal extraction experiments has been performed at the CERN SPS [108, 150, 151, 152], studying the feasibility of extracting protons from the halo of the circulating beam by means of a bent silicon crystal. These studies aim to model the beam parameters expected at the future Large Hadron Collider, and to develop possible applications of this technique for the beam extraction from a multi-TeV machine (Sect. 4.5); such an extracted beam would open up very interesting possibilities, e.g., for beauty physics [104].

4.3.1 Crystal Transmission of a Single Pass

One of the first steps in this research was a thorough investigation of the crystal transmission of 450 GeV protons [103] (Sect. 3.4). Both the crystal and the bending device were identical to those used in the first extraction experiments at the SPS [108]. The measured channeling efficiencies were found to be in good agreement with CATCH simulations (Sect. 3.4).

The detailed spatial and angular scans were done over the crystal face to investigate the spread of the channeling characteristics. Here we consider the bent-crystal angular distortions found in this work, which turned out to be essential for the understanding of the SPS extraction results.

The most noticeable distortion was a strong dependence of the angle of channeling on the vertical position at the crystal face (Fig. 4.5a). The range of the orientation of the Si(110) channeling planes was several hundred μrad over $\sim 10 \text{ mm}$ of the crystal vertical range. This twist (an ‘anticlastic bending’) was due to the ‘bridge’ design of the bending device (Sect. 3.2).

In general, agreement between the experiment and theory was obtained over small areas, $\delta x \leq 0.3 \text{ mm}$, selected on the crystal entry face. Averaged over the total face, the efficiency was measured to be lower by some factor, whereas the angular scan became broader. For certain vertical coordinates near the crystal center (Fig. 4.5a) *two* maxima in the angular dependence of bending efficiency appeared!

Following detailed analysis [103], the following explanation was found. The edges of the crystal face have been disaligned with respect to the centre, and

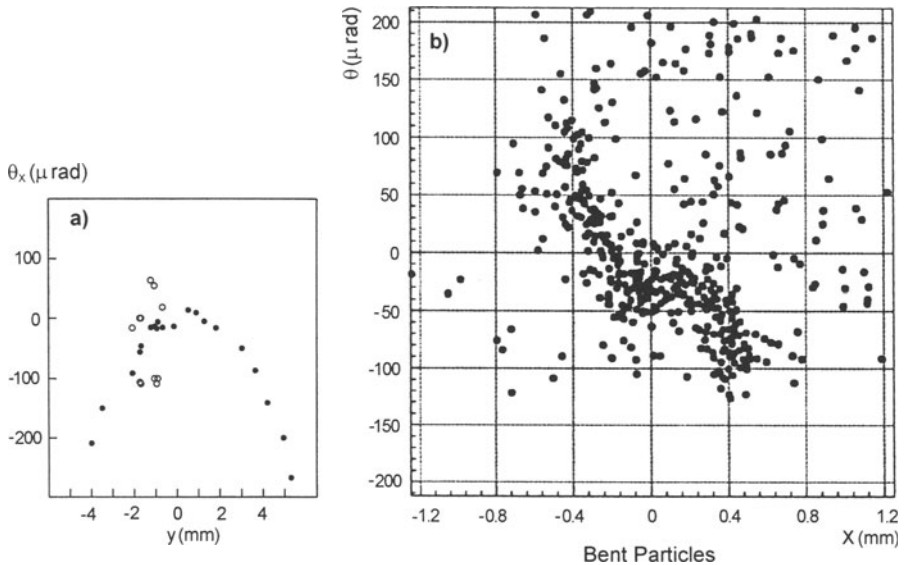


Fig. 4.5. Dependence of the angle of channeling on the vertical (a) and horizontal (b) coordinates at the crystal face. From the RD22 H8 experiment.

moreover seemed to have a large angular spread, of the order of 50–100 μrad . Figure 4.5b shows the bent particles in the phase plane (x, x'), where x is the coordinate of the incidence at the crystal face and x' is the angular position of the goniometer. The thickness of the disaligned ‘edges’ was of the order of 100–200 μm .

The ‘channeling phase-space’ distorted in the way of Fig. 4.5b was found for every one of about one hundred experimental runs, irrespective of the bending angle (from 3.0 to 8.5 mrad), at any vertical position. The observed additional (small) maxima were due to the crystal edge while the major maximum was due to the crystal center. This *horizontal* twist may also be a function of the bending technique. Obviously, for crystal extraction this effect can be more harmful than the vertical twist.

It was experimentally demonstrated [103] that the channeling efficiency at the edge is the same as that at the centre, despite different positions of the goniometer, but the accuracy was only about 65 μm (resolution of the drift chambers). This focusing-like twist in the horizontal plane agrees well with the survey of the edge twist effects given in Sect. 3.9.2. Further understanding of the crystal extraction experiments can be achieved with the measurements of the ‘septum width’ (in the range 40 to 60 μm) reported in Sect. 3.9.2.

The single-pass transmission for the same crystal was simulated also for 120 GeV protons with different incident angular distributions (Gaussian with angular divergence σ_θ). The results are shown in Table 4.1.

Table 4.1. Crystal bending efficiencies (%) computed for a Gaussian beam of angular divergence σ_θ . Bending angle = 8.5 mrad, proton energy = 120 GeV, θ_c = 14 μ rads.

	$\sigma_\theta \ll \theta_c$	$\sigma_\theta = \theta_c$	$\sigma_\theta = 40 \mu\text{rad}$	$\sigma_\theta = 80 \mu\text{rad}$	$\sigma_\theta = 160 \mu\text{rad}$
F	51.5 ± 2	24.8 ± 0.8	8.9 ± 0.7	4.4 ± 0.2	1.8 ± 0.2

4.3.2 The SPS Extraction Set-Up

The experimental scheme used to extract protons with a bent crystal from the circulating beam in SPS is shown in Fig. 4.6. Two silicon crystals, 18 mm high, 1.5 mm thick, and 30 mm long, were bent by 8.5 mrad and could be used for extraction alternatively. The particles could traverse the central 10 mm of the crystal height without touching the bending device (Fig. 4.6). The crystals were cut parallel to the (110) planes with an accuracy < 200 μ rad, then polished and etched (Syton technique) to obtain a flat surface. The goniometers could orient the crystal with a step size of 4 μ rad, and translate it normal to the beam.

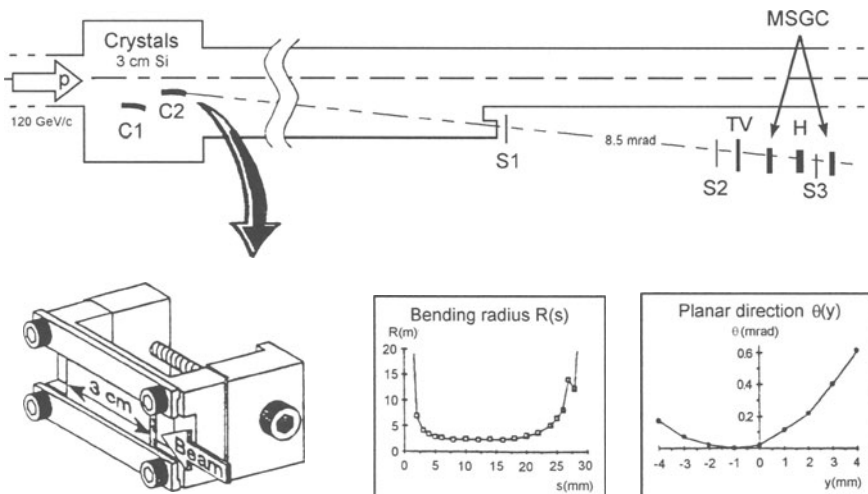


Fig. 4.6. The SPS experimental arrangement. Also shown are a crystal mounted on its bending device, the bending radius along the beam, and the orientation of the (110) planes as a function of the vertical position at the crystal face.

A crystal deflected the protons at 8.5 mrad horizontally towards the centre of the SPS. The extracted protons were detected 20 m downstream. The beam was observed with a scintillating screen (CsI), and its profile was monitored by a scintillating hodoscope of 32 horizontal by 32 vertical strips (1 mm

wide). Two sets of horizontal and vertical microstrip gas chambers (MSGC) with a pitch of 0.2 mm, placed 1 m apart, measured the divergence and profiles of the extracted beam. Three scintillation counters, S1, S2, and S3 were used in coincidence as a trigger for the detectors. The extraction efficiency was measured as the ratio of protons extracted to protons lost in the SPS during the same time interval. The proton loss was obtained from the beam lifetime measurements; the rate of protons extracted was determined by integrating the beam profiles measured by the hodoscope after subtracting the background.

The measurements were made with a 120 GeV coasting proton beam of 5×10^{11} intensity. The SPS shows hardly any nonlinear effects and natural diffusion at this energy, resulting in a beam lifetime > 100 hours. The crystal was placed at a distance of 10 mm (6–10 beam r.m.s size) from the closed orbit, where the undisturbed-beam halo has only a few particles. The beam was excited horizontally with a white noise induced on a pair of condenser plates, with a typical rms deflection of 0.001 μrad per pass. According to simulation [136] the protons should be incident on the crystal with the impact parameters in a sub-micron range and the angular divergence $< 5 \mu\text{rad}$.

4.3.3 A ‘Twisted’ Crystal

The first extraction experiments [108] were performed with a ‘Serpukhov-type’ bending device, as shown in Fig. 4.6. Typically, 6×10^5 protons were extracted per second, for a beam lifetime in the range of 10 to 30 hours. The extraction efficiency was found to be about 10%. When the crystals were prealigned with a laser system, the optimum crystal alignment could be found in about one hour. Most of the results obtained were more sophisticated than expected: (a) the extraction efficiency, around 10%, was smaller than expected for a parallel beam; (b) extraction occurred in the angular range of 200 μrad FWHM, much wider than the beam divergence or critical channeling angle $2\theta_c$; (c) two peaks appeared both in the horizontal and in the vertical profile of the extracted beam at a crystal orientation far from optimum; (d) the angular range of extraction depended on the vertical beam position.

It was suggested that these effects have their origin in the anticlastic bending of the crystal (a ‘vertical twist’). In laser measurements [108] it was found that the bent crystal is indeed deformed vertically. As a result, the planar direction at the entrance to the crystal was approximately a parabolic function of the vertical position shown in the inset of Fig. 4.6. The longitudinal curvature of the crystal was constant in the middle part, and died away to 0 at the ends (the inset of Fig. 4.6).

In order to experimentally investigate the twist effect, different vertical beam positions (bump) at the crystal location and different vertical emittances ϵ_V have been tried. The behavior of the beam profiles and of the angular scans was qualitatively as expected from the crystal geometry. Ta-

ble 4.2 shows the widths measured for the beam profiles and for the angular scans.

Table 4.2. Summary of the simulation compared to the measurements. The FWHMs are rough estimates.

	FWHM	Simulation bad surface	Simulation good surface	Experiment
nominal ^a				
	X /mm	1.9	1.7	2.0
	Y /mm	3.4	1.7	3.5
	angular scan / μrad	140	30	110 ^b , 200
	efficiency (%)	18	40	10
bump 1 mm				
	X /mm	3.5	1.1	1.6 ^b
	Y /mm	3.1	1.8	2.3 ^b -3.0 ^b
	angular scan / μrad	170	90	135 ^b
	efficiency (%)	16	24	8
bump 2 mm				
	X /mm	2.2 ^c	1.0	1.6 ^b -3.0 ^b
	Y /mm	2.2 ^c	2.0	3.3 ^b
	angular scan / μrad	260	200	170 ^b
	efficiency (%)	12	15	
$\epsilon_V = 1.5 + \text{scrapping}$				
	X /mm	1.6	0.8	0.8
	Y /mm	1.7	0.7	1.3
	angular scan / μrad	110	25	70
	efficiency (%)	19	52	

^a The nominal vertical position in the experiment could not correspond exactly to that of the simulation. ^b Data obtained with reduced ϵ_V . ^c Minimal values: since the peak was not prominent, these numbers varied up to 3.0 (X) and 2.7 (Y).

4.3.4 Computer Simulation of Extraction

A detailed computer simulation was performed [107] with parameters matching those of the SPS experiment. Earlier, the theoretical comparisons [143, 144] with extraction experiments [137, 138] were restricted by analytical estimates only, which gave the right order of magnitude. The computer simulations considered idealized models only and predicted the extraction efficiencies always in the order of 90%–99% (e.g. [143, 144]) while real experiments handled much smaller efficiencies, in the order of 0.01% [137, 138]. The considered-below theoretical work has been the first and rather detailed comparison between the realistic calculation from the first principles (computer simulation) and the experiment.

The measured crystal properties (including the vertical twist) were used as an input to the simulations with the CATCH code. The crystal was assumed to have a perfect lattice. Over 100 000 protons have been tracked both in the crystal and in the accelerator for many subsequent passes and turns until they were lost either at the aperture or in interaction with crystal nuclei.

In the simulation, the assumptions about quality of the crystal surface were rather conservative: miscut angle (between the Si(110) planes and the crystal face) $200 \mu\text{rad}$, surface nonflatness $1 \mu\text{m}$, plus $1 \mu\text{m}$ thick amorphous layer superposed. This defines a ‘septum width’ of a few μm . All these details were taken into account for the protons tracked near the surface (as well as at the *bent surface*). Two options were considered. The *first*, with impact parameter below $1 \mu\text{m}$ and surface parameters as described above, excludes the possibility of channelling in the first pass through the crystal. This is compared to the *second* option, in which the crystal surface is assumed perfect, i.e., with a zero septum width.

Table 4.2 summarizes the extraction efficiencies, the widths of the angular scans, and those of the extracted-beam profiles. The efficiency as a function of the crystal angle is shown in Fig. 4.7 for a bump of 1 mm. The beam profiles simulated with a crystal misaligned with respect to the maximum of the angular scan had the same characteristics as the measured ones and a sharp profile was reproduced for an aligned crystal; two-dimensional profiles are shown in Fig. 4.8a,b.

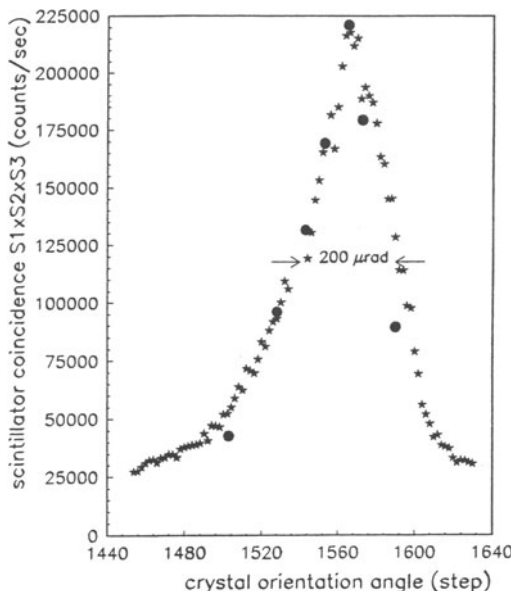


Fig. 4.7. Angular scans of efficiency for a twisted crystal. Measurement (*) and simulation at a bump of 1 mm (●).

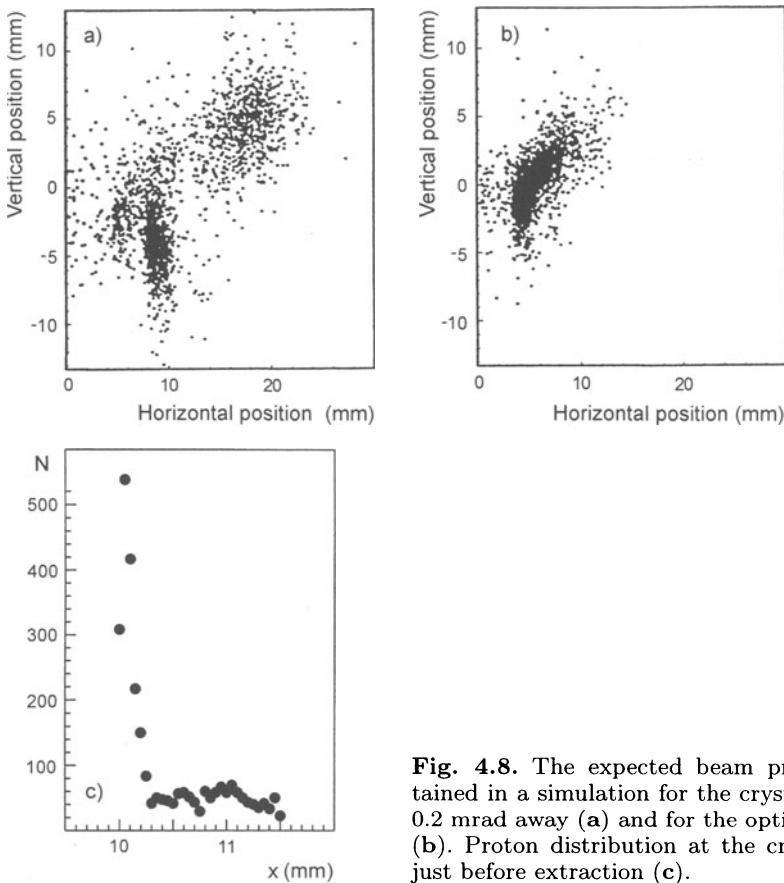


Fig. 4.8. The expected beam profiles obtained in a simulation for the crystal turned 0.2 mrad away (a) and for the optimal angle (b). Proton distribution at the crystal face just before extraction (c).

In the SPS experiment, the nominal vertical position was ~ 1 mm away from the ‘twist middle’. Typically, ϵ_V was $\sim 10\pi$ mm mrad. Therefore the number of 16% for the peak efficiency (and 170μ rad for the angular scan FWHM) seems the most relevant one to compare with the experimental results, namely $10 \pm 1.7\%$ and 200μ rad. In the simulation repeated with $\epsilon_V = 20\pi$ mm mrad the peak efficiency reduced to 15%–16% for the crystal in the nominal position (in the experiment, ϵ_V ranged up to 30 – 40π mm mrad). The systematic error caused by some uncertainties in the vertical position, ϵ_V , and twist detail was estimated as a few per cent for the peak efficiency.

The distribution of extracted protons over x at the crystal face, Fig. 4.8c, is of particular interest. About half of the protons were channeled at the crystal edge, $b \simeq 0.1$ mm. This peak is a contribution of pass 2; its weight and position are due to a low scattering in the first passage (through the very edge of the bent crystal) of the incident protons. This peaking, coupled with

the possible effect of Fig. 4.5b, could explain some (run-to-run) variability in the efficiency observed in the experiment, and also explain some of the overestimated efficiency in the simulation (see also Sect. 4.3.7).

From the analysis of the simulation results one sees that the perfect-surface simulation predicted narrow high peaks, which have not been observed. The imperfect-surface option, however, is approximately consistent with the experimental observations. Both the angular scan FWHM and the efficiency value depend on the bump in the same way as observed experimentally. The twist effect was not important for the peak efficiency, and cannot alone explain the large angular width of the extraction.

A Crystal with a New Geometry. Following the above analysis, the extraction was simulated [107] for a new crystal with another geometry ('U-shaped', Fig. 4.9) which has no twist. The simulation studies were performed prior to the measurements with the U-shaped crystal. The model followed the parameters and design of this crystal, with the same SPS setting. Again the two options, an imperfect or perfect edge, have been studied.

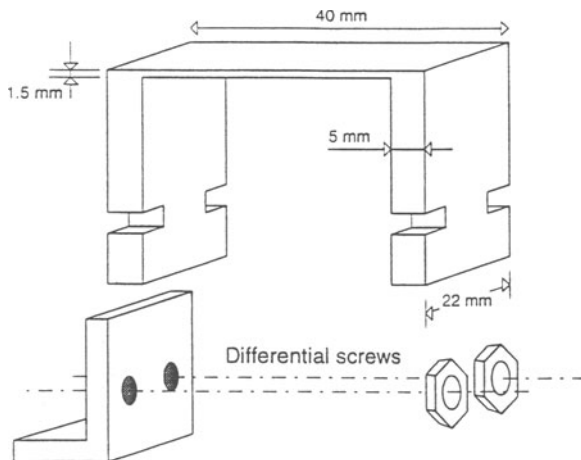


Fig. 4.9. U-shaped crystal.

Figure 4.10 shows the angular scan (as narrow as $70 \mu\text{rad}$ FWHM) of the efficiency simulated for the U-shaped crystal with edge imperfections; a comparison to the measurements shows a good agreement. As compared to the 'twisted' crystal, no sizeable change in the peak efficiency was expected, again in accord with the observations. This agreement indicates that this new crystal also has edge imperfections. For an ideal crystal and a parallel incident beam, the simulation predicted a peak efficiency of $\sim 50\%$ and a very narrow angular scan ($25 \mu\text{rad}$ FWHM).

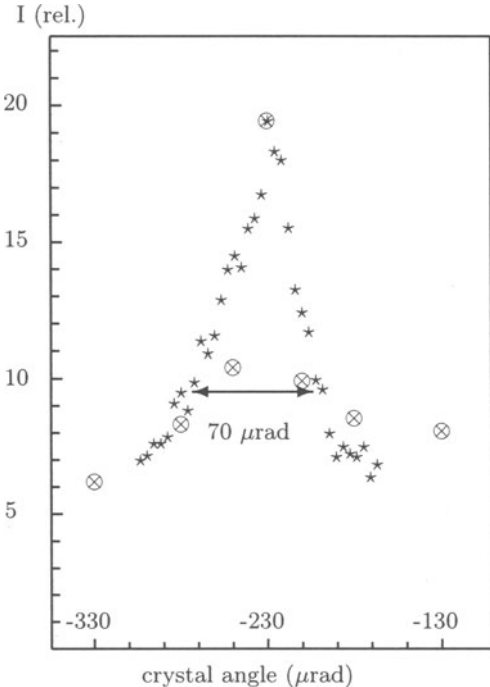


Fig. 4.10. The angular scan of extraction with a U-shaped crystal. Prediction (\otimes) and measurement ($*$).

4.3.5 A ‘U-shaped’ Crystal

In a later design of the bending device the dependence of the crystal-face orientation on the vertical coordinate was eliminated [150]. This was achieved with the U-shaped crystal slab shown in Fig. 4.9. The ‘legs’ of the U were 5 mm thick with a 3 cm long \times 1.5 mm thick part between; the overall length was 4 cm. As a result, the middle part (3 cm long) was uniformly bent, while both ends (5 mm long each) were straight. Laser measurements have confirmed the absence of a vertical twist in the crystal entry face and the uniform bending of the middle part.

With this crystal, the width of the angular scan is decreased to 70 μrad FWHM (Fig. 4.10). At the same time, the peak efficiency does not change. Both findings meet the theoretical expectations for a crystal with edge imperfections (see the section above).

Again, various beam positions at the crystal and various amplitudes of the noise were tried. However, no spectacular change in the crystal behavior was seen. Indirect evidence for multi-pass extraction was obtained in the form of a big vertical divergence of the extracted beam (scattered in the inefficient passes in the crystal).

4.3.6 A Crystal with an Amorphous Layer

In order to verify the idea [107] that the multi-pass channeling dominates in the crystal extraction at SPS, another SPS experiment employed a crystal with an amorphous layer at the edge to suppress the channeling in the first passage of the protons [152]. The layer was formed from SiO with a thickness of $\simeq 30 \mu\text{m}$. The ‘amorphosized’ crystal was one of the old twisted crystals used for earlier extraction studies.

The extraction efficiency with this crystal was indeed of the same order of magnitude as found without an amorphous layer, thus confirming the prediction [107] that the first-pass channeling is suppressed in the SPS crystals, because of either poor crystal quality or the SPS conditions. The experiment used different noise amplitudes to vary the primary impact parameters. Different vertical positions of the beam at the crystal have been tried, in analog with the earlier studies. The crystal behavior was similar to that of the older crystals.

4.3.7 A More Realistic Simulation

The CATCH simulations have shown a good qualitative agreement between the theory and measurements. The major result of these simulations was the prediction of the edge imperfection of the crystals used for extraction at SPS; it was confirmed by the SPS experiment using a crystal with an amorphous layer. The simulation was able to successfully predict the angular dependence for the crystal with a new geometry (‘U-shaped’), as well as the peak efficiency relative to the old crystal.

The major disagreement remained in the absolute value of the efficiency: the theory overestimated it by a factor of ~ 1.5 . The reasons for this discrepancy were investigated, by making a more detailed simulation [146]. Since the CATCH simulations for single-pass channeling in a well-defined situation have been in agreement with measurements, within $\sim 10\%$ or so, the above disagreement needs an explanation. Overestimate of the channeling efficiency might mean an underestimate of the scattering and/or losses in the multiple passes in the crystal. It is clear that the parameters influencing crystal extraction are not defined perfectly; there are several unknowns in the model, such as the impact parameters and quality of the crystal edge.

In the subsequent simulations the realistic details of the crystal design, such as the ‘legs of U’ (the scattering here was missed previously) were introduced. The window for the extracted protons was $\pm 30 \mu\text{rad} (\pm 2\theta_c)$ from the extraction line, in order to better match the experimental procedure (earlier, all protons bent at $>8.0 \text{ mrad}$ were accepted). The large-angle Coulomb and nuclear elastic scatterings have been taken into account.

One of the points to be clarified by the new simulation was whether one needs a big septum width of the crystal to explain a low efficiency. The qualitative trend in the modelling – from an ideal crystal to a more and more

realistic one – is clear. After a strong discrepancy between the real crystal and the ideal model, the first move was to introduce a vertical twist, Fig. 4.5a, and then a thin, $\sim 1 \mu\text{m}$, surface irregularity. The next step may be to adopt a horizontal twist, Fig. 4.5b, or just assume a bigger septum width t .

Figure 4.8c from the previous simulation gives a hint on why the efficiency at SPS can be sensitive to the septum width t in this range. About one half of the extracted protons have b in the range 50–100 μm , due to a gentle scattering in the first passage (through the crystal edge); this half of the protons extracted on pass 2, which has, thus, a big weight caused by a low divergence of the incident protons. Suppressing pass 2 with $t \simeq 100 \mu\text{m}$, one could possibly reduce the efficiency. Note, however, that suppression of channeling at these depths is poorly understood by the traditional methods of crystal-structure analysis, which claim the crystal surface perfection to be within 50 Å.

Table 4.3 shows the computed peak efficiency as a function of the septum width t (modelled as an amorphous layer) of the U-shaped crystal. The efficiencies are now in reasonable agreement with measurements. The dependence on t is rather weak; this agrees with the experiment where the 30- μm amorphous layer did not affect the efficiency.

Table 4.3. The peak efficiency F (%) for different septum widths t (μm). The statistical error is 0.6 %.

$t / \mu\text{m}$	1	20	50	100	200
F (%)	13.9	12.4	12.9	10.9	8.2

4.3.8 Crystal Optimization

The length of the Si crystal, 3 cm, used in the extraction experiment is optimal to bend the 120 GeV proton beam by 8.5 mrad with a *single* pass. However, the range of the optimal length is rather broad, roughly from 1 to 5 cm. The efficiency of the *multi-pass* extraction is defined by the processes of channeling, scattering, and nuclear interaction in the crystal. All these processes depend essentially on the crystal length L . As the scattering is added, it is qualitatively obvious that the optimal length is reduced as compared to bending with a single pass.

The optimization with the CATCH simulations was made with the assumption of a uniform crystal curvature, no twist and the parameters of Sect. 4.3.4. The results are plotted in Fig. 4.11. For a perfect surface there is almost no dependence for $L \geq 1 \text{ cm}$ in the range studied, but for an imperfect surface there is an important dependence. A new optimum around $L \simeq 0.7 \text{ cm}$ almost doubles the efficiency as compared to that for the 3 cm

crystal. A short length (~ 1 cm) could be a ‘cure’ for any imperfection of the crystal, because the reduction in a single-pass transmission is compensated for by the number of passes ($\sim 1/L$).

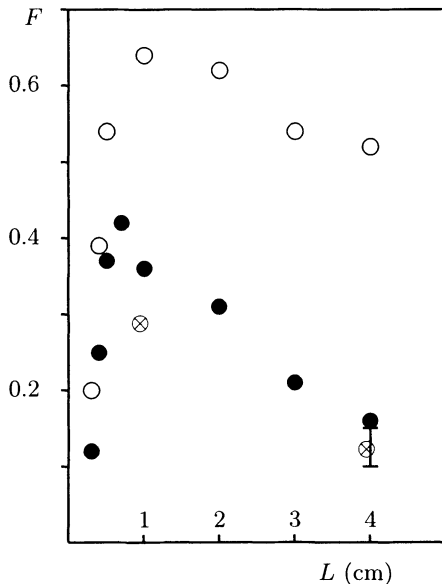


Fig. 4.11. The SPS extraction efficiency vs crystal length. For a perfect surface (○) and $t = 1 \mu\text{m}$ (●). The \otimes are for the U-shaped design and $t = 20 \mu\text{m}$. Also shown is the measured range of efficiencies, 10%–15% for the 4-cm U-shaped crystal.

While the crystal length affects the physical processes in the crystal (channeling, scattering, and nuclear interaction), the transverse size of the crystal may affect the geometrical considerations (‘geometrical efficiency’). Notice, however, that all the circulating protons with sufficiently large amplitudes are intercepted by the crystal irrespective of its thickness, sooner or later. Therefore, the thickness is only of marginal importance for extraction. It may matter if the protons are intercepted somewhere else other than by the crystal (e.g., in the crystal holder); however, such interceptions should be avoided. Greater thicknesses may even be unfavorable for the machine optics (Sect. 4.2.6).

Figure 4.11 shows also two points from a more realistic simulation (Sect. 4.3.7) with a U-shaped design and $t = 20 \mu\text{m}$. The shorter crystal had 1-mm ‘legs’ and 8-mm bent part (10 mm in total), and has shown an efficiency near 30%.

4.3.9 Conclusions

The extraction of protons by a crystal from the halo of a beam in the SPS was successfully demonstrated and proven to be reliable. The extraction results are to a large extent understood. Efficiencies of about 10 % have been measured irrespective of the proton impact parameters, in the multi-pass mode. The crystal-extraction theory provides a reasonably fair prediction for the experiment when the characteristics of the real crystals are taken into account. Moreover, such a theoretical analysis may be a useful tool for studying possible imperfection factors in the extraction. The efficiency of the SPS extraction may be strongly increased, either by improving the crystal-edge perfection (for the single-pass mode), or by shortening the crystal (for the multi-pass mode).

4.4 Crystal Extraction from the Tevatron

At Fermilab, the collaboration E853 between American and Russian physicists has performed crystal extraction experiment [54, 93] at the superconducting accelerator Tevatron at an energy of 900 GeV. The 900-GeV proton beam has been successfully extracted from the accelerator with a 4-cm silicon crystal [140]. Since the experimental data is being analyzed, we concentrate on the qualitative discussion and on the detailed Monte Carlo simulation. This experiment has several new features, which deserve special considerations [156].

4.4.1 Qualitative Discussion of the Extraction

The E853 experiment at Tevatron has several essential differences from its analog (RD22) at CERN SPS. The first one is the much higher energy (900 vs 120 GeV). The presence of superconducting magnets imposes an extra restriction on the particle loss localization. Another interesting difference is a ‘vertical’ extraction scheme instead of a ‘horizontal’. A vertical scheme is an extraction scheme with the crystal atomic planes *perpendicular* to the crystal face in touch with the beam. In both schemes, RD22 and E853, the crystal is horizontally offset from the beam; as a result, in both schemes the beam is diffused or kicked in the horizontal plane to reach the crystal. However, in RD22 the protons trapped by the crystal are channeled and bent in the same horizontal plane, whereas in E853 the channeling and bending occurs in the vertical plane.

In the RD22 scheme one has to align the crystal only in the horizontal plane, with an accuracy equal to the Lindhard angle ($14 \mu\text{rad}$ at 120 GeV), and with no restriction on the vertical plane. In the E853 scheme one should align the crystal in both planes: in the channeling plane (vertical) with the

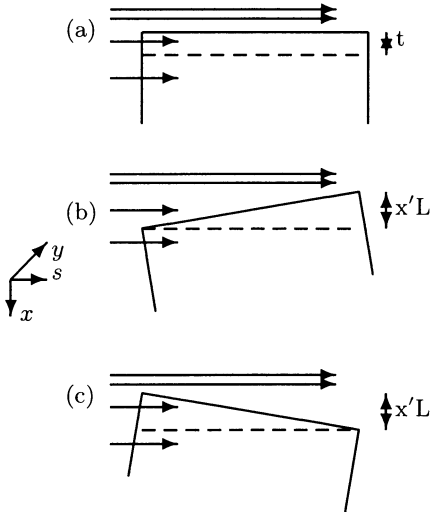


Fig. 4.12a–c. Sketch of a proton interaction with an edge of the horizontally tilted crystal. The direction of proton motion is shown with arrows. The vertical axis is normal to the figure plane. (a) Perfectly aligned crystal. The septum width t is shown. (b) Tilt with $x' > 0$. (c) Tilt with $x' < 0$. The range of inefficient impact parameters, $x'L$, is shown.

same accuracy ($6 \mu\text{rad}$ at 900 GeV), and in the horizontal plane, in order to keep the crystal face parallel to the incident protons (Fig. 4.12a–c).

This necessity to tune two angles may appear as a serious inconvenience. However, this extra degree of freedom provides an excellent possibility to study the process of crystal extraction in much detail. One can, e.g., measure the septum width of a crystal and the dependence of the extraction efficiency on it, the distribution of the primary and secondary impact parameters at the crystal, and the contributions to the efficiency from the first and secondary passes in the crystal.

Let us see what happens if the crystal is misaligned with respect to the beam particles. With a vertical tilt, y' , the protons are misaligned to the crystal planes at first incidence. After scattering in one or a few inefficient passes, and several turns in the accelerator, some protons come parallel to the crystal planes and hence are trapped in the channeling mode. The width of the vertical angular scan thus reflects the divergence of the incident beam, the angle of scattering in crystal, and the angular acceptance of the crystal planes (Lindhard angle).

With a horizontal tilt, x' , the orientation of the atomic planes y' with respect to the beam does not change. Depending on the sign of x' , either the upstream end of the crystal approaches the beam (we define $x' < 0$ in this case), or the downstream one ($x' > 0$); see Fig. 4.12a–c. Because of the x' tilt, a range for the inefficient impact parameters (*septum width*), as thick as $t = |x'|L$, occurs at the crystal edge; $L = 4 \text{ cm}$ is the crystal length. The protons incident in this range, $0 < b < t$, do not traverse the full length of the crystal (Fig. 4.12a–c). The result of the x' tilt depends dramatically on the sign of x' .

In the case of $x' > 0$, the protons traverse the downstream edge. This edge is misaligned by ~ 0.64 mrad (the crystal bending angle) with respect to the beam particles. Therefore, these protons pass through the crystal edge as they would through an amorphous substance. This case imitates the crystal with an amorphous near-surface layer (septum width) as wide as $t \approx x'L$. Measuring the extraction efficiency F as a function of x' for $x' > 0$, one measures the dependence of F on the septum width t . From theory [153, 154] one expects a very weak $F(t)$ dependence at high energies. The confirmation of this would be quite encouraging for multi-TeV applications of crystal extraction. Notice that the minimal step of the septum width scan could be very fine: with $\delta x' = 2.5$ μ rad and $L = 4$ cm one has $\delta t = 0.1$ μ m.

In the case of $x' < 0$, the protons traverse the upstream edge. The upstream face is aligned with respect to the beam. Therefore, many particles are trapped in the channeling mode. However, those incident in the range $0 < b < x'L$ traverse a reduced (< 4 cm) length, thus experiencing a reduced (< 0.64 mrad) deflection. Those particles deflected by a fraction of 0.64 mrad are mostly lost, as they do not fit the acceptance neither of the accelerator nor of the extraction beam line.

The inequality of the two cases, $x' > 0$ and $x' < 0$, causes a strong asymmetry of the $F(x')$ dependence. The efficiency difference, $\Delta F = F(x') - F(-x')$, is proportional to the number of protons incident (with the primary or secondary passes) in the range $0 < b < x'L$. Varying x' and observing ΔF , one investigates the distribution function of the incident protons over the impact parameters b at the crystal, with an accuracy of up to $\delta b = \delta x'L = 0.1$ μ m.

To understand this better, suppose that an ideal crystal is perfectly aligned to the beam. Of all the *extracted* protons, many (suppose, one half) are extracted with the first pass; others are extracted with the secondary passes. Now let us misalign the crystal at $x' = -b_{\max}/L$, where b_{\max} is the maximal impact parameter at the first incidence of protons. Still the same number of protons are trapped in the first pass; but these trapped protons are now *lost*. The other protons are scattered and return at later turns with the secondary impact parameters $b \gg b_{\max}$; some of them are extracted (in much the old manner). One sees that the overall number of extracted protons has been reduced at least by a factor of two over the x' change from 0 to $-b_{\max}/L$. Such a ‘step’ in the $F(x')$ function can be easily observed and interpreted. The ‘step’ width $\Delta x'$ is related to $b_{\max} \approx \Delta x'L$. The ‘step’ height ΔF is the contribution of the first-pass protons to the overall extraction efficiency.

Now suppose the crystal is imperfect: it has a quasi-amorphous layer of thickness $t > b_{\max}$ just at the edge (a septum width). This crystal is insensitive to $b \sim 1$ μ m; however, in just the same way one measures the particle distribution over the *secondary* impact parameters (in a broad range $b > t$).

Notice that for an imperfect crystal angled within $-t/L < x' < t/L$, the x' sign is not important. Both edges, upstream and downstream, are amorphous-like and cannot trap particles. Only for bigger tilts, $x' < -t/L$, can the upstream edge trap and loose protons, in the way discussed above. Therefore, for a septum width $t \neq 0$, one expects the $F(x')$ function to be symmetric within $-t/L < x' < t/L$, but asymmetric for $|x'| > t/L$. The threshold x'_{th} , where the asymmetry of $F(x')$ scan appears, is a measure of the crystal septum width: $t \approx x'_{\text{th}} L$.

The above picture is made more complicated by another interesting phenomenon. The protons incident on a perfectly aligned imperfect crystal with $b_{\max} < t$, have to traverse the full length of the crystal. The corresponding scattering angle, $\theta_s = 10 \mu\text{rad}$, and probability of nuclear interaction, ≈ 0.1 , over 4 cm of silicon are sizable. Suppose, this crystal is misaligned so that $b_{\max}/x'L \approx 0.1$. Then, at first incidence the protons traverse only the crystal edge, with the length ≤ 0.1 that of a crystal. The corresponding scattering, $\theta_s \leq 3 \mu\text{rad}$, and probability of nuclear interaction, ≈ 0.01 , over 0.4 cm of silicon are much smaller. In this case, with lower scattering and less absorption, the protons retain better chances for successful extraction with the later passes than in the nominal case of the perfect alignment. The secondary impact parameters of the scattered protons are still sufficiently large, $\approx 30 \mu\text{m} \gg x'L$, so the ‘gap’ $x'L$ is not harmful.

This analysis indicates that the peak efficiency with an imperfect crystal is achieved at some tilt $x' \neq 0$, i.e. not at perfect alignment. Interestingly, since in the real experiment one scans x' while searching the peak, one arrives at the above situation *automatically!* The case $b_{\max}/x'L = 0.1$ was used as an illustration; the optimal x' will be found automatically in the scan. Further on, we refer to this case as to the ‘pre-scatter’ case, when protons first gently pre-scatter in the crystal edge to come into consideration later with low divergence but high impact parameters.

Understandably, with imperfect crystals the pre-scatter case may appear also for a small negative tilt, $x' < 0$. Then, the $F(x')$ function may have *two* peaks, with a *dip* at $x' = 0$. The width of the dip at $x' \approx 0$ may also be an indicator for the b_{\max} value.

The above ideas [156] are explained again (quantitatively) below in the context of the simulation results, and we illustrate them with the realistic x' scans for different crystals in Figs. 4.13 and 4.14.

Notice that all the experimental data obtained so far indicate that the edge of a real crystal is of poor quality (Sects. 3.9.2 and 4.3). Direct measurement (with photoemulsion and 70 GeV channeled beam) for several crystals of Si and Ge, (110) and (111), gives a ‘septum width’ in the range 40 to 60 μm .

4.4.2 Simulation

With use of the CATCH code [37] tested at SPS, the crystal extraction of 900-GeV protons from the Tevatron beam halo was modelled in [156], with parameters matching the E853 experiment [54, 157].

Objectives. The main objective of this work, besides that of predicting the results of the E853 experiment, was to propose several ideas on how to measure key parameters of the extraction experiment. Since the realistic crystal has a nonvanishing irregularity at the surface, this defines some range of inefficient impact parameters at the edge ('septum width') where channeling is disrupted. In view of the very small impact parameters, the multi-pass mode of extraction may well be the only feasible one. This means the septum width and related issues make up a central point. The following information is essential for understanding the crystal extraction process:

- (a) the efficiency, and relative contributions from the first and subsequent passes;
- (b) the distribution of the primary and secondary impact parameters on the crystal;
- (c) the septum width;
- (d) the dependence of the efficiency on the septum width.

The methods for obtaining this information in the E853 experiment are proposed below. The simulation is used also to analyze the ways to optimize the experiment for the highest efficiency and the optimum conditions for measuring the key parameters.

Procedure. For most of the simulations the crystal was a Si(110) slab that was 40 mm long, 3 mm thick, 10 mm wide, and bent at an angle of 0.64 mrad. The crystal was assumed to have a perfect lattice and to be curved with a constant longitudinal curvature to deflect protons in a vertical direction. As an option, an amorphous layer at the crystal edge and/or irregularities of the surface were also modelled.

The crystal was located 61 m upstream of the C0 point on the Tevatron lattice, with the edge at a horizontal distance of $X = 1.75$ mm from the beam axis. At the crystal location, the machine parameters were $\beta_x = 105.7$ m, $\alpha_x = 0.109$ (horizontally), and $\beta_y = 21.5$ m, $\alpha_y = 0.148$ (vertically); the tune values were $Q_x = 20.5853$ and $Q_y = 20.5744$. The beam invariant emittance was 2.5 mm mrad (1σ), which corresponds to a vertical divergence of $\sigma_{y'} = 11.5 \mu\text{rad}$ and a width of $\sigma_y = 0.24$ mm at the crystal location. A Gaussian distribution of the incident particles over y, y' with the above sigmas was implied.

As mentioned, the horizontal parameters x, x' of the incident particles are defined by the mechanism of diffusion. Simulation of this diffusion, to predict the primary impact parameters and the intensity of the incident protons, is a complicated problem. Luckily, these two processes, diffusion and crystal

extraction, are perfectly unfold in the E853 scheme. The beam parameters in the channeling plane (vertical) are not disturbed by this diffusion. The horizontal impact parameters are quite close to the crystal edge X , being distributed between X and $X + b_{\max}$. Irrespective of the diffusion mechanism, one has $b_{\max} \ll X$, and x' is much smaller than the rms angle of scattering over the crystal length, $\theta_s \approx 10 \mu\text{rad}$. Therefore, the distribution of the secondary passes in the horizontal plane is also practically unaffected by the primary x, x' . The exact value of b_{\max} may have meaning only with respect to the (unknown) ‘septum width’ t . Since t is unknown for the real crystal, one can postulate $b_{\max} = 1 \mu\text{m}$, and then model the crystals with different t .

Results. Figure 4.13 shows the vertical, y' , angular scan of the overall efficiency of extraction for the crystals perfectly aligned in the horizontal angle, $x' = 0$. For an ideal crystal both the overall efficiency and the contribution from the first pass of protons are shown. The peak efficiency of an ideal crystal is $\approx 44\%$. The same figure shows the angular scans for the crystals with septum widths of $t = 1 \mu\text{m}$ (i.e. $t = b_{\max}$) and $t = 50 \mu\text{m}$, where the efficiency at perfect alignment, $y' = x' = 0$, comes down to about 36% and 32%, respectively. However, for the imperfect crystals the real peak was not at $x' = 0$ (see Fig. 4.14 and Sect. 4.4.2). With optimized x' , the peak efficiency increased to 42% and 35% for $t = 1 \mu\text{m}$ and $t = 50 \mu\text{m}$ respectively. The efficiencies and angular scans are quite weakly dependent on the crystal perfection. The width of the vertical angular scan was found to be 50–55 μrad FWHM in the considered cases.

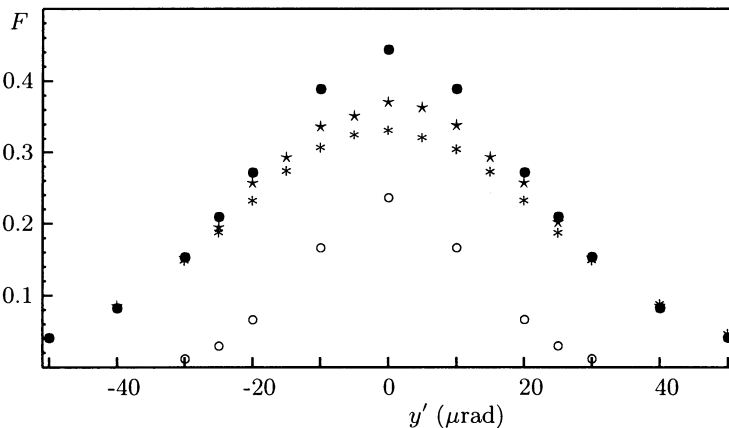


Fig. 4.13. Vertical angular scan of the efficiency for perfect horizontal alignment, $x' = 0$. Ideal crystal: (○) is the first-pass efficiency, and (●) is the overall efficiency. Imperfect crystal: (★) is the overall efficiency with $t = 1 \mu\text{m}$, (*) is the same with $t = 50 \mu\text{m}$.

The horizontal angular scan of efficiency $F(x')$, shown in Fig. 4.14, provides the most interesting information. First of all, the scan has double ‘peaks’ or shoulders as expected from the qualitative discussion in Sect. 4.4.1. The shoulder of ‘pre-scatter’ nature appears at $x' \approx 0.1\text{--}0.2$ mrad for the ideal crystal, at $x' \approx 0.1\text{--}0.2$ mrad and $x' \approx -0.05$ mrad for $t = 1\text{ }\mu\text{m}$, and is subtle for $t = 50\text{ }\mu\text{m}$. The depth of the dip at $x' \approx 0$ (i.e., for perfect alignment) is $\simeq 14\%$ and $\simeq 7\%$ with respect to the peak for $t = 1\text{ }\mu\text{m}$ and $t = 50\text{ }\mu\text{m}$ respectively. The width $\Delta x'$ of the peculiarity (either peak or dip) near $x' \approx 0$ is roughly b_{\max}/L which is 25 mrad in our simulation.

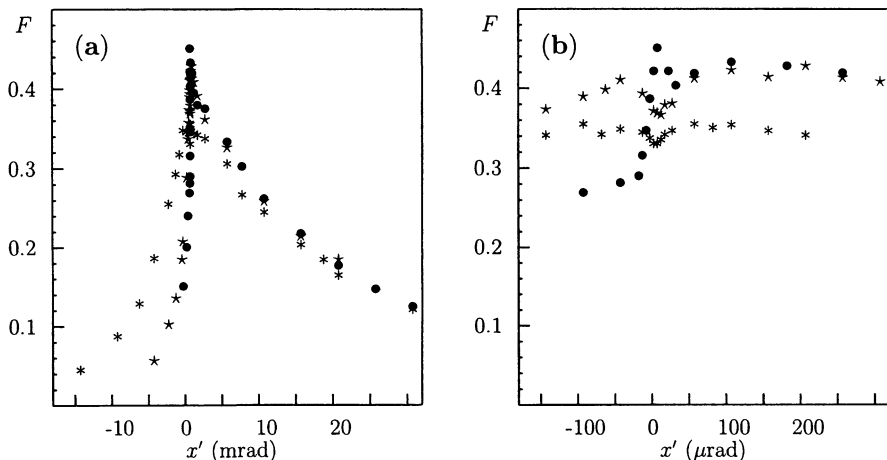


Fig. 4.14. (a) Horizontal angular scan of the overall efficiency for perfect vertical alignment, $y' = 0$. For ideal (\bullet) and imperfect crystals: ($*$) $t = 1\text{ }\mu\text{m}$, (\times) $t = 50\text{ }\mu\text{m}$. (b) Details of the peak.

The efficiency is $1/2$ of the maximum at $x' \simeq 14$ mrad and -0.3 mrad for an ideal crystal (FWHM of the horizontal scan is $\simeq 14$ mrad), at $x' \simeq 15$ mrad and -1.2 mrad for the crystal with $t = 1\text{ }\mu\text{m}$ (FWHM $\simeq 16$ mrad), and at $x' \simeq 18$ mrad and -5 mrad for the crystal with $t = 50\text{ }\mu\text{m}$ (FWHM $\simeq 23$ mrad).

The asymmetry of the scan, $F(x') \neq F(-x')$, is due to the loss of the protons trapped in channeling near the crystal edge (see Sect. 4.4.2). With an ideal crystal, the asymmetry exists for any x' . With a septum width t , the asymmetry can be seen for an angle $\pm x'$ larger than t/L only. In our simulation with $t = 50\text{ }\mu\text{m}$, the scan is symmetric indeed within ± 1.3 mrad but asymmetric outside this range of x' ; note that $50\text{ }\mu\text{m}/40\text{ mm} = 1.25$ mrad. One expects therefore that this x' threshold for an asymmetry will be a good measure of the septum width t . The magnitude of asymmetry also depends on t ; by comparing the scan measured with those simulated, one can deduce t as well.

Furthermore, if one plots the magnitude of asymmetry, $F(x') - F(-x')$, as a function of $x'L$, one obtains a rough estimate of the beam distribution over the impact parameter b at the crystal. We have noticed already that the minimal step $\delta b = \delta x'L = 0.1 \mu\text{m}$ is much finer than the precision of the coordinate detectors, about $100 \mu\text{m}$!

Notice an abrupt decrease in efficiency of the ideal crystal over the range of $x'L$ from 0 to $-b_{\max}$: from 44% at $x' = 0$ to 28% at $x' = -b_{\max}/L$. This provides an excellent possibility to measure the primary b_{\max} with a precision of $\delta b = 0.1 \mu\text{m}$. We point out that with an ideal crystal one can measure a distribution over the *primary* impact parameters (in the range of $\sim 1 \mu\text{m}$). An imperfect crystal ($t > b_{\max}$) is insensitive to b at $\sim 1 \mu\text{m}$; however, in just the same manner one measures the distribution over the *secondary* impact parameters (in the broad range from $\sim t$ to $\sim 1 \text{ mm}$). Clearly, the same idea is applicable to the case of a kick mode, where the impact parameters are very large (say $b_{\max} \sim 0.1 \text{ mm}$). In the kick mode any crystal seems ideal (i.e., $t \ll b_{\max}$); then, if the kicks are reproducible, one can measure the primary distribution over kick b .

The dependence $F(x')$ for $x' > 0$ actually gives the dependence of the extraction efficiency on the septum width $t \simeq x'L$. Since the crystal angling with $x' > 0$ is not exactly the same as the amorphous edge layer of thickness $t = x'L$, in Fig. 4.15 two functions, $F(x'L)$ and $F(t)$, are compared; the latter was simulated for a perfectly aligned crystal with a septum width t .

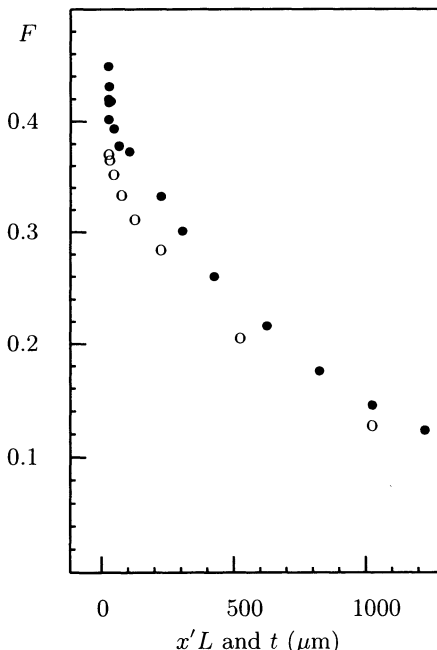


Fig. 4.15. Efficiency as a function of $x'L$ (●) for an ideal crystal, and as a function of the septum width t (○) for an imperfect crystal.

Notice that in the experimental set-up of E853 even an ideal crystal would have an effective septum width of order $0.1 \mu\text{m}$ defined by the finite minimal angular step of the horizontal goniometer, $2.5 \mu\text{rad}$, and a crystal length of 4 cm .

Scattering the channeled protons along the crystal length from the electrons and nuclei of the crystal causes a gradual dechanneling of the initially trapped protons. As the crystal is bent, the dechanneled protons are spread over an angle y' from ~ 0 to the crystal bending angle of 0.64 mrad with a roughly flat angular distribution downstream of the crystal. The number of dechanneled protons is ~ 0.2 times the number of protons in the bent peak. For a perfect Si(110) at 0.9 TeV , one expects $L_D \simeq 40 \text{ cm}$ in a straight or slightly bent crystal, (1.50). In the case of E853 the ‘local’ value of L_D [as derived from the data fit with $\exp(-L/L_D)$] is only $\sim 4 \text{ cm}/0.2 = 20 \text{ cm}$, due to a rapid dechanneling of the particles with the highest amplitudes of channeling.

The vertical profile of the extracted protons at the crystal location is close to that of the primary incident protons, with the width $0.60\text{--}0.65 \text{ mm FWHM}$ roughly independent of t . The primary protons have a width of 0.57 mm FWHM , with a Gaussian shape. The vertical divergence of the extracted beam is defined by the channeling properties of the Si(110) crystal; its full width, $2\theta_c$, was $\approx 12.8 \mu\text{rad}$ ($\theta_c \simeq 6.4 \mu\text{rad}$ is the Lindhard angle), and $\text{FWHM} \approx 9 \mu\text{rad}$. The horizontal divergence is $\simeq 5 \mu\text{rad FWHM}$ with the ideal crystal and $\sim 12 \mu\text{rad FWHM}$ with $t = 1 \mu\text{m}$. It was bigger than that of the incident beam due to a scattering in inefficient passes before extraction. The horizontal profile of protons at the crystal is peaked at the edge. One half of the protons extracted with multi-passes penetrated into the crystal depth by $> 0.3 \text{ mm}$; another half had $b < 0.3 \text{ mm}$.

The results are given for the crystal at room temperature. The actual crystal temperature in E853 may be somewhere between 293 K and 4 K . The extraction was also simulated with the same crystal cooled down to the absolute zero. With this cooling, the extraction efficiency increased by about 1.1 times. One does not expect, therefore, that the simulation results (scans and profiles) will be highly sensitive to the crystal temperature.

Optimization. The efficiency of extraction can be increased with the use of a shorter crystal, and/or with a smaller angular divergence of the incident protons (higher β_y or smaller emittance). Figure 4.16 shows the dependence of the extraction efficiency on the crystal length L , for a uniform bending at 0.64 mrad . Two cases were studied: an ideal crystal, and the crystal with $t = 1 \mu\text{m}$. The efficiency is maximal, near 70%, in the length range from 0.4 to 1.0 cm , irrespective of the crystal perfection and temperature.

The efficiency might be increased further with the use of a ‘horizontal’ scheme (see Sect. 4.4.2) as used at the CERN SPS, because the horizontal divergence of the incident particles is much smaller due to the small impact parameters. Even with the scattering in the inefficient first pass taken into

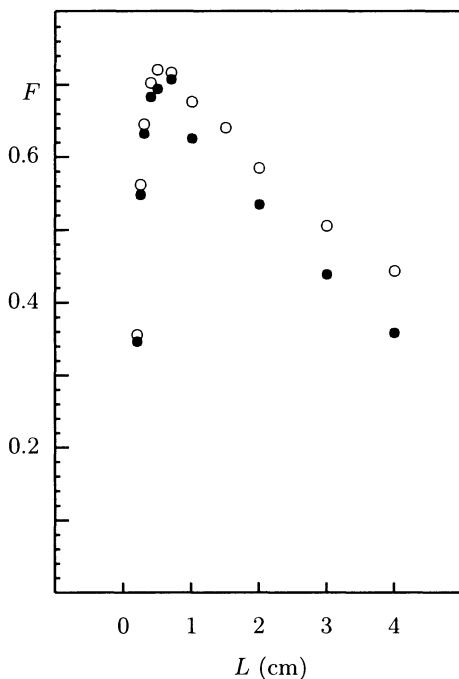


Fig. 4.16. Efficiency as a function of L for the ideal (\circ) and imperfect (\bullet), $t = 1 \mu\text{m}$, crystals.

account, this divergence is quite low and can easily fit the Lindhard angle at 900 GeV.

In contrast to the case with efficiency measurements, a measurement of such parameters as b_{\max} and t is easier when the relative contribution of the secondary passes is smaller. This is the case if the crystal is long (the longer the better), and/or if the beam divergence is smaller; the present length $L = 4$ cm is reasonably matched to these measurements.

4.4.3 Conclusions

We have shown that the key information from the multi-pass crystal extraction process, namely the septum width and the dependence of efficiency upon it, the distribution of particles at the crystal, and the contribution from the first and subsequent passes, can be obtained from the analysis of the horizontal angular scan of efficiency. Using crystal extraction one can study the impact parameters of halo particles and the structure of the crystal edge with an accuracy approaching $0.1 \mu\text{m}$.

The extraction efficiency is expected to reach $\simeq 40\%$, irrespective of the crystal septum width, and can be increased up to $\sim 70\%$ if one uses a shorter (≤ 1 cm) crystal.

The difference in efficiency between the ideal and imperfect crystals is very low, because of multi-pass extraction dominating at high energies, and partly due to the effect of gentle ‘pre-scattering’ in the edge of a crystal tilted horizontally. The small drop in the efficiency, from 44% to 42%, indicates that a double-scattering scheme for the extraction considered in Sect. 4.2.9 would have little advantage in E853. The studies described here provide an elementary (and automatic) solution to the problem of a finite septum width and infinitesimal impact parameters.

In [148] it was proposed that crystal extraction is used for cleaning the Tevatron beam halo. In addition to a bent crystal the use of two scattering elements, one amorphous and one thin crystalline is suggested, in order to increase the impact parameters with respect to the edge of the bent crystal; all the three elements have to be aligned in position and angle with high precision (few μm and μrad). In the computer simulation of the ‘horizontal’ extraction an efficiency of nearly 99% was found.

4.5 Proton Extraction from the Large Hadron Collider

4.5.1 Introduction

Recent studies have made significant progress in efficient steering of high energy charged-particle beams using bent crystal channeling. The CERN experiments on the crystal-assisted beam extraction from the SPS accelerator are of particular interest. These studies are aimed at the possible application of channeling for beam extraction from a multi-TeV machine [53, 54, 155], where an extracted beam would open up very interesting possibilities for fixed-target physics, e.g., beauty physics [53, 54, 104].

The extraction process is based on multiple passes of the beam particles through the crystal. It is therefore not straightforward to extrapolate the SPS experimental results to higher energies. On the other hand, computer simulation of the SPS experiments gave results in good agreement with the measurements (Sect. 4.3). Making use of the same simulation code [37], the crystal extraction of protons from the Large Hadron Collider (LHC) beam halo, has been modelled [158, 145]. Emphasis was given to the crystal extraction efficiency, the background produced with the aligned crystal, and the effects of multiple passes through the crystal. The influence of crystal edge imperfections, and compatibility of the crystal extraction with other accelerator systems was considered.

In this simulation protons were tracked through the curved crystal lattices in $\sim 5 \mu\text{m}$ steps by applying the CATCH code. The crystal was assumed to have a perfect lattice and a constant longitudinal curvature.

The distribution of particles in the LHC beam halo had been studied earlier [121] for the purpose of design of the LHC beam cleaning collimators. The halo is continuously being fed with scattered protons from the beam core.

At the design luminosity of $10^{34} \text{ cm}^{-2} \text{ s}^{-1}$ various scattering processes feed $\sim 4 \times 10^9$ protons per second [121] to the halo, which should be compared to the experimental needs of $\sim 10^8 \text{ s}^{-1}$ on a fixed target [104]. When the accelerator operates in a collider mode, strong nonlinear effects cause the halo particles to diffuse further into the halo region. Any collimator (or crystal) placed at the beam periphery would intercept the scattered protons. The impact parameters and divergence of the intercepted particles are defined by the transverse speed of the amplitude growth for the particle betatron motion in nonlinear fields. In the studies [121] of an LHC beam cleaning insertion it was found that protons hit a collimator very close to its edge, with an impact parameter $b \sim 1 \mu\text{m}$, and a rms. divergence $\sigma_\theta \sim 1 \mu\text{rad}$. To supply particles from the beam core into halo, one may also apply noise to the circulating beam [135, 136], thus providing a controllable source of halo while keeping the beam core undisturbed; however, b is still in the micron range. Such low values of b call for a high quality of the crystal edge. As an alternative to having a perfect edge, one should investigate the multi-pass extraction mode. This mode is also discussed below.

4.5.2 Simulation of a Single Pass

The feasibility of crystal extraction depends on the integration of the crystal into the accelerator lattice. The bending angle needed for proton extraction from the LHC is equal to 0.7 mrad [53]. First the crystal transmission is investigated, simulating a single pass of the 7.7 TeV proton beam (with $\sigma_\theta = 1.5 \mu\text{rad}$) through the aligned bent crystal. Figure 4.17 shows the computed angular distribution of the protons downstream of the 5-cm-long silicon (110) crystal.

About 40% of all incident protons are bent the full angle of 0.7 mrad. This fraction (crystal ‘efficiency’) is plotted in Fig. 4.18 as a function of the crystal length L . It saturates for $L \geq 5 \text{ cm}$, as the p/R ratio becomes much lower than the critical value (6 GeV/cm). This dependence agrees, within 5%, with a calculation from the continuum model of channeling (Fig. 2.2) if the critical distance x_c (maximal allowed amplitude of a channeled particle) is taken as $d_p/2 - u$, where $d_p = 1.92 \text{ \AA}$ is the interplanar spacing of Si(110), $u = 0.075 \text{ \AA}$ is the amplitude of the atomic thermal vibrations. Beam bending with (111) planes of silicon was also simulated. The ratio of efficiency, Si(110) to Si(111), was found to be 1.21 ± 0.03 for $L = 5 \text{ cm}$. Figure 4.18 shows one example for the crystal of germanium (110) which has a field twice as strong as that of silicon.

In the simulation, the critical angle θ_c (maximal angle of the channeled particle with respect to the atomic plane) was found to be equal to $2.3 \mu\text{rad}$ for Si(110) planes with small bend ($pc/R = 0.1 \text{ GeV/cm}$). The θ_c value has decreased down to $1.8 \mu\text{rad}$ for the stronger bend of 1.1 GeV/cm . Clearly, the crystal efficiency depends on the incident beam divergence σ_θ . For $\sigma_\theta > \theta_c$ the efficiency decreases like $1/\sigma_\theta$. For $\sigma_\theta < \theta_c$ some increase of efficiency may

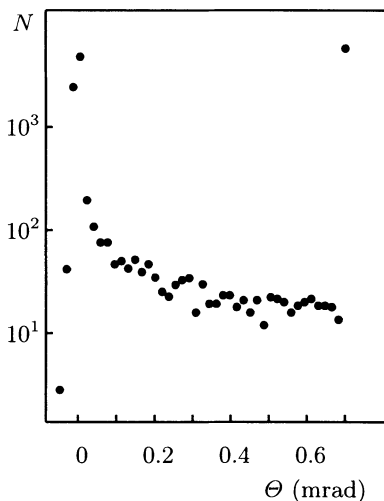


Fig. 4.17. Angular distribution of the primary protons downstream of the aligned bent crystal of Si(110).

be expected. In an example for $\sigma = 0$ the bending efficiency increased to $65 \pm 2\%$ (Fig. 4.18).

Figure 4.17 shows that a considerable fraction of the protons are scattered in a broad angular range, from ~ 0 to the bend angle of 0.7 mrad. This background is due to dechanneling of the protons captured initially, caused by the multiple scattering along the crystal. The fraction between the bent and unbent peaks contains about 25% with respect to the protons in the bent peak. The dechanneling loss caused by the scattering is commonly characterized by the dechanneling length L_D . For a perfect Si(110) at 7.7 TeV, one expects $L_D \simeq 340$ cm in a straight crystal, and $L_D \simeq 140$ cm with the bending of $p v / R = 1.1$ GeV/cm [27, 29]. However, dechanneling follows the law $\sim \exp(-L/L_D)$ only for L comparable with L_D ; for $L \ll L_D$ the dechanneling rate is essentially higher (see the discussion and simulations in Sect. 1.4). In our case the ‘local’ value of L_D [derived from the data fit with $\exp(-L/L_D)$] is only ~ 5 cm/0.25 = 20 cm; this is due to rapid dechanneling of the few particles with the highest amplitudes of channeling (of order and above x_c). In analytical estimates, such particles are simply considered as lost; in Monte Carlo (or a real) crystal this loss is actually a gradual process developed along the crystal length [27] due to nuclear scattering (it is slow at very high energies). Near the unbent peak the elastic scattering of the nonchanneled protons contributes to the background.

The full divergence of the bent peak is $2\theta_c$. The angular distribution near the unbent peak is of more interest. The rms. width of the unbent peak equals $2.4 \mu\text{rad}$. With $1.5 \mu\text{rad}$ for the rms. divergence of incident particles, this gives $1.9 \mu\text{rad}$ for the rms. angle of scattering in the crystal. This is higher than the $1.3 \mu\text{rad}$ of the rms. multiple Coulomb scattering angle over

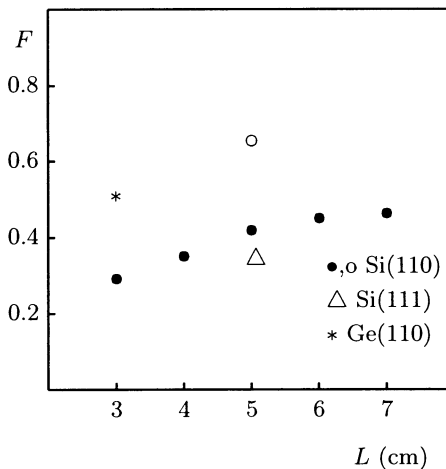


Fig. 4.18. The fraction of protons bent by the full angle of 0.7 mrad, as a function of the crystal length. The dots • and ○ are for a single pass through the Si(110) crystal, △ for Si(111), * for Ge(110). The incident beam divergence is $\sigma_\theta = 1.5 \mu\text{rad}$ for (•, *, △) and zero for (○).

5 cm of silicon. The remainder, also about $1.3 \mu\text{rad}$, comes from the coherent scattering in the field of atomic planes. Notice that the mean angle of the unbent peak is not zero, but $-1.8 \mu\text{rad}$ (about $-\theta_c$); this effect, a volume reflection, is the result of coherent scattering of the nonchanneled particles in a bent crystal. Most of the particles stay in the acceptance of the accelerator, and potentially can be trapped in channeling trajectories on their subsequent passes. However, this is sensitive to details of the accelerator and should be the subject of a more detailed analysis.

4.5.3 Simulation of the Extraction

Because of the absorption (nuclear reactions) and substantial scattering in the crystal, any particle may traverse it only a few times before eventual loss. This corresponds typically to some dozen turns in the accelerator. For such a short period one may assume linear dynamics for the protons in the accelerator described by transfer matrices.

Crystal extraction including multiple passes in the crystal was simulated. The following relevant parameters of the machine have been used: $\beta_x = 250$ m, horizontal tune $0.28 + \text{integer}$; crystal-edge position $X = 2$ mm ($6\sigma_x$) from the beam axis. The incident protons had a flat distribution over the horizontal coordinate x from X to $X + b_{\max}$, with $b_{\max} = 1 \mu\text{m}$; the angular distribution was Gaussian with a rms. value of $\sigma_\theta = 1.5 \mu\text{rad}$. The parameters roughly matched those proposed for the LHC beam cleaning system [121]. The crystal was $3 \text{ mm} \times 3 \text{ mm} \times 50 \text{ mm}$ in size, with a perfect surface, and was perfectly aligned with respect to the incident beam.

The overall extraction efficiency is plotted in Fig. 4.19 as a function of the crystal length L . This function is roughly constant in the studied range of

L. Taking into account the saturation of the first-pass contribution at $L \geq 5$ cm, a value of 5 cm is suggested as the optimal crystal length for the case considered.

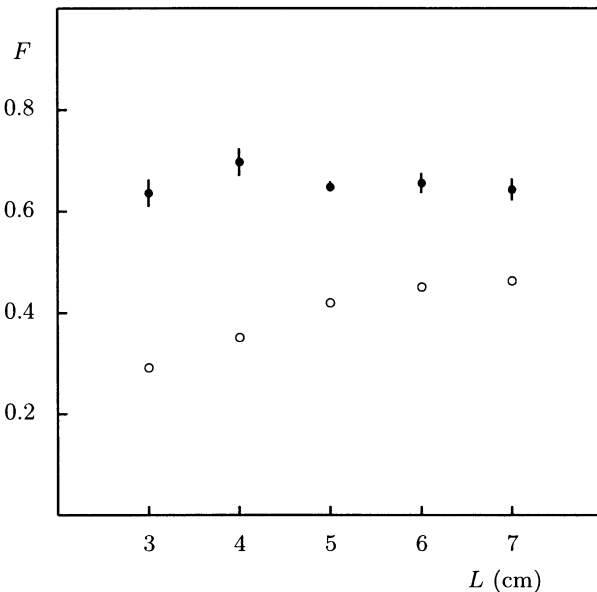


Fig. 4.19. Overall extraction efficiency (\bullet) as a function of the Si(110) crystal length. The \circ are for the first-pass efficiency.

For understanding both the interplay of the crystal with the other accelerator elements (collimators) and the requirements for the crystal-face perfection, knowledge of the distribution of the extracted particles over the transverse coordinate x at the crystal face is essential. Figure 4.20 shows this distribution for protons extracted with secondary passes (on pass 2 or higher), just before extraction. For a perfect crystal one should add a narrow ($\sim 1 \mu\text{m}$) first-pass peak at the edge. Figure 4.20 indicates that the extracted protons have penetrated, with secondary passes, $\sim 1-2 \sigma_x$ into the crystal. This simulation showed that multturn extraction is feasible, provided that

- (a) the cleaning collimators are positioned at least $\sim 1-2 \sigma_x$ outside the crystal edge, in order to reduce the effect on the extraction with *multiple* passes;
- (b) the scattered protons (with amplitudes of $6-8 \sigma_x$) survive in the accelerator for ~ 20 turns.

For a crystal with a perfect surface the first-pass contribution is sufficient and therefore multi-pass extraction is not needed. For b_{\max} comparable to

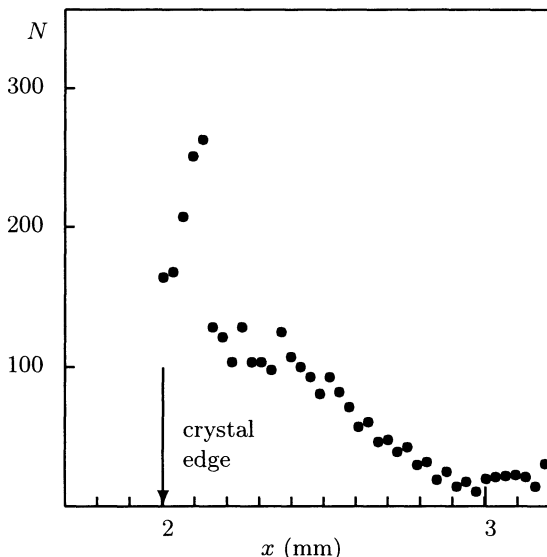


Fig. 4.20. The distribution of the protons extracted with multiple passes, over the transverse coordinate at the crystal face. For a perfect crystal one should add a narrow ($\sim 1 \mu\text{m}$) first-pass peak at the edge ($x = 2 \text{ mm}$).

(or even much lower than) the septum width, multiple passes are of primary importance. In any nonchanneling pass the proton is scattered by some angle θ_s , which in turn increases the amplitude x_{\max} of subsequent betatron oscillations. At some later turn this proton hits the crystal with the impact parameter b increased with respect to its old value by $\Delta b \approx \beta_x^2 \theta_s^2 / 2X$ (in our case $\Delta b \simeq 0.1 \text{ mm}$). The peak in Fig. 4.20 gives the most probable impact parameter $b_{\text{mp}} \sim 0.1 \text{ mm}$; b_{mp} corresponds to the most probable $\theta_s^2 \approx \theta_c^2$ (due to 'volume reflection'): $b_{\text{mp}} \simeq \beta^2 \theta_c^2 / 2X$. This scattering means that a septum width of $\sim 10 \mu\text{m}$ should not be dangerous for the multiple passes. Conversely, with a septum width of $\Delta b_{\text{dead}} \sim 1 \mu\text{m}$ the requirement imposed on the beta function is very weak: $\beta_x \gg \sqrt{2\Delta b_{\text{dead}} X} / \theta_s \approx 25 \text{ m}$, thus leaving us much freedom in designing the extraction optics.

Edge Imperfection. In order to study the influence of an edge imperfection on the extraction, the above simulation was repeated for a crystal with a nonflat surface. The amplitude of the surface 'bumps' was $1 \mu\text{m}$. Values for b_{\max} of $0.1 \mu\text{m}$ and 10 \AA were tried. The distribution of the extraction efficiency over the number of passes and turns was substantially changed. Nonetheless the overall efficiency was about constant and equal, within the accuracy of the simulation, compared to the efficiency of the perfect crystal (the top dots of Fig. 4.19). This encouraging result is due to the fact that a change in the beam divergence caused by scattering in the crystal is minor (in particular

near the very edge of a bent crystal), as compared to the crystal acceptance $2\theta_c$.

4.5.4 Conclusions

One can conclude that the extraction scheme proposed in [53] for the LHC, together with the beam parameters expected at this machine [121], favor an application of crystal channeling for LHC beam steering. An efficiency for the crystal extraction of about 60% is predicted [158, 145]. This value is much the same even with crystal-edge imperfection and extremely low impact parameters for incident protons, owing to the multi-pass mode of extraction. In order not to disturb this multi-pass mode, the other elements of the accelerator should be positioned horizontally $\sim 1\text{--}2 \sigma_x$ outside the crystal edge. With the basics of the crystal extraction physics understood, further work on the design of the extraction system for the LHC can begin. Although the results cannot be readily scaled to other experiments [54, 108], one can compare them to other simulations with CATCH (Sect. 4.3–4.4). One general trend in the results of these simulations, from SPS to Tevatron to LHC, is noteworthy: the difference in efficiency between the ideal crystal and a crystal with an imperfect surface vanishes with increasing energy E , because the scattering angle reduces faster ($\sim 1/E$) than θ_c does ($\sim 1/\sqrt{E}$).

5. The Use of Crystal Deflectors in Beam Lines

5.1 Crystals in Intense Particle Beams

In the first (1979) experimental tests of the idea of particle deflection by a bent monocrystal [57], the bent beam intensity was barely several particles per second. The low efficiency of particle deflection by crystals (mainly because the beam emittance did not match the crystal acceptance) and radiation damage to semiconductor crystals have led to the opinion that this beam-handling method is of limited use.

Special experiments have therefore been carried out to test the feasibility of the formation, by a single crystal, of an intense proton beam sufficient in principle for the generation of secondary-particle beams [98].

In this experiment a silicon crystal bent by 13 mrad was placed in the 70-GeV proton beam extracted from the IHEP accelerator. Part of the beam was captured into the channeling mode and deflected to a magneto-optic beam line, where detectors were located. The silicon crystal had the (111) orientation and its dimensions were $H \times V \times L = 0.5 \times 40 \times 30 \text{ mm}^3$ (horizontal width, vertical height, and length along the beam). The length of the bent part was 20 mm and the average bending radius was 1.5 m. The beam aimed at the crystal had an intensity of 1.3×10^{13} particles per cycle; it was rapidly extracted (in 5 μs) and the cycle repetition period was 9 s. The beam dimensions were $\sigma_x = \sigma_y = 1.4 \text{ mm}$ and the angular divergence in the x plane (beam-bending plane) was 0.8 mrad. In one cycle about 1.8×10^{12} particles directly reached the end face of the crystal and the time-average value of the released power was $\sim 1 \text{ W}$. The crystal was heated by the beam to 150°C . Moreover, it was subject to a dynamic mechanical stress at the moment the beam passed through it. The first attempts to deflect a fast extracted beam in this single crystal were unsuccessful. The crystal which had been bent by bonding it to a metal cylinder over the whole of its surface, fractured under dynamic stresses. However, success was achieved when the crystal was pressed against a metal base by spring supports (Fig. 3.2).

The crystal bent a maximum of 9.5×10^9 particles per cycle. The particle losses from the main beam were of the order of 1%, which was approximately 10 times the intensity of the deflected beam, i.e. the efficiency of the beam splitting by the crystal was $\sim 10\%$. For the incident beam parameters given

above, when the angular divergence was ~ 40 times greater than the critical channeling angle, this efficiency was in agreement with the calculations.

The intensity fluctuations from one cycle to the next were within the acceptable limit of 12%. At this fluctuation level no changes were found in the average intensity, confirming the optimistic theoretical predictions [34, 67] that the bending properties in the case of planar channeling have a weak temperature dependence.

The spatial stability of the deflected beam was monitored by a remote ionization chamber. The change in the bending angle of the crystal was $\Delta\Theta/\Theta < 10^{-2}$. The crystal not only withstood a flux of $\sim 10^{19} \text{ cm}^{-2}$ particles under thermal and mechanical stresses (it did not fracture), but it also retained the channeling properties without any significant deterioration. These results are quite promising. They demonstrate that crystals may be used for years in the typical beam lines.

Recently a special experiment [99] was carried out to investigate crystal's radiation damage resistance at a high proton fluence of $4 \times 10^{20} \text{ cm}^{-2}$. After irradiation of the crystal with a 28-GeV proton beam, the degradation was measured with MeV-range He ions by using Rutherford backscattering. The minimum yield from backscattering in a silicon single crystal increased from 2.3% to 4.1%.

Such high radiation doses may occur in crystal extraction from large TeV accelerators. Since the spot size in that case is very small, periodic translations could extend the crystal life.

Direct measurements of the bending properties of irradiated crystals at high energies have been recently taken place at CERN [101]. It has been demonstrated that after the crystal has been exposed to $\sim 2 \times 10^{20}$ protons per cm^2 , the bending efficiency decreases by only 25%. The results on the radiation resistance of crystals obtained in [98, 99, 101] remove all the doubts in the practical applications at accelerators.

5.2 Beam Attenuator

One of the first applications of crystals in accelerators was their use as the deflecting elements in magneto-optic beam lines. For example, the work done at the FNAL, reported in 1986 [111] involved the use of a crystal to form a low-intensity proton beam which reached an emulsion spectrometer. These experiments demonstrated for the first time that 800-GeV beams can be deflected by bent crystal.

A 26-mm long silicon crystal, placed in a beam line, replaced a pair of dipoles with a bending angle of $\Theta = 3.7$ mrad and deflected part of the incident beam with $10^8 - 10^9$ particles per cycle in the direction of an emulsion spectrometer: the intensity of the deflected beam was $10^4 - 10^5$ particles per cycle. The unbent beam was quenched in an absorber. The reports of this experiment stressed several positive features of the use of crystals as beam

attenuators, as compared with collimators. The conventional collimators can reduce the intensity by a factor of 10–100. Such collimators are heavy and therefore difficult to control. Moreover, they become sources of secondary particles and create a halo.

The real efficiency of beam bending by a crystal was found to be 0.54×10^{-3} . A theoretical estimate, which took into account the dechanneling factors, ≈ 0.27 , and the ratio of the crystal acceptance to the beam emittance, $\approx 1.2 \times 10^{-2}$, was 3.2×10^{-3} . The authors attributed the lower efficiency to the nonoptimal position of the crystal along a coordinate, a possible underestimate of the dechanneling effects, and a possible loss of particles through side faces (because of inaccurate cutting of a slab). In spite of this, the experiments showed that bent crystals in accelerators are not exotic devices, but an important tool in high-energy physics.

Bent single crystals of similar quality have been used in the U-70 accelerator at IHEP [109] and in the SPS at CERN [115]. In IHEP work [109] the ability of crystals to form low-divergent stable beams with variable intensity was noted as an excellent tool for calibration of the physical apparatus.

The CERN SPS tests with crystals [115] were initiated by a proposal [116] for a new precision measurement of the direct CP-violation parameter ε'/ε . In order to minimize systematic errors, the experiment requires simultaneously running K_S and K_L beams. A small fraction of the proton beam that has traversed the K_L production target should be recuperated and transported towards a second, K_S , target. The role of the crystal is to select a small

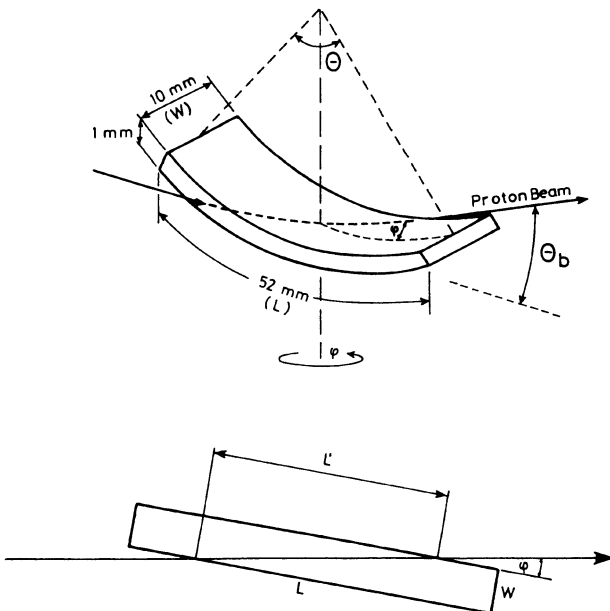


Fig. 5.1. The method used to adjust the effective deflection angle.

emittance beam suitable for the K_S production and at the same time provide the necessary attenuation and a minimal production of background.

The peculiarity of the application of crystals in that work is a simple method to adjust the deflection without mechanically changing the curvature of the bent crystal. The method is illustrated in Fig. 5.1. The crystal is rotated azimuthally in such a way that only part of the full crystal length is used. The beam enters and exits via the crystal sides. Geometrical considerations lead to a beam deflection angle Θ_b : $\Theta_b = (W/L)(\Theta/\tan\varphi)$, with $\tan\varphi > W/L$, where Θ is the angle by which the crystal is bent, W is the width of the crystal (10 mm), and L is the length of the crystal (52 mm).

Tests with a 450-GeV proton beam have shown that the method of entering and exiting the crystal from the sides in order to adjust the deflection angle via an azimuthal rotation of the crystal worked well; it will be used in the final application. The transmission obtained with this method was satisfactory and fulfills the intensity need of the future K_S/K_L beam.

5.3 Beam Splitting

The improvements in the technology for the bending of crystals have subsequently made it possible to split an extracted proton beam, so that several physical experiments could be carried out simultaneously.

Usually a beam is split by an electrostatic or a magnetic splitter [117]. This is a technically fairly complex approach requiring considerable space, since the angles of deflection of a beam by a conventional splitter are very limited. The use of crystals provides a simple means for beam splitting, which is unattainable by conventional techniques.

The task of beam splitting has become particularly topical in the case of the 70 GeV accelerator at IHEP, where several magneto-optic beam lines were constructed in the limited space of the old experimental areas, in the 1980s. This followed the commissioning of an accelerator-booster and an increase in the accelerated beam intensity to more than 10^{13} protons per cycle.

The first crystal beam-splitting station [110] began to operate at the end of 1988; it is shown schematically in Fig. 5.2. In the first tests a proton beam of 5×10^{11} particles per cycle, extracted slowly from the accelerator, was transported onto the target in a setup intended for the study of processes in a tagged-neutrino beam. A silicon single crystal bent to an angle of 60 mrad deflected part of a moderate-intensity beam to a magneto-optic beam line aimed at a target in a setup designed for hadron studies. The path of the channeled beam was aligned along the axis of the existing magneto-optic beam line by placing the crystal deflector inside a 6 m bender magnet M4.

Several different crystals were used as the deflectors: they included two silicon crystals, cut along the (111) crystallographic plane, and one germanium crystal cut along the (110) plane. The dimensions of the crystals were as follows: $0.5 \times 15 \times 60$ mm³ for Si-1, $0.55 \times 15 \times 60$ mm³ for Si-2, $0.6 \times 15 \times 45$

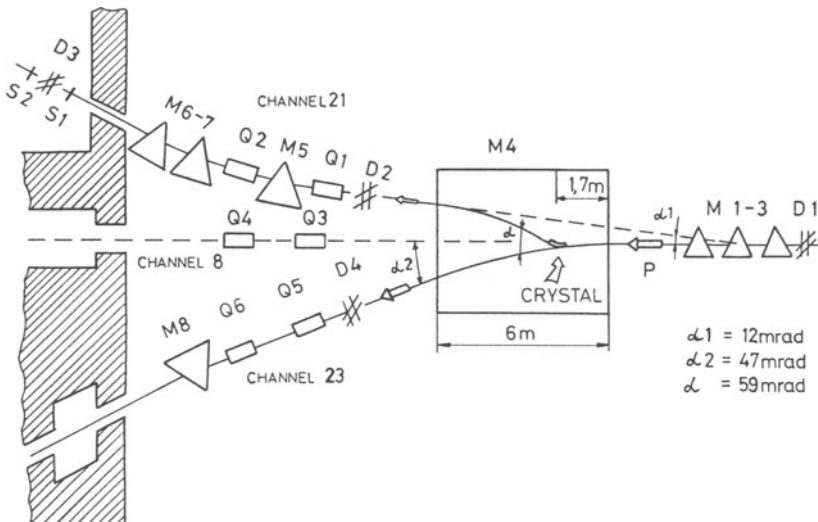


Fig. 5.2. Layout of the station for splitting an extracted proton beam in the beam lines of IHEP accelerator. M1–9 are bending magnets; Q1–6 are quadrupole lenses; D1–4 are multichannel beam profilers; S1–2 are scintillation counters.

mm^3 for Ge. The considerable lengths of the crystals were due to the requirement of a fairly large bending angle (as pointed out in Sect. 2.2, for each bending angle there was an optimal bending radius and length: if the crystal were too short, the particles would become dechanneled because of centrifugal effect, but if it were too long, a strong scattering would occur on electrons and nuclei, i.e. the ordinary dechanneling would prevail).

The crystals were bent in the device shown in Fig. 3.2. The first test established that a crystal could be used to split a beam of protons under working conditions in the magneto-optic beam lines with $I_{23} = 10^{13}$ particles per cycle, $I_{21} = 10^7$ particles per cycle; this was achieved when a crystal was placed in the halo region of the beam so that the particle losses did not exceed the permissible limit of $\sim 10^{10}$ particles per cycle (0.1% I_{23}).

Subsequent experience demonstrated that the crystal beam-splitting station was highly reliable. The Si-1 silicon crystal worked without replacement for five years: it withstood a particle flux in excess of $10^{18}/\text{cm}^2$ and retained its bending properties without significant deterioration.

Several additional crystals were placed subsequently in the beam lines and these made it possible to operate simultaneously several experimental set-ups [120].

5.4 Creation of New Experimental Areas

As noted in Chap. 2, the bending power of a crystal is $\Theta_D = L_D/R_c$. This angle does not depend on the particle energy, and equals, e.g., for Si ~ 0.3 rad. For multi-GeV energies it is a very large value compared to the bending angle in a conventional electromagnet $\Theta_M/\text{mrad} = 300Bl$ [Tl m]/ p [GeV/c]. For example the angle of deflection of a 1000-Gev/c beam will be ~ 3 mrad in a 6-m-long iron magnet.

This possibility of using a crystal for the abrupt bending of a beam fraction at a large angle allows researchers to organize over a short base an ‘unconventional’ beam line for carrying out physical experiments in any operating accelerators and in any accelerators under construction.

Recently a 150 mrad bent crystal was used this way to create the beam in a new experimental setup at the IHEP [128]. The 100 mm-long silicon (110) crystal inserted in the halo (about 10^{10} particles per second crossing the crystal) of the intense 70 GeV/c proton beam, extracts over the ~ 20 m base 10^6 protons per second beyond the 2-m iron-concrete shield (see Fig. 5.3). The background particles emerged in the direction of bending angle of the crystal had an energy some GeV (let us remember that in laboratory frame the average angle of secondary particle production is coupled with its momentum by relation p_s [GeV/c] = $400/\Theta_s$ [mrad] and in this case p_s [GeV/c] = $400/150 = 2.7$). It is not difficult to subtract these secondary particles and it is done with two small corrector magnets and collimator, as shown in Fig. 5.3.

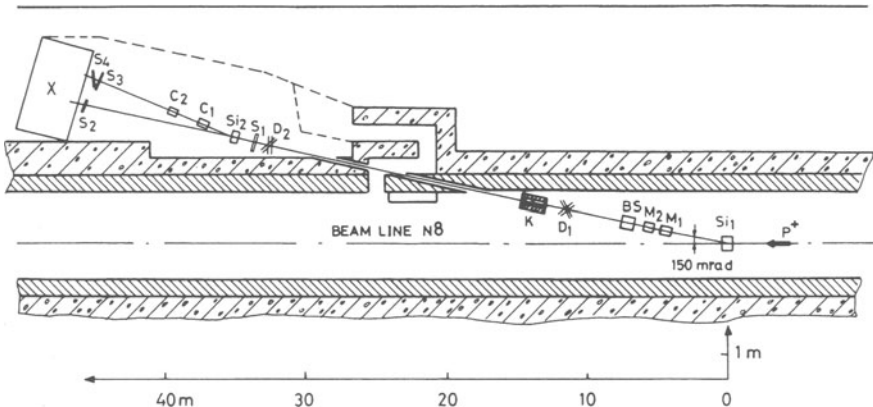


Fig. 5.3. The scheme of a crystal beam line and an experimental set-up: Si₁, Si₂ – deflecting and testing crystals; M₁, M₂ – corrector magnets; K – collimator; BS – beam stopper; X – beam absorber; D₁, D₂ – proportional chambers; S₁–S₄ – scintillation counters; C₁, C₂ – microstrip detector stations.

With these conditions the high quality of the beam, its low emittance and good stability, are achieved with the help of a monocrystal, at least in the plane of the deflection ('band' beam).

It is proposed initially to use this beam line for channeling experiments and microstrip-detector testing. Note that channeling beams are very suitable for microstrip-detector calibration because it is easy to provide beam spots less than $100 \mu\text{m}$ in diameter, by decreasing the thickness of the crystal plate or by using a crystal focusing technique. The new beam line can operate simultaneously with all other lines, consuming practically no electrical power.

If required, a crystal string can be used for beam steering instead of one crystal. Several crystals placed in succession have already been applied in this way (see Sect. 5.5).

5.5 Beam Diagnostics

Earlier work has already revealed that the ability of a bent crystal to modify a beam within a small phase volume $\varepsilon = 2\theta_c H$ (θ_c is the critical angle of channeling, H is the crystal thickness) can be used for particle beam diagnostics. For example, it is reported in [111] that it is possible to measure the beam emittance by recording the particles deflected by a crystal when this crystal is rotated and displaced transversely relative to the beam. It is demonstrated in [118] that a bent single crystal can provide full information on the beam characteristics (emittance, profiles, halo, momentum spread).

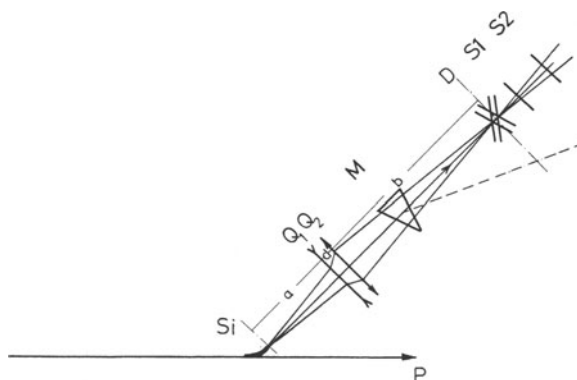


Fig. 5.4. Scheme for measuring the beam parameters. Here, Si is a bent single crystal; D is an analogue ionization chamber; S1, S2 are scintillation counters; Q_1, Q_2 are quadrupole lens doublets; M is a bending magnet. The solid lines are the paths of the rays in the horizontal plane and dashed line is the dispersion.

5.5.1 Method of Measurement

The measurement scheme is presented in Fig. 5.4. A bent Si monocrystal is introduced into a high-intensity beam of high-energy particles: the coordinate of this crystal is x and its orientation is x' . The part of the beam deflected by the crystal is directed along the axis of a long magneto-optic system (lenses Q_1 , Q_2 ; magnet M) and is recorded at the end of this system by an analogue ionization chamber D and scintillation counters S1 and S2, used in coincidence. The acceptance of the magneto-optic system makes it possible to record all the deflected and channeled particles and to remove completely the background of secondary particles formed in the interaction of the unchanneled beam fraction with the crystal matrix.

Under these conditions the number of particles recorded by the counters is

$$I(x, x') = \left[\int_{-H/2}^{H/2} \int_{-\theta_c}^{\theta_c} \rho(x, x') dx dx' \right] \eta_D(L, R, p),$$

where $\rho(x, x')$ is the beam phase density in the coordinate-angle space and $\eta_D(L, R, p)$ is the dechanneling factor which depends on the length of the crystal, on the bending radius, and on the momentum of the deflected particles. In view of the smallness of the crystal acceptance, we can write

$$I(x, x') = \rho(x, x') 2\theta_c H \eta_D,$$

which leads to

$$\rho(x, x') = \frac{1}{2\theta_c H \eta_D} I(x, x').$$

Thus the beam phase density at the point (x, x') is proportional to the number of particles bent by the crystal provided that the increase in the temperature of the crystal caused by the beam heating does not significantly alter the channeling properties.

5.5.2 Determination of the Spatial and Angular Characteristics of a Beam

The method for measuring the beam characteristics described above was applied to one of the beam lines of the accelerator at IHEP. Part of a 70 GeV proton beam, trapped into the channeling mode, was bent by an angle of 13 mrad and directed into a beam line where the front optics is provided by the system shown in Fig. 5.4.

The phase density $\rho(x, x')$ was measured for an extracted beam of 3×10^{12} particles per cycle. In Fig. 5.5a the results of measurements of $\rho(x, x')$ are plotted in the form of equipotential lines in the (x, x') plane; these lines link the experimental points. These points are the results of angular scanning with

the beam at each step of the displacement of the crystal along the horizontal. The five closed lines in this figure enclose the beam phase volume at the levels of (from the inside out) 0.75, 0.5, 0.25, 0.1, and 0.01 times the peak density. The values of the beam emittance corresponding to these levels are (π mm mrad): 0.26, 0.68, 1.2, 1.6, and 4.2, respectively.

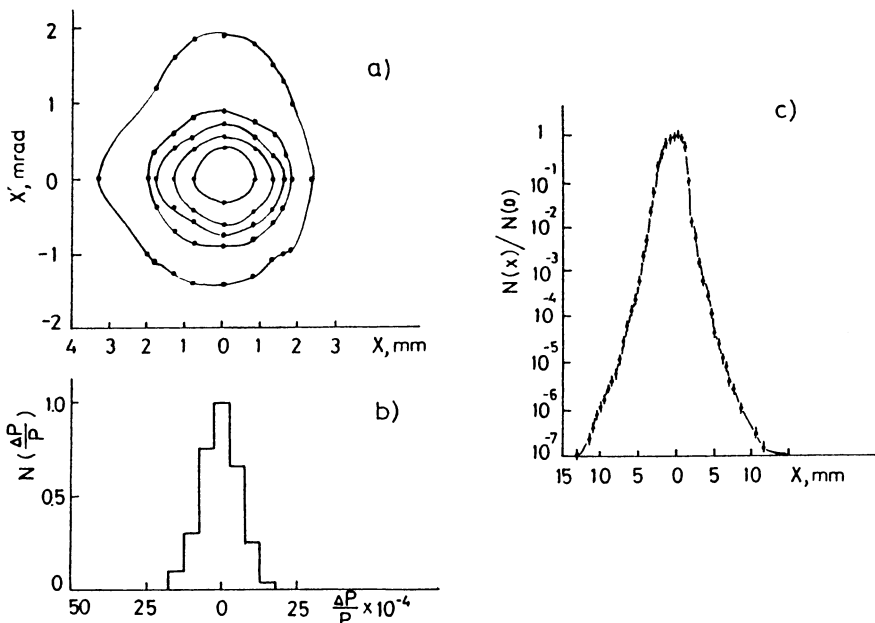


Fig. 5.5. (a) Family of closed curves corresponding to the following phase densities of particles (all relative to the maximum value): 0.75, 0.5, 0.25, 0.1, 0.01, from the inside out. (b) Relative distribution of the particle momenta in a beam. (c) Beam profile $\rho(x, 0) = N(x)$, measured by horizontal displacement of a crystal.

Displacement of a crystal oriented optimally in respect to the angle made it possible to measure the value of $\rho(x, 0)$, i.e. to determine the beam profile $N(x)$ in a wide dynamic range. The results of determination of the profile $N(x)$ extending down to 10^{-7} times the maximum are presented in Fig. 5.5c. It was possible to measure the halo of the high-intensity beam to such a very low level (10^{-7}) because of clear orientational dependence of the useful signal generated by the detectors. When the crystal was disoriented by an angle exceeding the acceptance of the magneto-optic system, the channeled beam disappeared and it was therefore easy to distinguish this beam from the background signal.

5.5.3 Determination of the Distribution of the Particle Momentum

The ability of a crystal to form a small-emittance beam and the spectrometric capabilities of the magneto-optic beam line can be used in combination in precision measurements of the distribution of the particle momenta.

The coordinate x of any particle (considered by ignoring the chromatic aberrations) at a detector D located at the position of the image of a crystal-deflected beam (Fig. 5.4) is

$$X = q_{11}X_0 + q_{13}(\Delta p/p), \quad (5.1)$$

where q_{11} is the linear magnification coefficient; q_{13} is the linear dispersion; $X_0 \leq H/2$ is the initial coordinate of a particle emerging from the crystal; $\Delta p/p$ is the relative spread of the particle momenta.

If the first term in (5.1) is much smaller than the second, the size of the beam image is governed entirely by the spread of the particle momenta and its profile corresponds to the distribution of these momenta. In the specific case under consideration ($q_{11} = 1/2$ and $q_{13} = 25$ mm per 1% $\Delta p/p$) this condition is satisfied for $\Delta p/p \gg 5 \times 10^{-5}$. The image distortions contributed by the chromatic aberrations of a pair of quadrupole lenses amount to $\delta x/x < 2 \times 10^{-3}$ in the ‘thin-lens’ approximation [117], so these distortions can be ignored.

The beam profile in the image was measured with the aid of an analogue ionization chamber D in steps of 1.25 mm. The distribution of the particle momenta in the beam deduced from this profile is shown in Fig. 5.5b. The momentum spread in the beam in the course of extraction was $\sigma_{\Delta p/p} = 6.4 \times 10^{-4}$.

This method of determining the beam characteristics can be used to measure the parameters of high-intensity accelerator beams when particle counters cannot be employed. Particularly promising is the feasibility of measuring in this way the halo of a circulating beam in large hadron colliders when the problem of particle losses is very severe.

5.6 Beam Focusing with Crystals

5.6.1 The Focusing Method

Bent crystals can not only deflect a beam, but also focus it. In principle, there are several ways of doing this. One of them is the focusing of a beam by a thin bent crystal oriented normally to the crystallographic planes [112]. Another possible approach is based on the deformation of the planes in a thick crystal when it is compressed.

In the mid-1980s A.I. Smirnov (PNPI Gatchina) proposed a promising method for focusing a parallel beam into a line and simultaneously deflecting

the beam through a considerable angle, so as to form ‘clean’ focused beams. In this method the surface of the exit face of a bent crystal is shaped so that the tangents to the crystallographic planes on this surface pass through the same line and, consequently, the particles in the deflection plane are collected in a line focus because of the difference between the deflection angles [113]. When the crystallographic planes are bent to form a cylinder of radius R (Fig. 5.6), it is essential to ensure that the line formed by the centers of curvature OO' is located on the surface of a cylinder of radius r representing the shape of the exit face of the crystal. The focal length is then $F = \sqrt{4r^2 - R^2}$.

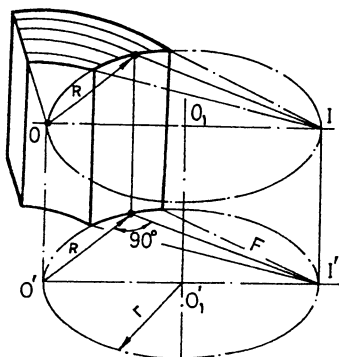


Fig. 5.6. Focusing a beam with a crystal. Here, OO' is a line through the centers of curvature of the crystallographic planes; $O_1O'_1$ is the axis of a cylinder of radius r representing the shape which is imposed on the face of a crystal; $I'I'$ is the focal line where the tangents to the bent planes converge, deduced on the basis of the well-known geometry theorem.

In the case of ideal bending and shaping of a crystal the beam size Δx at the focal point is $\Delta x = 2F\theta_c$ and it is governed by its angular divergence within the limits of the critical channeling angle. Since this critical angle is quite small ($\theta_c = 0.02 - 0.002$ mrad for particles of energies from 100 GeV to 10 TeV in the case of planar channeling in silicon) and the technology used to bend and shape a crystal makes it possible to achieve a focal length of the order of several centimetres, the attainable dimensions of the beam are $\sim 10 \mu\text{m}$ for GeV energies and $\sim 1 \mu\text{m}$ for the TeV range. The linear magnification in the course of focusing is $q = 2F\theta_c/H$, where H is the characteristic thickness of a crystal $\sim 1\text{mm}$, and can reach a fraction amounting to, respectively, hundredths and thousandths in the two energy ranges.

5.6.2 Focusing of a Parallel Beam to Form a Point in the Particle Deflection Plane

The described method of focusing was realized in a collaboration experiment involving IHEP and PNPI: it was carried out on a 70-GeV proton beam [113, 114]. The experts at the PNPI developed a technology for bending a focusing crystal and made several focusing devices. Three silicon crystals were used: their width, height, and length along the beam were 2 mm, 15 mm, and 70 mm, respectively; the orientation was (111). The crystals were bent

to form a cylinder of radius $R = 2.7$ m over a length of ~ 65 mm. Different focal lengths were obtained by shaping the exit ends of the crystals to form cylinders with radii listed in Table 5.1 and the angles of cut of the focusing edge were varied in accordance with $\alpha = \arccos(R/2r)$ in the geometry of Fig. 5.6.

Table 5.1. Characteristics of focusing crystals and beam sizes in focus.

Crystal	R [m]	r [m]	α [degrees]	F [m]	Focus size $2\sigma_x$ [μm]	
					calculated	measured
$N1$	2.7	2.21	58.2	3.5	175	200
$N2$	2.7	1.52	30.4	1.4	70	80
$N3$	2.7	1.374	11.9	0.5	25	43

A proton beam, $\sigma_x = 2$ mm, with a small angular divergence, 0.1 mrad, was incident on a crystal placed on a goniometer stage. The orientational dependence of the signal produced by remote detectors was used to set the crystal in the channeling mode. The intensities of the incident and deflected (by an angle $\simeq 24$ mrad) beams were measured by scintillation counters. In the optimal alignment the crystal deflected 3% of the particles in the incident beam (which agreed with the calculations in which the beam and crystal parameters were taken into account).

The focusing effect was detected by nuclear photoemulsions. Several layers of emulsion were placed at different distances from the exit face of a crystal. The exposed emulsions obtained for crystal N1 were analysed with a microphotometer; in the case of crystals N2 and N3 a direct count was made of the track density distribution over the beam cross section under a microscope. The size of the developed grains in a track ('track width') was about 1 μm .

Figure 5.7 shows the image of a beam focused by crystal N3 at a distance of 0.5 m (the strongest focusing). The beam dimensions at crossover $2\sigma_x$ (calculated and measured) are listed in Table 5.1. It is evident from this table that for crystals N1 and N2 the dimensions agreed to within 15%. In the case of crystal N3 the beam size at the crossover was considerably greater than the calculated value, which was due to an increase in the contribution of aberrations when the focal length was reduced.

This focusing method can be used to form particle beams of micron dimensions in the TeV range when a new generation of accelerators is used. In this method the image of a beam deflected by a crystal can be simply transferred to an experimental setup by optics with the magnification of unity.

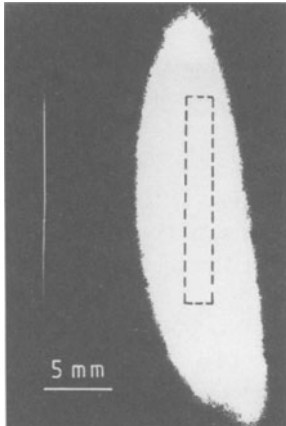


Fig. 5.7. Image at the crossover of the beam focused by the crystal N3. The profile of the deflected and focused beam can be seen on the left. The dashed rectangle on the right is the crystal cross-section.

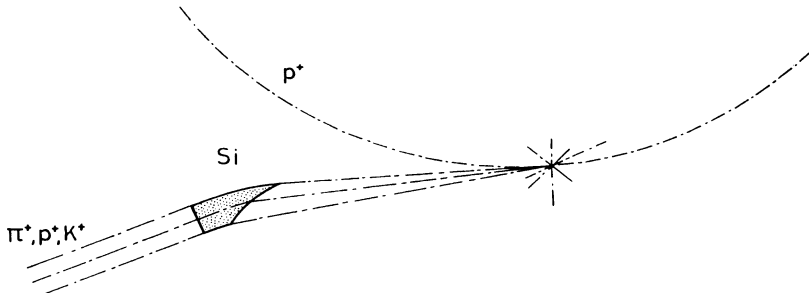


Fig. 5.8. The scheme of extraction of the secondary-particle beam from the accelerator by the focusing crystal.

5.6.3 Focusing a Beam Diverging from a Point-Like Source into a Parallel Beam

Another important application of a focusing crystal may be related to the reverse motion of particles – transformation of the beam diverging from a point-like source into a parallel one. To do this, the crystal entry face must have a special shape. The problem of focusing a divergent beam is typical for the steering of secondary-particle beams, and in particular for their extraction from colliders.

To extract most of the secondary particles produced in the target located in the vacuum chamber of the accelerator (at the crystal focal point; see Fig. 5.8), certain conditions must be fulfilled. It is known that most of the produced secondary particles exit in the angular range $\pm\theta = 0.4 \text{ [GeV/c]/}p$, where p is the momentum. The angular acceptance of the focusing crystal is

$$\pm\varphi = \frac{H}{2F}, \quad (5.2)$$

where H is the crystal thickness, and F is the focal distance; this acceptance should be about $\pm\theta$.

Highly efficient particle trapping into the channeling mode may be obtained if the target size in the bending plane is

$$\Delta x \leq 2\theta_c F. \quad (5.3)$$

Then the particles entering the crystal are aligned with respect to the crystal planes within θ_c , and the trapping efficiency η may be close to the theoretical limit $\sim 70\%$. In the realistic experiment the defects of the focusing device may lower η .

The above conditions for the efficient extraction of secondary particles can be easily met at TeV energies. The estimates for the LHC collider (where the energy of the protons is 7 TeV) show that in this way one can extract the secondary particles with an intensity of up to $\sim 10^8$ particles per second.

The experimental investigation of the efficiency of capture and deflection of the beam diverging from a point-like source was made at the extracted 70-GeV proton beam of the IHEP accelerator [119]. The experimental scheme is shown in Fig. 5.9.

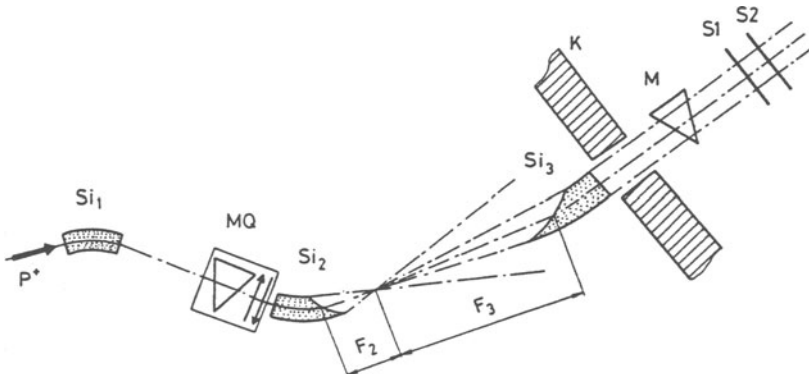


Fig. 5.9. Scheme of the experiment.

The crystal Si_1 (with flat faces and bent by 60 mrad) was exposed to the 70-GeV proton beam of 10^{11} particles per second, and bent the beam with moderate intensity, $\sim 10^7$ particles per second, toward the magneto-optic system MQ - M where two other crystals were placed. The beam formed with the forward part of the magnet system was brought onto the crystal Si_2 , which had the focusing end face. This crystal was 2 mm thick, 15 mm high, and 70 mm long, and was bent by 18 mrad. The crystal focused the beam at a distance of 0.5 m into a narrow vertical strip with a width of $\simeq 80 \mu\text{m}$ FWHM at the crossover and a divergence of ± 2 mrad. The beam formed in this way was used as a source of protons. In order to focus and deflect

this divergent beam, the crystal Si_3 , with a focal distance of 2.5 m was used. It had dimensions of $2 \times 20 \times 30 \text{ mm}^3$ and was bent by 6 mrad. (The first and second crystals had orientation (111), the third was cut along the (110) planes). This crystal had an angular acceptance of $\varphi = \pm 0.4 \text{ mrad}$. According to preliminary measurements, it gave for the parallel-to-point focusing a crossover size of $\sim 200 \mu\text{m}$ FWHM (the ideal value is $\Delta x = 2\theta_c F = 125 \mu\text{m}$). The crystals were successively aligned relative to the beam. Each of them had an independent goniometer.

The effect of focusing the beam from a divergent to a parallel one was detected by measuring the intensity of the beam deflected by the third crystal, during which the latter was rotated around the vertical axis crossing its entry face. The intensity obtained in this angular scanning is shown in Fig. 5.10.

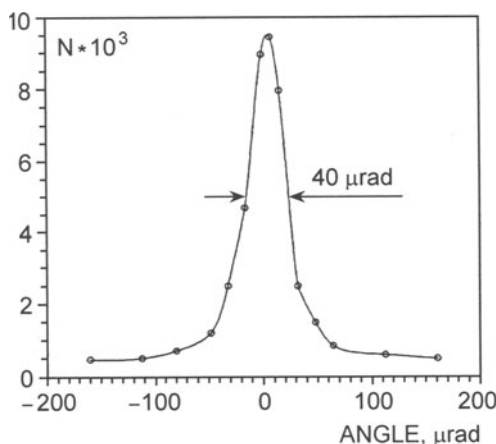


Fig. 5.10. Angular scan of intensity for the beam bent with the third crystal.

The scan FWHM approaches $2\theta_c$ ($\simeq 4\theta_c$ at the base), which attests a good-quality focusing. According to measurements with the remoted scintillation counters S1 and S2, crystal Si_3 at the best angle deflected ($15 \pm 2\%$) of the protons incident on its face, which is a factor of ~ 2 lower than the calculation for the ideal focusing.

The high-efficiency bending of the divergent beam is confirmed by the data of the developing beam profile on the nuclear emulsion, which was placed downstream of the crystal Si_3 at its optimal alignment. This profile is shown in Fig. 5.11.

The wide beam (excess over the background) corresponds to the divergent beam formed by crystal Si_2 . The dip at the right is the shadow of the crystal Si_3 , due to the capture of beam fraction in the channeling mode. From the ratio of areas one can find that $\sim 30\%$ of the particles are trapped in the channeling mode. On the left of the figure the contribution of particles bent by Si_3 is seen, superimposed on the broad profile of the beam divergent from

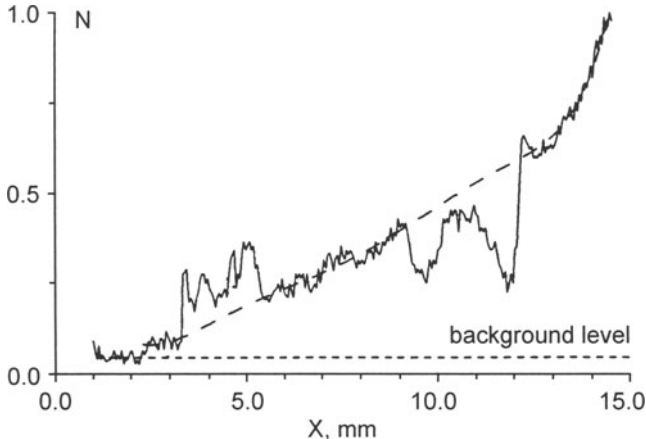


Fig. 5.11. Beam profile on the nuclear emulsion downstream the third crystal.

the crystal Si_2 . The bent-beam fraction, according to the figure, is 14% of the incident particles. This agrees well with the measurements by the scintillation counters. The reduction in the number of bent particles by a factor of 2.2, as compared to the particles trapped in the channeling mode, is explained by dechanneling.

Above ~ 500 GeV and for the same crystal size, the fraction of the bent particles will be close to 30%, as in this case the particle losses in the process of deflection are insignificant because of the growth in the dechanneling length. The obtained efficiency is high despite the defects of both Si_2 (the source) and Si_3 , and may be improved further.

As the results presented in Sect. 3.9 show, removal of the aberrations induced by surface imperfections and edge effects is a serious problem.

6. Application of Crystal Channeling to Particle Physics Experiments

6.1 Studying Short-Lived Particles: Ideas and Proposals

The third direction of crystal applications is aimed at experiments at high-energy accelerators, and is based on various effects discovered in interactions of high-energy particles with aligned crystals. Many ideas proposed in this direction are reviewed by Sun [159]. Here we touch, without details, on some of these ideas, which open new possibilities for the investigation of the characteristics of short-lived particles.

6.1.1 The Study of Decay Modes of Short-Lived Particles

The use of bent crystals as superstrong and compact magnets is attractive for separating the beams of short-lived positively charged particles like D^+ (mass 1869 MeV) and B^+ (mass 5271 MeV) mesons and Λ_c^+ (2281 MeV) baryons. Their lifetimes τ are 9.2×10^{-13} , 14.2×10^{-13} and 2.3×10^{-13} s, respectively. The decay length l over which the intensity of the unstable particles reduces by a factor $1/e$, grows in the ultrarelativistic case in proportion to the particle energy E :

$$l = c\tau\gamma, \quad (6.1)$$

where $\gamma = E/E_0$; E_0 is the particle's rest energy. Therefore the decay lengths for D^+ , B^+ and Λ_c^+ are very small even at 1 TeV: 14.2, 8.2 and 3.1 cm, respectively. Nonetheless, an application of a bent crystal and microstrip detectors with an accuracy of 10–20 μm could ensure the separation of at least D^+ with energy ~ 1 TeV.

The concept of the method is shown in Fig. 6.1. The high-energy hadron beam hits a target placed near the entrance face of a bent crystal. From all the secondary particles produced in the target, those positively charged and emitted forward are captured in the channeling mode preferentially (both short-lived and long-lived, e.g., π^+ mesons). The captured particles are bent with a crystal at a given angle, which should ensure a spatial separation between the channeled and unchanneled fractions of the beam over a short distance (several centimetres) from the crystal exit face. The channeled fraction of the beam is determined by the microstrip detectors C_1 and C_2 placed

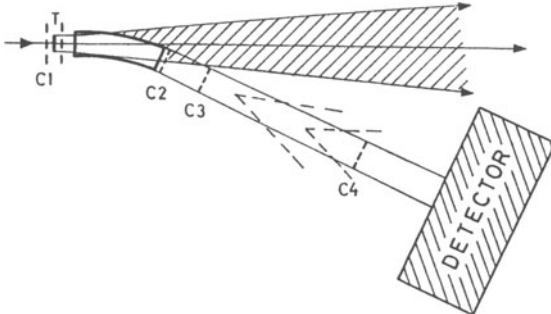


Fig. 6.1. The principle scheme of separation of short-lived particles.

at the entry and exit of the crystal, and by detector C_3 placed in the direction of the bent beam fully separated spatially from the unchanneled fraction. The detector C_3 is missed by most of the background particles produced in the nuclear interactions by the unchanneled beam. The signals from the corresponding strips of these three detectors are used in coincidence. Downstream of C_3 at a distance of order of the decay lengths, along the bent-beam path, another microstrip detector C_4 is placed. Between C_3 and C_4 , almost all the short-lived particles have decayed, and C_4 detects mostly the long-lived particles (K^+ , π^+ mesons, protons, etc.). In order to detect from the channeled beam the short-lived particles, detector C_4 is used in anticoincidence. In this way, the trigger for the separation of short-lived particles is

$$T = C_1^i C_2^i C_3^i \overline{C_4^i}, \quad (6.2)$$

where i is the number of the corresponding strip.

To study the decay modes of the tagged short-lived particles, the magnet spectrometer with drift chambers may be used. To ensure a preferable separation of the short-lived particles of a certain type at a given energy, one should carefully optimize the geometry of the principal scheme.

6.1.2 Measurement of Magnetic Moments

Baryshevskii [160] and Pondrom [161] have shown that the spin of a particle should precess at an angle substantially greater than the angle of deflection if the particle is channeled in a bent crystal. This effect opens up the possibility of measuring the magnetic moments of short-lived particles. Lyuboshits [162] and Kim [163] have developed a detailed theory of the spin precession, from which it follows that at high energies ($\gamma \gg 1$) the angle of spin precession φ is related to the angle of deflection Θ as follows:

$$\varphi = \gamma \frac{(g - 2)}{2} \Theta, \quad (6.3)$$

where g is the gyromagnetic ratio. With the given Θ and γ , and by measuring φ from the asymmetry of the characteristic decay of unstable particles we find g from (6.3) and, consequently, the magnetic moment μ :

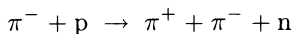
$$\mu = (ge/2mc)S, \quad (6.4)$$

where e , m , and S are the charge, mass, and spin of the particles.

This idea was realized in an experiment [164] at Fermilab with a beam of polarized Σ^+ hyperons (mass 1189 MeV, lifetime $\tau = 0.8 \times 10^{-10}$ s). The measured magnetic moment of the Σ^+ hyperons was in agreement with the data obtained earlier by a different method. The experiment demonstrated the spin precession of the channeled particles in a bent single crystal, as well as the feasibility of this method. The experiment is described in more detail in Sect. 6.2.

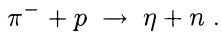
6.1.3 Measurement of Short-Lived-Particle Lifetimes

The use of the blocking technique – an effect opposite to channeling – opens the possibility of measuring the lifetimes of short-lived particles in the range 10^{-20} – 10^{-17} s. The essence of the blocking effect is as follows. The positively charged particles emitted at low angles to axis (plane) by a radioactive isotope implanted at a lattice site of a crystal, will not pass through the crystal along the axis (plane) due to scattering at large angles by the atoms of the axis (plane), i.e., the axis or plane will make a ‘shadow’ at the crystal exit. This ‘shadow’ effect called blocking was discovered experimentally in 1965 by Gemmel and Holland [165], by Domaj and Bjorkqvist [166], and by Tulinov [167]. At low energies the blocking technique is widely used for measuring the lifetimes of compound-nuclei [168]. As shown in [159, 169], this may be used at high energies for measuring the lifetimes of short-lived particles, e.g., the η meson (mass 549 MeV). The idea of the method is explained by Fig. 6.2. Suppose, a beam of high-energy (e.g., ~ 800 GeV) π^- mesons passes through the crystal at a low angle ($\sim 1^\circ$) to an axis. Through interaction of this beam with the nuclei of the axis atoms, various reactions may occur. If we describe the reaction as



and measure the yield of π^+ meson as a function of the angle φ relative to the axis, we obtain a typical blocking curve (1 in Fig. 6.2).

Let us consider now a reaction with the production of a short-lived particle, e.g., the η meson



An η meson which decays over a small (compared to the interatomic) distance from the crystallographic axis, can be distinguished by the main charged mode of decay (23.7% of all decays)

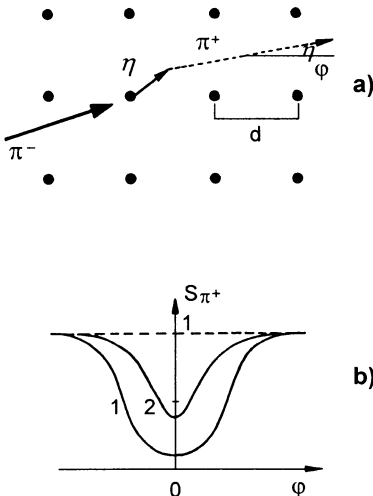
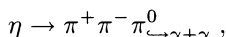


Fig. 6.2. The blocking effect and its application to measuring lifetime of the η meson: (a) η meson production and decay in crystal; (b) blocking curves for π^+ mesons produced in the reaction $\pi^- + p \rightarrow \pi^+ + \pi^- + n$ (1) and in the decay $\eta \rightarrow \pi^+ \pi^- \pi^0$ (2).



by detecting π^+ meson and 2γ quanta. If one builds in this case a blocking curve, its depth (see curve 2 in Fig. 6.2) is sufficiently smaller as compared to the normal blocking curve, because the products of the η meson decay are weaker ‘shadowed’ by the atomic strings. It is just this effect which is proposed for measuring the lifetime of the η meson and other short-lived particles.

6.2 Measurement of the Magnetic Moment of the Σ^+ Hyperon Using a Bent Crystal

The effect of the particle spin precession in a bent single crystal and feasibility of measuring its magnetic moment in this way have been demonstrated at FNAL [164] at the operating hyperon beam line. The experimental scheme is shown in Fig. 6.3. It includes a hyperon spectrometer made with a dipole magnet M_2 and three arrays of silicon strip detectors C_i , and a baryon spectrometer (two dipole magnets M_3 and M_4 , and four arrays of multiple wire proportional chambers D_i).

Two bent silicon crystals (Fig. 6.3b) were placed behind the hyperon spectrometer at the head of the decay zone. These crystals were oriented along the (111) planes and their dimensions were $xyz = (25 \times 0.4 \times 45)$ mm³. They were bent with a three-point scheme (with a mean bending radius of 27 m). The questions of selection, alignment and testing the crystals are reported in [170] in detail.

The upper crystal deflected the beam 1.65 mrad downward and the lower crystal deflected it the same angle upward. Therefore, the spin precession in

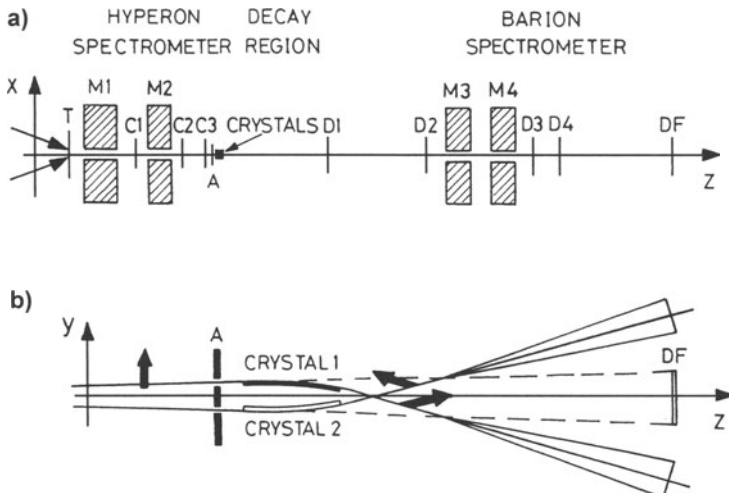


Fig. 6.3. (a) Experimental set-up: target T, bending magnets M_i , microstrip detectors C_i , drift chambers D_i , scintillation counters A and DF. (b) Spin precession effect in crystal.

the crystals was in opposite directions (black arrows in Fig. 6.3b). Ionization-loss detectors were implanted in the crystals in order to detect the channelled particles (see [170]).

The vertically-polarized beam of the Σ^+ hyperons was produced at the copper target by its irradiation with the proton beam of momentum 800 GeV/c. Here the proton beam was directed at the target in the horizontal plane under an angle of either +3.7 mrad or -3.7 mrad. The Σ^+ hyperons produced under these angles were selected by means of the magnet M_1 which bent the particles horizontally without changing their polarization, and by the collimating system. They were deflected to the experimental set up with the mean momentum 375 GeV/c and momentum scatter $\Delta p/p = 7\%$. Alternating between the two incident angles of the proton beam at the target allowed the researchers to alternate the sign of polarization. The measured polarization of the Σ^+ beam was $12 \pm 1\%$. At 10 m from the target the beam contained $\sim 1\%$ of the Σ^+ hyperons; the other particles were pions and protons.

The vertical dimension of the beam at the positions of the crystals was 1.8 cm and the angular divergence of the beam was 1.4 mrad (the horizontal dimension was 1.3 cm). With these dimensions, the beam covered the cross sections of both crystals, so they worked simultaneously. Only a small fraction of the beam, $\sim 2.5 \times 10^{-4}$ particles, was trapped into the channeling mode (this value agreed with the calculations).

The overall intensity of particles in the hyperon spectrometer was $\sim 10^5$ particles per second. The trigger was formed as follows. The scintillation counters placed near the strip detectors C_i (not shown in Fig. 6.3) selected the beam passed through the hyperon spectrometer and were used in coincidence.

Counter A, with rectangular holes matching the crystal entry faces, excluded the particles that missed the crystals, and counter *DF* did the same for particles not trapped in channeling. The channeled fractions of beam were detected by ionization-loss detectors. The trigger rate was 200 particles per second. The data were accumulated over 74 hours.

The Σ^+ hyperons with the $\Sigma^+ \rightarrow p\pi^0$ decay ($\sim 52\%$ of the total number of decays) were selected for the polarization measurements. This decay mode has a large asymmetry parameter $\alpha = -0.98$ and is therefore a sensitive criterion of the polarization state of Σ^+ . The needed Σ^+ hyperons were identified by measuring the direction and value of the momentum in the hyperon spectrometer with use of the magnet M_2 and strip detectors C_i (the rms resolution of momentum was 0.7%, of position 15 μm , of the angle of track inclination before the crystals 12 μrad horizontally and 7 μrad vertically).

The protons from the Σ^+ decay were identified in the baryon spectrometer by magnets M_3 and M_4 , and by drift chambers (the rms resolution of the momentum was 0.6%, and of the angle of track inclination 20 μrad horizontally and 13 μrad vertically). The Σ^+ decay vertex was measured in a 10-m long decay zone to within ~ 50 cm. The number of selected events was 2167 ± 47 when the event selection criterion was based on the kinematic variables. The results of the analysis are shown in Fig. 6.4. The average polarization vector for the two crystals was $P = 11.8 \pm 3.6\%$, which agrees with the polarization $P = 12 \pm 1\%$ measured for the unchanneled Σ^+ beam. The measured spin precession angles were $+51^\circ \pm 23^\circ$ and $-72^\circ \pm 26^\circ$ for the upper and lower crystals, respectively. The average spin precession for the two crystals, $60^\circ \pm 17^\circ$, was in agreement with the predicted value $62^\circ \pm 2^\circ$.

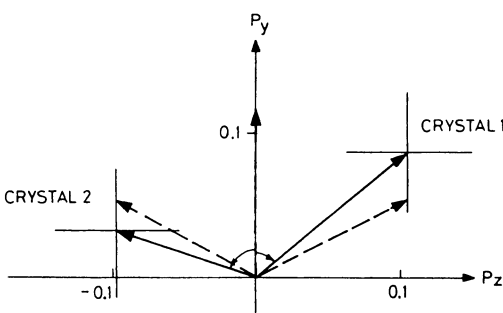


Fig. 6.4. Measured polarization of Σ^+ hyperons (an rms statistical error is shown). Dashed arrows show the expected polarization.

Substituting the measured precession angles in (6.3) and using (6.4) we find the Σ^+ magnetic moment to be $(2.15 \pm 0.61)\mu_N$ and $(2.74 \pm 0.71)\mu_N$ for the upper and lower crystals, respectively. Here $\mu_N = e\hbar/2m_p$ is the nuclear magneton, m_p the proton mass at rest. The average moment $\mu = (2.40 \pm 0.46)\mu_N$ is in agreement with the world data $\mu = (2.42 \pm 0.05)\mu_N$. The experiment has demonstrated the theoretically predicted spin precession of the channeled particles in a single bent crystal. The feasibility of this

technique for measuring the magnetic moments of short-lived particles A_c^+ and Ξ_c^+ is discussed in [171].

6.3 Radiation of High-Energy Electrons and Positrons in Aligned Single Crystals and Its Application in Physical Research

The radiation of high-energy electrons and positrons in aligned single crystals, as opposed to that in amorphous materials (incoherent bremsstrahlung – IB), can be strongly enhanced, i.e., it occurs in a coherent way which makes a crystal an efficient source of γ -quanta beams.

In aligned crystals one can observe two kinds of intense radiation. The first is the radiation due to sequential interaction of e^\pm with the periodically arranged atoms of the crystal lattice, when they move under an angle θ to an axis or plane of crystal much greater than the critical angle of channeling ψ_L or θ_L respectively (coherent bremsstrahlung – CB). The second kind is the channeling radiation (ChR), in which e^\pm moves in a strong averaged electric field of the crystal axes or planes.

A number of reviews [172–179] and monographs [15–17] and [180, 181], with an extensive bibliography therein, are devoted to the theory of electromagnetic processes in crystals and to analysis of the experimental data. Therefore we confine ourselves with a qualitative consideration, concentrating an attention on the most recent experimental results and on the opening possibilities of their application in the high-energy physics.

6.3.1 Coherent Bremsstrahlung

The possibility of coherent radiation in crystals was first analyzed by Feretti [182], Ter-Mikaelian [183, 184], and Uberall [185, 186]. The conditions under which the coherent and interference phenomena appear in bremsstrahlung follow directly from simple qualitative considerations. Suppose an electron (positron) of high-energy $E \gg E_0$ (E_0 is the electron energy at rest) moves in a crystal with velocity v at a small angle θ (see Fig. 6.5) to the major crystallographic axes of a certain type (e.g., $\langle 110 \rangle$) placed at a distance d one from another. We assume $1 \gg \theta \gg \psi_L$. With a period of d/θ , the electron collides with an atom and radiates photons in the forward cone of angles $\varphi \simeq 1/\gamma$. Suppose that the electron radiates photons of energy $\hbar\omega \ll E$ (here \hbar is the Plank constant divided by 2π ; ω is the circular frequency of the photon). Under this condition one may neglect changes in the electron velocity v .

At a large distance from the radiation point 1 (see Fig. 6.5), the electromagnetic wave propagating at an angle ψ to the direction of electron motion z , can be expressed as a plane wave

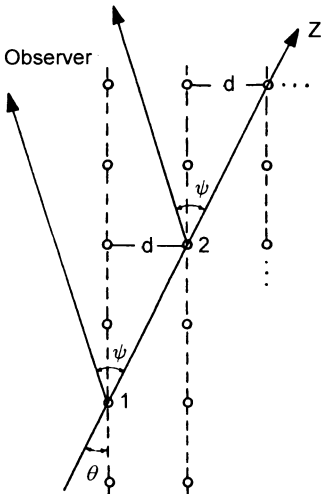


Fig. 6.5. Coherent radiation of an electron moving in a crystal at an angle θ relative to the crystal axis.

$$b \exp [i(\omega t - k \cos \psi z)] ,$$

where $k = \omega/c$. Then the wave emitted by the electron at point 2 will be

$$b \exp \{i[\omega(t - d/\theta v) - k \cos \psi(z - d/\theta)]\} .$$

Summing these waves at the point of observation, we get

$$\begin{aligned} b & \left\{ 1 + \exp \left[-i \frac{d\omega}{\theta v} (1 - \beta \cos \psi) \right] \right\} \exp [i(\omega t - k \cos \psi z)] \\ & = B \exp [i(\omega t - k \cos \psi z)] . \end{aligned}$$

From here we see that the amplitude B of the resulting wave doubles, and the intensity $I \sim B^2$ increases four-fold, under the condition

$$\frac{d\omega}{\theta v} (1 - \beta \cos \psi) = 2\pi n \quad (n = 1, 2, 3\dots), \quad (6.5)$$

i.e., when the phase difference between the two waves is a multiple of 2π . In this way, at the frequencies of (6.5) we shall observe a coherent N^2 -fold amplification of the radiation, where N is the number of atoms along the particle path.

The condition of interference (6.5) can be rewritten as

$$\omega = \bar{\omega}_0 n, \quad (6.6)$$

where $\bar{\omega}_0 = \omega_0/(1 - \beta \cos \psi)$ is the frequency $\omega_0 = 2\pi v \theta / d$ shifted by the Doppler effect.

Taking into account that in an ultrarelativistic case $\beta \simeq 1 - 1/2\gamma^2$ and $v \simeq c$, for the frequencies (6.6) where the coherent bremsstrahlung is amplified in the forward ($\psi = 0$) direction we obtain

$$\omega = \frac{4\pi c \gamma^2 \theta}{d} n. \quad (6.7)$$

One can see that the CB frequency grows quadratically with the particle energy. Equation (6.7) can be written as

$$d/\theta = 2\pi n l_c, \quad (6.8)$$

where

$$l_c = \frac{2c\gamma^2}{\omega} \quad (6.9)$$

is the so-called coherence length, along which the phase advance of the electromagnetic wave equals 1. It is proportional to the particle energy squared and inversely proportional to the radiation frequency. At high energies and low frequencies the coherence length may be of macroscopic size.

In general, the process of CB formation in a crystal for the electron traversing a sequence of axes or planes can be presented as follows. While traversing any of the axes, the electron will interact with $N \approx 2a_{TF}/a_i\theta$ atoms, where a_i is the interatomic spacing in the axis. Under the condition of $l_c \geq 2a_{TF}/a_i\theta$ all these atoms are positioned on the coherence length, and the total radiation of the electron on this group of atoms, because of the small phase difference, will occur coherently as on a single center with the effective charge NZe . If at the same time the condition (6.8) is also valid for l_c , then there is interference between the electron radiations on the effective centers of the sequence of axes, i.e., the radiation spectrum will have sharp maxima at the frequencies defined by (6.7). As the harmonics number increases, the peak height decreases because of the reduction in the coherence length ($l_c \sim 1/n$). When l_c fulfills $a \gg l_c \gg a_{TF}$, the electron radiation on every atom may be considered as independent, i.e., occurring as in amorphous medium. An excellent illustration of the above discussion is Fig. 6.6 where the measured radiation spectrum of 1-GeV electron in a diamond is shown [187].

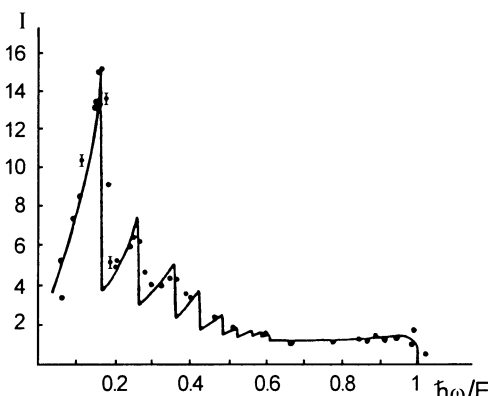


Fig. 6.6. Spectrum of coherent radiation of 1-GeV electrons passing a diamond crystal near the plane (001) at the angle of 4.6 mrad relative to the $\langle 110 \rangle$ axis. From [187].

When electrons have high energies, because of the significant (proportional to E^2) increase in the coherence length, the coherent and interference effects may appear at high frequencies ($\hbar\omega \sim E$). In this case, while studying the radiation process one should take into account the momentum transfer from electron to atom, i.e., one should apply the methods of the quantum radiation theory. Most often Born approximation is used for this purpose where the energy of the interaction between the colliding particles is considered as perturbation (see e.g. [177, 17]). Usually one is restricted to the first Born approximation. The developed theory of CB in crystals in the first Born approximation agrees fairly well with the results of the numerous experiments on the measurement of the spectra and the linear polarization of photon beams (the photon-beam polarization was first calculated in the first Born approximation by Überall [186]).

As an example, we show the measured CB spectra of electrons and positrons at high energies, which are essentially different from those at low energies because of the increased contribution from higher harmonics. Figure 6.7a shows the radiation spectra of electrons and positrons of 40 GeV moving in a Si crystal of 0.5 mm length under the angle of 0.52 mrad relative to axis $\langle 110 \rangle$ and 27 μ rad to planes (110) [188], i.e. in unchanneled mode (critical Lindhard angles at this energy for Si are $\psi_L = 72 \mu$ rad and $\theta_L = 24 \mu$ rad). One sees from the figure that the spectra of electrons and positrons are practically the same. The spectra identity for electrons and positrons follows from the qualitative consideration below. At high energies the coherence length l_c substantially exceeds the size of the effective region of the particle interaction with atom defined by the screening radius a_{TF} . Relativistic electrons and positrons with equal energies and equal initial conditions in the interaction region will be deflected to opposite sides by small angles that are equal in their absolute values. The deflection angles θ of electrons (positrons) can be estimated by using the uncertainty relation from Heisenberg:

$$\Delta p \Delta x \geq \hbar.$$

From this, taking $\Delta x = a_{TF}$ and $\Delta p = p\theta$, we obtain

$$\theta \simeq \frac{\hbar}{pa_{TF}} = \frac{1}{\gamma} \alpha Z^{1/3}, \quad (6.10)$$

where $\alpha = e^2/\hbar c = 1/137$ is the fine-structure constant. It directly follows from (6.10) that the scattering angles of electrons and positrons in the interaction region are substantially smaller than the effective angle of radiation $\theta_\gamma \simeq 1/\gamma$. This means that the difference in the trajectories of electrons and positrons due to scattering will not affect the radiation spectrum, which is formed by each interaction event over a long length l_c in the effective angle $1/\gamma$.

As Fig. 6.7a shows, the radiation intensity of a 40-GeV electron (positron) in a crystal compared to that in amorphous Si is higher by about one order for photon energies up to ~ 0.6 times the electron (positron) energy. Figure 6.7b

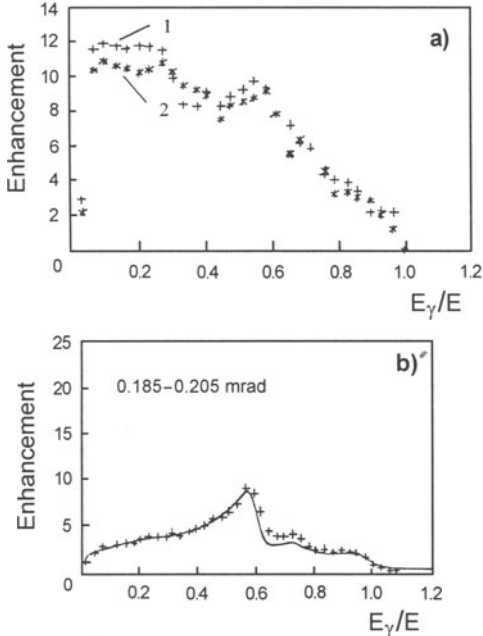


Fig. 6.7. (a) Spectra of coherent radiation of positrons (1) and electrons (2) of 40 GeV passing a Si crystal 0.5 mm thick at angle 0.52 mrad with respect to $\langle 110 \rangle$ axis and 27 μ rad with respect to (110) plane. (b) Spectrum of 150 GeV electron radiation in Si crystal 0.6 mm thick for the incidence at 0.185–0.205 mrad with respect to (110) planes and 8.2 mrad with respect to $\langle 110 \rangle$ axis. Solid line is for calculation in first Born approximation. From [188].

shows the radiation spectrum of the 150-GeV electrons with divergences of 0.185–0.205 mrad relative to the (110) planes, incident on the 0.6-mm-thick Si crystal; the beam angle relative to the $\langle 110 \rangle$ axis was 8.2 mrad [188]. The same figure shows the spectrum calculated in the first Born approximation (solid line), which is in reasonable agreement with the experimental data. The measurements of the photon beam polarizations and their comparison with the theory are discussed in Sect. 6.3.3.

In conclusion we briefly consider the radiation of electrons and positrons in an amorphous medium. The radiation cross section for the electron (positron) of high energy ($\gamma \gg 1$) interacting with the fully screened (at the radius a_{TF}) field of the atomic nucleus in the first Born approximation applied at $Z\alpha \ll 1$ may be defined by the well-known Bethe–Heitler formula [189]:

$$d\sigma = \frac{16}{3} Z^2 \alpha r_0^2 \frac{d(\hbar\omega)}{\hbar\omega} \left\{ \left[1 - \frac{\hbar\omega}{E} + \frac{3}{4} \left(\frac{\hbar\omega}{E} \right)^2 \right] \ln(183Z^{-1/3}) + \frac{1}{12} \left(1 - \frac{\hbar\omega}{E} \right)^2 \right\}, \quad (6.11)$$

where $r_0 = e^2/mc^2$ is the classic electron radius and $\hbar\omega = E - E_1$; E and E_1 being the electron energies in the initial and final states. The last term in the figure parentheses is of a small contribution and is usually neglected. Due to chaotic atomic arrangements in an amorphous medium the electron radiation energy loss over the length dx is

$$-dE = n_v dx \int_0^E \hbar \omega d\sigma = \frac{Edx}{L_R}, \quad (6.12)$$

where n_v is the atomic density of the medium, and

$$L_R = \left[4Z^2 \alpha r_0^2 n_v \ln(183Z^{-1/3}) \right]^{-1} \quad (6.13)$$

is the so-called radiation length, along which the electron energy decreases by $1/e$ times. To take into account the radiation from the interaction of the incident electron with the atomic electrons (the cross section for radiation from electrons is obtained from (6.12) by replacing Z^2 with Z), the formula for L_R becomes

$$L_R = \left[4Z(Z+1) \alpha r_0^2 n_v \ln(183Z^{-1/3}) \right]^{-1}. \quad (6.14)$$

The L_R values are 9.4 cm in Si, 2.3 cm in Ge, and 0.35 cm in W. From (6.12) we see that radiation energy losses of a relativistic ($\gamma \gg 1$) electron in the medium increase in proportion to E and dominates already in the GeV range of energies.

6.3.2 Channeling Radiation

The channeling of positrons and electrons may be accompanied by an intense radiation (ChR). Radiation, at axial channeling in a Si crystal, of electrons and positrons with energies of 16 and 28 MeV was observed for the first time in 1968 at the Lawrence Livermore Laboratory [190]. The properties of ChR theoretically predicted by Kumakhov and Terhune and Pantell in the mid-1970s [191] have raised a large amount of interest and stimulated a considerable series of experiments at many laboratories.

Let us consider some features of the coherent radiation in planar channeling of relativistic positrons. As mentioned in Chap. 1, the motion of high-energy particles in the field of crystal planes may be considered in the framework of classical mechanics. For the description of channeling radiation at energies of up to a few tens GeV, the classical theory of radiation is applicable. Below we restrict our consideration with the dipole approximation by assuming $\gamma \theta_L < 1$, i.e., assuming an unrelativistic transverse motion of channeled positrons. The positron motion in the harmonic interplanar potential $U = U_0(2x/d_p)^2$ is defined by (1.20). Its solution may be written as

$$x = A \sin(\omega_0 t + \varphi), \quad (6.15)$$

where the amplitude A and phase φ depend on the initial values x_0 and \dot{x}_0 , and the frequency

$$\omega_0 = \frac{2}{d_p} \sqrt{\frac{2U_0}{m\gamma}}. \quad (6.16)$$

The radiation intensity I may be estimated with the use of the known formula [192] for the radiation intensity of a relativistic particle:

$$I = \frac{2e^2}{3c^3} \frac{w^2 - [\mathbf{v}\mathbf{w}]^2/c^2}{(1 - v^2/c^2)^3}, \quad (6.17)$$

where w is the particle acceleration. In the case when the particle is accelerated in the transverse plane relative to the particle motion (z axis), the intensity formula in the dipole approximation ($v \simeq v_z$) will be

$$I = \frac{2e^2}{3c^3} \dot{w}_T^2 \gamma^4. \quad (6.18)$$

In our case ($w_T = \ddot{x}$) the acceleration squared is

$$w_T^2 = A^2 \omega_0^4 \sin^2(\omega t - \phi_0), \quad (6.19)$$

and its value averaged over time is

$$\langle w_T^2 \rangle = A^2 \omega_0^4 / 2. \quad (6.20)$$

Substituting it into (6.18), we have the average intensity of the radiation for planar-channeled positrons:

$$I = \frac{2}{3} \frac{A^2 e^2}{c^3} \left(\frac{32 U_0^2}{d_p^4 m^2} \right) \gamma^2. \quad (6.21)$$

The positron radiation frequency equals (6.16) shifted by the Doppler effect:

$$w = \frac{\omega_0}{1 - \beta \cos \psi}. \quad (6.22)$$

From here we obtain (for $\gamma \gg 1$) the frequency for the radiation in the forward direction ($\psi = 0$):

$$\omega = 2\omega_0 \gamma^2 = \frac{4}{d_p} \sqrt{\frac{2U_0}{m}} \gamma^{3/2}. \quad (6.23)$$

From (6.21) and (6.23) it follows that with an increase in the positron energy the radiation intensity grows quadratically, and the frequency grows as $E^{3/2}$.

One should note that the dipole approximation is valid for particle energies up to several GeV. In the energy range of tens of GeV the radiation character changes. It is necessary to take into account the coupling between the transverse and longitudinal motions; the higher harmonics of the radiation become essential. At multi-GeV energies one should also take into account a purely quantum effect – a recoil by radiation. In this case, a major contribution to the radiation is due to high harmonics; the radiation spectrum becomes quasi-continuous. For describing a radiation process one uses a method called the ‘constant field approximation’ (CFA) [16, 193]. Indeed, since at high energies both the radiation angular cone $\sim 1/\gamma$ and the radiation time are very small, one may neglect the transverse shift in the particle trajectory and field changes over a photon radiation, i.e., one may assume the

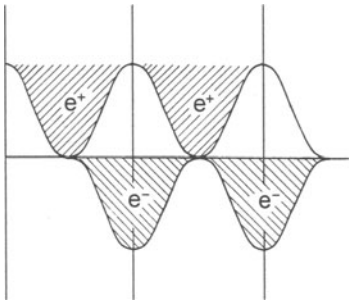


Fig. 6.8. Potential wells for planar channeling of positrons and electrons. Vertical lines are crystal planes.

radiation is in a constant field. The theoretical CFA approach is applicable for an incident angle with respect to crystal planes (axes) of $\theta \ll \theta_0$, where $\theta_0 = U_0/mc^2$. The critical angle θ_0 exceeds the Lindhard angle $\theta_L (\psi_L)$ at energies of hundreds of GeV, i.e., it covers the region of both the channelled and over-barrier particles experiencing an influence of planar (axial) fields. For $\theta \gg \theta_0$, as we have seen, another kind of radiation (coherent radiation) takes place; to investigate it one may use the Born approximation.

From (6.21) and (6.23) one sees that the dependence of the intensity and frequency on the crystal characteristics is defined by d_p and U_0 . In particular, since $U_0 \sim Z$ (atomic number), the intensity I is in proportion to Z^2 . The radiation intensity depends also on the initial parameters of the trajectory, x_0 and \dot{x}_0 , included in A . To find an overall intensity from all the beam particles, one should average over all particle trajectories. Since channeling of positrons and electrons occurs in different areas of the field, their radiation intensity may differ substantially. In the planar channeling mode, the positrons move in an interplanar potential well, while the electrons move in an overturned well of a plane (Fig. 6.8). Most of the intense radiation is due to positrons with high amplitudes of oscillation (as a result they reach the high-field area near the planes) and due to electrons with small amplitudes relative to the plane. Which fraction of particles (small or big amplitudes) will prevail, depends on the angle θ of incidence with respect to plane. At zero angle, most of the particles have small amplitudes of oscillation, and the intensity of radiation of electrons is higher than that of positrons. At $\theta \sim \theta_L$, when particles with large amplitudes dominate, the radiation intensity of positrons exceeds that of electrons (Fig. 6.9). In the angular range $\theta > \theta_L$, the particles are not trapped in a channeling mode and the intensities from positrons and electrons are equal.

To illustrate the above qualitative consideration, Fig. 6.10 (from [188]) shows the 150-GeV electron radiation spectra for planar channeling in Si(110). In particular, one sees that a maximal contribution to the radiation is due to electrons with small amplitudes, i.e., with small initial angles relative to the plane. The radiation intensity at the peak is higher than that

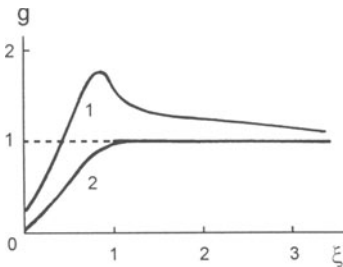


Fig. 6.9. The ratio g of the averaged radiation intensity of positrons to that for electrons (1) in Si(110) and (2) in W $\langle 110 \rangle$ as a function of $\xi = (\theta/\theta_L)^2$ and $\xi = (\theta/\psi_L)^2$, respectively. Data from [16].

in amorphous Si by a factor of ~ 40 . The calculations by CFA (solid line) are in satisfactory agreement with the experiment.

Now we shall consider axial channeling of electrons and positrons. The trapped electrons move along screw trajectories around an axis in a strong field. The radiation intensity of electrons in the axial channeling mode is higher than that of positrons (Fig. 6.9). The maximal difference in intensity is at zero angle of incidence with respect to axis. With an increase in the incident angle θ , the difference decreases due to an increase in the fraction of positrons with high transverse energy, which can approach an axis closer. For $\theta > \psi_L$, the intensities from positrons and electrons become equal. Since the axial fields are several times stronger than the planar ones, the radiation intensity for axial channeling is substantially higher than that for planar channeling (for positrons this is true for $\theta \geq \psi_L$).

Detailed studies of the radiation spectra from high-energy electrons and positrons in crystal channeling are carried out at CERN (see [188] and [194–204]). In these studies a peak was found in the radiation spectrum at a photon energy of $(0.7\text{--}0.8)E$, for axial channeling of electrons of 150 and 240 GeV in crystals with a thickness ranging from 0.2 to 1.4 mm (Fig. 6.11). This peak appeared for $\theta < 0.5\psi_L$. The radiation intensity at the peak's maximum exceeds the corresponding value in amorphous matter by about 110 times the

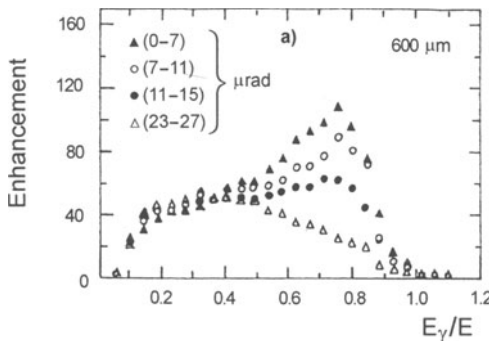


Fig. 6.10. Radiation of 150-GeV electrons in 0.6-mm-thick Si. Incident angles with respect to $\langle 110 \rangle$ plane are shown. The angle with respect to the $\langle 110 \rangle$ axis is 8.2 mrad. The solid line is the calculation via the CFA. From [188].

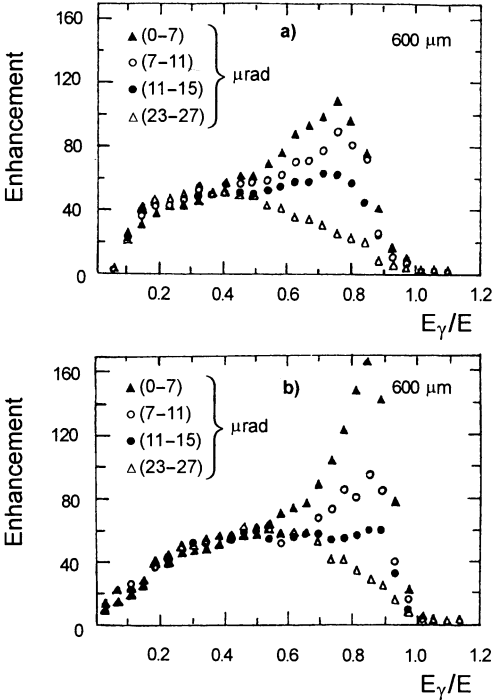


Fig. 6.11. Radiation spectrum of 150-GeV (a) and 240-GeV (b) electrons in 0.6-mm-thick Si (axis $\langle 110 \rangle$), for different incident angles with respect to the $\langle 110 \rangle$ axis [198].

electron energy at 150 GeV and by 160 times at 240 GeV. The theoretical calculations did not reproduce this peak. The most probable explanation of this peak is the multiple production of photons by the electrons moving along the axis close to it. Here all the produced photons will hit the detector.

Medenwaldt et al. [199] report on studies of the radiation spectrum in the case when one provides for the electron beams of 150 and 240 GeV the conditions for both planar channeling radiation and coherent bremsstrahlung on the atomic strings of the plane. Here the electron beam of divergence ($0 - \theta_L$) is directed at zero angle to $\langle 110 \rangle$ plane and at $\theta \gg \theta_0$ to $\langle 100 \rangle$ axis. The typical spectra of radiation in this case are shown in Fig. 6.12. The spectra have two peaks. The peak at low photon energy, $\sim 0.2E$, is due to channeling radiation (cf. with Fig. 6.10), whereas the peak at $\sim 0.7E$ is due to coherent bremsstrahlung (see Fig. 6.7b). Unlike the multi-photon peak in Fig. 6.11, due to the multi-production of photons, here we have a peak of nearly monochromatic photons of high energy. The radiation intensity at the peak exceeds the corresponding intensity in amorphous matter by 50 times. With an increase in the electron energy the second peak shifts toward that for the high-energy photons. The calculations according to the theory of [16] are shown in Fig. 6.12 (solid lines), and are in good agreement with the experimental data.

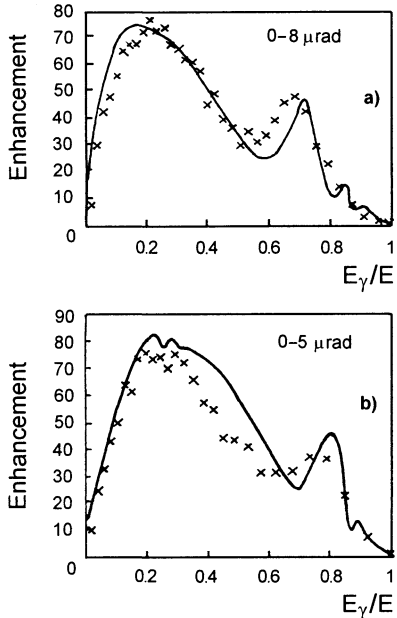


Fig. 6.12. Radiation spectrum of 150-GeV (a) and 240-GeV (b) electrons in 0.5-mm-thick diamond. The electrons were incident at an angle of 0.3 mrad with respect to the $\langle 110 \rangle$ axis. The angular range with respect to the $\langle 110 \rangle$ plane is shown. The solid line is from a calculation [199].

In conclusion we note that channeling radiation of electrons (positrons) is polarized. At low energies of ~ 1 GeV the experiments by the Tomsk group [209] have shown that electron radiation in the diamond (110) crystal under planar channeling has a high degree of linear polarization, $P \simeq (80 \pm 15)\%$.

6.3.3 Application of the Results to High-Energy Physics

High-Energy Photon Beams. The radiation emitted by high-energy electrons and positrons in crystals suggests possibilities for producing unique photon beams for setting up the experiments at accelerators. Today, the only source of electron–positron beams of hundreds of GeV are the cyclic proton accelerators. Here the positrons and electrons are produced via the processes $\pi^0 \rightarrow 2\gamma$ and $\gamma \rightarrow e^+e^-$. The π^0 mesons produced in proton interactions in the target (they make up one third of all π mesons) decay into two γ quanta, practically at the point of production since the decay length (m) is quite small

$$\lambda = 1.84 \times 10^{-7} p,$$

where p is the π^0 meson momentum (in GeV/c). Cleaning the beam of γ quanta from charged particles by a magnet just after the target, and placing in the beam path a convertor (not longer than one radiation length), we get a beam of electrons and positrons. The effective source of e^\pm will practically be equal to the source of π^0 mesons, since the exit angles of electrons and

positrons relative to those for the γ quanta are quite small at high energies: $\theta_e \simeq mc^2/E_\gamma$. In this scheme, the background particles (mainly π mesons) are due to neutron interactions in convertor and decay of neutral K mesons. To direct an electron (positron) beam produced in this way onto an experimental setup, one can use any universal beam line of an accelerator; the π -meson background can be kept below 1%.

The first electron beams at cyclic proton accelerators at energies of 26.6–40 GeV and intensities of 10^6 – 10^5 particles per cycle were obtained at the Serpukhov accelerator [205]. Placing in this beam an aligned crystal as a radiator, one can obtain the polarized beams of photons tagged by energy [206].

An example of this application is the photoproduction of particles at the Ω spectrometer at CERN. A polarized beam of photons tagged by energy in the energy range 25–70 GeV was created with an intensity of 10^6 particles per second [207, 208]. For this purpose the 80-GeV electron beam of intensity 2×10^7 electrons per cycle was used. The principle scheme of the photon-beam formation is shown in Fig. 6.13. Magnet M₂ directs an electron beam onto the crystal placed in the goniometer. The same magnet cleans the beam of photons radiated by electrons in detectors placed between magnets M₁ and M₂ to measure the electron beam characteristics. To ensure the optimal conditions for coherent radiation, an electron-beam angle of 0.75 mrad ($\sim 40\theta_L$) with respect to the (110) planes of a 2.2-mm-thick Si crystal was chosen.

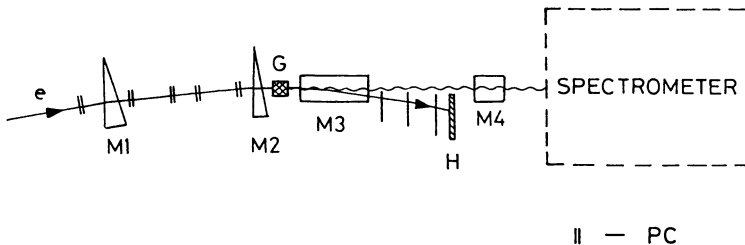


Fig. 6.13. Formation of tagged photon beams. M_{1,2} bending magnets; M₃ tagging magnet; M₄ cleaning magnet; G goniometer; H hodoscope; PC proportional chambers.

When passing a crystal, an electron loses energy via radiation; the emitted photon energy will be

$$\hbar\omega = E - E_1 ,$$

where E and E_1 are the electron energies at the crystal entrance and exit respectively. Since E is known, the photon spectrum can be reconstructed when the energy spectrum of the electrons is known. To do this, one uses magnet M₃ placed just after the crystal. It serves two purposes: first, it removes electrons from the photon beam and, second, it momentum-disperses

the electrons. The deflection angle in a magnetic field B is $\alpha = eBl/E_1$ over a length l . The energy spread transforms into a spatial one at a distance L from the magnet; the electron deflection is $x = \alpha L$. Via a scintillation hodoscope or calorimeter with a cell size Δx one can detect electrons with an energy spread of $\Delta E/E_1 = \Delta x/x$. To tag the energy of photons incident to the experimental setup, one uses the hodoscope and photon counter in coincidence. Figure 6.14a shows a typical CB photon spectrum radiated by 80-GeV electrons in a Si crystal. It covers energies from 25 to 70 GeV and agrees well with the calculation (solid line). The photon polarization could be found by the process of ρ^0 meson photoproduction, where ρ^0 takes the photon polarization. Selecting decays $\rho^0 \rightarrow \pi^-\pi^+$, one finds the polarization from the angular distribution of the decay products. A comparison of the calculated polarization with the measured one is given in Fig. 6.14b. The highest polarization, $\sim 60\%$, is due to low-energy photons (~ 25 GeV), and the lowest, $\sim 20\%$, is due to high-energy photons (~ 70 GeV). The considered scheme is typical for experiments with photon beams.

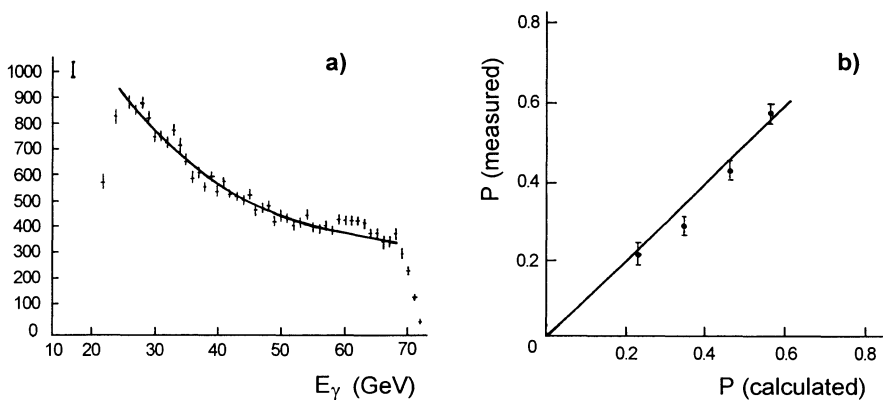


Fig. 6.14. (a) Coherent radiation spectrum of 80-GeV electrons passing a 2.2-mm-thick Si crystal at ~ 0.75 mrad with respect to the (110) plane. The solid line is from a calculation. (b) Comparison of calculated and measured polarization P .

In the above example the photon beam was formed at energies of 25–70 GeV. More recently, experiments have shown that, with use of crystal radiation of electron (positron) beams of 150–240 GeV, one can get photon beams of intensities up to two orders higher than that obtained with a corresponding amorphous matter. In a crystal of < 1 mm thickness the electrons lose $> 50\%$ of their energy. Under certain conditions a narrow ($\sim 10\%$) peak at energies of $(0.7\text{--}0.8)E$ appears in the photon spectrum. This effect will apparently give the possibility to produce a nearly monochromatic beam of high-energy photons.

The results of the studies performed at CERN will surely find an application at the electron–positron linear colliders under design with energies in the range of 250–500 GeV. The beam intensity of electrons (positrons) in these colliders will be several orders higher than that of e^\pm beams at cyclic proton accelerators. In this case, the possibilities of high-intensity photon beams produced by crystals will open a broad program of experimental studies.

Detectors of High-Energy e^\pm and γ Quanta. Aligned crystals may be also used to devise the detectors for high-energy photons and electrons (positrons) [16]. This possibility follows from the theoretical [16, 17] and experimental (see [196] and [200–204]) studies of the peculiar development of specific electron–photon showers in aligned crystals.

Let us consider this point in some detail. The main absorption process for the high-energy photons in a medium is the creation of the electron–positron pairs in the field of atoms. The e^\pm -pair creation may be considered as the process inverse to the bremsstrahlung effect. Indeed, the quantum-electrodynamics consideration of the e^\pm -pair creation is reduced to the photon absorption by an electron at the negative-energy level, and then transition of this electron to the normal state with positive energy. The created ‘hole’ in the continuum of the negative-energy electrons is a positron. Since the matrix elements for the transition between the initial and final states are equal for the forward and reverse processes, the cross section for the creation of the e^\pm pair with the energies E_+ (positron) and E_- (electron) is obtained directly from the formulae for the radiation cross section by a simple substitution ($E \rightarrow -E_+$, $E_1 \rightarrow E_-$, $\omega \rightarrow -\omega$) and multiplication by the phase-space ratio of positrons and photons in the final state:

$$\frac{E_+^2 dE_+}{(\hbar\omega)^2 d(\hbar\omega)} .$$

In particular, making the mentioned substitution in (6.11) for the cross section of the electron radiation at a single fully screened atom, one obtains the cross section for the creation of the e^\pm pair as follows:

$$\begin{aligned} d\sigma_\pm &= 4Z^2 \alpha r_0^2 \frac{dE_+}{(\hbar\omega)^3} \\ &\times \left[\left(E_+^2 + E_-^2 + \frac{2}{3} E_+ E_- \right) \ln 183 Z^{-1/3} - \frac{E_+ E_-}{9} \right] . \end{aligned} \quad (6.24)$$

Hence the probability for the creation of the e^\pm pair by a photon over a unit length is

$$W_\pm = n_v d\sigma_\pm .$$

The development of the electron–photon shower in an amorphous medium can be considered as follows. The high-energy photon creates the electron and positron. In turn, they radiate in the atomic fields the photons which again create e^\pm pairs etc. This process goes on until the electron and positron

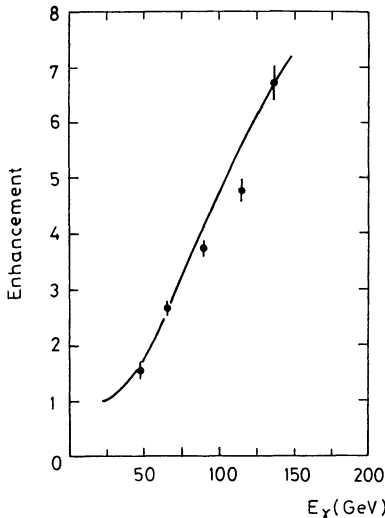


Fig. 6.15. Pair creation as a function of the photon energy near the $\text{Ge}\langle 110 \rangle$ axis (the initial divergence of the photon beam with respect to the $\langle 110 \rangle$ axis is less than 0.25 mrad). The solid line is for a calculation. From [200].

energies become so small that the ionization losses dominate. The longitudinal size of the developed shower is characterized by the radiation length L_R which is tabulated for some substances in Sect. 6.3.1.

In aligned crystals the spectra of radiation and pair creation are transformed due to coherence and interference effects. Therewith for a multi-GeV electron moving along the crystal axis the radiation enhancement, as we have seen, reaches two orders of magnitude as compared to that in the corresponding amorphous substance (misaligned crystal), and pair creation is enhanced by more than an order (see Fig. 6.15). For coherent pair creation by photons moving in the axial field of crystal, there is a threshold at the photon energy $\hbar\omega_t$, below which the pair creation occurs as in an amorphous medium. It follows from the CFA approximation [16] that the $\hbar\omega_t$ for Si, Ge and W are of the order of 120, 50, and 15 GeV, respectively.

At $\hbar\omega \gg \hbar\omega_t$ the radiation length L_{ch} substantially depends on the energy, and is several dozen times shorter than L_R in an amorphous substance, which is independent of energy unlike L_{ch} .

At $E \leq \hbar\omega_t$ the particles in strong axial fields continue to radiate a large number of soft photons, which can produce the e^\pm pairs through the Bethe–Heitler mechanism. Although here the probability of e^\pm -pair photoproduction is small, they can be produced due to a large number of photons. Therewith the number of photons in the shower will sizably exceed the number of charged particles. Thus, depending on the starting energy of a photon or electron (positron) in aligned crystals shorter showers of the following two types may develop: a ‘hard’ shower in the energy range $E \gg \hbar\omega_t$ and a ‘soft’ shower in the energy range $E \leq \hbar\omega_t$. Note that in both the hard and the soft showers the photon number N_γ will exceed the charged fraction N_e ; as Baier et al.

[16] have shown, the ratio $N_\gamma/N_e \simeq 11$ is valid in a broad range of energies. This feature may be used to determine the hard photon energy by measuring the energy of the charged particles only.

Figure 6.15 shows as an example the measured [200] e^\pm -pair production for a high-energy photon incident in an angular range of up to 0.25 mrad relative to the $\langle 110 \rangle$ axis of the Ge crystal, which was as thick as 0.5 mm and was cooled down to 100 K. Since the photon angles with respect to the $\langle 110 \rangle$ axis do not exceed the characteristic angle $\theta_0 = eU_0/mc^2$, equal to 0.53 mrad in this case, one may use the CFA to analyze the experimental data. The result of the CFA calculation (solid line) is in satisfactory agreement with the experiment.

Figure 6.16 shows the measured mean multiplicity of particles in the shower as a function of the incident angle of the electrons relative to the $\langle 110 \rangle$ axis of a 25-mm-thick Ge crystal and to the $\langle 100 \rangle$ axis of a 1.7-mm-thick W crystal [203]. The energies of the incident electrons were 287, 149, and 40 GeV. From the obtained functions one sees that by using a crystal as a detector, a high angular resolution is attainable. In particular, with use of a Ge crystal the HWHM is 0.75 mrad for 287-GeV electrons. As the energy of the incident electrons decreases, the angular resolution degrades. With a W crystal the resolution is ~ 1 mrad.

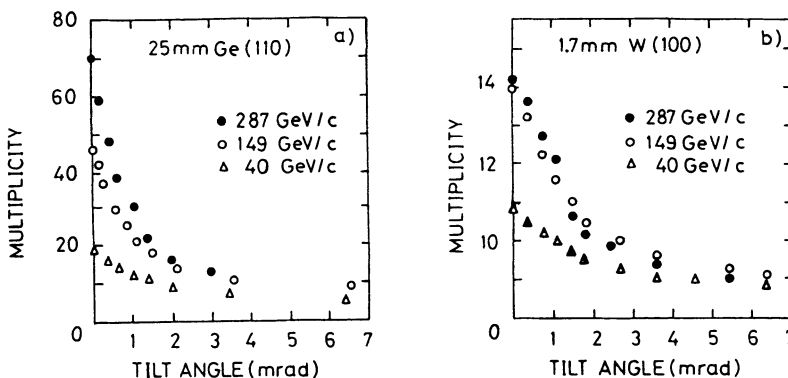


Fig. 6.16. Mean multiplicity of particles in a shower as a function of the electron incident angle relative to (a) the $\langle 110 \rangle$ axis of a 25-mm-thick Ge crystal and to (b) the $\langle 100 \rangle$ axis of a 1.7-mm-thick W crystal. The electron energies are shown. From [203].

The laws for shower development in aligned crystals indicate the possibility to devise detectors of e^\pm and γ quanta of high energies. The detectors could have the following advantages: small size and automatic hadron rejection, and high angular resolution. For example, by placing an aligned crystal as long as $\sim L_R$ in the beam and measuring the multiplicity, one can have rapid information on the energy of the photons or e^\pm producing the shower,

with a rough energy resolution. Note that the conventional calorimeter should have ~ 30 radiation lengths of material to absorb a shower at ~ 1 TeV.

Detectors with mosaics of crystals aligned to the interaction region of colliding beams and placed over the sphere surrounding this region would be useful for the mass-spectroscopy of bosons decaying into e^+ and e^- , for example. Calorimeters with high angular resolutions and crystal cross sections of the order of 1 m^2 will probably find application in γ astronomy for discovery of γ -radiation sources of high energies (above 100 GeV).

The studies in this field are progressing and will undoubtedly give results with the creation of the super-high-energy accelerators.

Epilogue

Nil adeo magnum, nec tam mirabile quicquam
Principio, quod nonminuant mirarier omnes
Paulatim.¹

Lucretius

We have considered the physical bases of the channeling of high-energy charged particles in oriented crystals and have given much attention to their application at accelerators. The results of research and development on the application of oriented crystals bring the hope that in the near future they will take up an important place in the arsenal of techniques for the steering of a high-energy particle beam and will ensure the realization of the experiments that earlier seemed problematic or unfeasible. Bent crystals have already found application in particle beam lines and in systems for the extraction of an accelerated beam, new opportunities for setting up the experiments are opened, and the efficiency of the use of accelerators has increased. Thus, the application of crystals at accelerators gradually changes from the area of exotics into usual practice.

Very wide prospects for the application of crystals are opened on the accelerating-storage complexes under design and construction at energies from several TeV up to tens of TeV. As the computations show (see Chap. 4), in the TeV energy domain it is possible with bent crystals to efficiently extract some accelerated particles from a beam halo, thus not infringing on a collider mode and by that providing simultaneous realization of experiments, both with the colliding beams and on fixed targets.

There is also an opportunity to create compact beam lines consuming almost no electric power, where the focusing bent crystals are used as optical elements. Such beam lines can find application in the transportation of proton beams extracted from an accelerator of the beams of positively charged secondary particles. The dechanneling length of particles in crystals grows almost linearly with energy, reaching several meters in specific energy ranges. Hence, in beam lines made of several crystals with a total length of

¹ There is nothing, however great and amazing it seemed at first sight, that people do not begin to look on with less amazement.

some tens of centimeters, the losses of particles from dechanneling will be small. Moreover, the emittance of an accelerated beam decreases with momentum p , as $1/p$, and at TeV energies becomes close to the acceptance of the crystal, $2\theta_L H \sim 1/p^{1/2}$, where θ_L is the Lindhard critical angle and H is the thickness of the crystal. As to secondary particles, they are produced on a target mainly in an angular cone, also decreasing with energy as $1/p$. In this connection, in the TeV energy ranges the efficiency of capture into a channeling mode grows both for the extracted proton beams and for the secondary particles.

As favorable conditions develop for the application of oriented crystals in physical experiments, in particular, as far as the decay lengths of astable particles grow linearly with energy, investigations into the properties of short-lived particles become feasible with the use of bent crystals.

Also promising is an application in which oriented crystals are placed in electron (positron) beams for the production of high-energy photon beams. Thus there are broad opportunities for research into the processes of photo-production of various particles, the peculiarities of the electromagnetic showers developing in crystals, and the quantum-electrodynamic phenomena in strong fields of crystals which exceed the critical field $E_{cr} = m^2 c^3 / e\hbar = 1.32 \times 10^{16}$ V/cm in the reference frame of an electron moving with $\gamma \geq 10^6$.

In conclusion let us note that if, after reading this book, the reader wishes to go in for problems of crystal applications in the high-energy domain, he/she should expect a fascinating journey full of hopes and gains.

References

1. Stark J. *Phys. Zs.* **13**, 973 (1912)
2. Robinson M.T., Oen O.S. *Phys. Rev.* **132** (5), 2385 (1963)
3. Piercy G.R., Brown F., Davies J.A. et al. *Phys. Rev. Lett.* **10**(4), 399 (1963)
4. Lindhard J., *K. Dan. Viddensk. Selsk. Mat. Phys. Medd.* **34**(1) (1965)
5. Gemmel D.S. *Rev. Mod. Phys.* **46**(1) (1974)
6. Kumakhov M.A., Shirmer G. *Atomnie stolknovenija v kristallach* (Atomic Collisions in Crystals) (Atomizdat, Moscow 1980)
7. Feldman L.C., Mayer J.W., Picraux S.T. *Materials Analysis by Ion Channeling* (Academic Press, NY 1982)
8. Ohtsuki Y.-H. *Charged Beam Interaction with Solids* (Taylor & Francis, London 1983)
9. Kittel C. *Introduction into Solid State Physics* (Wiley, New York 1956)
10. Blakmore J.S., *Solid State Physics* (Cambridge University Press, Cambridge 1985)
11. Landau L.D., Lifshits E.M., *Statisticheskaya Fizika* (Statistical Physics) (Nauka, Moscow 1973)
12. Seeger A. in *Relativistic Channeling* R.A. Carrigan, Jr. and J. Ellison, eds. (Plenum, NY, 1987) p.423
13. Moliére G., *Z. Naturforsch. A* **2**, 133 (1947)
14. Baryshevsky V.G., Tichomirov V.V. *Usp. Fiz. Nauk* **159**, 527 (1989)
15. Bazylev V.A., Zhevago N.K. *Isluchenie bystryh chastis v veshestve i vo vnesnih poljah* (Radiation of Fast Charged Particles in Matter and External Fields) (Nauka, Moscow 1987)
16. Baier V.N., Katkov V.M., Strakhovenko V.M. *Electromagnitnie processy pri vysokih energijah v orientirovannyh kristallah* (Electromagnetic Processes in Aligned Crystals under High Energies) (Nauka, Novosibirsk 1989)
17. Akhieser A.I., Shulga N.F. *Electrodynamica visokih energiy v veshestve* (High Energy Electrodynamics in Matter) (Nauka, Moscow 1991)
18. Forster J.S., Hatton H., Toone R.J., Este G., Baker S.I. et al. *Nucl. Phys. B* **318**, 301 (1989)
19. Andersen J.U., Bak J., Bonderup E., *Nucl. Instr. and Meth. B* **33**, 34 (1988)
20. Shih H.J. and Taratin A.M. *Bent Crystal Extraction of the SSC Beam with RF Noise Induced Diffusion*, SSCL report SSCL-389, 1991
21. Biryukov V., Vita P.F., in *Proc. of Europ. Part. Accel. Conf.* (World Scientific, London 1994) p. 2394
22. Bøgh E., *Radiat. Eff.* **12**, 261 (1972)
23. Abel F. et al. *Phys. Lett.* **42A**, 165 (1972)
24. Beloshitsky V.V., Komarov F.F., and Kumakhov M.A. *Phys. Reports* **139**, 293 (1986)
25. Beloshitsky V.V., and Kumakhov M.A. *Dokl. Acad. Nauk USSR* **212**, 846 (1973)

26. Waho T. *Phys. Rev.* **14**, 4830 (1976)
27. Biryukov V.M. et al. *Nucl. Instr. and Meth. B* **86**, 245 (1994)
28. Ohtsuki Y.-H. and Nitta H. in *Relativistic Channeling* R.A. Carrigan, Jr. and J. Ellison, eds. (Plenum, NY, 1987) p.59
29. Bavizhev M.D., Biryukov V.M. *SSCL report SSCL-N-775*, 1991
30. Robinson M.T. *Phys. Rev. B* **4**, 1461 (1971)
31. Barrett J.H. *Phys. Rev. B* **3**, 1527 (1971) *Nucl. Instr. Meth. B* **44**, 367 (1990)
32. Bak J.F. et al. *Nucl. Phys. B* **242**, 1 (1984)
33. Taratin A.M., Tsyanov E.N. and Vorobiev S.A. *Phys. Lett. A* **72**, 145 (1979)
34. Taratin A.M., Vorobiev S.A. *Nucl. Instr. and Meth. B* **47**, 247 (1990)
35. Kudryashov N.A., Petrovsky C.V., Strikhanov M.N. *Yad. Fiz.* **48**, 666 (1988); *Zh. Tekh. Fiz.* **59**, 68 (1989)
36. Biryukov V., *Phys. Rev. E* **51**, 3522 (1995)
37. Biryukov V.M. *Crystal Channeling Simulation. CATCH 1.4 User's Guide* SL/Note 93-74 (AP), CERN, 1993
38. Gould H., Tobochnik J., *Computer Simulation in Physics* part I. (Addison-Wesley, Reading, MA 1988)
39. Esbensen H. and Golovchenko J.A., *Nucl. Phys. A* **298**, 382 (1978); Esbensen H. et al. *Phys. Rev. B* **18**, 1039 (1978)
40. Particle Data Group *Phys. Lett. B* **239**, (1990)
41. Kitagawa M., Ohtsuki Y.-H., *Phys. Rev. B* **8**, 3117 (1973)
42. The LUND Monte Carlo Programs, CERN 1 November 1989
43. Taratin A.M., Vorobiev S.A. *Zh. Tekh. Fiz.* **55**, 1598 (1985)
44. Taratin A.M. et al. *Phys. Stat. Sol.(b)* **100**, 273 (1980)
45. Taratin A.M. and Vorobiev S.A., *Phys. Stat. Sol.(b)* **107**, 521 (1981)
46. Landau L.D., *J. Phys. (USSR)* **8**, 201 (1944)
47. *Relativistic Channeling* R.A. Carrigan, Jr. and J. Ellison, eds. (Plenum, NY, 1987)
48. Uggerhoj E. in *Relativistic Channeling* R.A. Carrigan, Jr. and J. Ellison, eds. (Plenum, NY, 1987) p. 5
49. Møller S.P. in *Relativistic Channeling* R.A. Carrigan, Jr. and J. Ellison, eds. (Plenum, NY, 1987) p. 49
50. Forster J.S. in *Relativistic Channeling* R.A. Carrigan, Jr. and J. Ellison, eds. (Plenum, NY, 1987) p. 39
51. Samsonov V.M. in *Relativistic Channeling* R.A. Carrigan, Jr. and J. Ellison, eds. (Plenum, NY, 1987) p. 129
52. Landau L.D., Lifshits E.M., *Mechanika* (Mechanics), (Nauka, Moscow, 1973)
53. Jensen B.N., et al. "A proposal to Test Beam Extraction by Crystal Channeling at the SPS: A First Step Towards a LHC Extracted Beam", DRDC/P29, CERN (1991)
54. Carrigan R.A., Jr. et al. "Proposal for a Test of Low Intensity Extraction from the Tevatron Using Channeling in a Bent Crystal", FNAL Proposal P853 (1991)
55. Jensen B.N., et al. *Nucl. Instrum. Meth. B* **71**, 155 (1992)
56. Tsyanov E.N. *Fermilab Preprint TM-682, TM-684* Batavia, 1976
57. Elishev A.A., et al. *Phys. Lett. B* **88**, 387 (1979)
58. Ellison J.A., et al. *Nucl. Instr. and Meth. B* **2**, 9 (1984)
59. Taratin A.M. and Vorobiev S.A. *Phys. Lett. A* **119**, 425 (1987)
60. Kudo H. *Nucl. Instr. and Meth.* **189**, 609 (1981)
61. Ellison J.A. *Nucl. Phys. B* **206**, 205 (1982)
62. Kaplin V.V. and Vorobiev S.A. *Phys. Lett. A* **67**, 135 (1978)
63. Ellison J.A. and Picraux S.T. *Phys. Lett. A* **83**, 271 (1981)
64. Biryukov V.M. *IHEP Preprint 91-59*, Protvino, 1991

65. Bavizhev M.D., Biryukov V.M. and Gavrilov Yu.G. *IHEP Preprint* 89-222, Protvino, 1989
66. Bavizhev M.D., Biryukov V.M. and Gavrilov Yu.G. *Sov. Phys. Tech. Phys.* **36**(2), 203 (1991)
67. Bavizhev M.D., Biryukov V.M. and Gavrilov Yu.G. *Rad. Effects* **25**, 139 (1993)
68. Gibson W.M., et al. *Nucl. Instr. and Meth. B* **2**, 54 (1984)
69. Gibson W.M., in *Relativistic Channeling* R.A. Carrigan, Jr. and J. Ellison, eds. (Plenum, NY, 1987) p. 101
70. Carrigan R.A., Jr., in *Relativistic Channeling* R.A. Carrigan, Jr. and J. Ellison, eds. (Plenum, NY, 1987) p. 339
71. Biryukov V.M., p. 54 in *Proc. of the Workshop on Channeling Application in High Energy Physics*, Protvino (1991)
72. Dearnaley G. *Can. J. Phys.* **46**, 587 (1968)
73. Markus A.M. et al. *Sov. Phys. Zh. E. T. F.* **61**, 332 (1971)
74. Biryukov V.M. et al. *Nucl. Instr. and Meth. B* **73**, 153 (1993)
75. Andreev V.A. et al. *Pis'ma v Zh. Eksp. Teor. Fiz.* **36**, 340 (1982), **38**, 58 (1984), **44**, 101 (1986)
76. Chesnokov Yu.A. et al. *Nucl. Instr. and Meth. B* **69**, 247 (1992)
77. Biryukov V.M., *Phys. Lett. A* **205**, 340 (1995)
78. Mannami M. et al. *Nucl. Instr. and Meth. B* **33**, 62 (1988)
79. Biryukov V.M. in *Proc. of the IVth All-Union Conf. on Interaction of Radiation with Solids* Moscow, p.171 (1990); *Radiat. Effects* **25**, 143 (1993)
80. Biryukov V.M., *Phys. Lett. A* **205**, 343 (1995)
81. Clement M. et al. CERN SL/92-21 (EA) 1992
82. Kosevich A.M. *Dislocations in the Theory of Elasticity*, (Naukova dumka, Kiev, 1978)
83. Quere Y. *Phys. Stat. Sol.* **30**, 713 (1968); *Radiat. Effects* **13**, 57 (1972)
84. Kudo H. *J. Phys. Soc. Jpn.* **40**, 1645 (1976); *Nucl. Instr. Meth.* **170**, 129 (1980)
85. Wielunski L. et al. *Nucl. Instr. Meth.* **168**, 323 (1980)
86. Ellison J.A. and Picraux S.T., *Phys. Lett. A* **83** (6), 271 (1981)
87. Kimura K., Mannami M. and Natsuaki N. *Jap. J. of Appl.Phys.* **21**, 1769 (1982)
88. Gärtner K. et al. *Nucl. Instr. Meth. B* **4**, 63 (1984)
89. Van Vliet D. *Phys. Stat. Sol. (a)* **2**, 521 (1970)
90. Mazzone A.M. *Nucl. Instr. Meth. B* **42**, 317 (1989)
91. Picraux S.T. et al. *Phys. Rev. B* **18**, 2078 (1978)
92. Biryukov V.M., *Phys. Rev. E* **52**, 2045 (1995)
93. Carrigan R.A. et al. *Nucl. Instr. and Meth. B* **90**, 128 (1994)
94. Deutsch M. et al. *Appl. Phys. Lett.* **18**, 1410 (1987)
95. Biryukov V.M., Bavizhev M.D., and Tsyanov E.N. *Estimate of the Influence of Dislocation Defects on Crystal Deflector Efficiency at 20 TeV*, SSCL report SSCL-N-777 (1991)
96. Kudo H. *Phys. Rev. B* **18**, 5995 (1978)
97. Baker S.I. in *Relativistic Channeling* R.A. Carrigan, Jr. and J. Ellison, eds. (Plenum, NY, 1987) p. 391
98. Chesnokov Yu.A. et al. in *Proc. of 15 International Conference on High Energy Accelerators*, 1, (DESY, Hamburg 1992) p.173
99. Baker S.I. et al. *Nucl. Instr. and Meth. B* **90**, 119 (1994)
100. Elsener K. et al. in *Proc. of Europ. Part. Accel. Conf.*, London (1994), p. 2385
101. Kirsebom K. et al. contrib. to the Workshop on *Channeling and other coherent crystal effects at relativistic energy*, Aarhus (1995)

102. Møller S.P., Uggerhøj E., Atherton H.W., Clement M., Doble N. et al. *Phys. Lett. B* **256**, 91 (1991)
103. RD22 experiment *Status Report on H8 Analysis* by Biryukov V.M., Carboni G. and Costantini F. (INFN Pisa, 1992)
104. Costantini F. *Nucl. Instr. and Meth. A* **333**, 125 (1993)
105. Møller S.P., Worm T., Clement M., Doble N., Elsener K. et al. *Nucl. Instr. and Meth. B* **84**, 434 (1994)
106. Biryukov V.M., *Nucl. Instr. and Meth. B* **117**, 357 (1996)
107. Biryukov V.M. SL/Note 93-78 (AP), CERN, 1993
108. Akbari H., Altuna X., Bardin S., Belazzini R., Biryukov V. et al. *Phys. Lett. B* **313**, 491 (1993)
109. Afonin A.G. et al. *IHEP Preprint* 87-121, 1987
Bavizhev M.D. et al. *IHEP Preprint* 87-148, 1987
110. Bavizhev M.D. et al. *IHEP Preprint* 89-77, 1989
111. Baker S.I. et al. *Nucl. Instr. and Meth. A* **248**, 308 (1986)
112. Andreev V.A. et al. *Pis'ma v Zh. Eksp. Teor. Fiz.* **41**, 408 (1985)
113. Denisov A.S. et al *Nucl. Instr. and Meth. B* **69**, 382 (1992)
114. Kotov V.I. et al. in *Proc. of 15 International Conference on High Energy Accelerators*, 1, (DESY, Hamburg 1992) p. 128
115. Clement M. et al. CERN SL 92-21 (EA), 1992
116. Proposal CERN SPSC 90-22 (P253), 1990
117. Kartashev V.P. and Kotov V.I. *Osnovy magnitnoy optiki pukov zaryazennyh castic visokih energiy* (Principles of Magnetic Optics of Charged High Energy Particle Beams) (Energoatomizdat, Moscow: 1984)
118. Chesnokov Yu.A. et al. *Nucl. Instr. and Meth. B* **63**, 366 (1992)
119. Baranov V.I. et al. *Nucl. Instr. and Meth. B* **63**, 366 (1995)
120. Chesnokov Yu.A. et al. Proc. of PAC-91, V1, p192, San Francisco, 1991
121. The LHC Study Group, "Study of the Large Hadron Collider", CERN 91-03 (1991)
122. Sumbaev O.I. *Kristall-difrakcionnye gamma spectrometry* (Crystal-diffractive Gamma Spectrometers) (Gosatomizdat, Moscow: 1963)
123. Samsonov V.M. *LNPI Preprint* N. 278, Leningrad, 1976
124. Jensen B.N. et al. CERN SL 92-14 (EA), 1992
125. Baublis V.V. et al. *Fermilab Preprint* FN-608 Batavia, 1994
126. Chesnokov Yu.A. Autoref. Ph.D. Thesis, IHEP note 93-94, Protvino, 1993
127. Kovalenko A.D., Mikhailov V.A., Taratin A.M., Boiko V.V., Kozlov S.I. and Tsyanov E.N., presented at the Workshop "Channeling and other coherent crystal effects at relativistic energy", Aarhus (1995)
128. Biryukov V.M. et al. *IHEP Preprint* 95-14, Protvino, 1995; to appear in Proc. of the Part. Accel. Conf. (Dallas, 1995)
129. Baranov V.I. et al. *IHEP Preprint* 95-13, Protvino, 1995; to appear in Proc. of the Part. Accel. Conf. (Dallas, 1995)
130. Carrigan R.A. *Fermilab Preprint* FN-454 Batavia, 1987
131. Greenenko A.A. and Shulga N.F. *Nucl. Instr. and Meth. B* **90**, 179 (1994)
132. Bodyagin et al. p. 45 in *Proc. of the Workshop on Channeling Application in High Energy Physics*, Protvino (1991)
133. Bak J.F. et al. *Nucl. Phys. A* **389**, 533 (1982)
134. Koshkarev D.G. *Preprint ITEP* N. 30 (1977), Moscow
135. Newberger B.S., Shih H.-J. and Ellison J.A., *Phys. Rev. Lett.* **71**, 356 (1993); *Nucl. Instr. and Meth. A* **235**, 9 (1993)
136. Herr W., CERN SL/92-53 (AP), 1992
137. Avdeichikov V.V. et al. *JINR Communications* **1**, 3 (1984) [English translation: Fermilab FN-429 (1986)]

138. Asseev A.A., Bavizhev M.D., Ludmirsky E.A., Maisheev V.A. and Fedotov Yu.S., *Nucl. Instr. and Meth. A* **309**, 1 (1991)
139. Asseev A.A. et al. *Nucl. Instr. and Meth. A* **324**, 31 (1993)
140. Murphy C.T., presented at the Workshop "Channeling and other coherent crystal effects at relativistic energy", Aarhus (1995)
141. Bavizhev M.D. and Dzyba A.R., IHEP Preprint 89-76. Protvino, 1989
142. Murthy et al. *Nucl. Phys.* **92**, 269 (1975)
143. Biryukov V.M. *Nucl. Instr. and Meth. B* **53**, 202 (1991)
144. Taratin A.M. et al. *Nucl. Instr. and Meth. B* **58**, 103 (1991)
145. Biryukov V., *Nucl. Instr. and Meth. B* **117**, 463 (1996)
146. Biryukov V.M., to be presented at the 5-th Europ. Part. Accel. Conf. (Sitges, 1996)
147. Taratin A. et al. SSCL-545 (1991)
148. Tsyganov E. and Taratin A., "Beam Halo Extraction from the Tevatron During Collider Runs", SSCL-Preprint-569 (1994)
149. Biryukov V., in Proceed. of Europ. Part. Accel. Conf., (World Scientific, London 1994), p. 2391
150. Ferroni F. et al. (RD22 Collab.), *Nucl. Instr. and Meth. A* **351**, 183 (1994)
151. Akbari H. et al. (RD22 Collab.), in Proceed. of Europ. Part. Accel. Conf., (World Scientific, London 1994), p. 199
152. Altuna X. et al. CERN SL/95-41 (DI), 1995
153. Biryukov V.M., p. 27 in Proc. of the Workshop on Channeling Application in High Energy Physics, Protvino, 1991
154. Biryukov V.M., Bavizhev M.D. and Tsyganov E.N., "On the Influence of Imperfect Surface of the Crystal Deflector on the Multiturn Extraction Efficiency", SSCL-N-776 (1991)
155. Carrigan R.A., Jr., Toohig T.E. and Tsyganov E.N., *Nucl. Instr. and Meth. B* **48**, 167 (1990)
156. Biryukov V., *Phys. Rev. E* **52**, 6818 (1995)
157. Murphy C.T., Mokhov N.V. and Carrigan R.A., private communication (1994/95)
158. Biryukov V.M., *Phys. Rev. Lett.* **74**, 2471 (1995)
159. Sun C.R. in *Relativistic Channeling* (ed. by R.A. Carrigan, Plenum, New York, 1987) p.379
160. Baryshevsky V.G. *Pis'ma v Zh. Teh. Fiz.* **5**, 182 (1979) [Sov. Tech Phys. Lett., **5**, 73, 182 (1979)]
161. Pondrom L. in *Proc. of 1982 Summer School on Elementary Particle Physics and Future Facilities*, Snowmass, Colorado, edited by R. Donaldson (Fermilab, Batavia, 1983)
162. Lyuboshits V.L. *Yad. Fiz.* **31**, 986 (1980)
163. Kim I.J. *Nucl. Phys. B* **229**, 251 (1983)
164. Chen D. et al. *Phys Rev. Lett.* **69**, 3286 (1992)
165. Gemmel D.S., Holland R.E., *Phys Rev. Lett.* **14**, 945 (1965)
166. Domeij B., Bjorqvist K., *Phys. Lett.* **14**, 127 (1965)
167. Tulinov A.F., DAN USSR, **162**, 546 (1965)
168. Gibson W.M., *Ann. Rev. of Nucl. Sci.* **25**, 465 (1975)
169. Nilsen H., Andersen J.U., Uggerhoj E., Invited talk given by H. Nilsen at the Workshop on Channeling at High Energies, Fermilab, April 7-8, 1978
170. Baublis V. et al. *Nucl. Instr. and Meth. B* **90**, 150 (1994)
171. Baublis V. et al. *Nucl. Instr. and Meth. B* **90**, 112 (1994)
172. Diambrini-Palazzi G., *Rev. Mod. Phys.* **40**(3), 611 (1968)
173. Timm U., *Fortschritte der Physik* **17**(12), 765 (1969)
174. Wedell R., *Phys. Stat. Sol. (b)* **99**(1), 11 (1980)

175. Beloshitsky V.V., Kumakhov M.A., *Phys. Rep.* **93**(1), 118 (1982)
176. Bazylev V.A., Zhevago N.K., *Usp. Fiz. Nauk* **137**(4), 605 (1982)
177. Akhieser A.I. , Shulga N.F., *Usp. Fiz. Nauk* **137**(4), 561 (1982)
178. Baier V.N. , Katkov V.M. , Strakhovenko V.M., *Usp. Fiz. Nauk* **159**, 455 (1989)
179. Sørensen A.N., Uggerhøj E., *Nucl. Science Appl.* **3**, 147 (1989)
180. Ter-Mikaelyan M.L. *High Energy Electromagnetic Processes in Condensed Media* (Wiley, New York, 1972)
181. Kumakhov M.A., Komarov F.F., *Izluchenie zariagenikh chastic v veschestve i vo vneshnikh poliakh* (Radiation of Charged Particles in Matter and External Fields) (Minck, izd. "Universiteteskoe" (1985))
182. Ferretti B., *Nuovo Cimento* **7**, 118 (1950)
183. Ter-Mikaelyan M.L., *Sov. Zh. Eksp. Teor. Fiz.* **25**, 289 (1953)
184. Ter-Mikaelyan M.L. *Sov. Zh. Eksp. Teor. Fiz.* **25**, 296 (1953)
185. Überall H., *Phys. Rev.* **103**, 1055 (1956)
186. Überall H., *Phys. Rev.* **107**, 223 (1957)
187. Barbiellini G. et al. *Phys. Rev. Lett.* **8**, 454 (1962)
188. Medenwaldt R. et al. *Phys. Lett. B* **260**, 235 (1991)
189. Heitler W., *The quantum theory of radiation*, 3rd ed., Oxford–New York (1954)
190. Walker R.L. et al., *Phys. Rev. Lett.* **25**, 5 (1970)
191. Kumakhov M.A., *Phys. Lett. A* **57**, 17 (1976); Tezhune R.W., Pantell R.H., *Appl. Phys. Lett.* **30**, 265 (1977)
192. Landau L.D. and Lifshits E.M., *Teoria polia* (The field theory), Fizmatgiz (1963)
193. Shulga N.F., *Zh. E. T. Ph. Lett.* **32**, 179 (1980)
194. Belkacem A. et al. *Phys. Rev. Lett.* **54**, 25, 2667 (1985)
195. Belkacem A. et al. *Phys. Lett. B* **177**, 2, 211 (1986)
196. Belkacem A. et al. *Phys. Rev. Lett.* **58**, 12, 1196 (1987)
197. Medenwaldt R. et al. *Phys. Rev. Lett.* **63**, 2827 (1989)
198. Medenwaldt R. et al. *Phys. Lett. B* **242**, 517 (1990)
199. Medenwaldt R. et al. *Phys. Lett. B* **281**, 153 (1992)
200. Bak J.F. et al. *Phys. Lett. B* **202**, 615 (1988)
201. Bak J.F. et al. *Phys. Lett. B* **213**, 242 (1988)
202. Del Fabbro R., Murtas G.P., *Physica Scripta* **23**, 690 (1981)
203. Medenwaldt R. et al. *Phys. Lett. B* **227**, 483 (1989)
204. Uggerhøj E. in *Proc. of the Intern. Symposium on Radiation of Relativistic Electrons in Periodical Structures* edited by Yu.L. Pivovarov and A.P. Potylitsin (Tomsk Univ. Press, Tomsk, 1993) p. 163
205. Gershtein S.S. et al. *Sov. Atom. Energia* **35**, 181 (1973)
206. Maisheev V.A. et al. *Sov. Zh. Eksp. Teor. Fiz.* **77**, 5, 1708 (1979)
207. Aston D. et al. *Nucl. Instr. and Meth.* **197**, 287 (1982)
208. Bussey P.J. et al. *Nucl. Instr. and Meth.* **211**, 301 (1983)
209. Adishev Yu. N. et al., *JETP Lett.* **33**, 478 (1981)

Further Reading

210. Møller S.P., *Nucl. Instr. and Meth. A* **361**, 403 (1995)
211. Proceedings of the Aarhus Workshop on Channeling and Other Crystal Effects at Relativistic Energy, *Nucl. Instr. and Meth. B* **119**, No. 1–2 (1996)

Subject Index

- absorption length 128
alignment 83
alpha function 129, 135
amorphous layer 145
angular acceptance 110
anticoincidence 90
atomic string 122
autocollimator 86
axial channeling 27, 122
- bcc lattice 2
beam attenuator 170
beam focusing 178
beam fragmentation 120
beam line 169
beam momentum 98
beam splitting 172
beam transmission 92
beauty physics 140
bending angle 100
bending capture 56
bending dechanneling 33, 101
bending device 83
bending moment 84
bending power 174
bending radius 84
bent crystal 31
bent crystal acceptance 34
bent crystal channeling 31
beta function 129, 134
betatron oscillation 129
betatron tune 129
Bethe–Heitler formula 195
blocking effect 187
Born approximation 194
Bravais lattice 2
- calorimeter 207
centrifugal force 31, 99
channeling 12, 83
- channeling radiation (ChR) 191
cleaning system 165
coherence length 193
coherent bremsstrahlung (CB) 191
collider mode 163
collimator 171
computer simulation 60
concave mirror 84
constant field approximation 197
convertor 201
convex mirror 84
critical angle 14
critical radius 32, 84
critical transverse coordinate 14
crystal 1
crystal deflector 169
crystal extraction 125
crystal holder 84
crystal lattice 1
crystal mosaicity 73, 84
crystal string 175
crystallographic plane 4, 83
curvature 31, 93
curvature gradient 46
- decay length 185
decay mode 186
dechanneling 17, 98
dechanneling length 19, 99
deflection efficiency 34, 90
detector resolution 118
diffusion equation 18
diffusion factor 18
diffusion mode 138
diffusion theory 17
dipole approximation 196
dislocation 69
dislocation dechanneling 77
dislocation loop 74
dislocation-free silicon 101

- Doppler effect 192
doughnut scattering 124
drift chamber 89
dynamic equilibrium 50, 105
- edge dislocation 69, 71
edge effect 117
effective potential 31
efficient bending 83
elastic scattering 103
electronic scattering 21
electron–photon shower 204
electrostatic splitter 172
emittance 175
end-face capture 102
energy loss 25, 94
equilibrium orbit 129
extraction efficiency 131
- fast extracted beam 169
fcc lattice 2
feed-in 50, 110
feed-out 50, 106
fixed target 162
focal length 180
focusing crystal 179
Fokker–Planck equation 18
four-point bending 86
friction factor 18
- gamma astronomy 207
germanium 6, 116
goniometer 89
gradient capture 114
gradient effect 46, 98
gyromagnetic ratio 187
- hadron rejection 206
halo 125, 140
harmonic approximation 40
heavy-atom material 115
heavy ion 124
high harmonic 197
- impact parameter 130
ingot 115
interatomic spacing 193
internal target 125
interplanar channel 88
interplanar potential 10
- kick mode 139
laser interferometer 86
- lattice defect 67
least-squares fit 106
lifetime 185
Lindhard angle 14
Lindhard potential 9
linear collider 204
linear polarization 194
loaded console 86
- magnetic moment 186
magnetic rigidity 124
magnetic splitter 172
master equation 18
microphotometer 119
microstrip detector 89
Miller indices 4
miscut angle 145
Moli re potential 9
momentum spread 175
monochromatic beam 203
multi-pass efficiency 131
multi-pass extraction 127
multi-photon peak 200
multiple scattering 109
multiplicity 206
- narrow (111) plane 92
nuclear interaction 131
nuclear photoemission 89
nuclear scattering 19
- optimal bending 41
ordinary dechanneling 98
orientation 83
oscillation period 14
- pair creation 204
particle motion in a bent channel 31
phase density 176
photon beam 201
photoproduction 202
planar channeling 12
planar potential 10
polarized beam 187, 202
pre-scatter 137
- quadrupole lenses 178
quasi-channeling 12
- radiation 191
radiation damage 80, 170
radiation enhancement 205
radiation length 196
radiation spectrum 193

- radiator 202
relaxation length 19
reversibility rule 51, 105
rosette-type trajectory 122

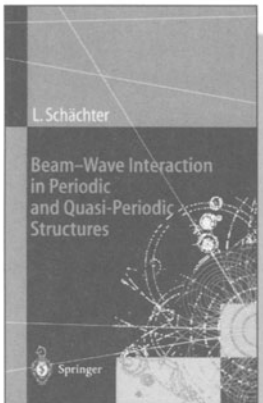
screening radius 7
screw dislocation 71
selection criterion 94
semiconductor detector 88
septum 125
septum width 141
shape effect 120
short-lived particle 185
skew plane 123
spin precession 186
stepping motor 89
stereogram 123
surface imperfection 117
surface nonflatness 145
synchrophasotron 126

tagged beam 202
tagging 98
target 88
thermal vibration 43
Thomas-Fermi potential 7
three-point bending 86
transverse energy 13
trigger 90, 99
tune resonance 136
tungsten 11
twist effect 87, 143

valence electron 139
variable curvature 46
vertex 190
veto 90
volume capture 50, 110
volume reflection 34, 128

wide (111) plane 91

Electron Interaction



L. Schächter

Beam-Wave Interaction in Periodic and Quasi-Periodic Structures

1997. XIII, 356 pages,
109 figures, 1 table.
Hardcover DM 138.-
ISBN 3-540-61568-7

The main topic of this book is the interaction of electrons with electromagnetic waves, primarily, but not only, for the generation and amplification of radiation. It discusses the various methods of electron-beam generation and propagation and the basic electron-wave interaction schemes. Then an idealized picture of the beam-wave interaction in a dielectric loaded waveguide is presented. Gradually the complexity of the analysis is increased by presenting the effect of reflected waves and further by considering the beam as an ensemble of macroparticles. The author discusses the interaction in periodic and in quasi-periodic metallic structures and the fundamentals of the beam-wave interaction in a periodic field. The book concludes with a brief discussion of particle acceleration, including novel acceleration schemes.



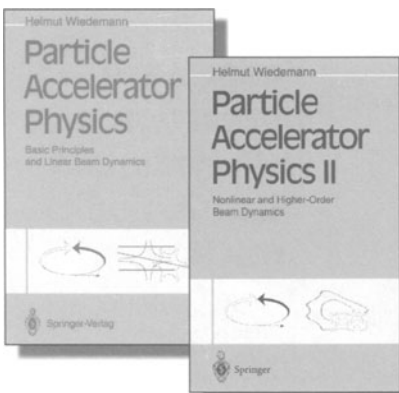
Prices subject to change without notice.
In EU countries the local VAT is effective.

Please order by
Fax: +49 - 30 - 827 87-301
e-mail: orders@springer.de
or through your bookseller



Springer

Fundamental particles



H. Wiedemann **Particle Accelerator Physics**

**Basic Principles and
Linear Beam Dynamics**
1993. XVI, 445 pages. 160 figures.
Hardcover DM 108.-
ISBN 3-540-56550-7

After covering the dynamics of relativistic particle beams, the basics of particle guidance and focusing, lattice design, characteristics of beam transport systems and circular accelerators, the author goes on to treat particle-beam optics in the linear approximation, including sextupoles to correct for chromatic aberrations. Perturbations to linear beam dynamics are analyzed in detail, together with their correction measures, and basic lattice design features and building blocks leading to the design of more complicated beam transport systems and circular accelerators are studied. The book is aimed at students and scientists who are interested in an introduction to the subject while also forming a broad basis for further, more detailed studies.

H. Wiedemann **Particle Accelerator Physics II**

**Nonlinear and Higher-Order
Beam Dynamics**
1995. XVI, 464 pages. 118 figures.
Hardcover DM 108.-
ISBN 3-540-57564-2

This volume continues the discussion of particle accelerator physics beyond the introduction in Vol. I. Basic principles of beam dynamics already discussed in Vol. I are expanded into the nonlinear regime in order to tackle fundamental problems encountered in present day accelerator design and development. Nonlinear dynamics is discussed both in terms of the transverse phase space to determine chromatic and geometric aberrations which limit the dynamics aperture as well as the longitude phase space in connection with phase focusing at very small values of momentum compaction. Whenever possible, effects derived theoretically are compared with observations made with existing accelerators.

Prices subject to change without notice.
In EU countries the local VAT is effective.

Please order by
Fax: +49 - 30 - 827 87-301
e-mail: orders@springer.de
or through your bookseller



Springer

Springer and the environment

At Springer we firmly believe that an international science publisher has a special obligation to the environment, and our corporate policies consistently reflect this conviction.

We also expect our business partners – paper mills, printers, packaging manufacturers, etc. – to commit themselves to using materials and production processes that do not harm the environment. The paper in this book is made from low- or no-chlorine pulp and is acid free, in conformance with international standards for paper permanency.



Springer